INTERFACIAL PROPERTIES OF ULTRATHIN-FILM METAL ELECTRODES: STUDIES BY COMBINED ELECTRON SPECTROSCOPY AND ELECTROCHEMISTRY

A Dissertation

by

KYLE DOUGLAS CUMMINS

Submitted to the Office of Graduate Studies of
Texas A&M University
in partial fulfillment of the requirements for the degree of

DOCTOR OF PHILOSOPHY

May 2012

Major Subject: Chemistry

Interfacial Properties of Ultrathin-

Film Metal Electrodes: Studies by Combined Electron

Spectroscopy and Electrochemistry

INTERFACIAL PROPERTIES OF ULTRATHIN-FILM METAL ELECTRODES: STUDIES BY COMBINED ELECTRON SPECTROSCOPY AND ELECTROCHEMISTRY

A Dissertation

by

KYLE DOUGLAS CUMMINS

Submitted to the Office of Graduate Studies of
Texas A&M University
in partial fulfillment of the requirements for the degree of

DOCTOR OF PHILOSOPHY

Approved by:

Chair of Committee,	Manuel P. Soriaga
Committee Members,	Gyula Vigh
	James D. Batteas
	Xinghang Zhang
Head of Department,	David H. Russell

May 2012

Major Subject: Chemistry

ABSTRACT

Interfacial Properties of Ultrathin-
Film Metal Electrodes: Studies by Combined Electron
Spectroscopy and Electrochemistry. (May 2012)
Kyle Douglas Cummins, B.S., Rockhurst University
Chair of Advisory Committee: Prof. Manuel P. Soriaga

A pair of studies investigating the deposition and surface chemical properties of ultrathin metal films were pursued: (*i*) Pt-Co alloys on Mo(110); and (*ii*) Pd on Pt(111). Experimental measurement was based on a combination of electron spectroscopy (low energy ion scattering spectroscopy, X-ray photoelectron spectroscopy, Auger electron spectroscopy, and low energy electron diffraction) and electrochemistry (voltage efficiency, voltammetry, and coulometry).

Mixed-metal preparation of Pt-Co films by thermal vapor deposition (TVD) resulted in a thin-film binary alloy. Careful analysis revealed a substantial divergence between the composition at the interface and that in the interior. This outcome was observed for all compositions and allowed for the construction of a "surface phase diagram". The proclivities of the alloys of pre-selected compositions towards enhanced catalysis of the oxygen-reduction reaction were assessed in terms of their voltage efficiencies, as manifested by the open-circuit potential (OCP) in O_2-saturated dilute sulfuric acid electrolyte. The

particular alloy surface, Pt_3Co ($\chi_{Pt} = 3, \chi_{Co} = 1$), whether from the thin film or a bulk single crystal, exhibited the highest OCP, a significant improvement over pure Pt but still appreciably lower than the thermodynamic limit. Under test conditions, the degradation of thusly-prepared films was primarily due to Co corrosion.

Ultrathin Pd films on well-defined Pt(111) surfaces, with coverages from 0.5 to 8 monolayers (ML), were prepared by surface-limited redox replacement reaction (galvanic exchange) of underpotentially deposited Cu. Spectroscopic data revealed that films prepared in this manner are elementally pure, pseudomorphic to the substrate, and stable, independent of the surface coverage (Θ_{Pd}) of palladium. Analysis of the voltammetric profiles in the hydrogen evolution region revealed unique properties of hydrogen adsorption unseen in bulk electrodes. Notably, at 1 ML coverage, a step-free film was produced that did not exhibit hydrogen absorption. At higher coverages, digital (layer-by-layer) deposition gave way to 3D islands in a Stranski- Krastanov growth mode; under these conditions, onset of bulk-like behavior was observed. This method makes possible the synthesis of well-ordered noble-metal films in the absence of high-temperature treatment.

DEDICATION

This work is dedicated to my loving wife, Emily, and our daughter, Lily.

"And I asked myself about the present: how wide it was, how deep it was, how much was mine to keep."

— Kurt Vonnegut

ACKNOWLEDGMENTS

I wish to express deep gratitude to my mentor and advisor, Dr. M. P. Soriaga, for the countless hours of collaboration and advice. Imparted to me, through his encouragement and scholastic stewardship, were the virtues of academic creativity and intellectual accountability. A very special thanks is due to Dr. D. Wayne Goodman for providing me with the opportunity to expand my research horizons. Also, I give a special thanks to Dr. Wayne Hung and Dr. Bing Guo.

I would also like to state my appreciation for the efforts of my committee members: Dr. Gyula Vigh, Dr. James Batteas, and Dr. Xinghang Zhang for their illuminating contributions. Moreover, I would like to thank Dr. Marian Hyman, Dr. Larry Brown, and Dr. Steven Wheeler for their magnanimous assistance.

I wish to thank Fr. James D. Wheeler, Dr. James Chapman, and Dr. Annie Lee for taking a keen interest in my personal accomplishments.

I am grateful for the generous support I received from Soriaga group members Jack Baricuatro, Jean Sanabria-Chinchilla, Xiaole Chen, Juan Cruz, Ding Li, and Alnald Javier. Akhtar Mohammed Hossain deserves a special thanks for his collaborative work. Thanks also to Stephanus Axnanda, a co-worker in the study of alloy cathodes.

I am ever-so-grateful for the support and camaraderie I received from the many friends I have made at Texas A&M. Particular thanks to the Great Scotts, Brothers and Dempsey.

To my family whose love and support brought me my many opportunities- to my father, whose self-sacrifice and audacious insistence on self-reliance; to my mother's unending patience and adoration; to my brothers and sisters cavorting revelry; to my in-laws generosity- I am eternally in debt. Through your kinship, instilled in me were the virtues of integrity, ingenuity, persistence, deliberation, and the confidence to take an expansive embrace of life.

Lastly, I wish to thank my wife, Emily, for her everlasting love and inspiration. Without her, the denouement of this endeavor would have been insurmountable and evanescent.

NOMENCLATURE

ADC	Analog-to-Digital Converter
AES	Auger Electron Spectroscopy
CE	Counter Electrode
CHA	Concentric Hemispheric Analyzer
CMA	Cylindrical Mirror Analyzer
CPD	Controlled-Potential Deposition
CV	Cyclic Voltammetry / Voltammogram
EC	Electrochemistry
GCS	Guoy-Chapman-Stern
ICSD	Inorganic Crystal Structure Database
IMFP	Inelastic Mean Free Path
ISS	Ion Scattering Spectrum
LEED	Low-Energy Electron Spectroscopy
LEISS	Low Energy Ion Scattering Spectroscopy
LSV	Linear Scan Voltammetry
MFP	Mean Free Path
NHE	Normal Hydrogen Electrode
PEMFC	Proton Exchange Membrane Fuel Cell
ORR	Oxygen Reduction Reaction
PZC	Potential of Zero Charge
PZFC	Potential of Zero Free Charge

PZTC	Potential of Zero Total Charge
RDS	Rate-Determining Step
RE	Reference Electrode
RFA	Retarding Field Analyzer
SE	Sensing Electrode
SEM	Scanning Electron Microscopy
SLR^3	Surface-Limited Redox Replacement Reaction
STM	Scanning Tunneling Microscopy
TPD	Temperature Programmed Desorption
UHV	Ultra-High Vacuum
UPD	Underpotential Deposition
WE	Working Electrode
XPS	X-Ray Photoelectron Spectroscopy

TABLE OF CONTENTS

Page

LIST OF FIGURES

INTRODUCTION TO PART I: PLATINUM-COBALT ULTRATHIN FILMS*

Introduction

A fuel cell can be thought of as a cold-combustion device, capable of converting stored chemical energy into usable electrical energy. Without a large heat transfer, a fuel cell is not plagued by the conversion efficiency penalties that hot-combustion devices are subject to. However, unlike a battery, the fuel cell is not a closed system, as fuel and oxidant must be continuously supplied for operation. In an operating fuel cell, the fuel is introduced through the fuel feed plates, to the surface of the anode. Simultaneously, oxygen is delivered through oxidant feed plates to the surface of the cathode. The reactions that occur at the electrodes are facilitated by the surface properties of the catalyst present. At the anode, H_2 is oxidized to H^+ through the following reaction

$$H_2 \rightarrow 2H^+ + 2e^- \quad E^{0'} = 0.0V \qquad (1)$$

The positively charged protons will diffuse down their concentration gradient through the electrolyte, towards the cathode. The electrons will travel through the completed external circuit towards the cathode, where reduction of the oxidant will occur. Once at the cathode, electrons will recombine with H^+

This dissertation follows the style of the Journal of Electroanalytical Chemistry.

from the previous step and in the presence of oxygen, will react to form water:

$$\tfrac{1}{2}\mathrm{O_2} + 2\mathrm{H^+} + 2e^- \rightarrow \mathrm{H_2O}\ E^{0'} = 1.229V \qquad (2)$$

the overall reaction is the sum of reactions (1) and (2):

$$\mathrm{H_2} + \tfrac{1}{2}\mathrm{O_2} \rightarrow \mathrm{H_2O}\ E^{0'} = 1.229V \qquad (3)$$

This process is relatively simple and work on the hydrogen fuel cell is over 200 years old. Fuel cell research has grown from the work of Nicholson and Carlisle in 1800 concerning electrolysis of water [1]. In 1833, Michael Faraday proposed his laws of electrolysis [2] and two years later presented his theory on the "inter-relation of chemical affinity, electricity, heat, and magnetism" [3] to the Royal Institution. In 1843, William Robert Grove constructed and demonstrated the first functioning hydrogen fuel cell [4], or what he called the "gas battery". For much of the 19th century, the operation of the fuel cell remained a scientific mystery, until Friedrich Wilhelm Ostwald, founder of the field of physical chemistry, formulated, in 1893 the theoretical underpinnings of how the hydrogen fuel cell operates [1, 5, 6]. Following another 50 years of development, Francis Tomas Bacon introduced the first practical hydrogen-oxygen fuel cell. Bacon's work produced an alkaline fuel cell, which relies upon effective migration of anionic species to the anode. In his design, a 45% KOH

solution was used as the electrolyte, a nickel anode, and a lithiated nickel oxide cathode. By increasing the operating temperature to around 205 ^{o}C and the pressure to about 600 psi, Bacon was able to generate useful currents without boiling off the electrolyte. It wasn't until his team was able to increase the catalyst- electrolyte- gas interfacial area, by incorporating "dual-porosity" gas diffusion electrodes, that he was able to generate a 5kW system, capable of powering a welding machine, a circular saw, and a 2-ton capacity fork-lift truck [6, 7].

Of the common types of fuel cells, proton exchange membrane fuel cells (PEMFCs) show the most potential for commercialization and were the first to find practical implementation. In the 1960s, NASA's Gemini space flight used PEMFS for on-board power generation. Twenty years later, the California Environmental Government and the US Partnership for a New Generation of Vehicles program (PNGV) elected to promote the use of PEMFC in transportation applications [8]. Interestingly, a PEMFC employs a solid proton conducting membrane, commercially Nafion, which allows the PEMFC to operate at low temperatures with specific power (W/kg) and power densities (W/cm^3) higher than other designs. Therefore, in PEMFCs, the membrane and the electrode are the critical components. A major advancement towards commercialization of fuel cell technology is the development of the membrane electrode assembly (MEA). Presently however, two major obstacles remain: high cost and low reliability. The fuel cell catalyst is the main contributor to these problems. In current PEMFC construction, Pt metal dispersed on a support (for

both the anode and the cathode) is the most widely used electrocatalyst. Major drawbacks in employing Pt as the catalyst include high cost, sensitivity to contaminants, and loss of electroactive surface area [9, 10]. In 2007, the U.S. department of energy commissioned a multi-year fuel cell research program, the primary focus of which is to advance the technology for transportation application of fuel cells. The target, by 2015, is to develop a durable hydrogen fuel cell, which operates at 60% peak-efficiency and a cost of $30/kW[11].

Background

The mechanisms and reaction pathways of the oxygen reduction reaction (ORR) have been investigated thoroughly as an attempt to realize the promise of low cost, low temperature hydrogen fuel cells. As will be treated in a later section, the oxygen reduction kinetics are very sluggish compared with those at the anode, and remains a major bottleneck in the overall performance of fuel cells. Slow electrode kinetics result in large overpotentials associated with activation of the charge transfer reaction in the desired direction at an appreciable rate. The overpotential, η, is defined as the deviation of the electrode potential from its equilibrium value required to drive a given current density to flow through the electrode. Minimizing this excess potential is the ultimate goal of efforts to develop better electrocatalysts.

Cell Overpotentials

When a net current flows from a fuel cell, the terminal voltage of the cell, E_{cell}, drops from the open circuit voltage by a value that is proportional to the current flowing from the cell. In this case, the cell is said to be polarized. Polarization of a cell can be further classified into distinct categories, commonly three: activation polarization, concentration polarization, and ohmic polarization [12]. Polarization in each regime gives rise to net overpotentials; the effects of which and the role of the above stated polarizations are shown in Figure 1.

Activation Overpotential

Activation polarization is the potential drop across the cell that results from a net flow of current for reactions exhibiting slow electron-transfer rates. When this occurs, an amount of the output potential of the cell must first be supplied as energy of activation to the process, to keep up with the current demands of the cell. Many factors play a role in this loss: structure of the compact layer, interactions with solvent and electrolyte, interactions with the electrode surface, and low intrinsic reactivity. For most hydrogen-oxygen fuel cells, electron transfer is the rate-determining step (RDS); the oxygen-reduction rate at the cathode is on the order of 10^5 times less than the rate of hydrogen oxidation at the anode. This low rate constant is the most significant source of overpotential with respect to ORR at a Pt electrode and can quickly rise to 300-400 mV. The majority of studies on fuel cells are aimed at solving this problem.

Ohmic Overpotential

Ohmic polarization, or, ohmic losses in the cell are the result of the electrical resistance of the electrolyte, i.e. solution resistance. This overpotential scales linearly with current density, following Ohm's Law. This is an unavoidable drop, but can be minimized with careful materials selection and cell construction.

Concentration Overpotential

Concentration polarization is the potential drop across the cell that results from mass transfer requirements in the conditions of high current. It results from the need to deliver electroactive species from the bulk solution to the inner Helmholtz plane before electron transfer can occur. Even in cases of very large rate constants, concentration polarization will be present in perhaps tens of millivolts. However, fuel cells are rarely operated in the current range where this loss is significantly large compared to activation losses.

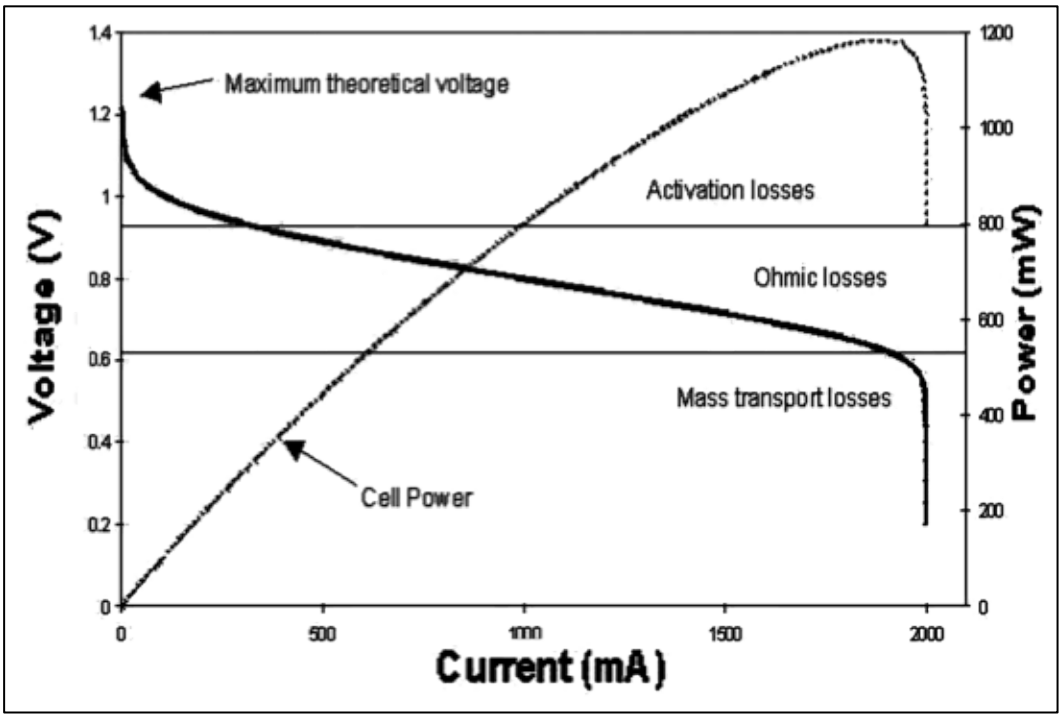

Figure 1. The sources of power losses within a fuel cell. Losses are due to activation polarization, Ohmic polarization and concentration polarization.

ORR Mechanism on Pt

As demonstrated by Gubbins and Walker, reduction of oxygen can proceed by one of two global pathways in acidic aqueous media [13].

1. Direct 4 e^- pathway:

$$O_2 + 4H^+ + 4e^- \rightarrow 2H_2O \; E^{0'} = 1.229V \tag{4}$$

2. Peroxide pathway:

$$O_2 + 2H^+ + 2e^- \rightarrow H_2O_2 \; E^{0'} = 0.67V \tag{5}$$

followed by either reduction of the peroxide

$$H_2O_2 + 2H^+ + 2e^- \rightarrow H_2O \; E^{0'} = 1.77V \tag{6}$$

or its decomposition

$$2H_2O_2 \rightarrow 2H_2O + O_2 \tag{7}$$

At the cathode, one or both of the reactions may be present simultaneously, and the products may feed into each other. More detailed descriptions of the overall mechanism and reaction process have been proposed

for various conditions [13]. A pathway that considers likely reaction intermediates and accounts for feedback from side reactions was proposed by Appleby and Savy (Figure 2) [14]. For a Pt surface, the "4 e^- direct reduction" process (so-named because it does not proceed through a peroxide intermediate) can be described as following a bridge-type Griffith's model of a transition metal oxide [15]. In this schema, bridge interactions with surface atoms sufficiently weaken the O-O bond, such that scission and step-wise protonation, accompanied by step-wise electron transfer, will occur. In the peroxide pathway, the O-O bond is insufficiently activated and after the transfer of two electrons, a stable peroxide (H_2O_2) is formed.

Some important considerations of these points are as follows. In the case where oxygen coverage of the electrocatalyst surface can be increased, more reduction will occur on oxide-covered sites, proceeding via k_1, thus favoring the direct $4e^-$ mechanism and operation closer to the reversible cell potential is realized. Additionally, the adsorption model proposed by Yeager indicates an importance on the spacing of metal centers relative to the oxygen. This gives us a good impetus to pay attention to the lattice parameters of alloy surfaces and how they pertain to catalysis.

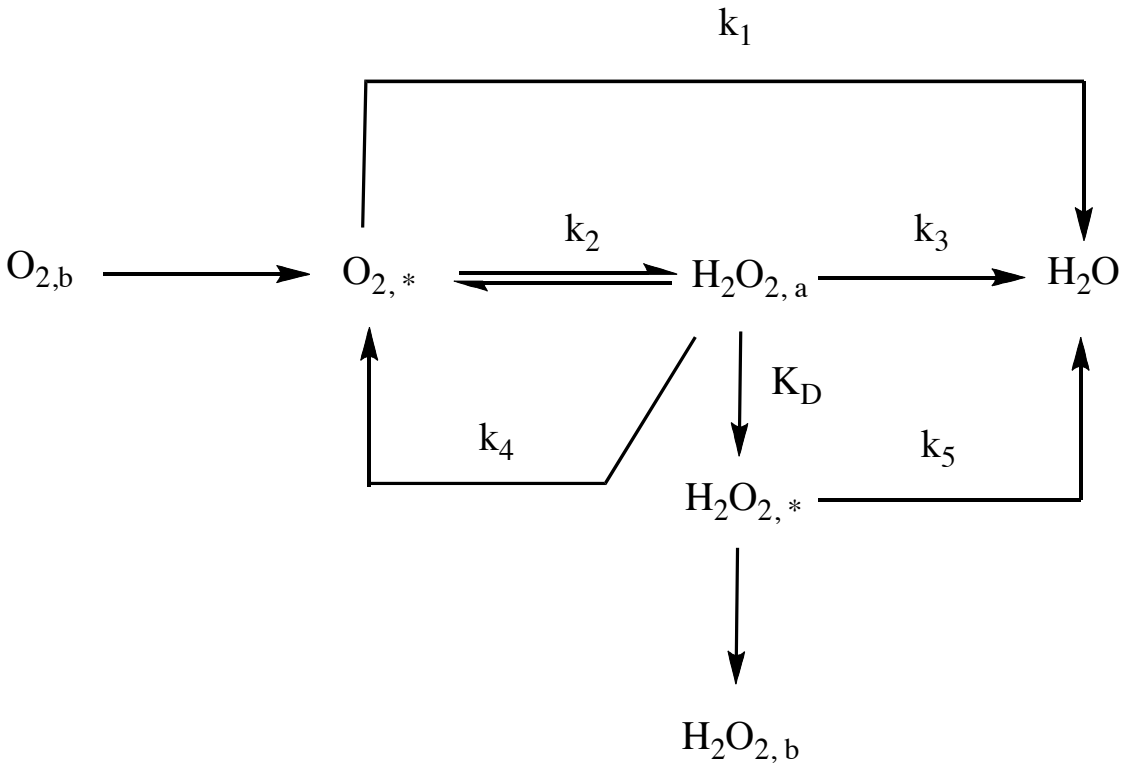

Figure 2. Reaction pathways for oxygen reduction as given by Appleby.

ORR Kinetics

Overall, the poor reactivity of oxygen can be explained in terms of the molecule possessing a large reorganization energy, λ, giving rise to a large free energy of activation for reduction, $\Delta G_{\mathrm{f}}^{\dagger}$, as predicted by the *Gerischer- Marcus* model of electron transfer:

$$\Delta G_{\mathrm{f}}^{\dagger} = \frac{\lambda}{4}\left(1 - \frac{\mathrm{E} - \mathrm{E}^{0}}{\lambda}\right)^{2} \tag{8}$$

where $\Delta G_{\mathrm{f}}^{\dagger}$ is related to the forward rate constant, k_{f}, by

$$k_{\mathrm{f}} = K \exp\left(-\Delta G_{\mathrm{f}}^{\dagger}\right) \tag{9}$$

and K is a collection of prefactors. Assuming an ideal quiescent solution at thermodynamic equilibrium; following a cathodic step for a one-step process, the current i_{f}, will be given by (10)

$$i_{\mathrm{f}} = nFk_{\mathrm{f}}C_{\mathrm{O}}^{*} \tag{10}$$

with the total current, i, given by the sum of cathodic (forward) and anodic (backward) currents.

$$i = i_f - i_b \tag{11}$$

satisfying the condition at equilibrium that there is no net current:

$$i_0 = i_f = -i_b \tag{12}$$

for a cathodic potential step,

$$k_f = k^0 \exp\frac{(-\alpha nF(E - E^{0'}))}{RT} \tag{13}$$

$$k_b = k^0 \exp\frac{((1-\alpha)nF(E - E^{0'}))}{RT} \tag{14}$$

substituting equations (10)-(14) yields

$$i = \left[nFk^0 \exp\frac{(-\alpha nF(E - E^{0'}))}{RT} \right] - \left[nFk^0 \exp\frac{((1-\alpha)nF(E - E^{0'}))}{RT} \right] \tag{15}$$

by defining the deviation of the electrode potential from the standard potential of the reaction as the cell overpotential (η) and factoring, the *Butler-Volmer equation* eqn. (18)(15) is obtained.

$$E - E^{0'} = \eta \tag{16}$$

$$f = \frac{F}{RT} \tag{17}$$

$$i = i_0 \left[e^{-\alpha n f \eta} - e^{(1-\alpha) n f \eta} \right] \tag{18}$$

for large values of $|\eta|$, i.e. a large negative or positive potential, the equation simplifies and rearranges to the *Tafel equation* (19),

$$\eta = \frac{2.3RT}{\alpha F} \log i_0 - \frac{2.3RT}{\alpha F} \log i \tag{19}$$

such that a plot of log i vs η gives two useful parameters, the exchange current i_0 and the transfer coefficient, α. By constructing a Tafel plot and relating i_0 to the activation energy, $\Delta G_f^{\dagger}$, of a given reaction, we can relate the electronic structure of an interface to the possible reactivity towards the surface. It is this relationship between orbital states and heterogeneous kinetics that paves the way for tuning materials for enhanced activity [12]; this tuning is the impetus behind catalyst screening and characterization efforts.

The theoretical underpinnings for the approach taken by many researchers can be traced back to work conducted in 1963 by Rao et. al., which

compared the oxygen coverage of various noble metals to their respective levels of *d*-band occupancy. In this experiment, clean electrodes were exposed to solutions bubbled with oxygen until they achieved a steady rest potential. After that, the amount of oxygen present on the surface was determined by coulometry in deaerated solutions and the coverage was calculated. The results of these experiments showed that the number of unpaired *d*-electrons per atom (*d*-band vacancy) is proportional to the amount of oxygen surface coverage (Θ_O) [16]. This study made a reasonable simplification that oxygen adlayer formation followed a closest packing structure, such that a layer of adsorbed oxygen atoms was composed of a stoichiometric PtO surface. In recent years however, the nature of the adsorbed oxygen species is shown not to be so well defined and likely contains multiple moieties, including PtO, PtOH, PtOHH, PtOOH [17]. Thus, absolute coverages given in the study cannot be relied upon. Nevertheless, the platinum group metals used in the correlation would be expected to have similar intermediates (coverage) because they all function as efficient cathodes. Therefore, the results are with relative merit and the conclusions still hold.

Because the level of oxygen coverage is a good indicator of the strength of the M-O bond and since oxygen chemisorption is a likely first step in the reaction mechanism, see Figure 3, the strength of this bond greatly affects the reaction rate. In their conclusion, the authors suggest that future work should be conducted with alloys, and a study performed in 1966 by Brooman et. al. did just that. Although the methodologies differ, the authors were attempting to

uncover a possible effect on ORR activity by alloying Pt with another metal, even though there was "little theory that might predict marked increases in activity [18]." What they uncovered was that even small amounts of Ru or Rh led to marked increases (4 times to 9 times the rates on pure Pt) in the rate of oxygen reduction. Up to that point, pure Pt had been the material of choice of all the metals as it showed the highest reactivity.

The invocation of *d*-band character as the primary influence on reaction rates continued to develop and reached maturity in the mid 1990s. The most notable developments are the studies that established the framework, which future studies would follow for tuning electronic properties of ORR catalysts. In 1995, Mukerjee et. al. conducted experiments which established parameters for selecting alloy systems based on empirical electronic properties and ORR activity[19]. In this study, the authors determined the *d*-band vacancy for a number of Pt-M/C supported alloys based on XANES spectra. The results were plotted against the cathodic current at 900 mV and compared to pure Pt/C. It was shown (Figure 4) that a limited increase in *d*-vacancies brought on by an alloying metal corresponded to increased electrocatalytic activity. Another notable development was a study published by Hammer and Nørskov [20]. Previously it had been accepted that for catalytically active metals, the inner orbitals are relatively constant as you move across the periodic table, therefore differences in activity can be accounted for by changes in the *d*-orbital occupancy.

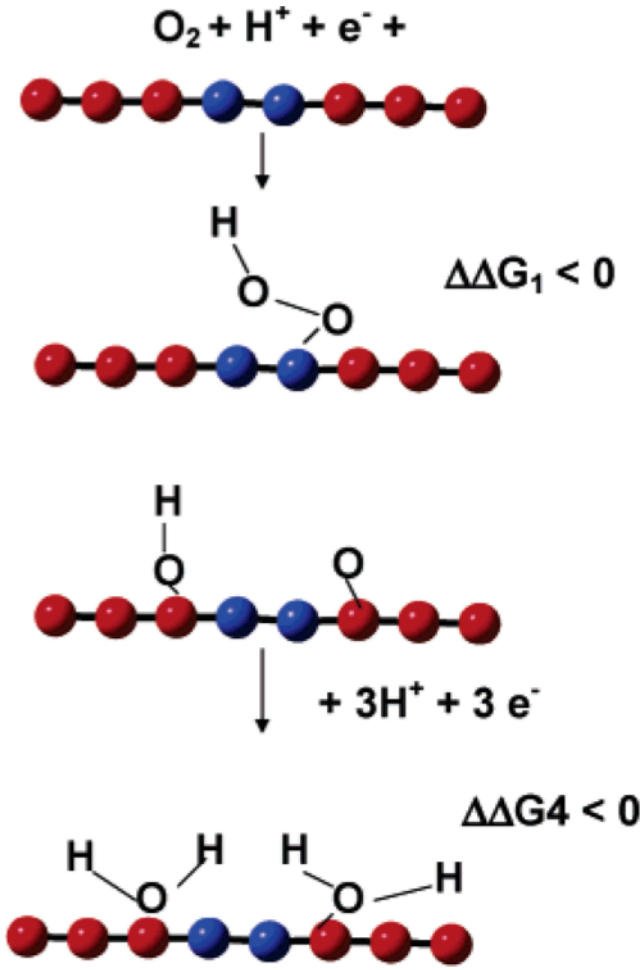

Figure 3. Proposed model for ORR, with dissociative adsorption occurring at electropositive metal sites [17]*.

*Reprinted with permission from "Design of Oxygen Reduction Bimetallic Catalysts: Ab-Initio-Derived Thermodynamic Guidelines" by Wang, Y. X.; Balbuena, P. B, 2005. *Journal of Physical Chemistry,* 109, 18902-18906, Copyright [2005] by American Chemical Society.

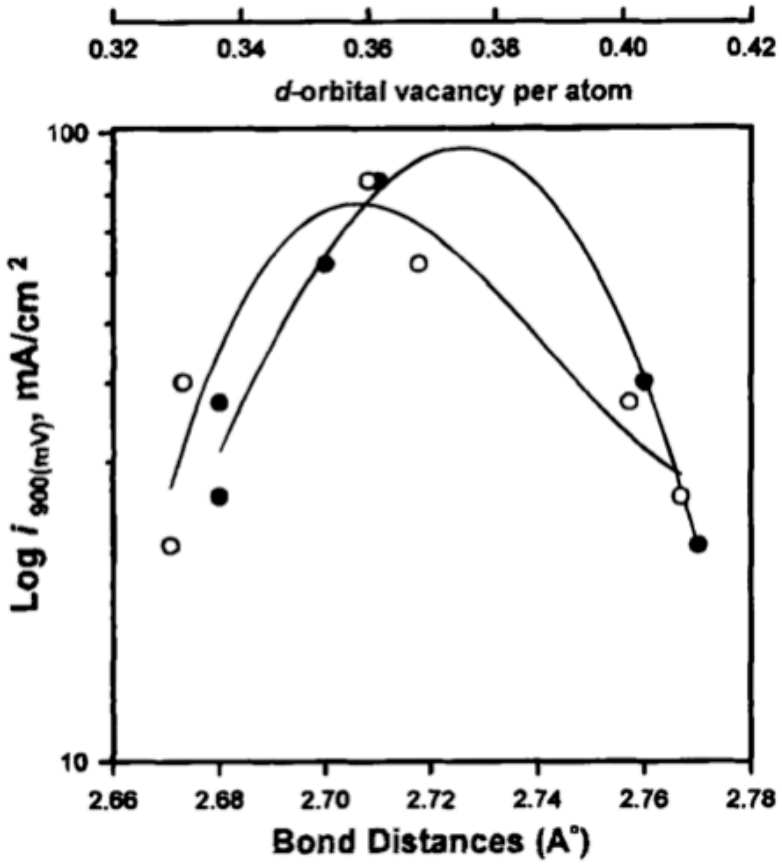

Figure 4. Correlation of oxygen electrode performance (Log $i_{900\,mV}$, mA cm-2) of Pt and Pt alloy electrocatalysts in PEMFC with Pt-Pt bond distance {●} and the *d*-orbital vacancy of Pt {○} obtained from *in situ* XAS .

While this explanation is a good starting point, more work needed to be done to establish the particular effects of *s*, *p* and *d*-orbitals along with the shifts in electronic density of states (DOS) caused by bonding and anti-bonding molecular orbitals in the metal–adsorbate interaction. It was concluded that the factor most affecting reactivity is the distribution of DOS of the metal relative to the Fermi level, or as a quick measure a weighted average of them, also known as the *d*-band center. With these studies, a mechanism of enhancement was put forth that explained the electronic considerations of selecting materials. What was lacking at this time was an explanation linking these effects to the ORR mechanism itself.

In 1999 Watanabe et. al. provided a convincing explanation for the volcano-type plots observed in previous studies of oxygen reduction on an alloy surface [21]. In this mechanism, the first step in the reaction is assumed to be an adsorption of oxygen to the metallic surface involving a lateral interaction of the O_2 2π orbitals with an empty Pt $5d_z^2$ orbital with backbonding from a partially filled Pt $5d_{xz}$ or $5d_{yz}$ to the O_2 $2\pi^*$. Assuming the RDS is the oxygen chemisorption (first electron transfer), the enhancement due to the alloying metal can be described as follows. Because less noble transition metals (i.e. Ni, Co, or Fe) have more 5*d* vacancies than Pt, the addition of these atoms into the Pt lattice increases the vacancies of the alloy over pure Pt. Increased vacancies result in a larger 2π electron donation from O_2 to the surface resulting in, not only increased O_2 adsorption, but a stronger M-O_{ads} bond. This causes a weakening of the O-O bond facilitating bond scission and transfer of the first

electron to oxygen. We can refer to this process as adsorption and O_2 dissociation (or dissociative chemisorption). When the O-O bond breaks, electrons are instantaneously donated from Pt 5*d* orbitals to the O 2*p*. When 3 electrons, accompanied by $2H^+$, have been transferred the oxygen-- atoms leave the surface as water molecules. This step can be referred to as product formation and desorption. Combined, the two overall processes are adsorption/ O-O bond breaking and product formation/ desorption. The first process (adsorption), accompanied by donation of electrons from O to the surface, is facilitated by increased d-band vacancies. The second process (desorption), accompanied by backdonation of electrons from the surface to O, is facilitated by decreased *d*-band vacancies; thus an increase in *d*-band vacancy would promote the first step and impede the latter. This could explain why plots of activity vs. % alloy composition always rise to a maximum and then drop. As vacancies (% alloy) increase up to the optimum value, faster reaction rates are observed due to higher O_2 coverage and rate of bond scission. When the content of the alloying atom exceeds the optimum value, the resulting d-band vacancy is too large and contributes only to bond scission and with decreasing backdonation, less desorption and the surface becomes "passivated".

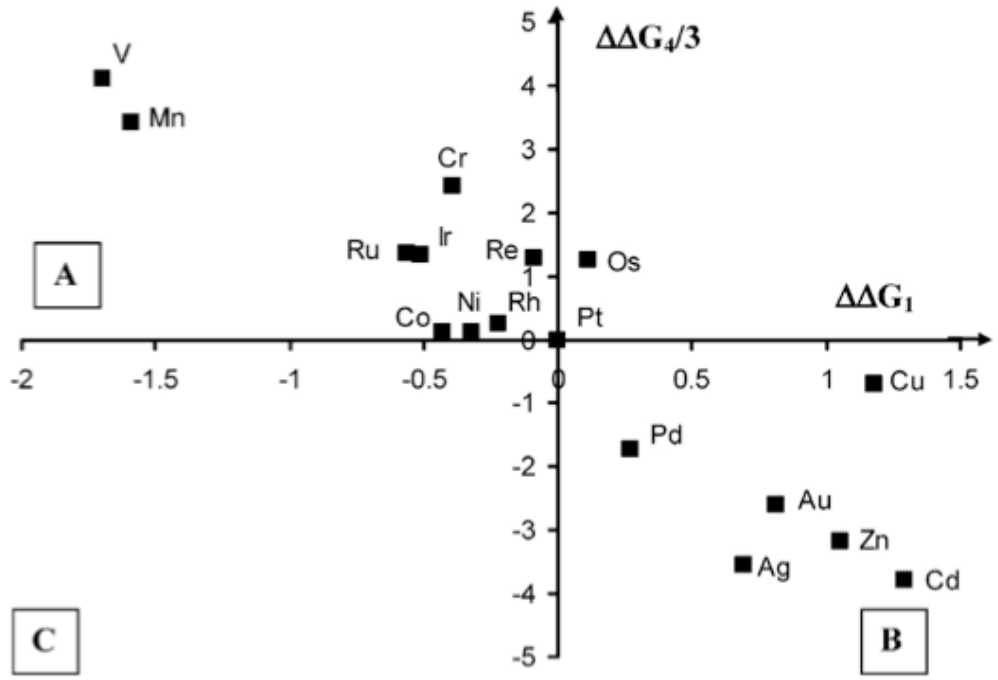

Figure 5. Plot of $\Delta\Delta G_4/3$ vs. $\Delta\Delta G_1$ for a number of transition metals. The values represent the free energy of O_2 adsorption and O_{ads} reduction respectively, relative to pure Pt. Elements in quadrant [C] are ideal candidates for ORR [17]*.

*Reprinted with permission from "Design of Oxygen Reduction Bimetallic Catalysts: Ab-Initio-Derived Thermodynamic Guidelines" by Wang, Y. X.; Balbuena, P. B, 2005. *Journal of Physical Chemistry,* 109, 18902-18906, Copyright [2005] by American Chemical Society.

Recently, a set of thermodynamic guidelines for the selection of materials in alloy systems for oxygen reduction was developed by Allen Bard [22]. In this study, the authors simplified the overall mechanism similar to the work above. The process is described as O_2 adsorption with bond cleavage followed by reduction with product desorption. Following this logic a scheme was described that treats oxygen adsorption as "surface metal oxidation." Metals that strongly favor oxidation will favor O-O cleavage and highly stable (MO) intermediates. These materials are unusable for power generation because the potentials required to reduce the adsorbed oxygen are too negative. On the other hand, materials that oppose M-O bond formation would be suitable for the reduction but lack an ability to adsorb dissolved O_2. The approach, then, is to combine effective oxygen bond cleaving metals with a second metal that is efficient at O_{ads} reduction. Using this scheme, an approximate model was put forth and is shown in Figure 3. In this approach, bimetallic alloy systems would have oxygen adsorbing on the sites which favor M-O bond formation, followed by O_{ads} migration to sites which favor reduction.

Continuing upon this work, Balbuena added considerations for the elementary steps involved in the overall mechanism and provided theoretical calculations for the free energy associated with each [17]. The clever graphical approach allows for a quick determination of which materials are suitable for alloying and why. In Figure 5, the axes labeled as $\Delta\Delta G_1(x)$ and $\Delta\Delta G_4/3(y)$ correspond to the reactions (21) and (24), respectively, with $\Delta\Delta G$ equal to the difference between ΔG of the indicated reaction on a given metal and ΔG of the

same process on Pt. It becomes abundantly clear why Pt is the most suitable pure electrocatalyst: it offers the minimization of $\Delta\Delta G_4/3$ and $\Delta\Delta G_1$ e.g., the smallest ΔG for both processes depicted in Figure 5, which can be labeled, adsorption/dissociation and reduction/ desorption.

$$\mathrm{O_2 + M + \partial e^- \rightarrow OO^{\partial-}\text{–}M}$$
$$\mathrm{OO^{\partial-}\text{–}M + H^+ + (1-\partial)e^- \rightarrow OO\text{-}M} \quad (20)$$

$$\mathrm{O_2 + M + H^+ + e^- \rightarrow HOO\text{-}M} \quad (\Delta G_1) \quad (21)$$

$$\mathrm{HOO\text{-}M + M \rightarrow HO\text{-}M + O\text{-}M} \quad (\Delta G_2) \quad (22)$$

$$\mathrm{O_2 + 2M + H^+ + e^- \rightarrow O\text{-}M + HO\text{-}M} \quad (\Delta G_3) \quad (23)$$

$$\mathrm{HO\text{-}M + O\text{-}M + 3H^+ + 3e^- \rightarrow 2H_2O + 2M} \quad (\Delta G_4) \quad (24)$$

It is also clear which metals offer good choices as alloy components and why certain alloys display higher reactivities than Pt alone. For instance, Co and Ni both have more negative $\Delta\Delta G_1$ with a minimal increase in $\Delta\Delta G_4$. The ideal electrocatalyst alloy would exhibit negative $\Delta\Delta G_1$ and $\Delta\Delta G_4$. To this end, alloying Pt with a less noble transition metal, such as Co or Ni, has been the subject of numerous investigations and has the added benefit of decreasing specific materials costs and improved stability.

Approach

Proposed explanations of the origin of Pt_3Co activity towards ORR previously studied by many groups [21, 23-25], can be divided into 3 main categories: (i) change in electronic structure of Pt (5*d* orbital vacancies)[26]; (ii) change in Pt-Pt bond distance and coordination number[27]; (iii) change in adsorption site for oxygen-containing species from Pt or alloying element [28]. Recently, a combined UHV (LEIS and AES) and electrochemical study was undertaken by Stamenkovic et. al. to characterize the surface properties of Pt_3Co and Pt_3Ni alloy catalysts and relate the information to the intrinsic catalytic activity towards ORR in acid electrolytes [26, 29]. In their study, LEIS was used to analyze the surface composition of the system before and after the catalytic activity determinations. They found that when Pt_3Co and Pt_3Ni are annealed at 1000 K, the surface will consist only of Pt atoms, which they called "Pt skin".

However, when lightly sputtered, the Pt_3Co surface became 75% Pt. They then compared the catalytic activity of the annealed (Pt skin) and unannealed catalysts. From voltammetric experiments of Pt_3Co (unannealed) in 0.1 M $HClO_4$, they observed a diminution in the H_{upd} pseudocapacitance compared to H_{upd} of pure Pt. They attributed this to the lower number of available Pt atoms on the surface compared to pure Pt. Interestingly, the "Pt-skin" electrode's voltammetry data exhibited similar H_{upd} results. They attributed this to the change in electronic state of surface Pt affected by the presence of underlying alloying metals. However, they mentioned that a "Pt-skin" electrode shows changes in cyclic voltammetry after the first cycle but did not provide any

stability data of the catalyst after each CV. In the present study, LEIS, XPS and electrochemistry were combined to develop a surface composition diagram of Pt-Co with varying bulk composition using LEIS as the main characterization technique. This is the first study considering the difference in surface versus bulk composition of Pt-Co. From this study, it is shown experimentally that Pt will surface segregate when the catalyst is annealed to 900 K (the temperature required to achieve intermixing).

Following the idea of tuning surface electrocatalytic properties by underlying metals, Brankovic, Wang, and Adzic [30] introduced a novel method to conduct atomic layer deposition of *noble metal* films onto *noble metal* surfaces via a process called surface-limited redox replacement reaction (SLR^3). This method is also referred to as galvanic displacement [31-33]. Presumably, modification of an overlayer metallic film by the underlying constituents will exert the electronic effects needed to affect catalysis. The SLR^3 method exploits the unique property of UPD to form uniform and epitaxial adlayers for templating noble-metal deposition. In this approach, a sacrificial less-noble metal (e.g., Cu) is first deposited on a noble metal (such as Pt) by UPD. Subsequently, ions of a more noble metal (e.g., Pd^{2+}) spontaneously oxidize the sacrificial adlayer and are reduced and deposited onto the substrate at open circuit potential (OCP). The step-wise reaction cycle may be repeated seemingly *ad-infinitum* to produce ultrathin films of desired thickness. The positive potential difference between the equilibrium potential of the noble metal in contact with its solvated ions and the equilibrium potential of the sacrificial or

mediator admetal is the driving force of the spontaneous deposition of noble metals in SLR^3 [30]. In SLR^3, one atomic layer of a noble metal is deposited at a time. Hence, it may be termed as *digital deposition*, i.e., the reverse process of *digital etching*, which is the removal one atomic layer at a time [34-36]. Another remarkable significance of the galvanic displacement method is its ability to deposit epitaxial metal films even for systems with a large lattice mismatch such Cu on (111)-oriented Au (11% mismatch) [37]. Epitaxial growth of metal films on such systems by conventional electrodeposition method is not possible.

Galvanic displacement has been successfully employed to produce monolayer electrocatalysts. Adzic and coworkers have synthesized monolayer Pt ORR electrocatalyst shells on Pd [31], Pd_3Co [38], PdPb, PdFe, PdPt [39], Pd_2Co/C [40], $AuNi_{0.5}Fe$ [41], and PdCo/C [42] cores via galvanic displacement of a UPD adlayer of a sacrificial metal. It has been found that the Pt_{ML}@Pd or Pd alloys with core-shell structures have approximately 4 to 5 times higher mass activity towards ORR compared to those of massive state-of-the-art Pt catalysts [40].

EXPERIMENTAL METHODS FOR PART I

Ultrahigh Vacuum (UHV) Surface Analysis

Materials interact with the outside world through their surfaces; inscrutably then, heterogeneous catalytic reactions occur at surfaces. Therefore, the role of the surface in the reaction must be determined if one is to understand the processes transpiring. This enlightenment is achieved by characterizing various aspects of the surface. Such aspects include surface order, surface structure, surface composition, local electronic structure, and surface segregation. Further, each reaction gives rise to surface products and reactants (adsorbed/desorbed), which may also interact with the surface atoms-substrate-support system. Because of this complex system, fundamental studies of a catalyst must include the study of a model surface. Such substrates are termed *well-defined* and are provided through the use of single-crystals. By employing single crystals in the study of surfaces, results are more meaningful because reproducible qualitative and quantitative comparisons of surface behavior, before and after each set of reaction conditions, can be achieved.

The overriding complication in the characterization of single-crystal surfaces is the effect of ambient gases near the interfacial region. Production and maintenance of the *well-defined* surface requires that the surface remain free of contaminants. This necessitates surface-atmospheric conditions that provide contaminant-free environments. Further, experiments that are designed to provide surface physical and chemical information must employ methods which interact only with the surface and near-surface regions. This obviates the use of

classical analytical tools of materials science- because their methods lack the cleanliness required and are indiscriminate towards analysis of bulk and surface atoms. To overcome these obstacles, two interdependent requirements must be met to allow the use of well-defined surfaces: 1.) The use of ultra-high vacuum (UHV) atmospheres (UHV chambers); and 2) The use of low-energy particles in analysis.

The interdependence of the above requirements is given by the very short mean free path (MFP) of particles in UHV. Pressure conditions maintained in the UHV-range are typically $\leq 10^{-9}$ torr; for perspective, this is roughly the pressure of interstellar space between the earth and moon. In this pressure range, the MFP of residual gases is so large as to minimize contact with the surface under study for the timescale of the experiment. The Kinetic Theory of Ideal Gases states that the rate (R/ molecules$\cdot$cm$^{-2}\cdot$s^{-1}) a surface is bombarded will be given by

$$R = \frac{1}{4} nv \tag{25}$$

where n is the number of molecules per unit volume and v is the mean speed of molecules. These values are dependent on gas pressure P and temperature T, by

$$P = nk_{\mathrm{B}}T \tag{26}$$

$$v = \sqrt{\frac{8k_B T}{\pi m}} \tag{27}$$

with k_B representing the Boltzmann constant and m the molecular weight of the ambient gas. Following substitution and unit-conversion, the bombardment rate can be re-expressed as

$$R = 3.52 \times 10^{22} \frac{P}{\sqrt{mT}} \tag{28}$$

Equation (28) represents a functional, where the bombardment rate can be calculated from P/ torr, m/ g·mol^{-1}, and T/ K. Most solids exhibit a surface packing density (Γ_{sub}/ atoms·cm^{-2}) of around 10^{15}. Assuming a sticking coefficient of 1, the length of time required to saturate a surface, i.e. Θ_{ads}=1 (where $\Theta_{ads} = \Gamma_{ads} / \Gamma_{sub}$), at T=300 K is given in Figure 6. From this plot, a few conclusions can be made. First, at atmospheric pressures, a clean surface will be maintained for nearly a microsecond. Next, so-called high-vacuum conditions (HV, P~ 10^{-6} Torr), those readily attainable by turbo-molecular pumps, result in a surface that is only clean for about 2 seconds. Finally, UHV conditions can maintain clean surfaces for thousands to tens of thousands of seconds, i.e. hours to days. Furthermore, to a smaller degree of necessity, without such a long MFP gas particles within the chamber would be free to interact with the particles and photons involved in surface analytical techniques.

Surface analysis techniques are thus named due to their unique sensitivity to the surface and near-surface region. The surface of a material possesses a remarkably low population of atoms, typically on the scale of 10^{15} atoms·cm^{-2}, relative to that of bulk atoms, typically 10^{23} atoms·cm^{-3}. This very low surface area-to-volume ratio gives rise another complication; how to restrict analysis to the surface? It would make sense to increase the surface area-to-volume ratio of the sample, but doing so is at the sacrifice of the well-defined surface. An alternative to this approach is the employment of techniques whose probe and signals are restricted to the surface atoms. This task is accomplished through the use of electrons/photons/ions of low, well-defined energy.

In essence there are two reasons for the widespread use of such particles. (i) Charged particles are easy to produce, maneuver, and detect. (ii) It was found empirically that particles with energy in the range of 10 to 1000 eV have *inelastic mean free paths (IMFP)* in solids of 3 to 20 Å, the atomic scale [43-45]. This limitation means no signal able to escape the material is due to bulk species; this fact forms the basis of surface sensitivity and is exploited by all surface analytical techniques. Figure 7 demonstrates this relationship in what is known as the "universal curve" [46-48]. The curve is representative of all materials and it can be seen that the ideal range for surface sensitivity is in the region indicated above, the so-called "sweet-spot". At lower KE (<50 eV) the IMFP increases with decreasing KE; at these low energies, the available states into which electrons may be scattered is diminishing. At larger KE (>100 eV) the IMFP increases with increases KE; at these energies, the interaction time is short and thus the electron

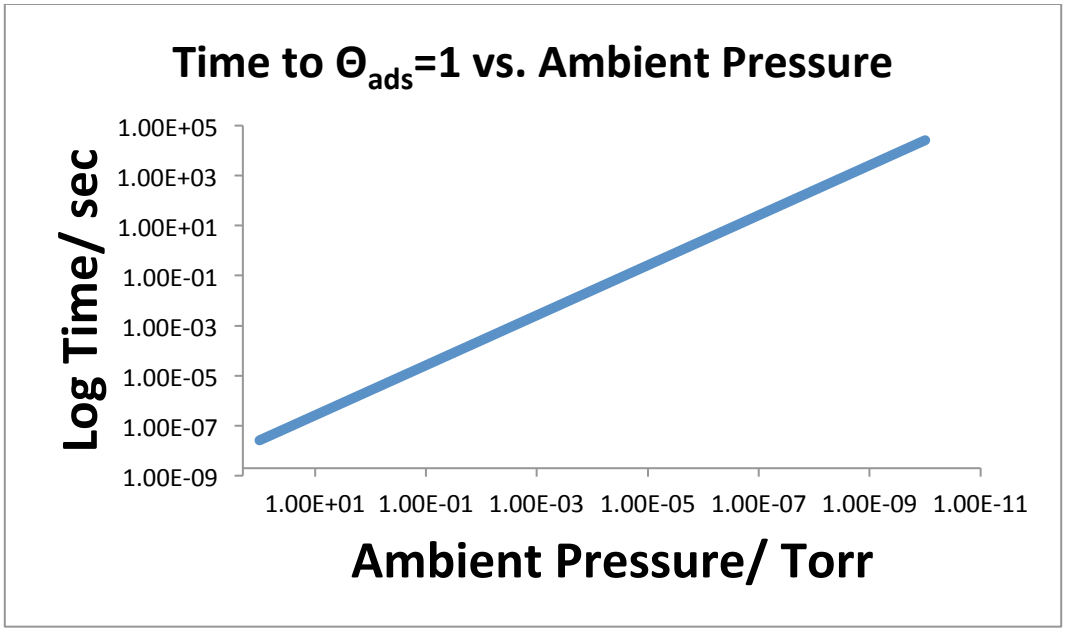

Figure 6. The amount of time needed to saturate a surface at indicated gas pressure. Calculated for CO at 300K assuming unity sticking probability. Only UHV conditions provide sufficient clean time.

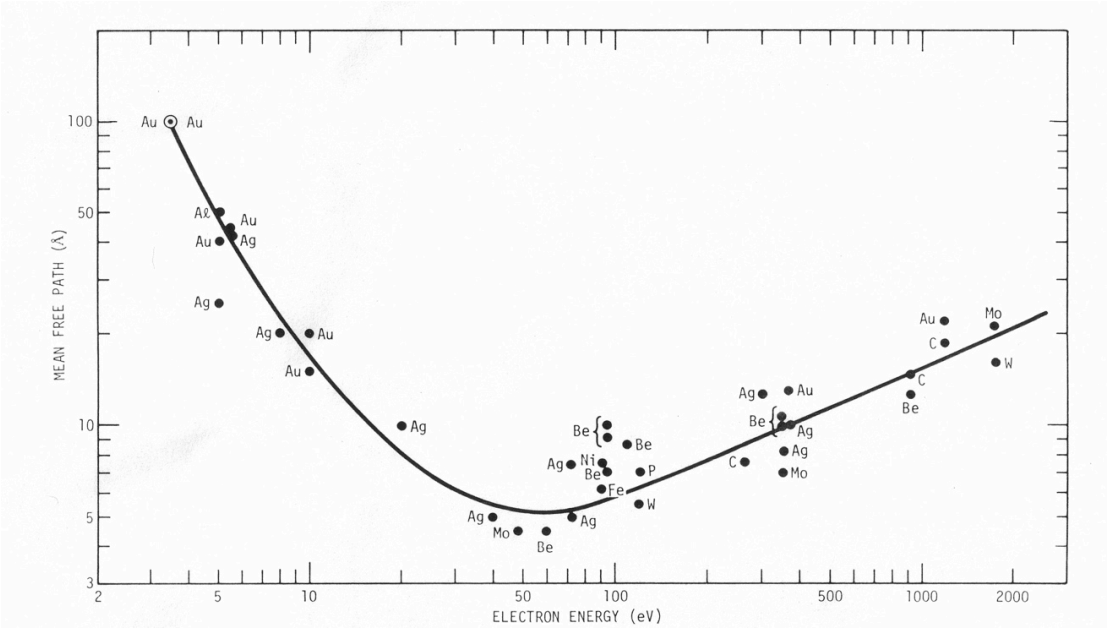

Figure 7. "Universal curve:" Electron IMFP as a function of electron kinetic energy. Adapted from [48].

travels undisturbed through the material. Within the "sweet-spot," electrons have just enough energy to penetrate a few atomic layers while allowing accessible electronic states to inelastically scattered processes. It should be underscored that UHV is required to allow probe and signal particles to travel without suffering collisions from contaminating gas particles.

All the surface-sensitive methods used in this dissertation will be described. In PART I, XPS, LEISS, and TPD will be discussed. In PART II, AES and LEED will be presented.

X-ray Photoelectron Spectroscopy

As described previously low energy particles, such as electrons, are used to probe a sample surface. In these electron spectroscopies, photons or electrons are impinged upon a surface and an emission of electrons (or photons) occurs, provided the energy of the projectile is greater than the work function (Φ) of the material. The work function of a solid is defined as the minimum energy required to remove an electron from the highest occupied energy level in to the "vacuum level".

One of the most time- honored of these techniques is X-ray Photoelectron Spectroscopy (XPS). The major benefit to this techniques is that it provides information on the electronic structure of near-surface atoms [49, 50]. In this technique, photons of energy $h\nu$ impinge upon a surface and induce electron emission from lower-lying core levels. A related technique is Ultraviolet Photoelectron Spectroscopy (UPS), in which much lower energy photons are

used and the emitted electrons come from valence states. Figure 8 illustrates the X-Ray photoemission process.

As shown, a monochromatic beam of X-Rays penetrate the sample surface, causing emission. These core levels correspond to electrons at inner quantum shells (strongly-bound), while valence levels correspond to electrons in the partially filled outer quantum shells (weakly- bound). By convention, the binding energy (E_B) of the ejected electron is reported. The total energy exchange involved in this one-hole process cannot exceed the energy of the photon hν, i.e.,

$$h\nu = E_B + E_{kin} + \phi \tag{29}$$

more commonly, this is expressed to reflect the spectral convention,

$$E_B = h\nu - E_{kin} - \phi \tag{30}$$

where E_{kin} is the kinetic energy of the final detected particle. For a given element a set of characteristic peaks result and this may be used for identification purposes, provided a suitable reference or complementary technique is used. More important, however, is that as the bonding environment of the atom changes, so will E_B for a given orbital. These subtle changes can be used to identify differences in oxidation state [51, 52].

XPS measurements made in this study were performed using a Perkin-Elmer 5500 XPS system (Perkin-Elmer- Waltham, Massachusetts), equipped with a Mg/Al water-cooled dual anode, operating with an un-monochromatized Al K_α (1486.6 eV) source at a 45° emission angle. Resulting

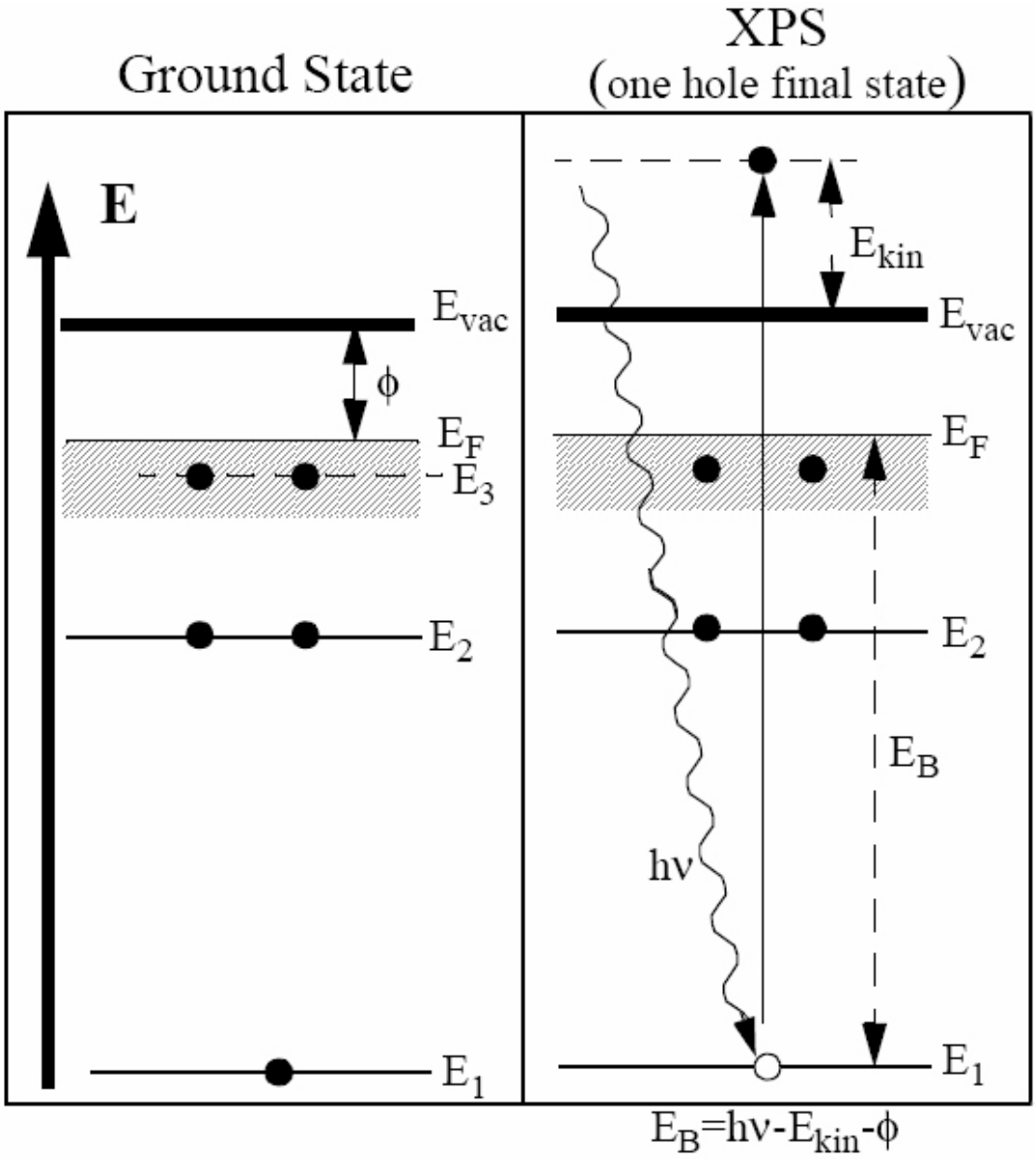

Figure 8. Schematic of the *x*-ray photoelectron emission process occurring in an XPS measurement.

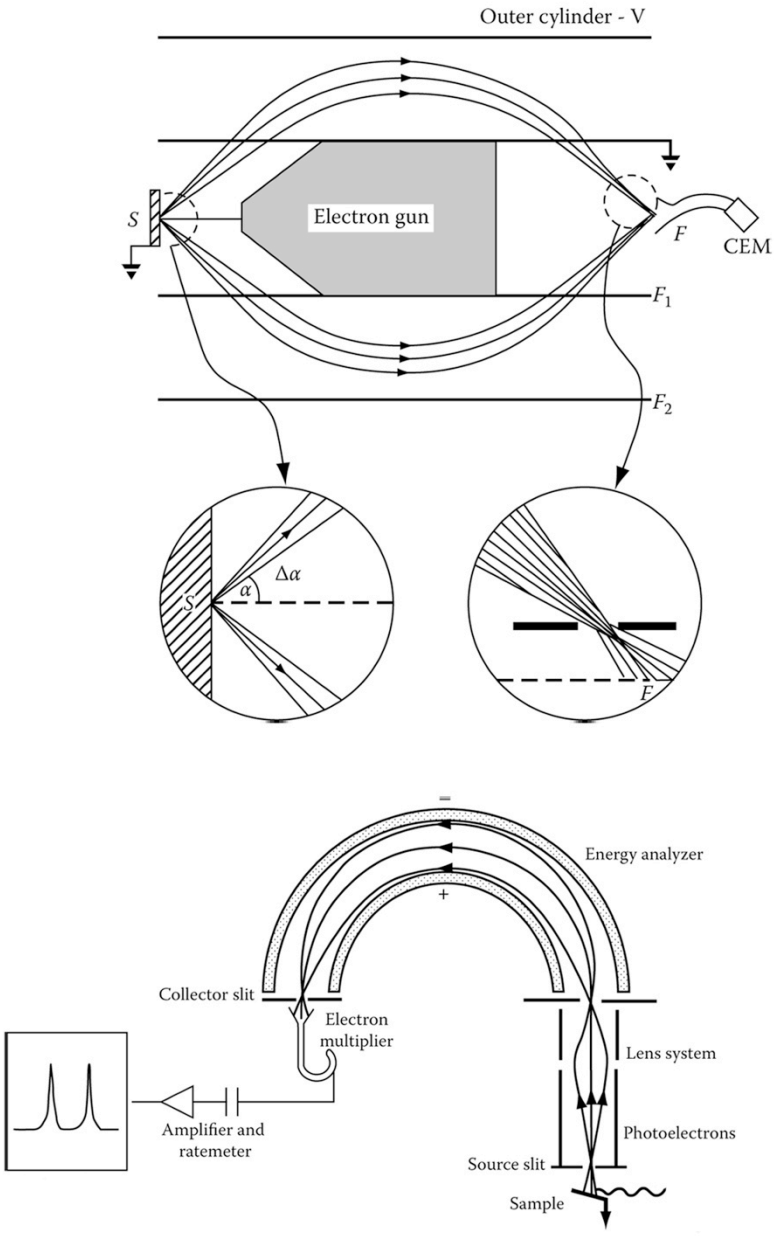

Figure 9. Schematics of energy analyzers used in the following studies. CMA (top) used for AES. CHA (bottom) used for LEISS and XPS.

photoelectrons were collected and analyzed using a PHI Precision Energy 10-360 (PHI- Chanhassen, MN) Spherical Capacitor Analyzer (SCA), in 16-channel multiplex, constant pass-energy mode with typical pass energy of 58.70 eV and an analyzer resolution of 0.59 eV. A schematic of the analyzer is given in Figure 9. Survey scans were collected to ensure sample purity. High-resolution scans were used in data analysis and represent the signal average of five scans. Data collection time was kept to 60 s or less to mitigate sample charging effects.

Low Energy Ion Scattering Spectroscopy

In a LEISS experiment, a target surface is irradiated with a beam of inert-gas ions (He^+, Ne^+ or Ar^+) of energy between 20 eV to 500 eV, and the backscattered primary ions are energy-analyzed, Figure 10. The backscattering can be modeled as a classical two-body inelastic collision between the incident ion and the topmost surface atom that obeys the conservation laws of energy and momentum.[53]

If the incident ion has a mass of M_1^+ and kinetic energy of E_0, and the ion backscattered angle θ (relative to the direction of the incident ion) has energy E_1, the classical two-collision model (with the surface atom of mass M_2) allows the determination of the surface elemental composition based on equation (31):

$$\frac{E_1}{E_0} = \left(\frac{1}{(1+A)^2} \right) \cdot \left(\cos\theta \pm \sqrt{A^2 - \sin^2\theta} \right)^2 \qquad (31)$$

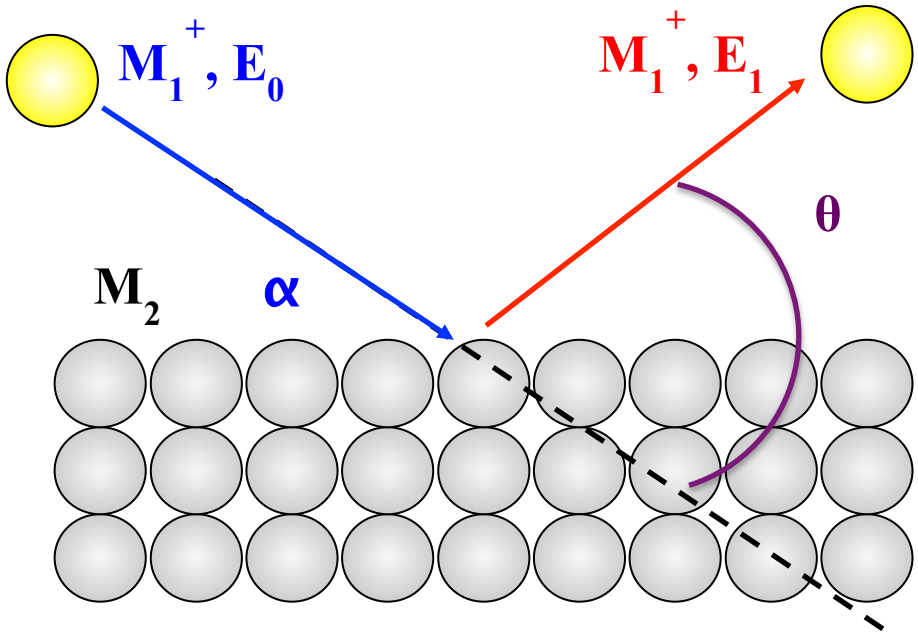

Figure 10. Schematic of the inelastic scattering process of low energy ions occurring in LEISS.

where $A = M_2/M_1$; the positive term represents solutions for A >1, whereas the negative term is for $| \sin \theta | \leq A \leq 1$. Since the energy of the incident ion is relatively low, there is virtually no damage to the surface. In addition, because of the repulsive nature of the ion-atom interaction, a shadow cone is formed past the target surface atom and a blocking cone is generated at adjacent surface atoms; these cones prevent interactions between the incident ion and subsurface which renders LEISS its unique sensitivity only to the outermost atoms.

In a LEISS spectrum (*vide infra*), the backscattered intensity is plotted against E_1/E_0; a high-intensity peak corresponds to a topmost atom of a given mass, and the relative intensities provide a measure of the surface concentrations. Since the atoms scatter with different intensities, sensitivity factors f_{ij} for each element must be obtained by calibration. For example, for an alloy film consisting of Pt and Co, the surface concentrations C_{Pt} and C_{Co} can be extracted from the following equations:

$$C_{Pt} = \frac{I_{Pt}}{I_{Pt} + \left(f_{Co-Pt}\right)\left(I_{Co}\right)}$$
$$C_{Co} = \frac{I_{Co}}{I_{Co} + \left(f_{Pt-Co}\right)\left(I_{Pt}\right)} \qquad (32)$$
$$C_{Co} = \frac{I_{Co}}{I_{Co} + \left(f_{Pt-Co}\right)\left(I_{Pt}\right)}$$

where $f_{Pt\text{-}Co}$ is the ratio of the scattering intensities for the pure Pt and pure Co films, and I_{Pt} and I_{Co} are the scattering intensities from Pt and Co in the alloy.

The power of LEISS lies in its ability to assay the elemental composition of the outermost layer of an alloy surface.

In this study, LEISS measurements were made using using a PHI 04-303 differentially pumped ion gun (PHI- Chanhassen, MN), with UHP He as the primary ion source. Measurement area was relegated to a 250 μm-diameter spot in the center of the sample surface without rastering. The primary ion beam energy was adjusted to 1.05 keV with a beam current of less than 10 nA- measured directly via the biased stage. Experiments were conducted at room temperature unless otherwise indicated. Scattered ions were analyzed using a PHI SCA 10-360 concentric hemispherical analyzer (CHA) Figure 9 (PHI-Chanhassen, MN) at a scattering angle of $\theta = 135°$. As with XPS, a survey scan was collected to identify topmost surface species present. Data analysis was performed on high-resolution scans, which represent the signal of a single scan. Data was collected at room temperature unless otherwise indicated.

Temperature Programmed Desorption

Temperature programmed desorption (TPD) is a simple technique for studying surface-adsorbate adsorption enthalpy and kinetics of desorption. In this experiment, the temperature of a sample is increased linearly with time and desorbed species are detected using a mass spectrometer. Plots produce a spectrum of signal intensity for a given m/z as a function of time.

Useful analytical tools exist for quantitative analysis of TPD spectra, though none were employed here. Pertinent kinetic and thermodynamic parameters of the adsorption/desorption process may be determined by

Redhead analysis, leading edge analysis, or application of the Clausius-Clapyron equation [54].

In the present study, TPD spectra were collected as a set of curves to provide semi-quantitative information on alloying metal concentration. Analysis of the desorbed gas phase species was conducted by continuous monitoring of the 59 amu signal using a UTI 100C precision mass analyzer (UTI Instruments Company- Sunnyvale, CA). For most experiments a 5 K/s temperature program was employed. The quadrupole mass spectrometer (QMS) was mounted behind a 1/8" diameter aperture closely positioned (~1 mm) to the front side of the sample in a direct line of sight [55]. The heating is restricted only to the sample, avoiding signal from other ad-atom sources, such as the sample holder.

Electrochemistry

Voltammetry

Voltammetry is a widely used group of routine potentiodynamic electrochemical methods in which current flow at the WE is recorded as a function of applied potential. In this method, the WE is initially held at potential E_0 and swept to a desired potential E_1 at a rate v. In linear sweep voltammetry (LSV), the experiment is complete upon reaching E_1 and subsequent analysis is pursued. In cyclic voltammetry (CV), E_1 represents a switching potential, at which the polarity of the electrodes is reversed and scanning continues to E_2; electrode polarity is then reversed again and scanning is terminated at E_f. typically, E_0=E_f and is often OCP for the system under study. The greatest value of cyclic voltammetry in this study derives from its high sensitivity to the small

changes accompanying the elemental identity of species on the electrode surface. Appropriately, two limitations are low peak resolution and the consideration that changes in recorded current lag behind the actual faradaic processes at a given potential. These limitations are partly mitigated by the use of very low scan rates, allowing kinetically hindered surface processes to be observed [12].

Cyclic voltammetry was conducted according to the following procedure. Once introduced to the electrolyte, the system was allowed to remain at rest for twenty minutes to reach a steady state. Before any experiments started, the open-circuit potential (OCP) of the system was recorded. Scans started at OCP and were commenced cathodically to the hydrogen region and reversed. The upper switching potential was dependent upon the experiment. After scans were complete, the OCP was recorded and the sample removed. CVs were collected at a scanning rate of 1 mV/s unless otherwise indicated. Chronoamperometry was employed for all potential holding experiments. The Amperograms were recorded, but not presented here. E_0= OCP; E_1= indicated holding potential; t_1= indicated holding time.

ORR Voltage Efficiency Analysis

The OCP values for test electrodes immersed in an electrolytic solution saturated with O_2 gas are simple to determine, yet provide a reliable diagnostic on the viability of a given material as an oxygen cathode. Figure 11 provides a schematic of this experiment and the *theoretical* OCP of an $O_{2(g)}$-saturated cathode relative to a standard hydrogen electrode (SHE) would be 1.229 V. Since

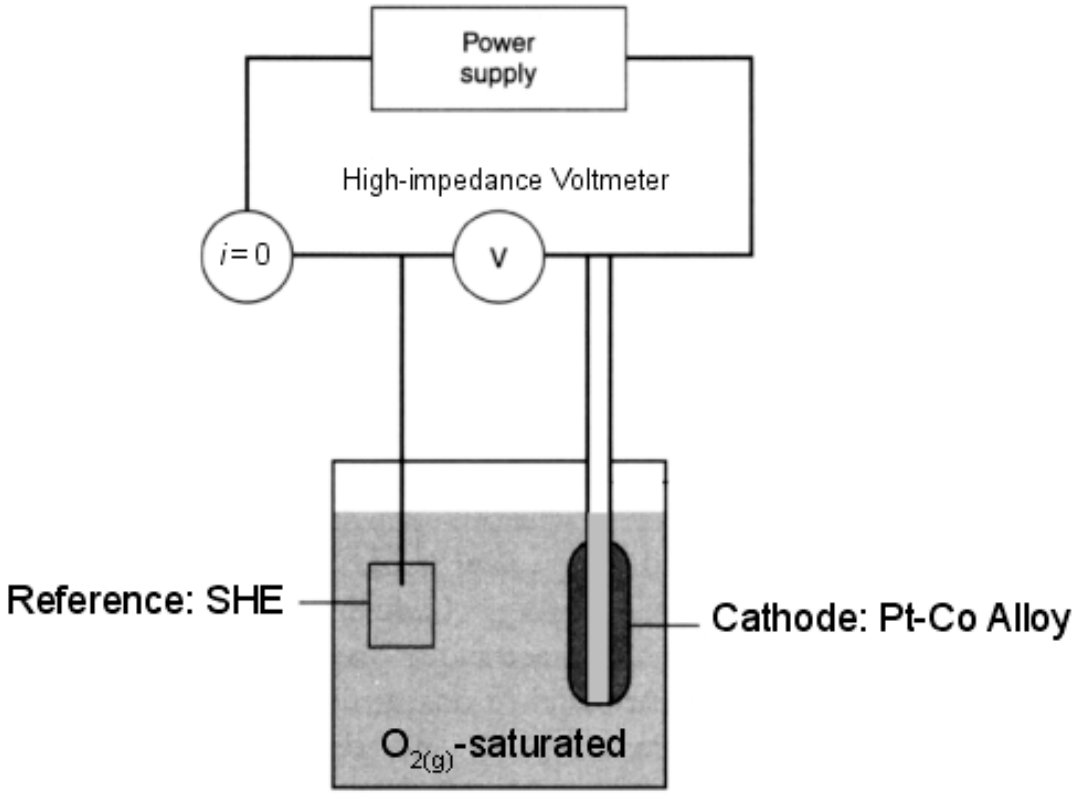

Figure 11. Schematic of voltage efficiency analysis.

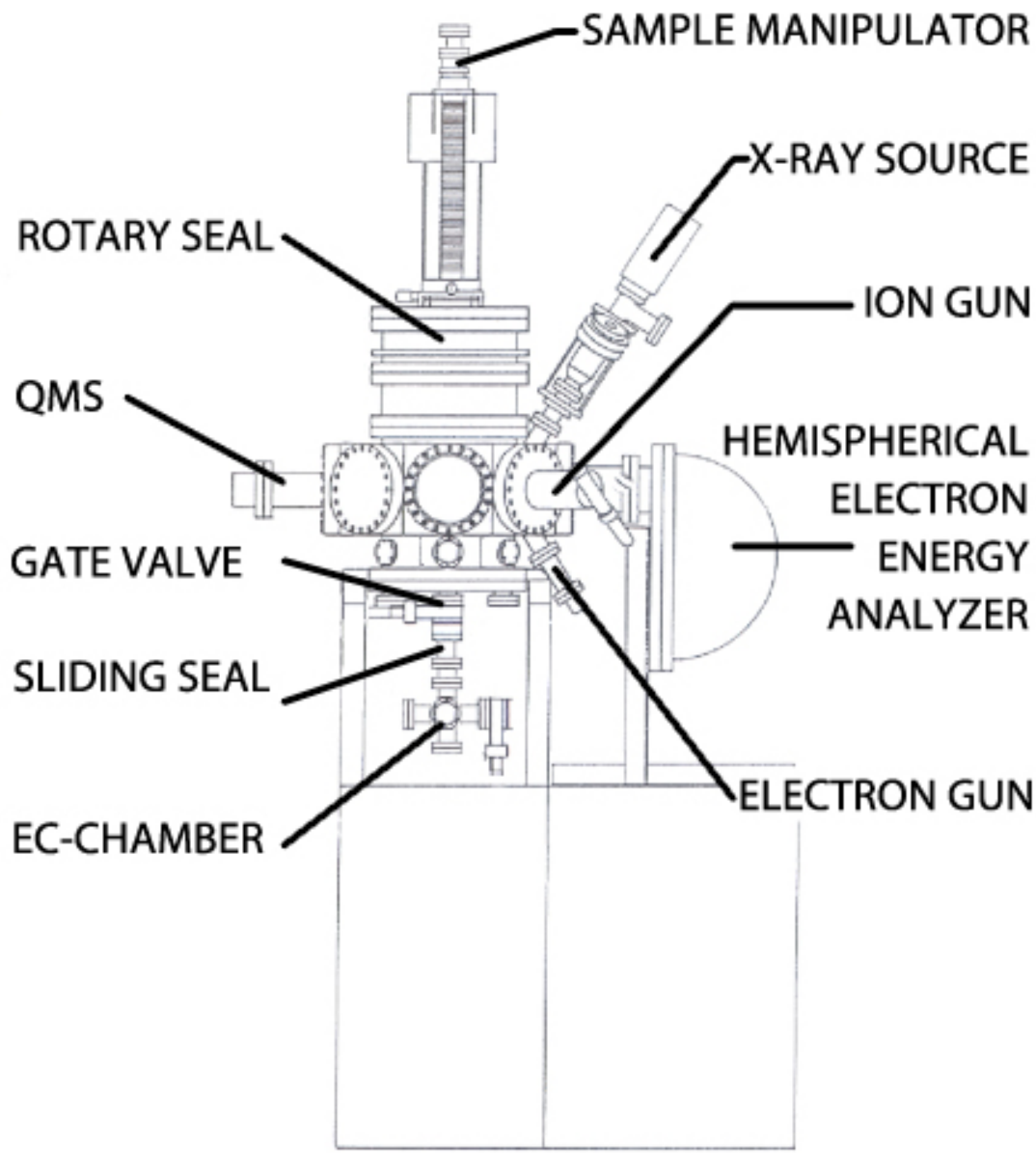

Figure 12. Schematic diagram of an integrated LEED-TPD-XPS-LEISS-EC apparatus. SIDE VIEW

the magnitude of a hydrogen fuel cell voltage (E_{Cell}) is given by $E_{Cathode} - E_{SHE} = E_{Cathode}$, an alloy electrode that yields an OCP closest to the thermodynamic value would be best choice.

UHV-EC Instrumentation

The UHV-EC system employed in this investigation was based on a customized all stainless steel UHV chamber (Perkin-Elmer, Eden Prairie, MN). Diagrams of the instrument are given in Figure 12 (head-on view) and Figure 13 (top-view). For the characterization of Pt-Co thin films, the chamber is equipped with a XPS-LEISS-LEED-TPD-EC setup. The relative position of these instruments to the sample (central axis of chamber) can be seen in Figure 13. The base pressure of the vacuum chamber is 5×10^{-10} Torr after extensive bakeout, with a day-to-day operating pressure of 1×10^{-9} Torr. XPS and LEISS spectra are collected using the concentric hemispherical analyzer. The sample is mounted to a sample probe at the top of the chamber. The probe is made out of a highly polished stainless steel tube. On the feed-through, there are four connections; two thermocouple leads, and two oxygen-free highly conductive (OFHC) copper leads for resistive heating of the sample up to 1500 K. For higher temperature heating, electron bombardment via a W emitter with a sample bias of 600 volts is used. For low-temperature studies, liquid nitrogen can be filled into the probe to lower the sample temperature to around 80 K. Attached to the surface analysis chamber is a "high-pressure" EC ante-chamber designed for electrochemical experiments. For such experiments, the sample was transported

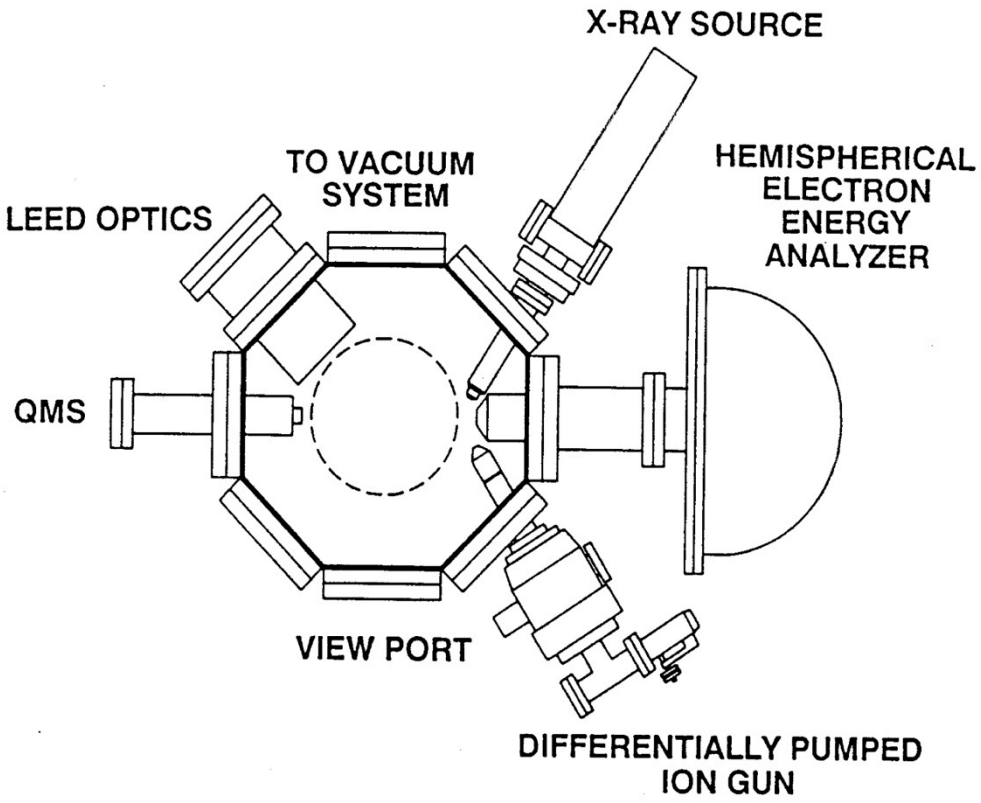

Figure 13. Schematic diagram of an integrated LEED-TPD-XPS-LEISS-EC apparatus. TOP VIEW

to the antechamber, under clean transfer conditions, which was back-filled with UHP N_2 or O_2. The sample probe is maneuvered by using an upright linear motion table driven by an electrical motor to provide movement in the Z-axis. For movement in X and Y axes, a manipulator at the base of the bellows having two mico-manipulators is used. To exact the clean sample transfer, no exposure to atmosphere was allowed and this was accomplished by a series of differentially pumped sliding seals between the analysis chamber and the ante-chamber. The sliding seal design consists of three spring-loaded Teflon seals locked in place by a snap-ring and separated from each other by two pump-down ports. The pump-down port in the bottom part is fed to the mechanical pump, while the upper void is pumped by the turbomolecular pump. The inner diameter of the Teflon seals fits perfectly over the polished probe. When the probe is passed through the seals and the differential pumping lines are connected, the UHV chamber is isolated from the adjacent volume. The main advantage in this setup is the ease of operation. Its design allows UHV conditions inside the analysis chamber, while conducting "high-pressure" EC experiments; a reality made possible by the differential pumping across the seal. It should also be noted that the active pumping also allows the probe to be rotated when the sample is in EC position [56].

The analysis chamber was of, primarily, octagonal geometry with a volume of about 100L. Initial pumping of the chamber from ambient pressure to 10^{-3} Torr, as well as roughing the turbo-pump, was achieved by rotary-vane

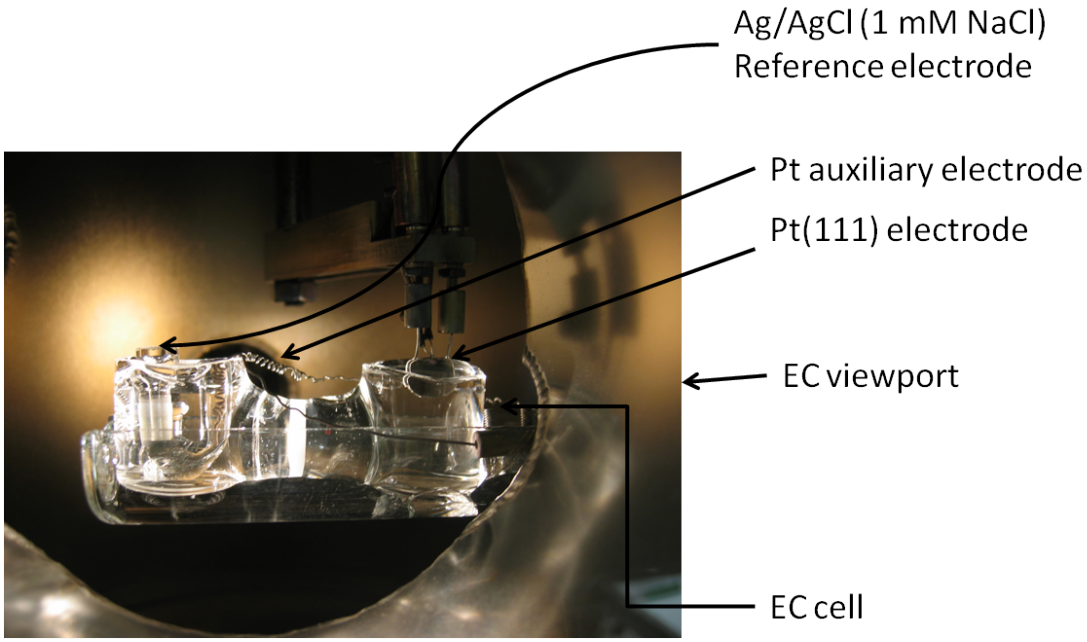

Figure 14. Photograph of the custom electrochemical cell used in the following studies.

mechanical pumps (Alcatel- France). A 330 L/s turbo-molecular pump (Pfeiffer-Balzers- Germany) was used to lower the pressure to 10^{-7} torr. The final pumping stage consisted of a 200 L/s ion pump (Perkin-Elmer- Eden Prairie, MN) and a cryogenically cooled titanium sublimation pump. The UHV-EC system was periodically baked at 150 – 200 °C for up to 99 hours to maintain a day-to-day pressure of 10^{-9} torr. All UHV seals were made by double-Conflat flanges, with well-maintained knife-edges, crushed into single-use OFHC Cu gaskets.

A single-crystal Mo(110) disc electrode (99.999% purity) and 1.0 mm thickness was used for UHV-EC experiments. The disc electrode was oriented to within ±0.5° of the (110) plane and metallurgically polished to a mirror finish. A similar Ru(0001) single crystal was employed for a subset of experiments. For a few comparative studies, a Pt_3Co(111) single-crystal (Honda Motor Corp.) was used. Two segments of Ta wire of 0.5 mm thickness (99.99% purity, Aldrich) were spot-welded to the top edge of the disc to provide electrical contact and mechanical support. A Type C thermocouple (W-5%Re||W-26%Re, provided by H. Cross Co.- Moonachie, NJ)- was spot-welded to top dead center of the backside of the substrate to provide temperature monitoring and feedback control of a crystal temperature controller (Omega Engineering).

Electrochemistry experiments in the UHV-EC system were performed using a custom-built two-compartment glass cell, a Ag/AgCl (1 mM NaCl) reference electrode (also custom built), and a Pt-wire counter electrode. In order to minimize Cl^- contamination of the working electrode a low concentration of

Cl^- in the reference electrode was used. EC experiments were conducted using an EG&G PARC model 273 potentiostat, in a three-electrode arrangement, interfaced with a Windows PC running EChem software and in a three-electrode assembly. Figure 14 shows a photograph of the cell configuration. Potentials referenced are vs. the reversible hydrogen electrode (RHE).

Reagents and Gases

All solutions were prepared using 18.2 Ω Millipore water (Millipore Systems- Houston, TX). All glassware was cleaned using hot chromic acid (3% $K_2Cr_2O_7$ dissolved in 10 M H_2SO_4). The following high-purity reagents were used to prepare all solutions: fuming H_2SO_4 (Aldrich- Milwaukee, WI), and $K_2Cr_2O_7$ (EM Science- Gibbstown, NJ). High purity gases, specifically nitrogen (99.999% purity, BOTCO- Bryan, TX), helium (BOTCO), and oxygen (BOTCO) were used in the experiments. Prior to any EC experiment, solutions were sparged with high purity nitrogen for at least 20 minutes.

Experimental Protocol

The experiments were carried out in the chamber described *vide supra*. A well-defined Mo(110) single-crystal electrode was used for these experiments. Prior to each experiment, the single crystal was cleaned by cycles of e^--bombardment, Ar^+ sputtering, and thermal annealing in UHV to restore the clean and smooth surface. Surface cleanliness is confirmed by LEISS before any further steps are taken. The electrode is then treated to a metal-deposition

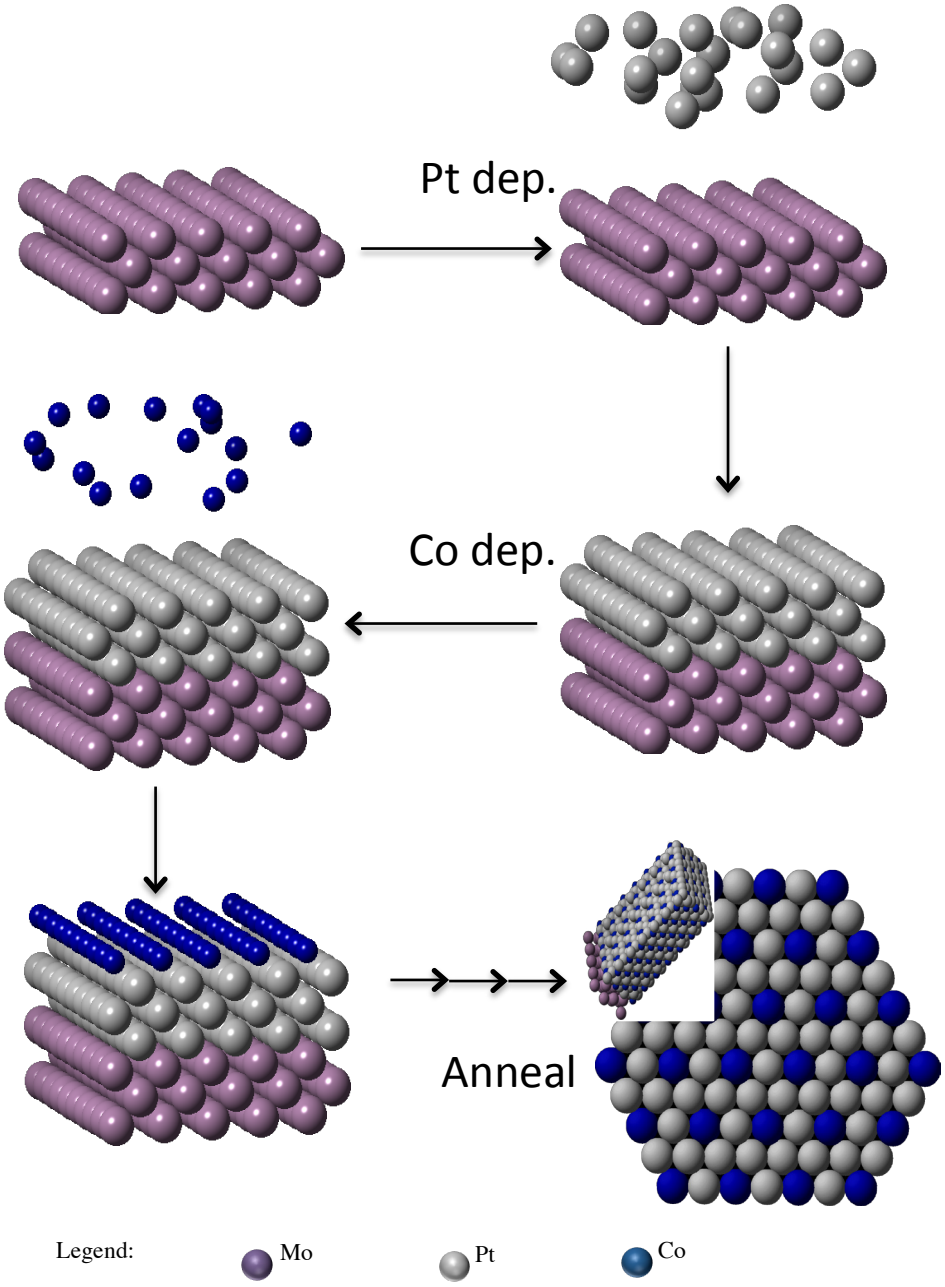

Figure 15. Block diagram of the Pt-Co film preparation process is shown for a 4 ML film of Pt_3Co. Also shown is the result of a bulk-truncated 20 ML deposit of Pt_3Co spontaneously aligned to the {111} plane. Pt_3Co is known to adopt the ordered fcc $L1_2$ superlattice structure.

process (Figure 15), which allows careful control over the thickness of deposited films. Once the desired film is deposited, the sample is then resistively heated to facilitate intermixing of metallic components and formation of a thin film alloy. This film is characterized before and after introduction to the EC chamber.

For EC experiments the reference electrode and auxiliary electrode were separated from the working electrode by a fine glass frit. For UHV-EC work, the experiments were conducted as follows: the surface composition of the test catalyst was determined by XPS and LEISS. Once prepared, the sample catalyst was transferred through the sliding seal to the "high-pressure" chamber, which was then backfilled to 1 atm of either O_2 or N_2 gas. Here, electrochemical experiments were conducted. One the EC treatment was complete, the high-pressure chamber was evacuated and the sample transferred back to the main chamber for post-EC surface analysis.

RESULTS AND DISCUSSION FOR PART I

Preparation Alloy Films

Thin films were prepared by thermal vapor deposition in ultrahigh vacuum (UHV). A doser was constructed by tightly winding wires of the Pt and Co metals in small segments around a Ta filament. The filament was heated resistively at a current sufficient to initiate sublimation of subject metals onto a cold (room temperature ruthenium or molybdenum) substrate; the latter was located close to the doser to enable a well-controlled deposition rate.

Calibration of the dosing (film-formation) rate was conducted via an "XPS breakpoint analysis". In this procedure, a plot of the XPS intensity is obtained as a function of dosing time (Figure 16); from submonolayer to full-monolayer coverages, the intensity-versus-time plot has a constant slope. The time at which the slope changes marks the time at which a second monolayer begins to form; it is also taken as the total time (t_{ML}) required to deposit one full monolayer [57, 58]. In the preparation of an n-ML film, the total dosing time was simply equated to ($n \times t_{ML}$). At the end of each deposition, the alloy films were annealed at 900 K for 20 minutes to ensure that Pt and Co had become alloyed. Surface composition was determined by LEISS, XPS or TPD prior to and subsequent to the electrochemical experiments.

The initial step in the preparation of the mixed-metal films consisted of the vapor deposition, one metal at a time, of the alloy components onto a refractory substrate; sequential deposition was necessary in order to track the

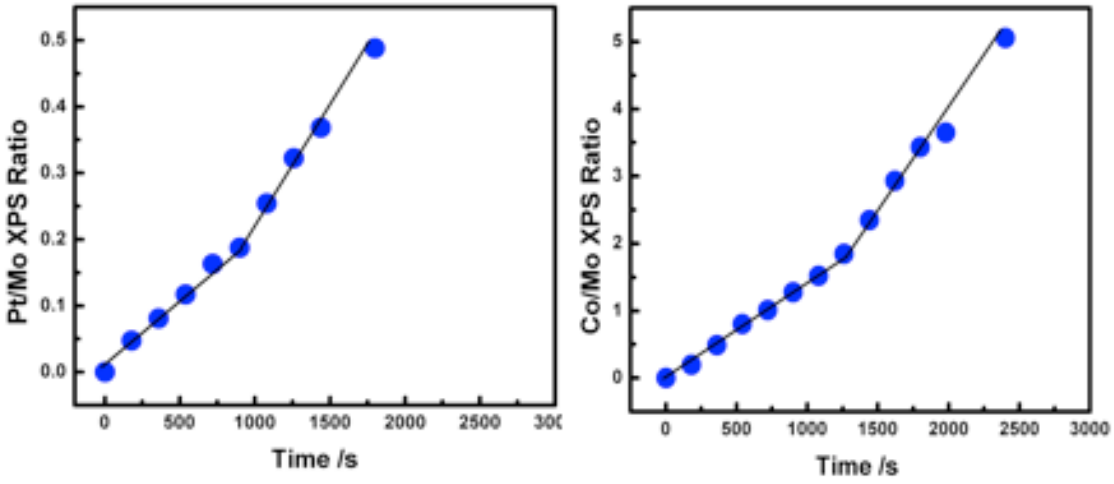

Figure 16. The "XPS break point" metal-doser calibration method. The break in slope signals the completion of one full monolayer (1 ML) and the onset of the second monolayer. The data shown are for the Pt and Co dosers employed in this work and a Mo(110) substrate.

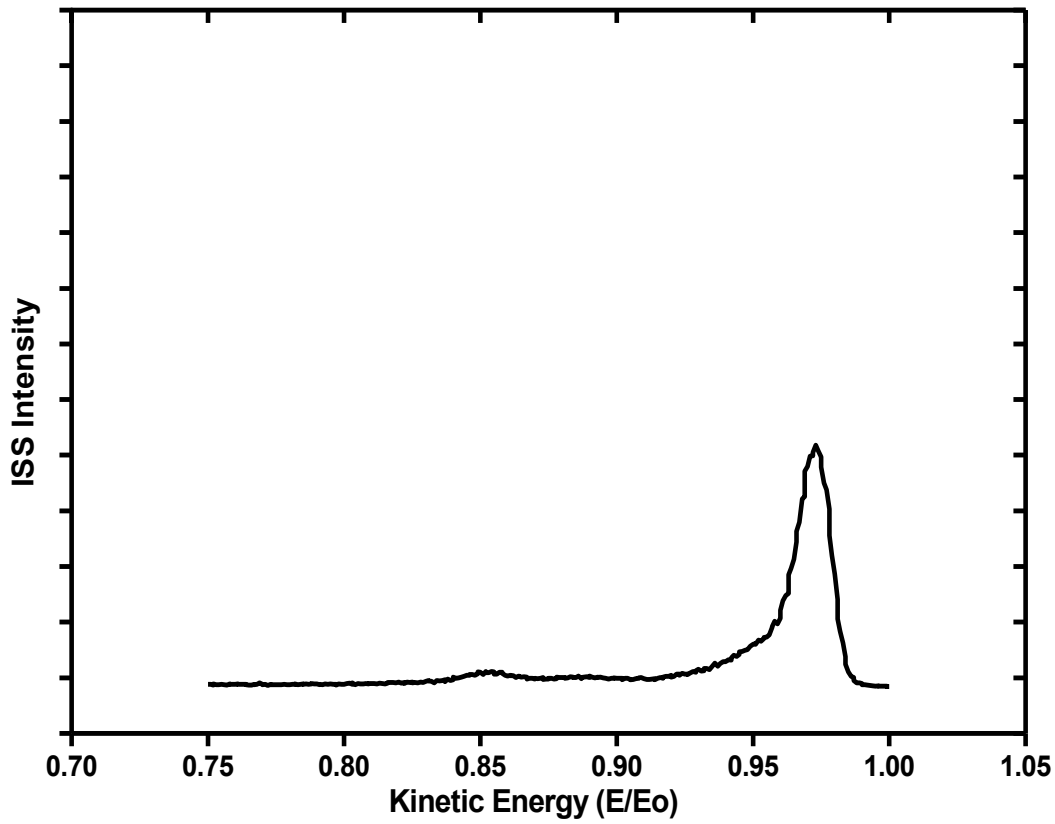

Figure 17. LEISS spectrum of as-deposited 2 ML Pt/Mo(110).

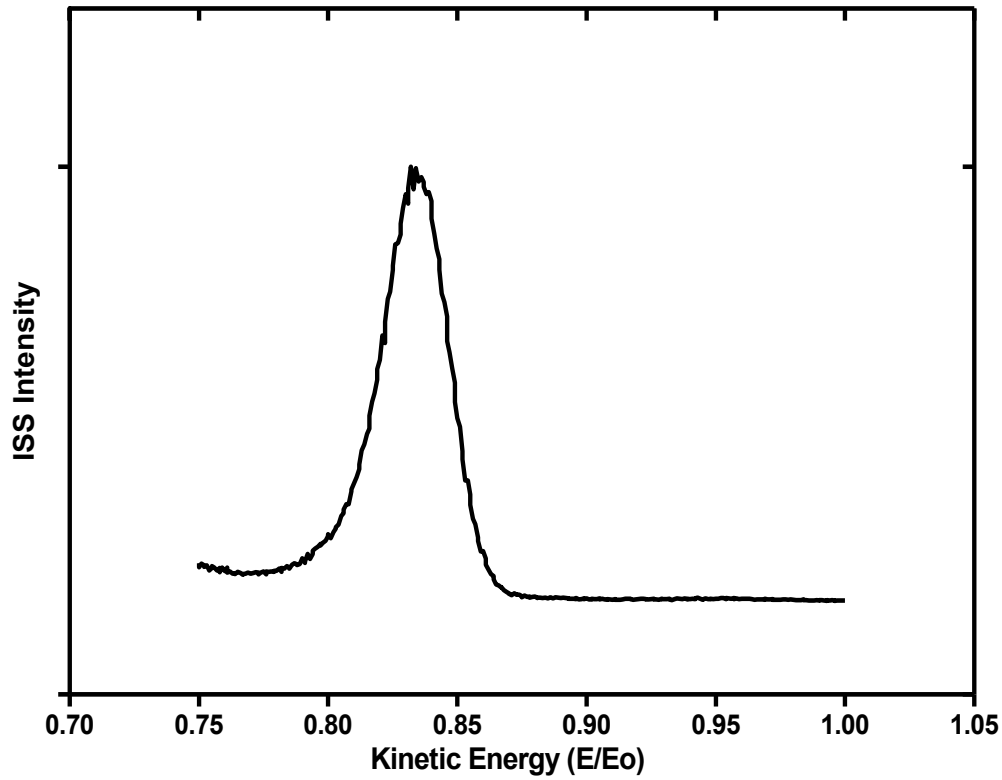

Figure 18. As-deposited spectrum of Co/Mo(110). Same scale as Figure 17.

doser-calibration procedure. Figure 17 shows the ISS of a thin Pt-only deposit on a clean Mo substrate. A peak at lower energy is observed and is due to some exposed Mo following deposition. Shown in Figure 18 is the same spectrum for Co on a clean Mo substrate plotted on the same scale as Pt. For alloy film preparation, the desired thickness of each component is deposited one on another.

Figure 19 shows LEISS spectra of a Mo(110) substrate onto which a 10-monolayer film was prepared from a 1:4 Pt-to-Co co-deposition ratio. In Figure 19a, 2 ML of Pt were initially deposited, followed by 8 ML of Co; in Figure 19b, the reverse deposition sequence was used in which 8 ML of Co were deposited first.

There are five notable features in Figure 19a: (i) Below 600 K, no Pt peak is observable; this suggests that 8 ML of Co completely covers the 2 ML of Pt. (ii) At 700 K, a Pt peak emerges; at this temperature, the Pt underlayer and the Co overlayer have started to intermix. (iii) Between 800 and 1000 K, the ratio of the Pt and Co peak areas is invariant; this provides evidence for the formation of a stable fixed-composition alloy. (iv) At $T < 1000$ K, no Mo substrate peak ($E/E_0 \sim 0.89$) is found; this signifies that the alterations in the Co and Pt signal intensities at lower temperatures are due to alloy formation and not to thermal desorption of Co and/or Pt. (v) At temperatures greater than 1000 K, the peak intensities for both Co and Pt decrease while a peak for Mo appears; thermal desorption of one or both components is indicated.

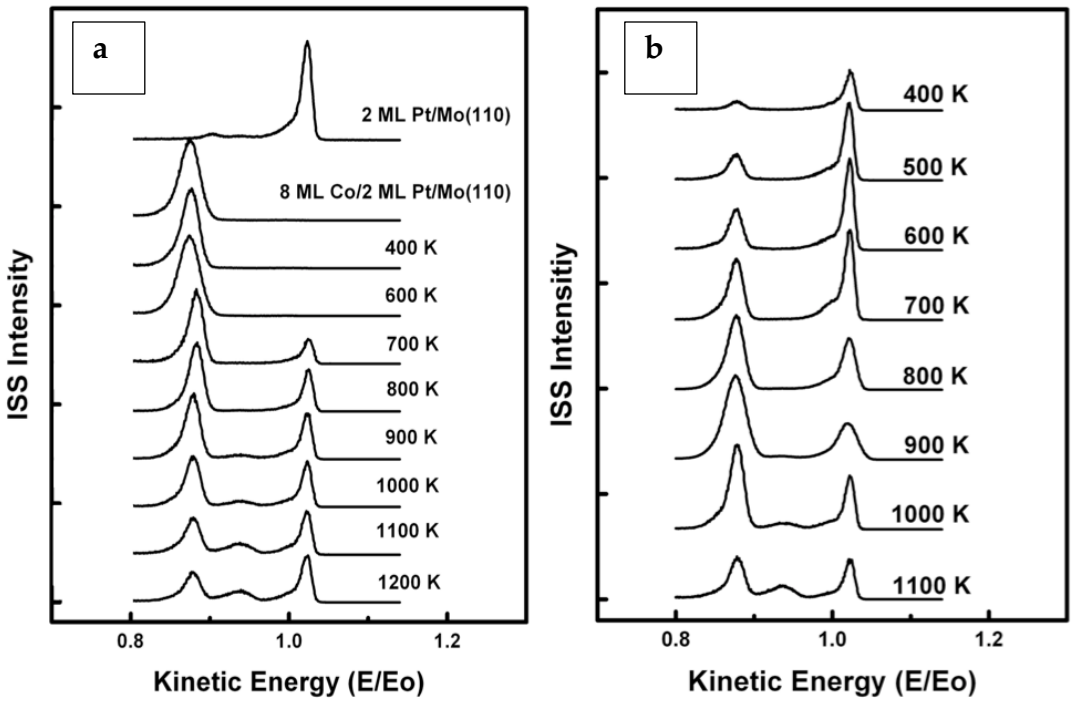

Figure 19. LEISS spectra of Pt-Co films on a Mo(110) substrate after a 30-minute temperature treatment. (a) 2 ML of Pt were first deposited followed by 8 ML of Co. (b) 8 ML of Co were initially deposited followed by 2 ML of Pt. The peak at E/E_0 ~ 0.83 is due to Co; that at E/E_0 ~ 0.98 is for Pt. The LEISS spectra were collected at 300 K.

In Figure 19b, three features are noteworthy: (i) Below 600 K, a Co peak is present; this signifies that a 2-ML Pt overlayer is not sufficient to completely mask the Co underlayer. (ii) Between 800 and 1000 K, the peak-intensity ratios are identical to those in Figure 19a; this documents the fact that, irrespective of the order of metal deposition, alloy formation takes place at the same temperature range. (iii) Above 1000 K, the LEISS spectra are identical to those in Figure 19a; the implication is that the temperature-induced desorption of one or both components has transpired to expose the Mo substrate.

Additional Pt-Co films were prepared, each consisting of a total of ten monolayers but with variable Pt:Co vapor-deposition stoichiometric ratios. The results, in terms of LEISS spectra, are summarized in Figure 20. Although not shown in Figure 20, it was found that, in all cases, stable interfacial alloys were formed when the mixed-metal deposits were annealed at 1000 K; this is expected from the previous set of spectra. Figure 21 gives immediate evidence of intermixing. However, as can be seen in Figure 20, the peak-intensity ratios varied, depending upon the initial Pt:Co vapor-deposition stoichiometric proportion.

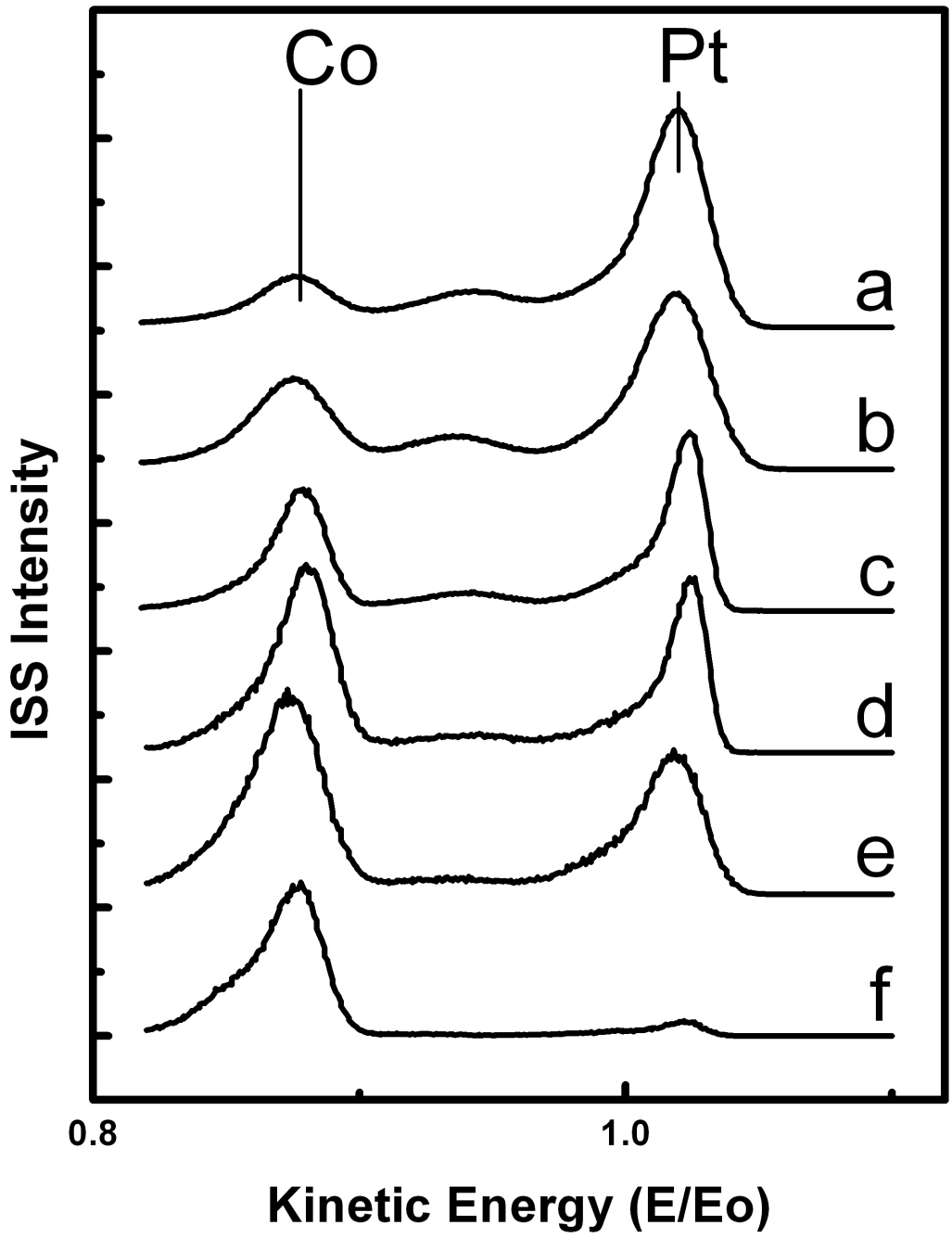

Figure 20. LEISS spectra of Pt-Co alloys at various bulk compositions annealed at 1000 K for 30 minutes. Each spectrum was acquired at 300 K. The ML_{Co}-to-ML_{Pt} ratios for the films were as follows: (a) 1:9; (b) 2.5:7.5; (c) 5:5; (d) 7.5:2.5; (d) 8.8:1.2; and (f) 9.5:0.5.

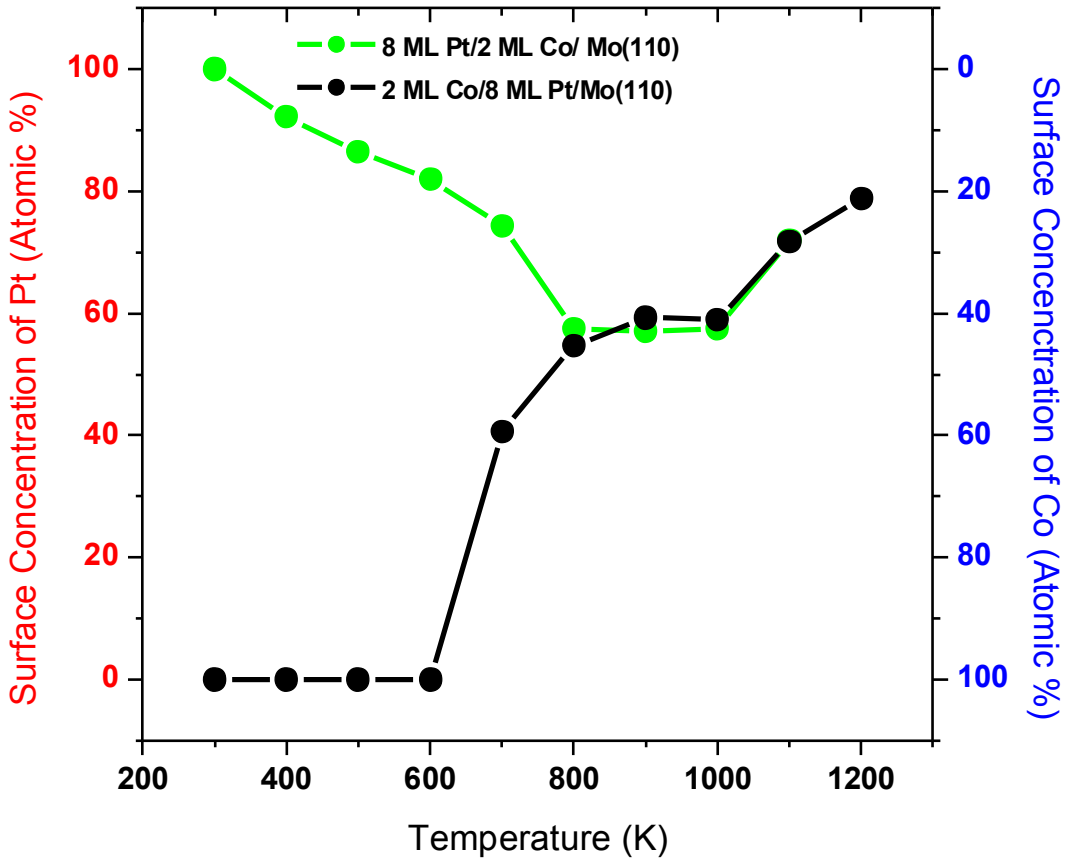

Figure 21. Effect of annealing temperature on surface composition of co-deposited Pt and Co. Evidence for intermixing.

Surface Phase Diagrams

Qualitatively, it can be readily gleaned from the data in Figure 19, Figure 20, and Figure 21 that, in the intermixed state generated at 1000 K, the elemental composition at the *outermost* layer, as measured by the LEISS Pt:Co peak-intensity ratio, is vastly different from that in the *bulk*, as given by the Pt:Co vapor-deposition fractions. The peak intensities can be quantitatively converted to surface concentrations through the use of the relationships given in equation (32), where the value of $f_{\text{Pt-Co}}$ was determined from experiment to be 0.5.

The divergence between the elemental composition at the topmost layer and that in the bulk is appreciated best when the percent composition of Pt (or Co) at the alloy surface is plotted as a function of the percent composition of Pt (or Co) in the bulk. Such a plot, which represents the surface phase diagram of the Pt-Co alloy, is shown in Figure 22; the open circles are data for when Pt was deposited initially, while the closed circles are for when Co was deposited first.

The circle diameter is approximate absolute error. Three features are noteworthy: (i) The surface phase diagram is independent of the order or sequence of metal deposition. (ii) The convergence between the surface and bulk compositions occurs only when the bulk composition is almost entirely Co or is predominantly Pt. (iii) The discrepancy is most dramatic when the fraction of Co in the bulk is higher than 90%. At Co bulk compositions between 30% and 70%, the surface concentration of Pt is almost a constant, not too different from 70%. From these trends, it is plausible to infer that: (i) Pt preferentially segregates to the surface, as may be anticipated because it has a lower surface free energy

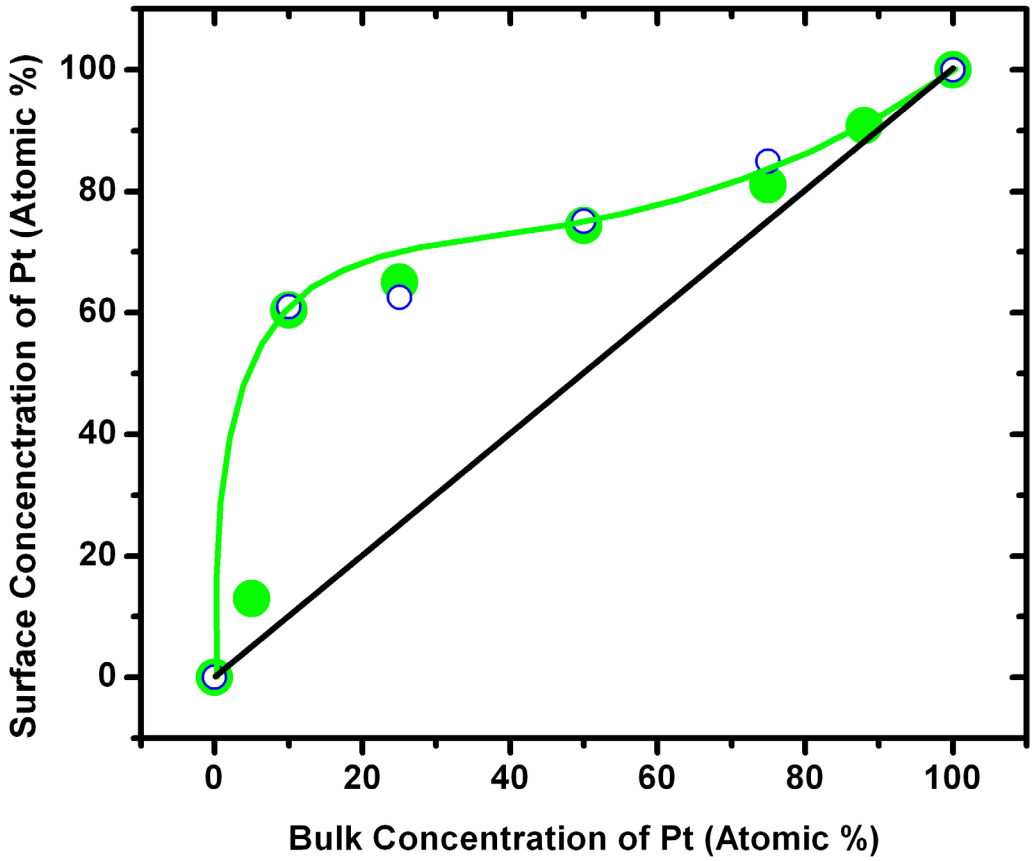

Figure 22. Surface phase diagrams (atomic % of Pt at the outermost layer *versus* atomic % of Pt in the bulk) of the Pt-Co films on Mo(110) annealed at 1000 K for 30 minutes.

than Co; and (ii) At the topmost layer of the alloy, the thermodynamically favored composition is essentially a 3:1 Pt-to-Co stoichiometric ratio; that is, Pt_3Co. Additionally, the effect of substrate (Figure 23) was explored and appears to have no effect on 20 ML thin-films.

Long-Range Surface Order

The two-dimensional order of the Pt-Co alloys was investigated by low-energy electron diffraction. The results, in terms of LEED patterns are shown in Figure 24-Figure 27. First, the fact that distinct LEED spots are observed indicates that the alloy interface is well-ordered. Figure 27 shows a typical LEED pattern for alloys that contain between 50% to 75% of Pt; such a hexagonal pattern is reminiscent of that exhibited by a pure Pt(111) surface. Since the surface phase diagram (Figure 22) indicates an increase in the fraction of Pt under these conditions, the outermost layer is most probably heterogeneous, dominated by Pt(111) domains of at least 10 nm in coherence length. Figure 24 and Figure 26 show that a different LEED pattern is obtained when the amount of Co is increased beyond 50%. Coupled with the data in Figure 22 that points to a surface composed largely of Pt_3Co, the LEED pattern is probably that for a bulk-truncated $Pt_3Co(111)$ plane. The LEED pattern for a pure Pt film adopts a slightly different structure. Though it is difficult to tell because of the poor quality of the photograph, the spots appear to take on a known phase of Pt(110). At such low coverage, the Pt is expected to adopt the structure of the substrate; moreover, it appears that the film has also undergone the familiar Pt(110)-(1x2) "missing row" reconstruction [59, 60]. Erroneously, the experimental conditions

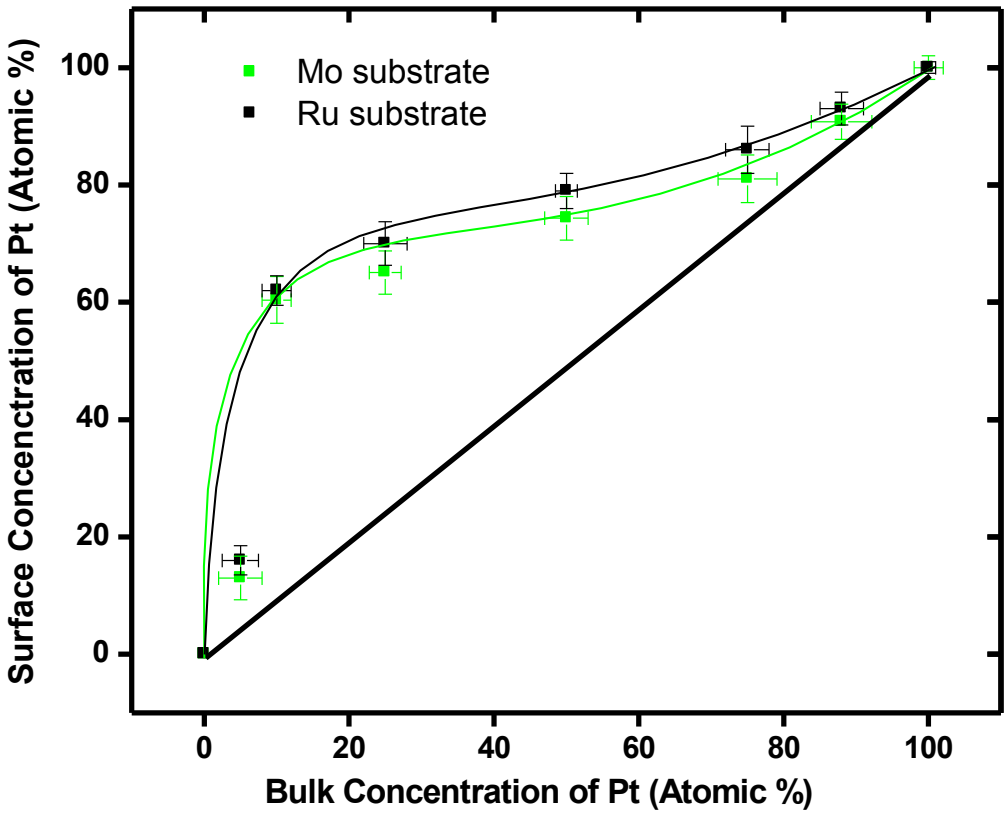

Figure 23. Surface phase diagrams (atomic % of Pt at the outermost layer *versus* atomic % of Pt in the bulk) of the Pt-Co films on Mo(110) and Ru(0001) substrates after annealing at 1000 K for 30 minutes.

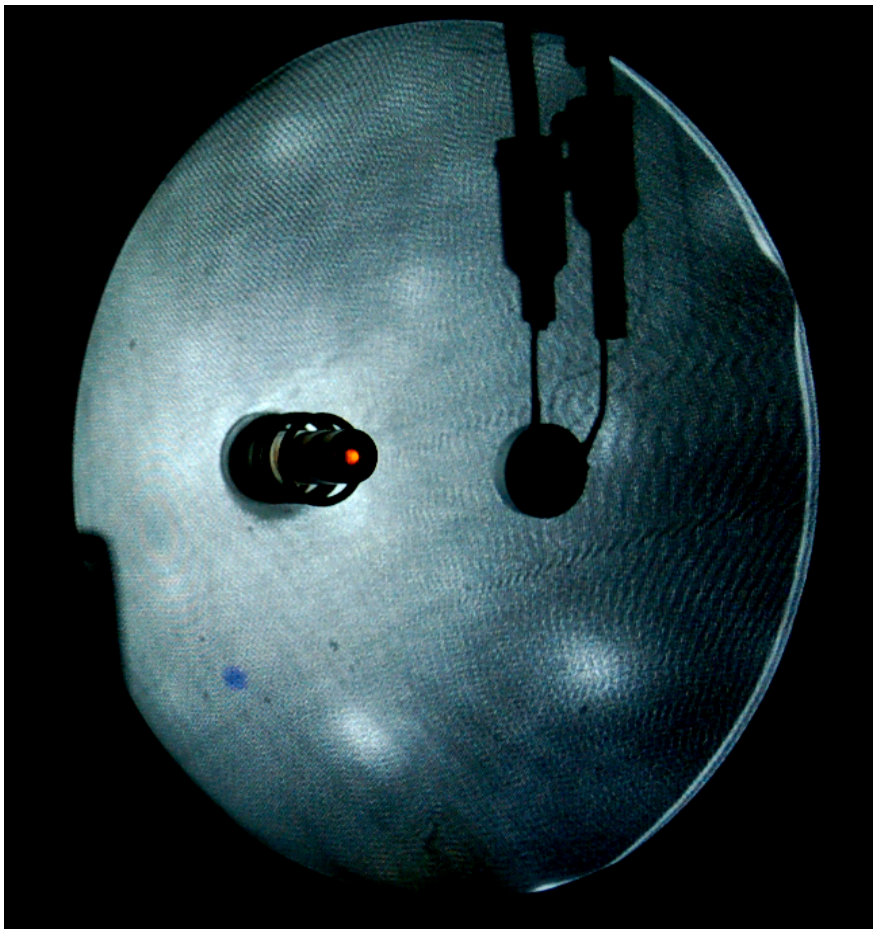

Figure 24. LEED pattern of 10 ML PtCo9/Mo(110). Beam energy and current uncertain, see text for likely values.

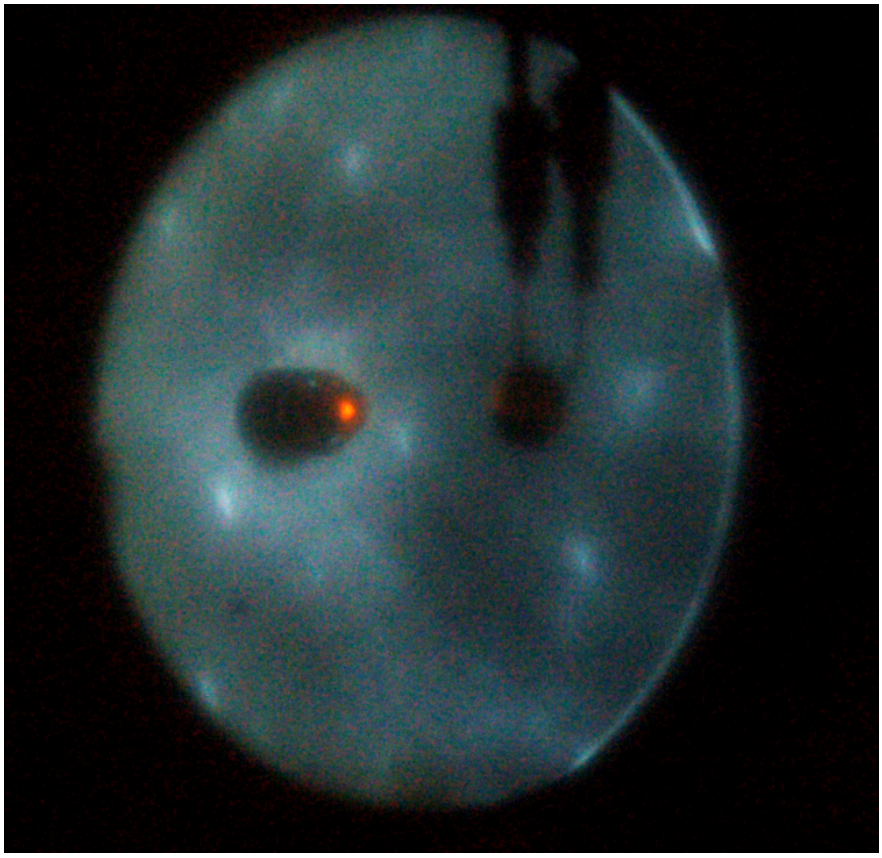

Figure 25. LEED pattern of 2 ML Pt/Mo(110). Beam energy and current uncertain, see text for likely values.

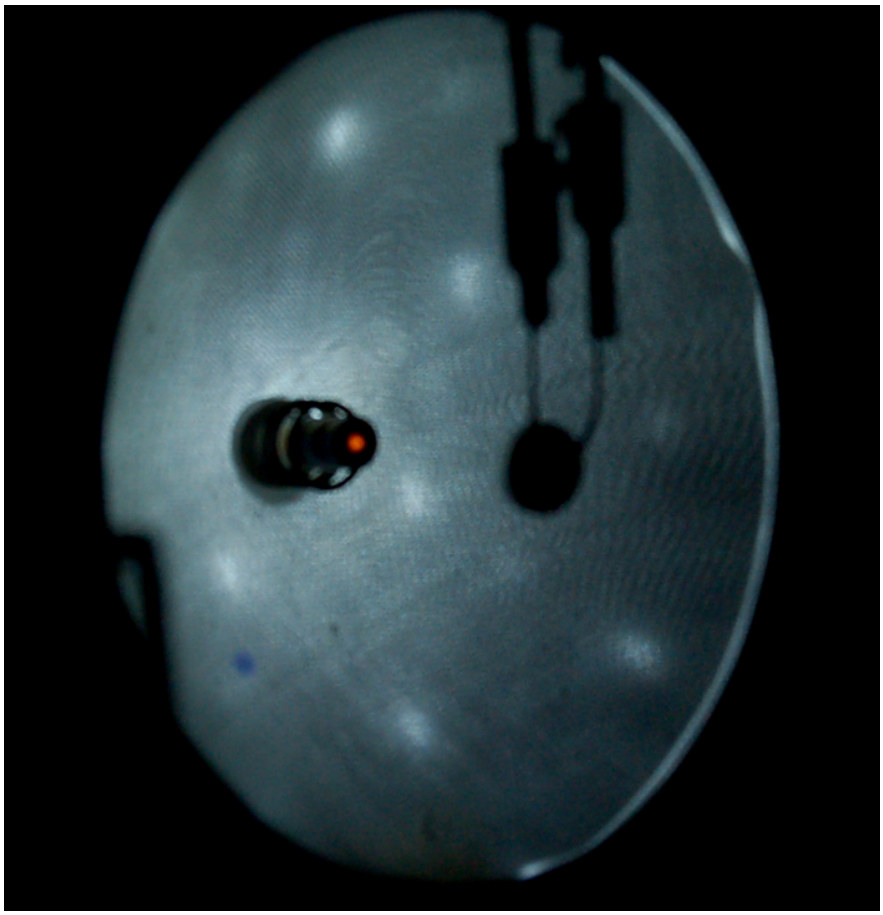

Figure 26. LEED pattern of 10 ML PtCo3/Mo(110). Beam energy and current uncertain, see text for likely values.

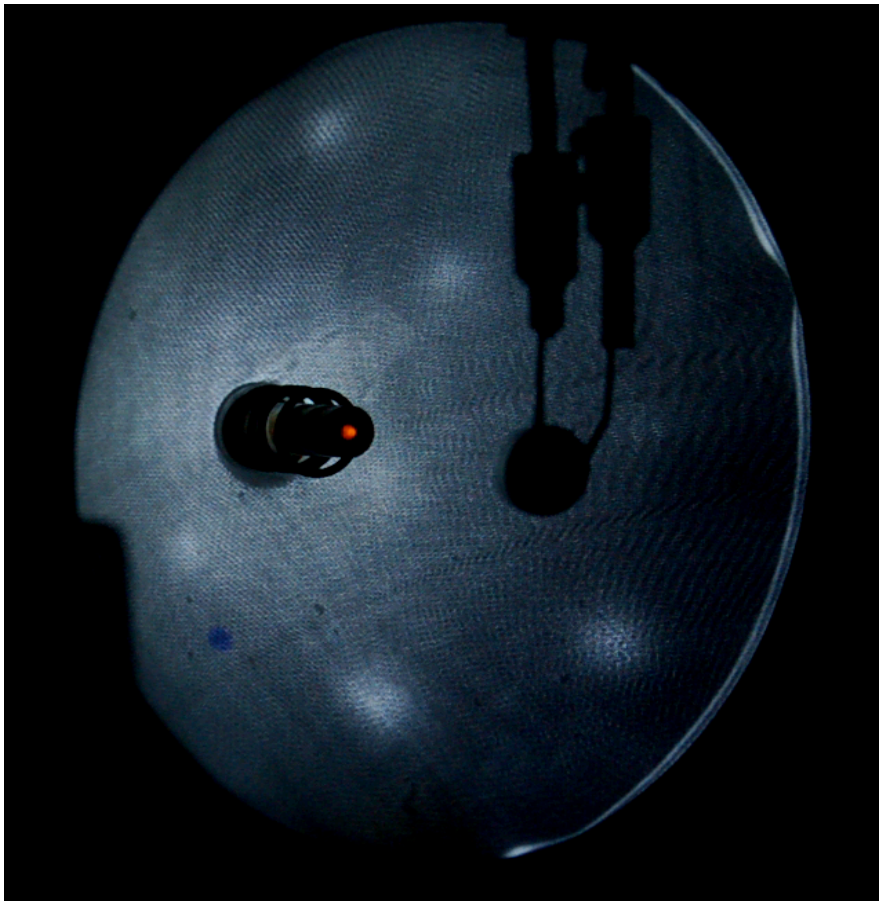

Figure 27. LEED pattern of 10 ML Pt3Co/Mo(110). Beam energy and current uncertain, see text for likely values.

for LEED patterns are unavailable. Consulting Figure 28 and the experimental LEED patterns obtained in PART II of this dissertation, it is likely that the beam energy was ca. 50-60 eV.

Electrochemical Properties

Voltage Efficiency As an Oxygen Cathode

Figure 29 shows a plot of the measured open-circuit potential values as a function of the alloy-surface composition expressed as % Pt; for these measurements, the 0.1 *M* H_2SO_4 solution was saturated with O_2 gas. The highest voltage, 0.86 V, was obtained for the alloy for which the composition corresponded to Pt_3Co; this value was 0.68 V higher than for pure Co and 0.22 V better than for pure Pt. Nevertheless, the value is still considerably lower than the ideal potential of 1.229 V. Although not shown in Figure 29 no dependence on surface composition was noted for the OCP values when the solutions were thoroughly deaerated with ultrapure $N_{2(g)}$; the values centered around 0.5 V.

When set against the cyclic voltammogram of pure Pt in either deaerated or O_2-saturated 0.1 *M* H_2SO_4, 0.68 V is a potential just prior to that required for the formation of surface oxide (or hydroxide). That is, even at saturation concentrations, O_2 gas is unable to oxidize pure Pt; or, stated differently, pure Pt is unable to activate dioxygen. The effect of Co has been surmised to facilitate O_2 activation; since the OCP of pure Co in O_2-saturated 0.1 *M* H_2SO_4 is even less than that of pure Pt, it is further conjectured that the oxygen atoms formed "spills over" irreversibly to the Pt sites instead of recombining back to dioxygen

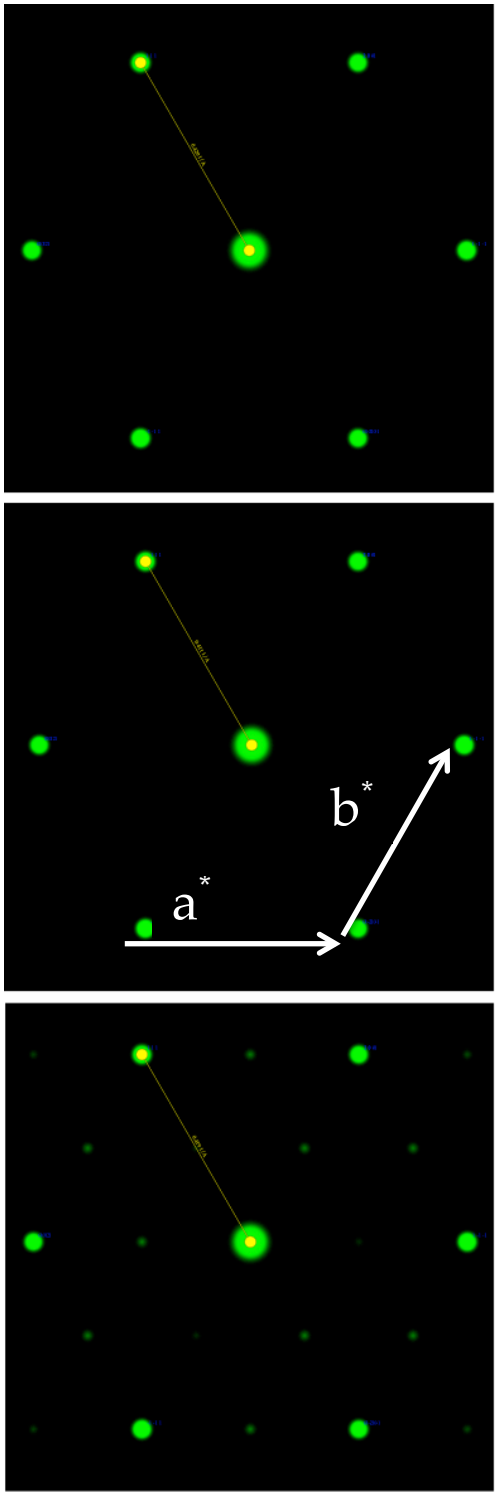

Figure 28. Simulated LEED patterns of (a) Pd(111)-showing the reciprocal lattice vectors, (b) Pt(111), and (c) $Pt_3Co(111)$.

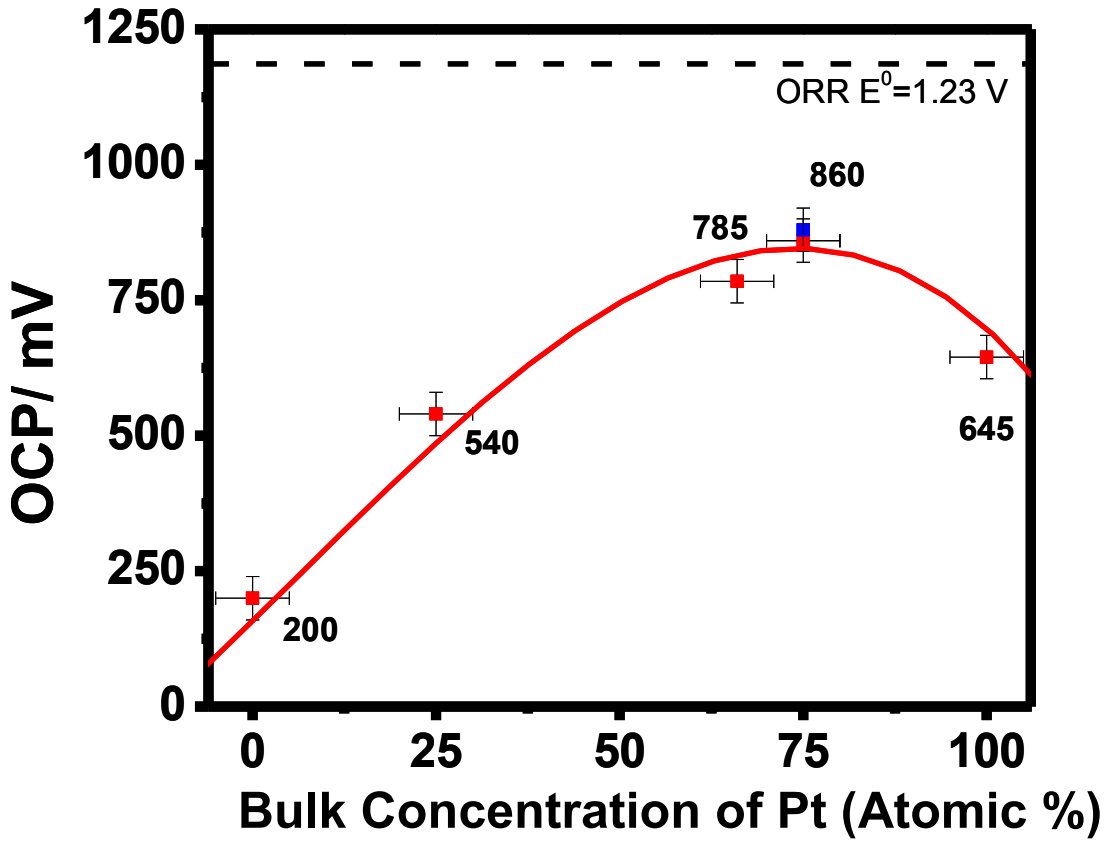

Figure 29. Measured open-circuit potential (OCP) values as a function of the surface concentration of Pt. Absolute error given by bars. Blue dot is data obtained for a $Pt_3Co(111)$ single crystal.

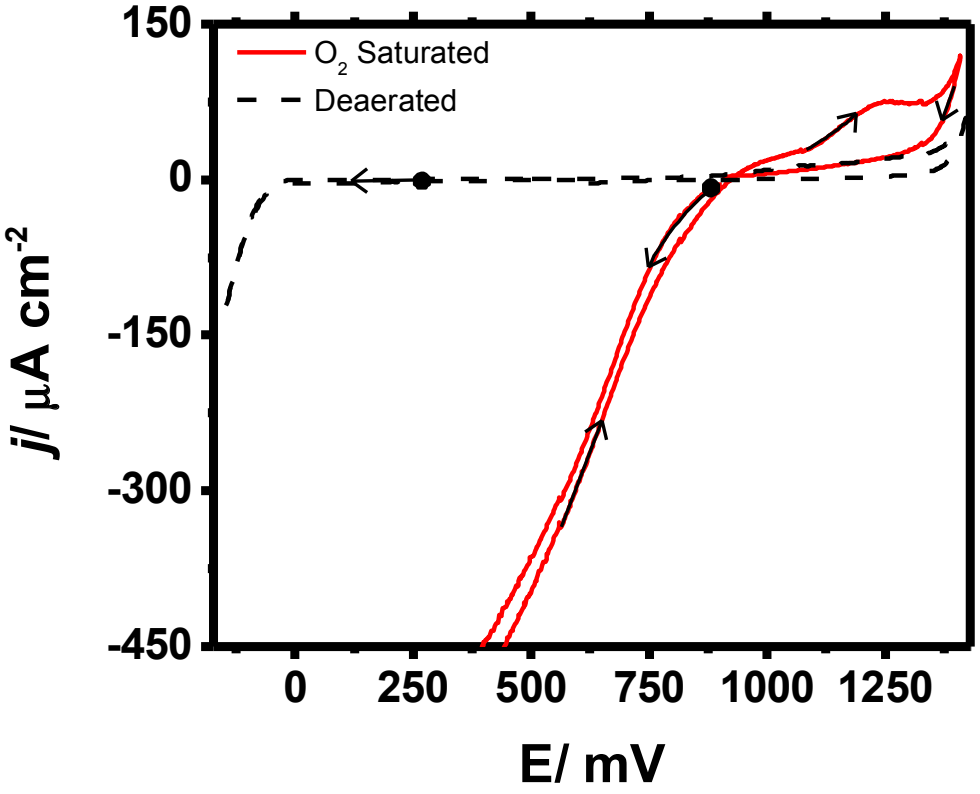

Figure 30. First-scan cyclic voltammograms for Pt_3Co in 0.1 *M* H_2SO_4. Dotted curve: N_2-saturated (deaerated) solution; solid curve: O_2-saturated solution.

gas. As indicated in the present work, the optimal Pt-Co composition is associated with the Pt_3Co alloy[61].

Cyclic Voltammetric Behavior

Cyclic voltammograms for alloys of different Pt-Co concentration ratios were collected in deaerated and O_2-saturated 0.1 *M* H_2SO_4. The particular single-cycle set of CVs for the Pt_3Co cathode is shown in Figure 30**;** the voltammograms were initiated from OCP and the potential was first scanned in the negative direction to the hydrogen evolution region. The morphologies of the current-potential curves are not too different from those of pure Pt: (i) In deaerated solution, there is an appreciably wide double-layer "window" between the hydrogen evolution and oxygen evolution regions. (ii) In O_2-saturated 0.1 *M* H_2SO_4, a massive cathodic wave, due to the reduction of dioxygen, appears at potentials immediately below the OCP; the high cathodic current persists even after the potential sweep is reversed. These results are not too different from those for pure Pt, as may be as expected since the surface is made up of a large fraction of Pt.

Potential-Dependent Corrosion

Only little can be gleaned about the nature of the alloy interface from only the cyclic current-potential curves. An important question that needs to be addressed is whether or not the cyclic voltammograms are accompanied by changes in the surface composition of the alloy; while a qualitative solution to this problem can easily be obtained from multiple voltammetric scans, a

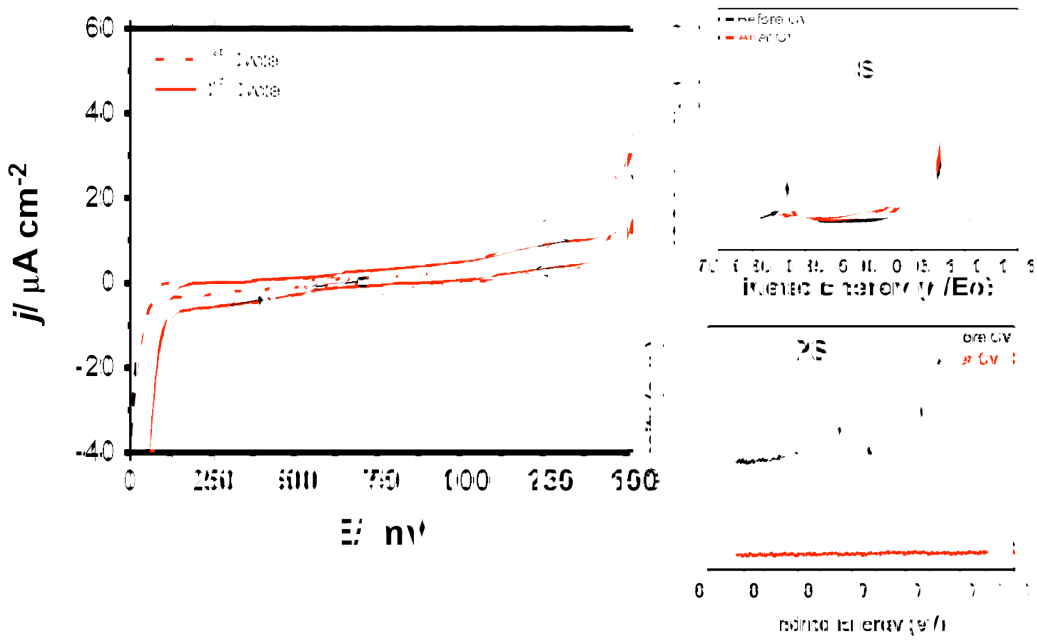

Figure 31. CV of Pt_3Co in deaerated electrolyte solution; accompanying ISS and XPS before and after electrochemical treatment.

quantitative answer is needed. In fact, a more critical matter involves the stability the Pt_3Co alloy under fuel-cell operating conditions; that is, after prolonged use at the OCP or under electrolytic conditions, such as those encountered in start-up and shut-down procedures, in an O_2-saturated solution [62]. All of these issues can be simultaneously tackled by monitoring the surface composition of the Pt_3Co alloy from voltammetric scans and as a function of time at selected applied potentials from the voltammogram. For such measurements, the alloy electrode is withdrawn from the N_2 or O_2-saturated electrolyte at the test potential and, prior to transfer into the surface analysis chamber, rinsed in deaerated ultrapure (Millipore) water to remove *emersed* sulfuric acid. In Figure 31 and Figure 32 the surface composition for two different alloy electrodes are given, prior and subsequent to potentiodynamic treatment. The following important trends are noted: (i) in both cases, a major change in the voltammetric profile occurs between scans 1 and 3. In addition, all changes are complete by the third cycle. (ii) It follows that such changes are caused by a change in the composition of the electrode surface. This fact is underscored by the observed loss in surface and bulk Co as seen in the ISS and XPS data. (iii) For the Co-rich surface, onset of surface oxidation begins at overpotentials some 500 mV cathodic of the Pt-rich surface. This outcome matches the expectation: Co is more easily oxidized and the observed voltammetric feature is generally associated with a surface oxide formation. (iv) High potential excursions appear to be driving the observed changes. (v) Comparing the steady-state CV and ISS for both electrodes post EC-treatment

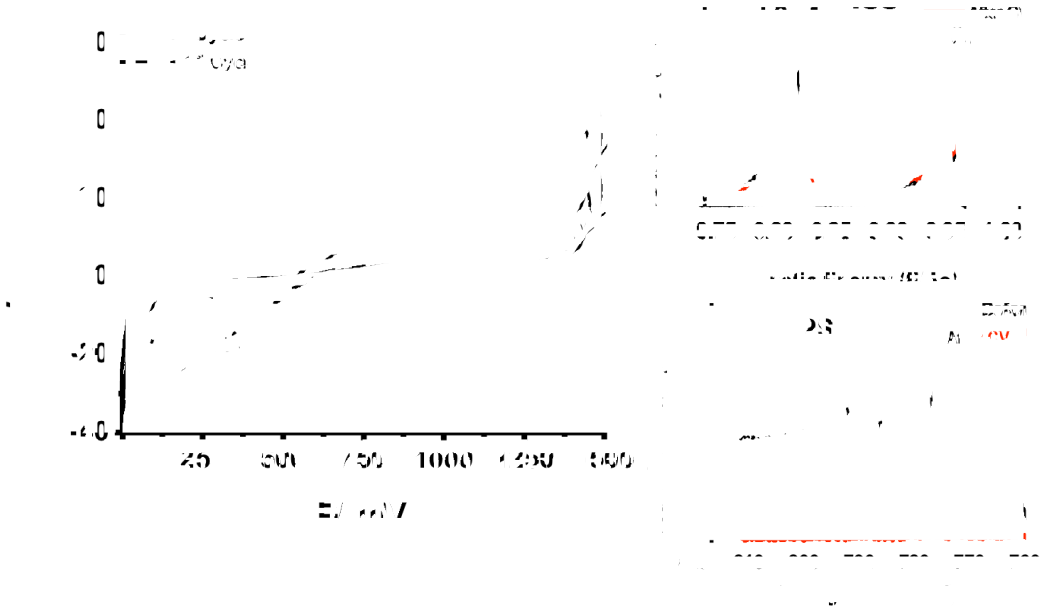

Figure 32. CV of $PtCo_3$ in deaerated electrolyte solution; accompanying ISS and XPS before and after electrochemical treatment.

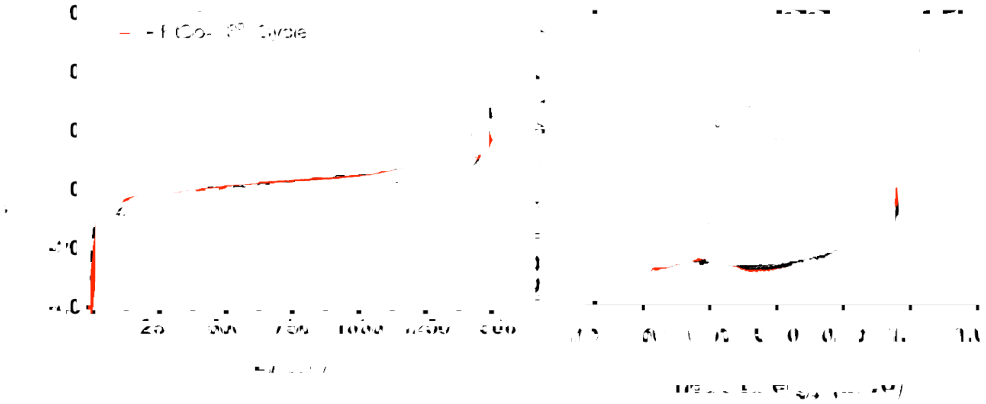

Figure 33. Overlay of steady state CVs from Figure 31 and Figure 32.

reveals a striking outcome. Figure 33 demonstrates what appears to be a convergence of the surface composition under these corrosion conditions. Given the large Pt signal, this demonstrates a *leaching* of Co from the alloy. This has been dubbed the Pt-skeleton structure [63].

Because voltammetry changes the applied potential to the surface in a time-controlled manner, it is difficult to say whether the observed changes in surface composition are due to the applied potential or the amount of time applied. To delineate these two aspects, a series of experiments were designed to characterize a given surface composition after application of a prescribed potential at various time intervals. The LEIS spectra for one set of experiments are given in Figure 34. Here, a Pt_3Co film was potentiostated at 1.23 volts for the indicated amount of time in oxygen-saturated electrolyte. The ISS was collected after each time interval and the results compared. Parallel experiments were performed in deaerated solutions; the extent of Co dissolution appeared to be irrespective of the gas chosen. In this figure, the spectrum has been normalized with respect to the Pt peak in order to highlight the changes in Co surface concentration.

The experiment was repeated for Pt_3Co at 0.26 V, 0.46 V, 0.66 V, OCP, and 1.23 V in oxygen-saturated solutions. The results are shown in Figure 35**.** The following important trends are to be noted: (i) Regardless of the applied potential (at OCP, the potential is "applied" by the presence of the saturation concentration of O_2 gas), there is an immediate drop of *ca.* 2% in the proportion of Co at the interface after only a few minutes. (ii) Regardless of the external

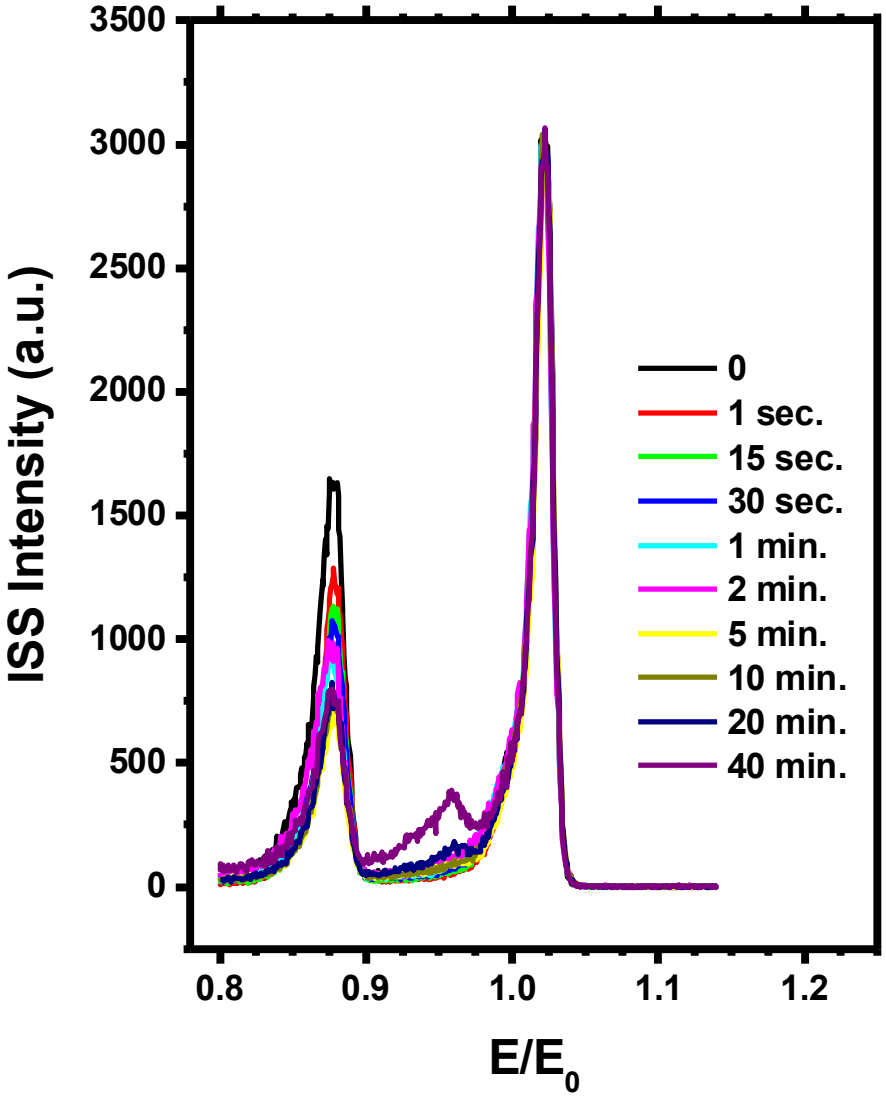

Figure 34. ISS after 1.23 Normalized to the Pt peak.

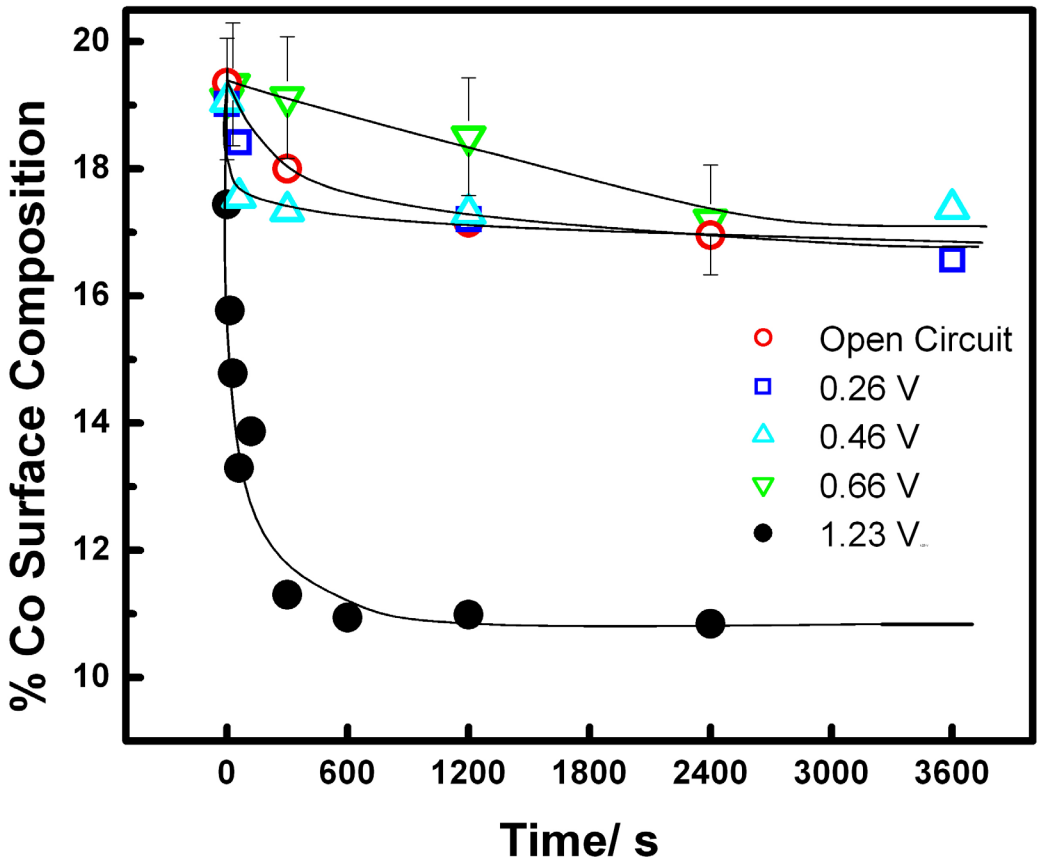

Figure 35. Dissolution profile of Co in Pt-Co films. Co Surface composition analyzed using LEISS at the stated time intervals under application of indicated potentials in O2 saturated 0.1 M H2SO4.

potential, the surface concentration of Co becomes time-invariant after about 5 minutes. (iii) At $E_{Applied} \leq E_{OCP}$, the Co surface concentration quickly converges to a constant value of approximately 18%. (iv) At potentials more positive than OCP, there is an immediate precipitous decline in the surface composition of Co from 20% to 11%, with the latter unchanged even after extended periods.

It can be seen in Figure 30 that anodic oxidation of the alloy surface transpires at potentials above the OCP. This may account for the net 45% decrease in the Co surface concentration at $E_{Applied} > E_{OCP}$ because, whereas the surface oxide (or hydroxide) of pure Pt is resistant to dissolution even in more concentrated sulfuric acid solutions, the oxidized surface of Co is not as impervious to acid-driven dissolution. The fact that 55% of the initial Co concentration is retained on the surface suggests that an appreciable quantity of Co is rendered comparatively inert when alloyed to Pt.

The primary emphasis of this project is the use of LEISS to interrogate the outermost layers of Pt-Co alloys in order to correlate interfacial composition with electrocatalytic reactivity towards oxygen reduction. In some instances, it becomes desirable to compare the properties of the outermost layer with those of the (near-surface) bulk; an example is when it is considered necessary to explain the retention of Co even under anodic-oxidation potentials in acid solutions. In such cases, X-ray photoelectron spectroscopy and temperature-programmed desorption may be employed since both methods are also able to generate information on the electronic (binding-

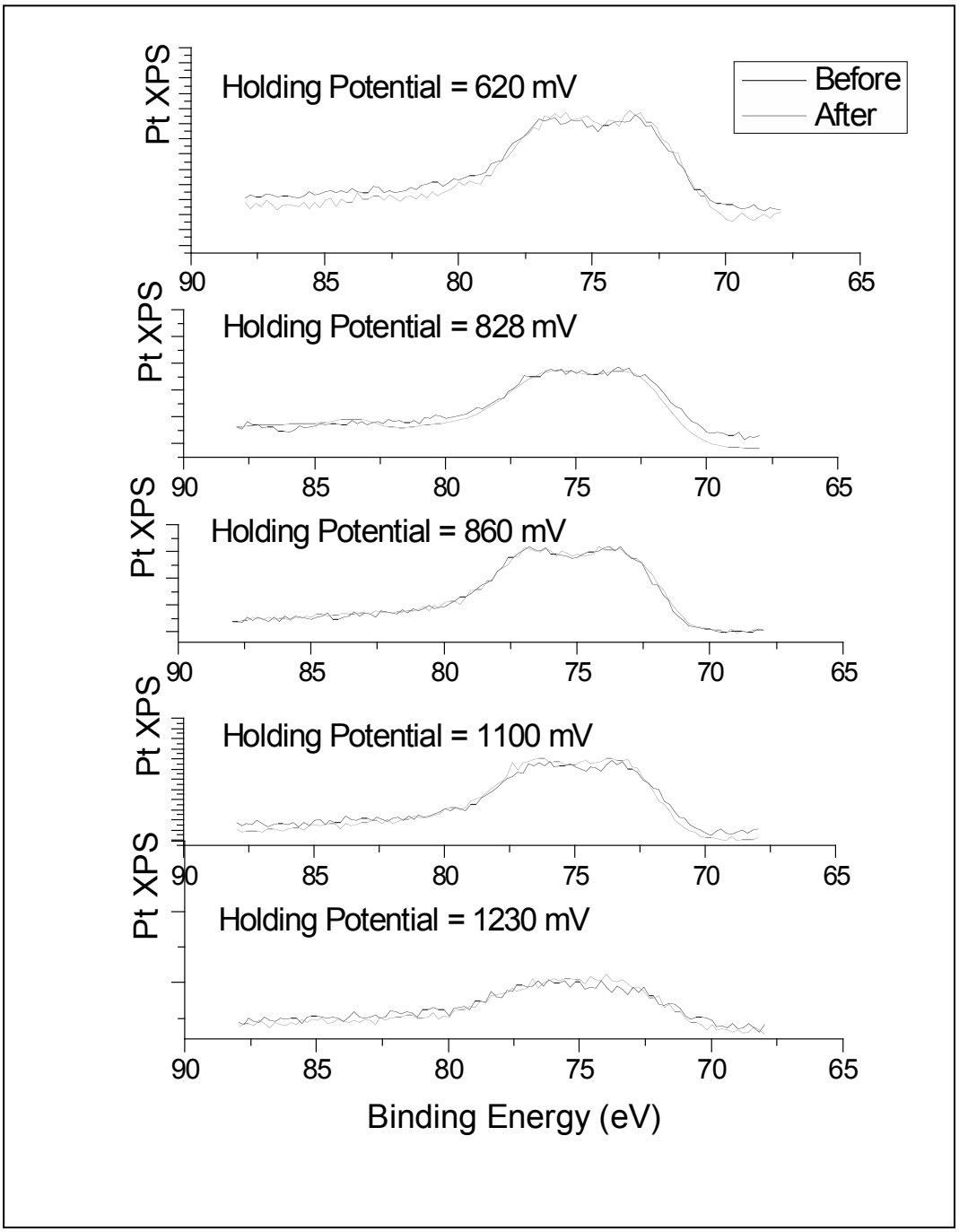

Figure 36. Pt-4f core level XPS spectra of the alloy thin film after various holding potentials.

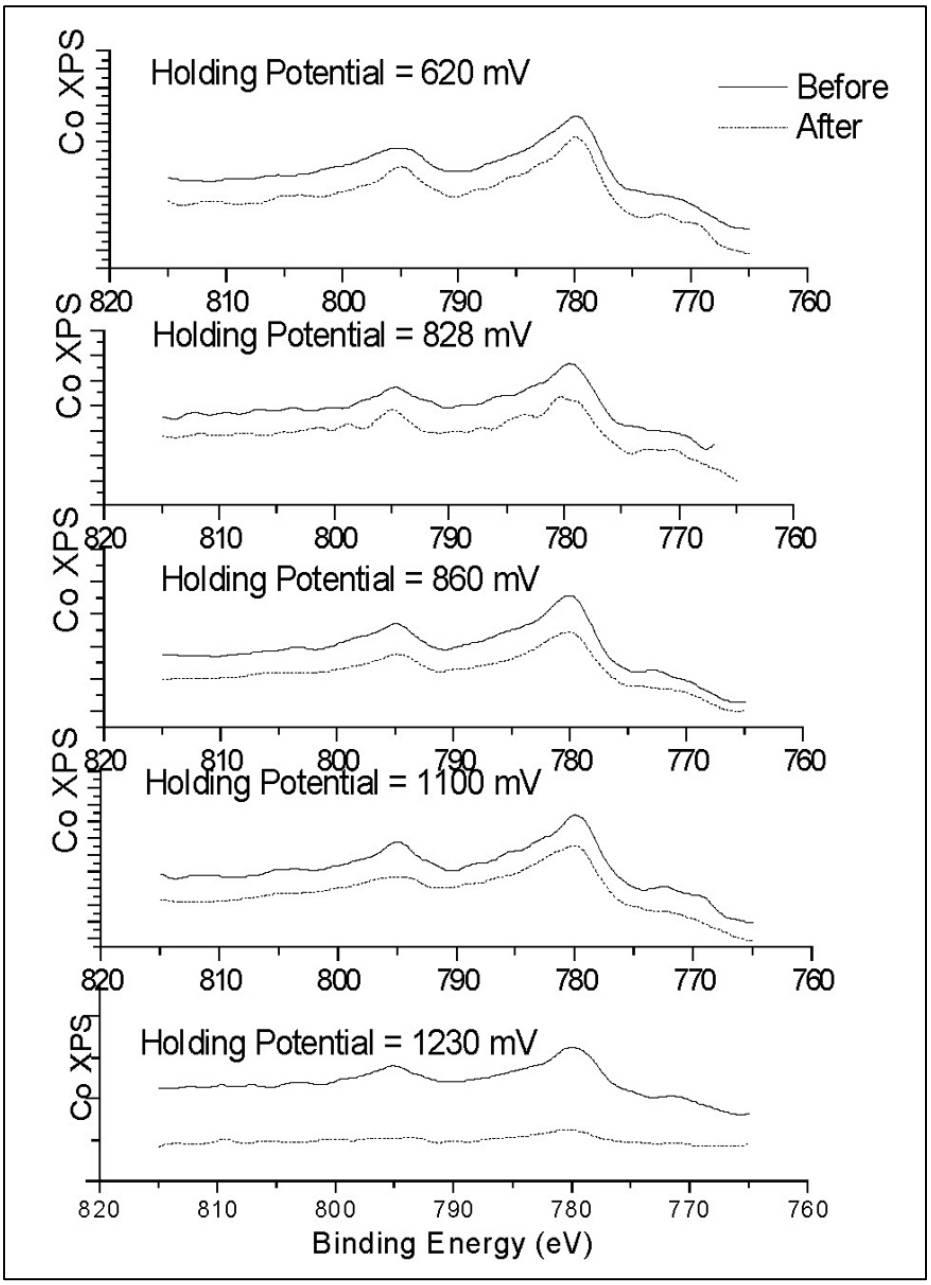

Figure 37. Co-2p core level XPS spectra of the alloy thin film after various holding potentials.

energy shift measurements by XPS) and thermochemical (adsorption enthalpy determinations by TPD) properties at the sub-surface.

A combination of LEISS, XPS and TPD was used to establish the source of the dissolved Co; that is, whether the atoms that are oxidatively desorbed into the solution phase emanate only from the topmost layer or also originate from the sub-surface. Figures 36 and Figure 37 show Pt and Co XPS data, respectively, after the Pt_3Co thin film was subjected to ten-minute constant-voltage exposures at different potentials. When the applied potential was kept between 0.6 V and 1.1 V, the post-EC spectra show constant peak intensities. However, when the potential was increased to 1.23 V both the LEISS (Figure 35) and XPS (Figure 37) data show a considerable decrease in the Co peak intensity. The loss of Co from the selvedge layer is indicated by the LEISS results. Since XPS peaks also bear information on at least two sub-surface layers, the lowered Co XPS peak intensity is suggestive of cobalt dissolution also from the sub-surface region.

The above corrosion scenario is supported by TPD experiments. Figure 38 shows TPD spectra for unalloyed (Figure 38a) and Pt-alloyed (Figure 38b) Co thin films. The decrease in the intensities of the post-EC TPD peaks is simply too drastic to be rationalized only in terms of Co corrosion from the topmost layer; a dissolution mechanism that includes atoms from the near-surface (or even bulk) regions is necessary.

When Pt is alloyed with Fe-group metals, the 5*d*-band vacancy in Pt is increased because of the higher 5*d*-band vacancy in the less-noble metals. As

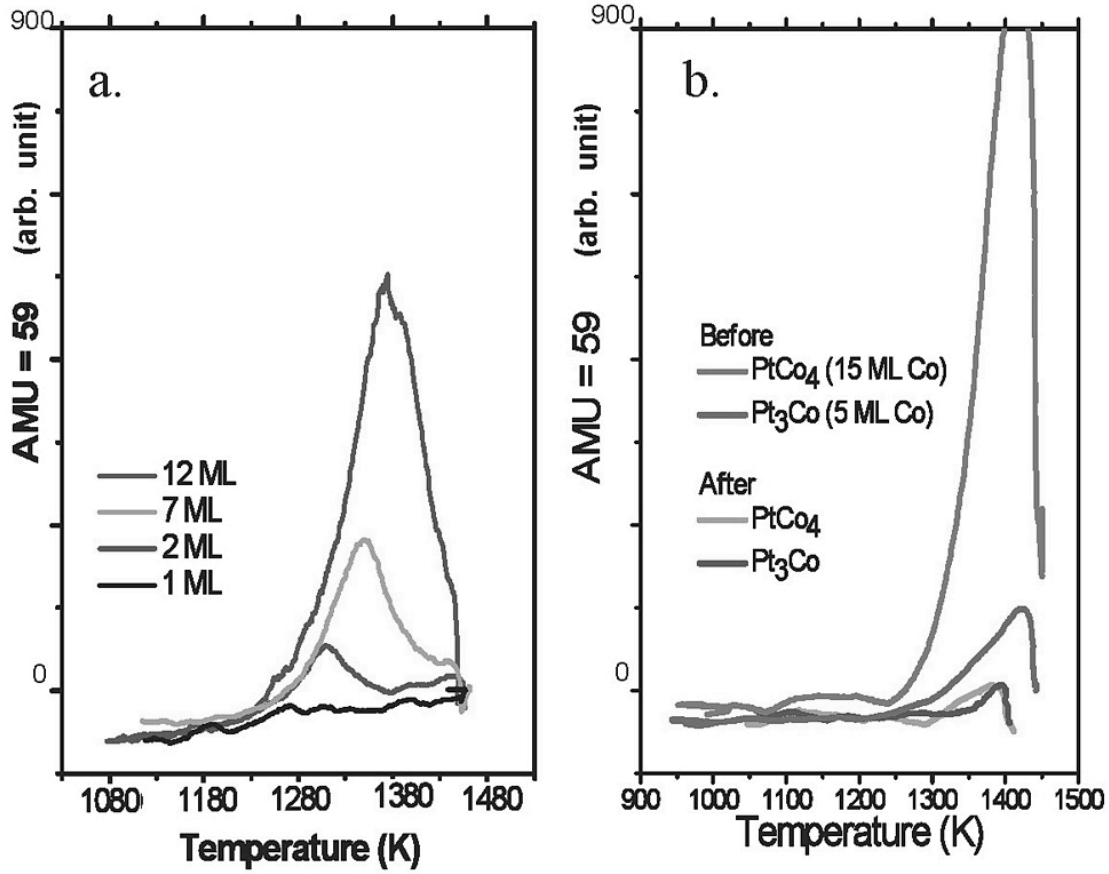

Figure 38. TPD of cobalt from (a) pure Co and (b) Pt-Co alloy thin films.

discussed in the introduction, it has thus been postulated that any enhancement in the activity of Pt-M alloys (where M is an Fe-group metal) can be rationalized in terms of an increase in the 5*d*-band vacancy in Pt [21]. The model suggests that this facilitates the initial charge transfer from the 2π molecular orbital of O_2 to the 5*d* band of Pt which, in turn, leads to an increase in the Pt-to-O_2 $2\pi^*$ back-donation; as a consequence, the O=O bond is weakened and easily broken (activated). Since a measure of the extent of 5*d*-band vacancy in alloyed Pt can be obtained from the (positive) shift in its binding energy E_B, XPS measurements were carried out for alloys of four different Pt:Co stoichiometric ratios; the results are shown in Figure 39. It can be seen that the binding energy of Pt is shifted upward by 0.3 eV when the bulk Pt:Co ratio was 3:1. When the amount of Co was increased to $PtCo_4$, the E_B shift was elevated by 0.9 eV, the same value measured at still higher Co fractions. Since, as shown above, the Pt_3Co alloy yielded the highest voltage efficiency, a shift of 0.3 eV in E_B is evidently the optimum value. Presumably, too high a 5*d*-band vacancy serves to strengthen the Pt-O bond that then leads to a retardation of the O_2-reduction reaction rate [21].

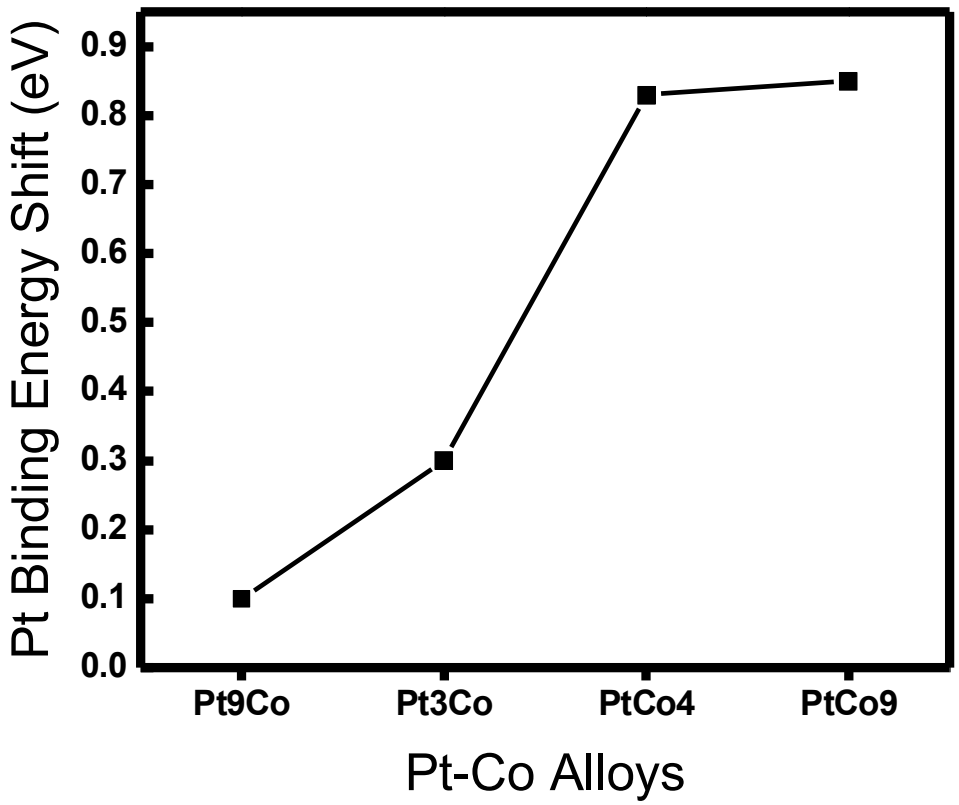

Figure 39. Pt-5d binding energy shifts (from XPS spectra) for various Pt-Co alloy compositions.

CONCLUSION FOR PART I

Pt-Co thin-film electrocatalysts have been characterized using low-energy ion-scattering spectroscopy (LEISS), X-ray photoelectron spectroscopy (XPS), low-energy electron diffraction (LEED), temperature-programmed desorption (TPD) and electrochemistry (EC). For comparative purposes, LEISS and EC were also carried out on a $Pt_3Co(111)$ bulk single crystal. Based on the observations made in this study the following conclusions can be drawn:

1. The surface phase diagram of the alloy film was marked by a substantial divergence between the composition at the interface and that in the interior.
2. When a dual-layer deposit of Pt and Co was annealed at high temperatures, alloy formation transpired in which the outermost layer became single-crystalline and enriched in Pt. The preferential surface segregation of Pt, however, was not sufficient to generate a platinum-only overlayer or "skin".
3. Invariably, Co was found to intermix with Pt, independent of the substrate [Mo(110) or Ru(0001)] employed; Pt_3Co was the most favored composition. Alloy formation was strongly indicated.
4. The absence of a Pt skin was indicated at the surface of a thermally annealed bulk $Pt_3Co(111)$ single crystal. For alloy-film surfaces more enriched in Pt than Pt_3Co, the topmost layer was constituted primarily, but not exclusively, of Pt(111) domains.

5. Thin films divergent from pure compositions showed enhanced ORR voltage efficiency. Multiple compositions displayed an enhancement over pure Pt.
6. The Pt_3Co surface, whether from the thin film or the bulk single crystal, exhibited the highest OCP, a significant improvement over pure Pt but still appreciably lower than the thermodynamic limit.
7. The degradation of the Pt_3Co thin film surfaces was predominantly due to Co corrosion. A minimal amount was spontaneously dissolved upon simple immersion in solution; slightly higher dissolution occurred at potentials above the OCP. The (major) fraction that was not immediately corroded proved to be stable even after prolonged periods at potentials more positive than the OCP.
8. An increase by +0.3 eV of the Pt-5d binding energy shows alloy formation and results in improved ORR catalysts.

INTRODUCTION TO PART II: SLR^3 PALLADIUM THIN FILMS

Ultrathin films of *noble metal* on *noble metal* substrates have elicited considerable attention, due to their exceptional catalytic, electrocatalytic, electronic, and magnetic properties [64-68]. Pd films on noble metal surfaces have drawn interest due to unique properties not normally observed in the bulk material [64, 69-73]. In particular, they exhibit enhanced catalytic activity for a number of reactions, including the oxidation of small molecules (methanol, formic acid, carbon monoxide, etc.) and oxygen reduction [74, 75]. Of special interest is the system Pd/Pt due to the identical lattice parameters of the two noble metals. Additionally, Pt and Pd possess similar atomic radii, comparable lattice energies, but different cohesive energies [76]. Moreover, the surface free energy of Pd is lower than that of Pt. Consequently, favorable deposition of Pd on Pt with minimal lattice strain is expected [77]. As a result, this system has been extensively studied [78-83].

Prior studies reported the influence of the substrate on electrosorption properties of Pd thin films; these include Pd/Pt(*hkl*) for (pc) [84], (111)[85], (100) [86, 87], (110) [86, 87]. The voltammetric features of a Pt surface modified by irreversibly adsorbed submonolayer and monolayer Pd displayed reversible hydrogen adsorption/desorption reactions, which are not observed on pure Pd electrodes[88]. To date, ultrathin Pd/Pt(111) [70, 78-80, 83, 89-96] has been widely studied as a model system in the investigation of well-defined adlayers.

Our research group has been investigating the interfacial structure and properties of ultrathin Pd films on platinum surfaces, particularly Pt(111), due to

possible emergence of properties which are otherwise nonexistent in the pure state of each individual element [95, 97, 98]. Previously in our laboratory, sub-monolayer to 8 ML Pd films prepared via direct potentiostatic deposition [99] and potentiodynamic deposition [97, 99] were characterized. We aim to build upon this study by employing the SLR^3 technique for depositing Pd ultrathin films on Pt(111) surfaces. Of particular interest is the possible existence of unique properties generated by this concatenation, not displayed by films prepared using direct physical or electrochemical deposition. The objective of the present study is to explore the interfacial structure and electrochemistry of ultrathin Pd films prepared by this novel method.

EXPERIMENTAL METHODS FOR PART II

Electron Spectroscopic Techniques

Low Energy Electron Diffraction

Low energy electron diffraction (LEED) is commonly employed to determine the long-range order of periodic surface structures, such as those encountered in single-crystal electrodes. It is a highly surface-sensitive technique and can provide information on surfaces exhibiting even near-perfect order. Unlike X-ray diffraction, LEED provides structural information regarding the surface unit mesh, again, due to the low IMFP of the electrons used in analysis.

In this technique, a hairpin-emitter is used to provide electrons which are then extracted, monochromatized, and accelerated to a surface normal at energies in the 10 to 150 eV range. Such an energy selection allows for λ of the incident electrons to be on order with the interatomic spacing. Due to short-range surface interaction, electrons are scattered by the repeating surface lattice points (i.e. surface atoms), giving rise to a pattern of interfering escaping primary electrons. The electrons produce a pattern of bright spots on a phosphor-coated screen that corresponds to the interference experienced and ultimately the long-range surface order. As such, the pattern will vary depending on the periodicity of the surface and can be deconstructed to provide the 2D surface structure. Moreover, in-depth analysis of diffraction spot beam current as a function of beam energy can provide detailed information on the atomic positions.

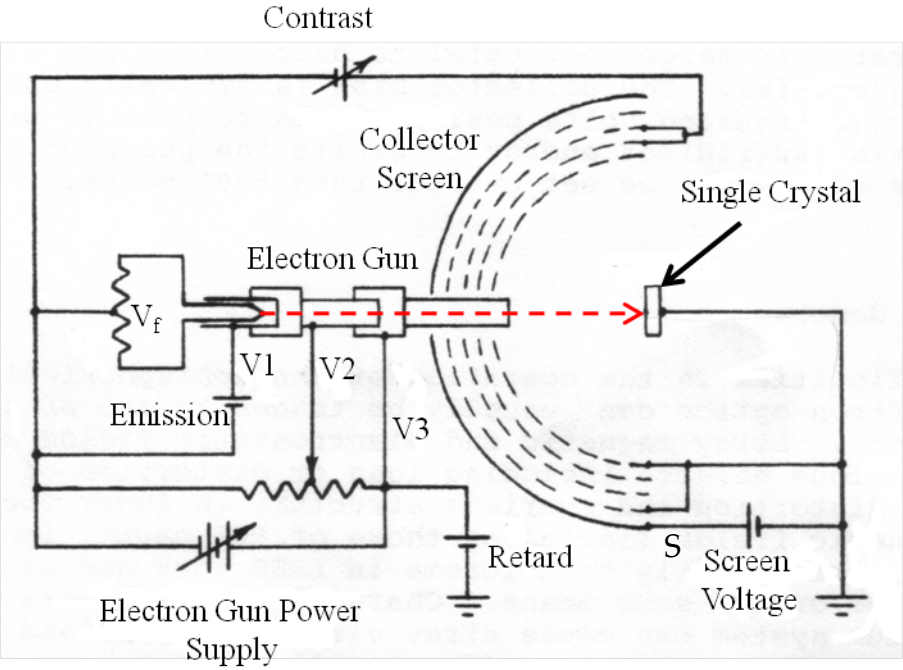

Figure 40. Schematic of LEED instrument used in this study. Details in text.

The LEED instrument follows a very simple theory of operation and design (Figure 40). It is composed of an e^- beam source, retarding field analyzer (RFA) and a concentric phosphor-coated collector screen. A filament (usually 2%- thoriated tungsten) is engaged via voltage V_F until thermionic emission is achieved. Current density is increased by an extraction voltage, V1, and electrons are accelerated by applying potentiometer-adjusted field V2; in conjunction with retarding field V3, this effectively acts as a band-pass amplifier, resulting in a mono-energetic electron beam. Following diffraction, the 4-grid RFA controls the passage of electrons to the screen. Grid G1 (plus drift-tube) is held at ground to provide a field-free drift space for the passage of primary incident and diffracted electrons. Grid G4 is also held at ground and isolates G2/G3 from the high-voltage conditions of the screen. The retarding grids themselves, G2 and G3, are negatively biased to act as high-pass amplifiers, thus filtering out lower-energy inelastically scattered electrons. Those above this threshold experience screen voltage S (few kV) and such a large field forces acceleration of electrons to an energy allowing excitation of the phosphor material upon impingement.

The resulting diffraction pattern is related to the interatomic spacing of the sample surface, made possible by the temporal coherence of the source and spatial coherence given by the surface lattice points acting as a diffraction grating; provided the source λ is on the atomic scale, following the de Broglie equation:

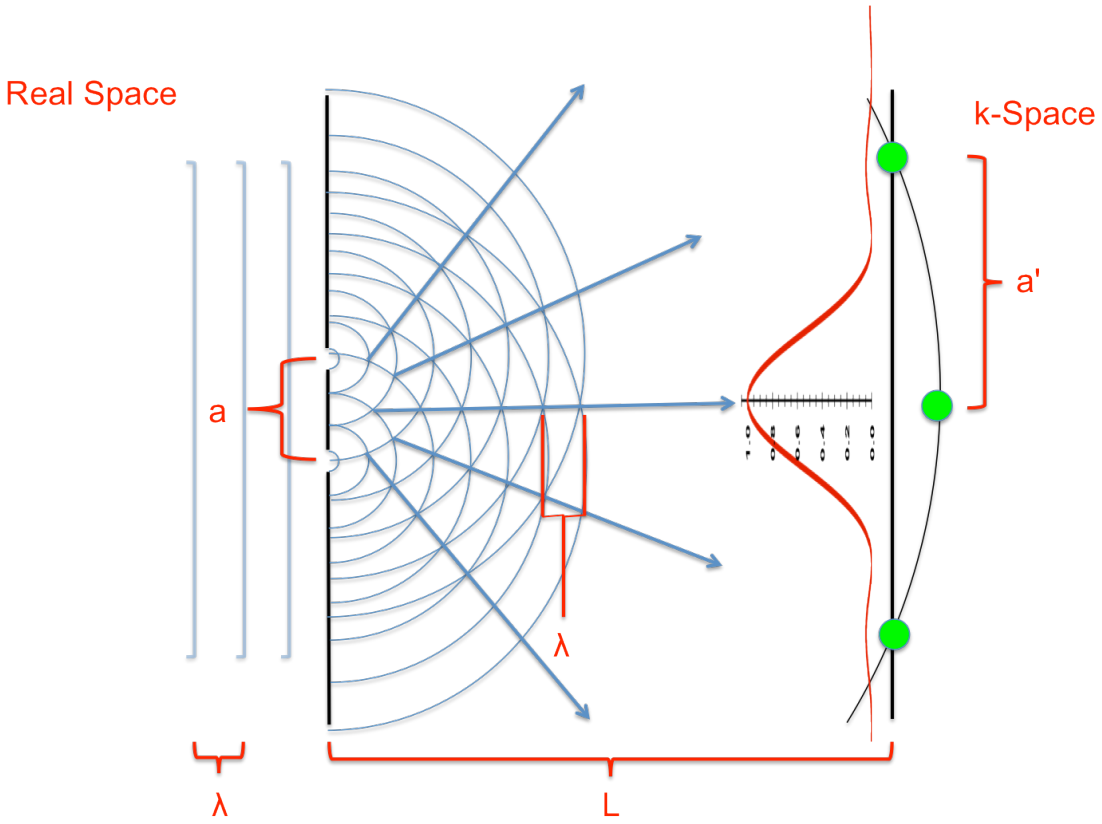

Figure 41. Classic two-slit diffraction of a plane wave.

$$\lambda = \frac{h}{\sqrt{2m_e E}} = \sqrt{\frac{150.6}{E}} \tag{33}$$

where λ is in Å, E is in *eV*, *h* is Planck's constant, and m_e is the electron mass. The simplest case of diffraction may be considered for a 1D array of point scatterers following Young's classical double-slit experiment (Figure 41). For an unobstructed incident wave, the slit width (a) would correspond to the atomic spacing; for diffraction of light with wavelength λ, the elastically scattered waves propagate away from the surface with wavelength equal to the initial wavelength. This gives rise to a convolution (5 shown here) of constructive interferences and a high degree of temporal coherence; as these project onto an external surface, the high degree of constructive overlap is observed as bright lines or points on an otherwise dim background. The spacing of these points is governed by the following relationship

$$n\lambda = \frac{aa'}{L} \tag{34}$$

where *n* refers to the diffraction order (0,1,2…*n*), with an intensity distribution (or local intensity of each *n*-point) governed by the Fraunhofer equation for the far-field condition [100].

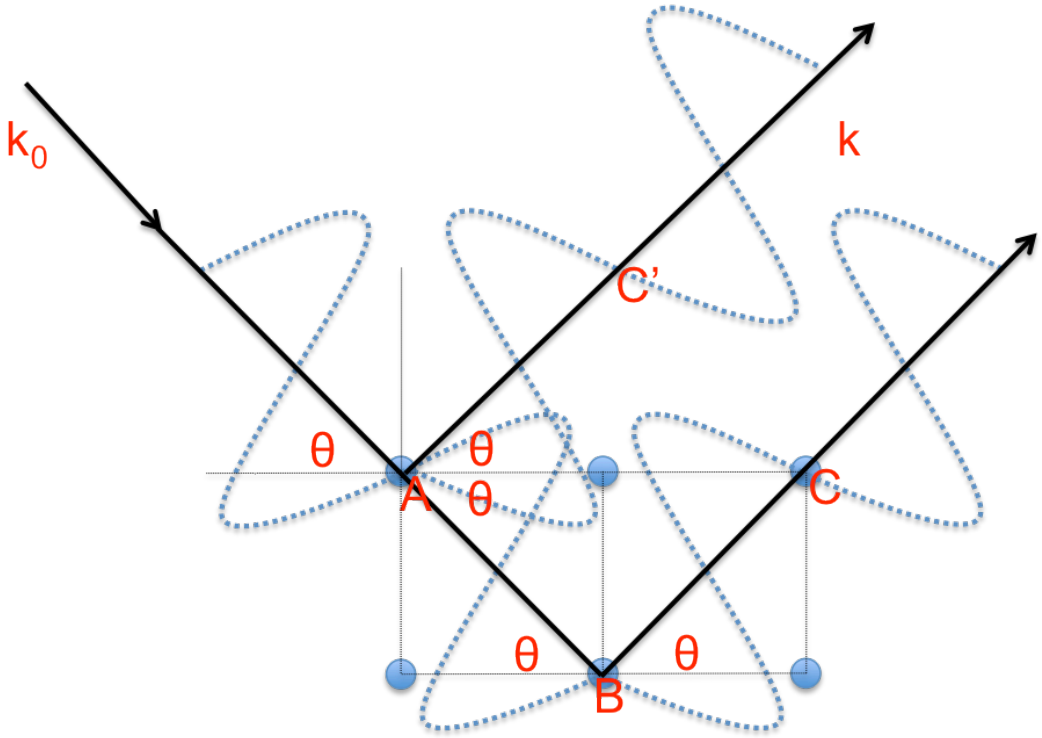

Figure 42. Side view of elastically scattered electrons in the LEED process.

Extension of this rationale to LEED patterns produced by a given surface structure gives rise to the *geometrical theory* of LEED [49]. In the more advanced framework, *dynamical theory* of diffraction, a thorough description of the diffraction process is applied, and can explain the effect of surface morphology on differences in spot intensity and shape [101, 102]. However, this method requires considerable effort and only a portion of results may have pertinence to surface structure. Hence, practitioners of LEED generally ignore the intensity information and perform analysis on diffraction patterns alone. First, the model for backscattered electrons must allow for the short IMFP of the primary electron beam. Here, the top two surface layers are viewed as a 2D array of 3D points in Figure 42. For constructive interference of backscattered waves it is easy to see that:

$$n\lambda = (\mathrm{AB}+\mathrm{BC})\text{-}\mathrm{AC}' \tag{35}$$

from trigonometric identities, it can be shown that

$$n\lambda = 2d\sin\theta \tag{36}$$

equation (36) is known as the Bragg condition, where d is the atomic spacing of a solid. Predicting the arrangement of diffracted spots from real materials (or inversely the periodicity of the surface mesh from diffraction patterns) requires the use of an Ewald sphere projected into a plane. The Ewald sphere is a scaled

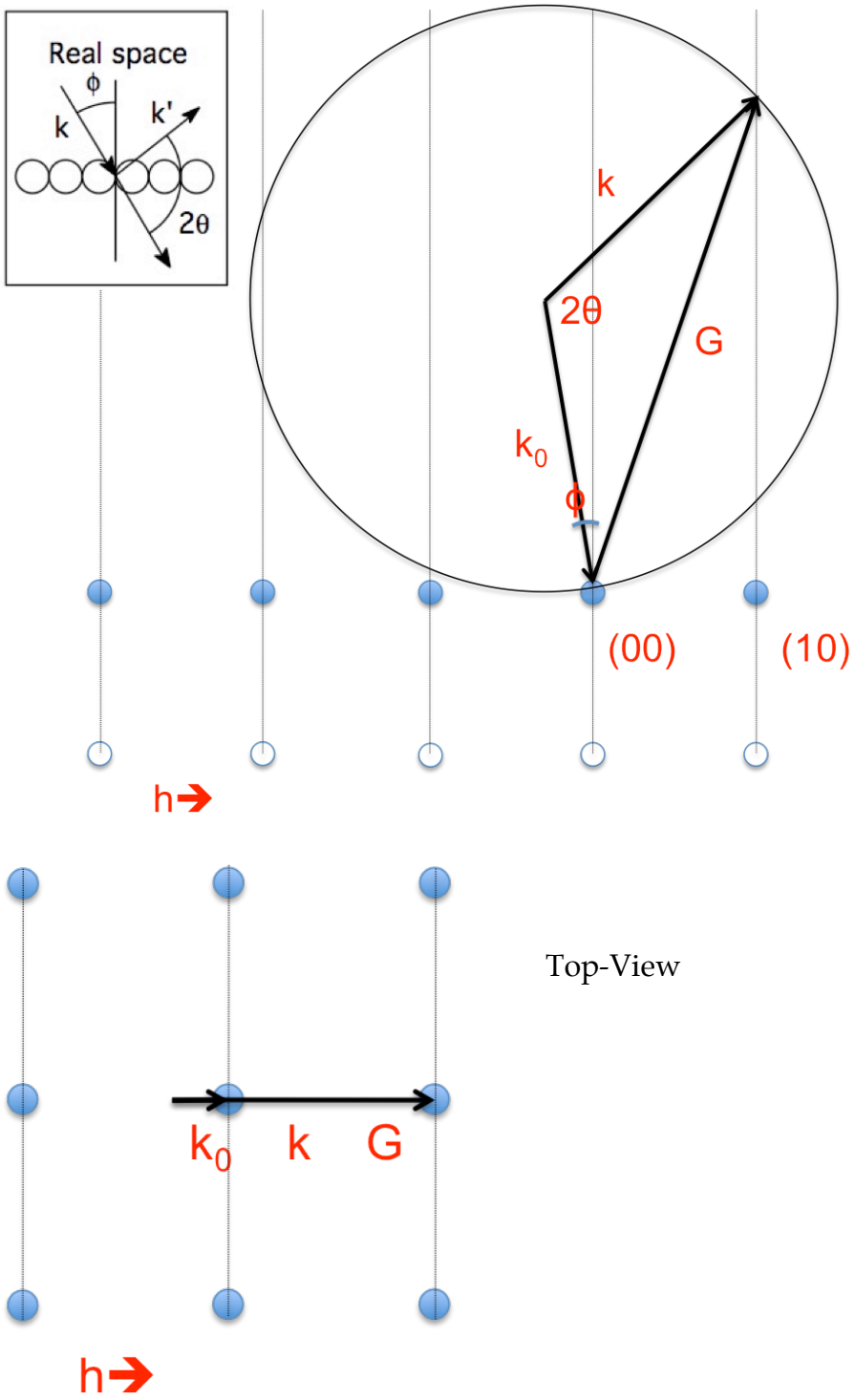

Figure 43. Ewald Sphere in two dimensions.

version of a real lattice, with lattice points separated by k as opposed to d. Here, k_0, the incoming wavevector (Figure 43) is equal to $2\pi/\lambda$ (where λ is the de Broglie wavelength given in equation (33)), k is the outgoing wavevector, and G is the scattering vector (Laue condition). Since elastic scattering only is considered, both the energy and magnitude of momentum of the scattered electron are conserved, i.e. $|k_0| = |k|$, but the direction of momentum is changed.

The Ewald construct is drawn to touch a lattice point (always the specular rod) and has radius equal to k. The position on the Ewald boundary intersected by a lattice rod (vertical line) is the position of a reciprocal lattice point. Each reciprocal lattice point is generated by a scattering vector, G_{hk}, and from this each outgoing wavevector can be determined ((38). In LEED the incoming wavevector, k_0, is incident along surface normal. This, along with the 2D limitation, provides some simplifications. Namely, the Ewald construction simplifies to Figure 44 and the Bragg and Laue conditions are restricted to:

$$n\lambda = d\sin\theta \tag{37}$$

$$G_{hk} = k^{\parallel} - k_0^{\parallel} \tag{38}$$

with only the wavevector components parallel to the surface considered. As such, the relationship between the lattice vectors in real-space and the lattice vectors in k-space are given by

$$\mathrm{G}_{hk} = h\mathrm{a}^{*} + k\mathrm{b}^{*} \tag{39}$$

$$\left.\begin{aligned} \left|\mathrm{a}\times\mathrm{b}^{*}\right|\cos\alpha = 0 \\ \left|\mathrm{b}\times\mathrm{a}^{*}\right|\cos\alpha = 0 \end{aligned}\right\} \text{implies } \mathrm{a}\perp\mathrm{b}^{*}$$
$$\left.\begin{aligned} \left|\mathrm{a}\times\mathrm{a}^{*}\right|\cos\alpha = 1 \\ \left|\mathrm{b}\times\mathrm{b}^{*}\right|\cos\alpha = 1 \end{aligned}\right\} \text{implies } \mathrm{a}\propto\frac{1}{\mathrm{a}^{*}} \tag{40}$$

$$\left|\mathrm{a}\right| = \frac{1}{\cos\alpha}\frac{1}{\left|\mathrm{a}^{*}\right|} \tag{41}$$

where (a, b) are the primitive real-lattice vectors, G_{hk} is the reciprocal lattice vector and is the sum of primitive translation vectors a^{*} and b^{*}, (*h, k*) is a set of integers, and $\alpha \equiv \mathrm{a}\angle\mathrm{a}^{*}$ [103, 104]. A useful form of the above relationships is expressed in equation (41) and reconstruction of the real-space lattice vectors can be accomplished after determining the direction of a from equation (40) and evaluating equation (41) for α; the inverse relationship is clearly seen. In the presence of adsorbates, more work is required to determine the *adsorbate* mesh (a_2, b_2) and the *substrate* mesh (a_1, b_1) vectors for the matrix *M* [105]. First, the reciprocal lattice vectors $\left(\mathrm{a}_1^{*},\mathrm{b}_1^{*}\right)$ are determined as above for the substrate (clean surface). Next, for the superstructure, the matrix elements m_{ij}^{*} are determined from the LEED pattern according to

$$\begin{aligned} \mathrm{a}_2^{*} &= \mathrm{m}_{11}^{*}\mathrm{a}_1^{*} + \mathrm{m}_{12}^{*}\mathrm{b}_1^{*} \\ \mathrm{b}_2^{*} &= \mathrm{m}_{21}^{*}\mathrm{a}_1^{*} + \mathrm{m}_{22}^{*}\mathrm{b}_1^{*} \end{aligned} \tag{42}$$

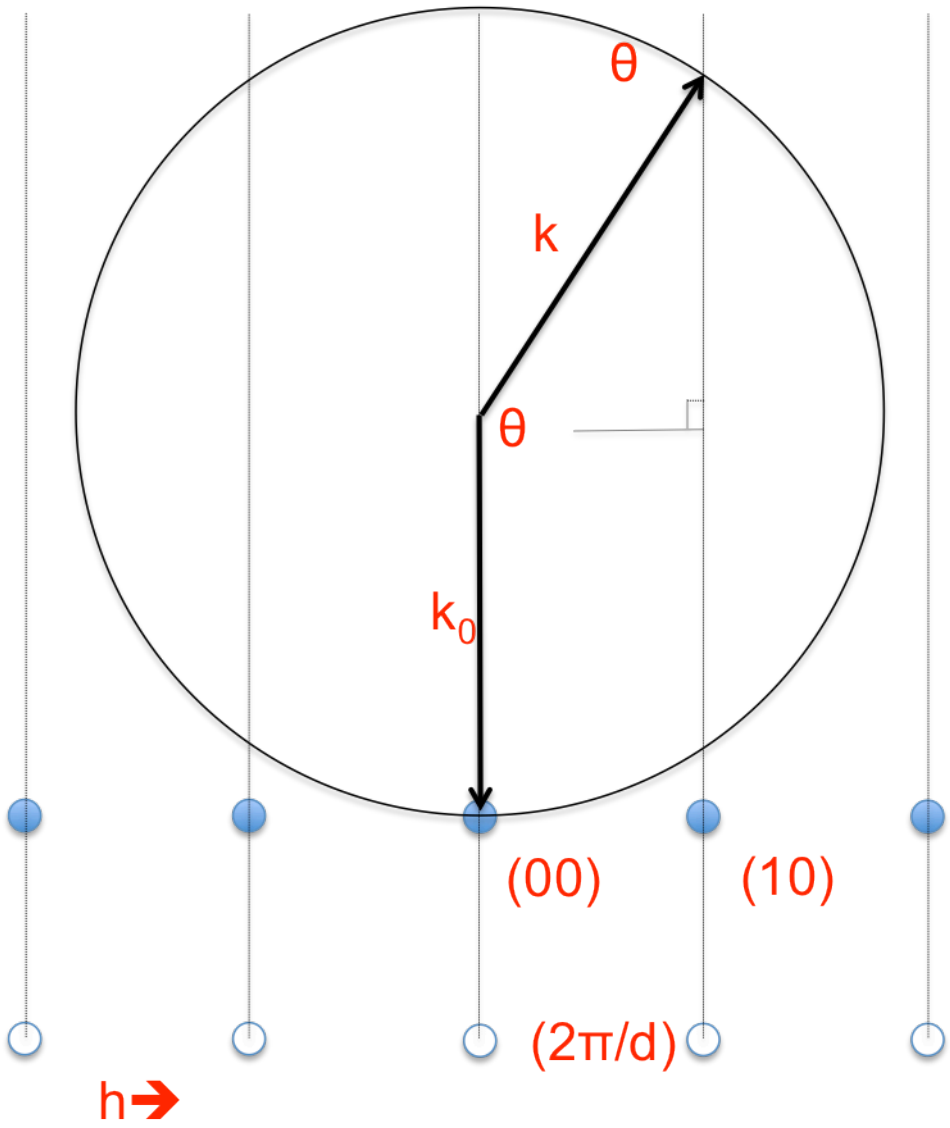

Figure 44. Ewald construction with surface limitations.

with

$$M^* = \begin{pmatrix} m_{11}^* & m_{12}^* \\ m_{21}^* & m_{22}^* \end{pmatrix} \tag{43}$$

where M^* is the reciprocal matrix and is defined as the inverse transpose of M:

$$M^* \equiv \tilde{M}^{-1} \tag{44}$$

it can be shown that the elements of the reciprocal and real space matrices are related:

$$\begin{pmatrix} m_{11} & m_{12} \\ m_{21} & m_{22} \end{pmatrix} = \frac{1}{\det M^*} \begin{pmatrix} m_{22}^* & -m_{21}^* \\ -m_{12}^* & m_{11}^* \end{pmatrix} \tag{45}$$

finally, the primitive lattice vectors of the reconstructed ad-layer (a_2, b_2), can be written as a linear combination of the substrate:

$$\begin{aligned} a_2 &= m_{11}a_1 + m_{12}b_1 \\ b_2 &= m_{21}a_1 + m_{22}b_1 \end{aligned} \tag{46}$$

hence, the real space lattice vectors of the overlayer (a_2,b_2) are known. This method reveals ad-structure along with any rotations with respect to the substrate.

Displayed in Figure 28 is a series of simulated LEED patterns for Pt, Pd, and Pt_3Co, in the viewing direction of $[\bar{1}1\bar{1}]$ with a line drawn to the [11] spot. For each, a sampling depth of 3 Å was considered along with a primary beam energy of 60 eV at a camera distance of 25 cm. Patterns were produced using CrystalMaker and SingleCrystal software, with data obtained from FIZ/NIST Inorganic Crystal Structure Database (ICSD [106]) [107-109].

For this study, LEED data was acquired with a PE 15-120 LEED Optics and PE 11-020 LEED Electronics system (Perkin-Elmer, Eden Prairie, MN) and images were recorded with a digital camera. The beam current was adjusted to 2 μA above background. In most images, the $[0\ \bar{1}]$ spot is obscured by the sample holder. Initially, the crystal-surface unit mesh was assigned by visual inspection of the diffraction spots. The geometry of subsequent LEED patterns were analyzed; with those obtained from calculations and structural information herein is reported using Wood's notation [110]. The images were recorded with a digital camera (Canon PowerShot S410), in manual programming mode with the following settings (unless otherwise indicated): ISO = 50, exposure = 15 s.

Auger Electron Spectroscopy

The tandem of LEED and Auger electron spectroscopy (AES) comprise the workhorse techniques of surface analysis. They are the most widely used, highly sensitive (capable of detecting sub-monolayer coverages), and suitable for study of a multitude of interfaces. In an AES experiment photons, ions, or most typically electrons with primary energies (E_P) of 1-10 keV bombard a sample surface. Despite such high energy, AES is still a surface-sensitive technique, because the resulting Auger electrons have energies in the range of the "sweet-spot" of Figure 7, thus only the Auger electrons from the surface region have sufficiently low IMFP and can escape**.** The resulting excitation may elicit an Auger transition, noted by a 3-electron process following a "hole"-formation of an inner electron shell. If electrons of an inner shell have $E_B<E_P$ they may be ejected, giving rise to an excited state, which may produce a number of relaxation processes. The singly ionized atom may undergo relaxation via two competing processes: (1) photoemission by X-ray fluorescence or (2) the radiationless Auger sequence. In the Auger process, the first electron in a core shell (S) is ejected. Following this, an electron from a higher core shell (S′) falls to neutralize the hole formed in step 1. The energy released during the electron transition in step 2 can be transferred to an electron in shell (S″); if the excess energy from the transition is step 3 exceeds the binding energy, $E_{B\text{-}S''}$, it will be ejected into the vacuum with an energy E_{kin}. This final state is a doubly charged ion and the second emitted electron is the Auger electron. Because it is a three-electron process, H and He cannot undergo Auger emission (Figure 45).

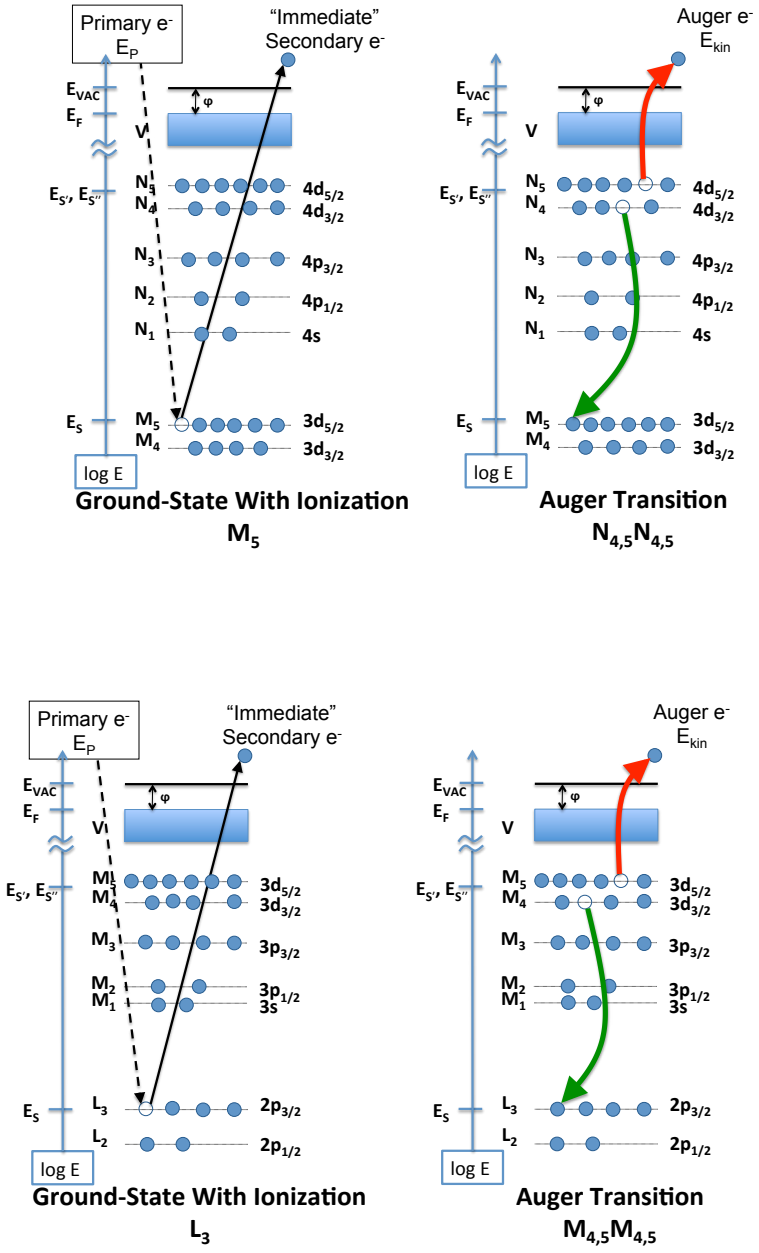

Figure 45 Schematic illustrations of the $M_5N_{4,5}N_{4,5}$ Auger transition for the 330 eV Pd peak TOP; and the Cu $L_3M_{4,5}M_{4,5}$ transition for the 920 eV peak BOTTOM. Following the description below, the overall transition can be denoted (SS′S″).

For AES, an electron originates from a core level and the overall process is described as a ($C_1C_2C_3$); this is contrasted with the case where transitions from valence states could occur (C_1VV). For simplification, higher shells are omitted. Specifically, the orbitals whence electrons are is given in X-ray notation for a particular transition; thus, for the $M_5N_{4,5}N_{4,5}$ and $L_3M_{4,5}M_{4,5}$ transitions, it can be seen that like XPS, E_{kin} is related to E_B of the ejected electron; however, unlike XPS the E_{kin} for a given AES peak is independent of E_P.

$$E_{kin} = \left[E_S - E_{S'}\right] - E_{S''} - e\phi_{SP} \qquad (47)$$

for (a), this would correspond to

$$E_{kin} = \left[M_5 - E_{N_{4,5}}\right] - E_{N_{4,5}} - e\phi_{SP} \qquad (48)$$

where the $\left[M_5 - E_{N_{4,5}}\right]$ term refers to the excess energy available to the Auger electron as an N-shell electron fills the M-shell hole, $E_{N_{4,5}}$ is the E_B of the Auger electron, and the final term accounts for the energy requirement to escape to vacuum; e is the electron charge and ϕ_{SP} is the work function of the spectrometer. For exact solutions of equation (48) it is important to see that $\{E_{S'}, E_{S''}\}$ are E_B for the singly- and doubly-ionized states, respectively. Nevertheless data obtained E_{kin} is characteristic for a given (SS′S″) for a given elemental identity and is what allows AES to be used for elemental analysis [49].

A schematic for a typical spectrometer used in AES is given in Figure 9 and the experimental design will be discussed here. The apparatus consists of a cylindrical mirror analyzer (CMA) for electron energy discrimination, a coaxial electron gun operating in a similar fashion to the source used in LEED, and a variable gain electron multiplier detector. The initial S transition is induced by an electron beam at incidence normal. As illustrated in a massive flux of secondary electrons as well as Auger electrons (occurring at, generally, sub-unity emission probability) are passed to the CMA. Energy analysis is accomplished applying a negative DC ramp voltage to the outer cylinder while holding the inner cylinder at ground. Under these conditions, only those electrons with appropriate kinetic energy can pass through the exit slit and reach the electron multiplier: hyper-energetic electrons crash into the outer cylinder and hypo-energetic, the inner cylinder. If the resulting signal is read directly, peak identification would be arduous task; recall that both Auger and secondaries enter the CMA so the analytical signal is a composition of the Auger current and the secondary electron current. Because of this spectra contain the Auger signal superimposed on a large sloping background. To rectify this, the signal N(E) (i.e. the detector counts for a given E [really E_{kin}]) is differentiated with respect to energy and spectra reported as dN(E)/dE vs. E. Differentiation may be accomplished numerically, or as in this study, via analog signal demodulation. In any case, sensitivity is greatly enhanced, allowing practical detection limits of 0.1% of a monolayer [111]. Ultimately, the resolution capability of the CMA determines the bandwidth of the detected electrons.

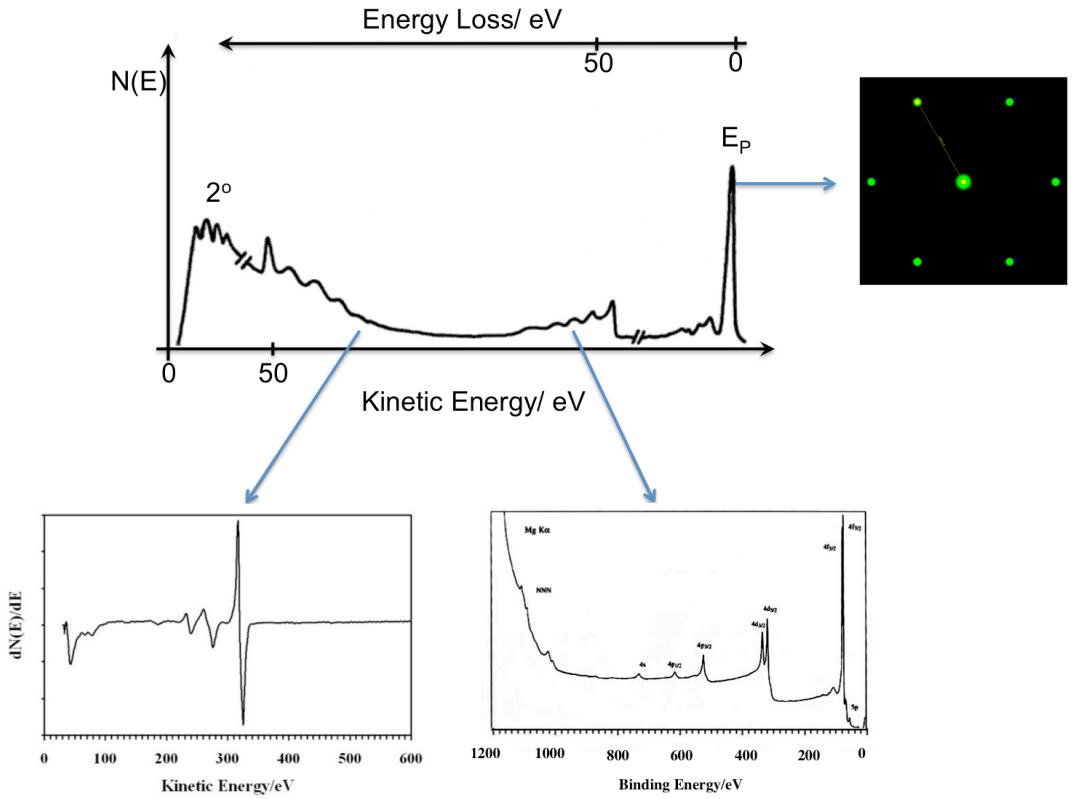

Figure 46. Example of energy losses experienced by electrons upon interaction with a surface. Examples of their application to this study are inset.

Even though the Auger yield trails off at higher atomic numbers (Z>20), characteristic peaks due to Auger transitions are still present in the electron emission spectrum Figure 46 [50]. Following differentiation of the analytical signal, peak assignments can be made against a suitable standard or reference library and this provides a routine method for identification of surface species [112]. Given a deviation of the spectrum from a pure sample, the extent of impurity can be determined from equation (49**)**; because of the surface specificity, this type of analysis yield quantitative information regarding absolute coverage of adsorbates. The mole fraction of an adsorbate, x_A, in a binary system can be obtained from the following [113]:

$$\chi_A = \frac{I_A / f_A}{I_A / f_A + I_B / f_B} \tag{49}$$

where, I_A and I_B are the integrated peak areas for the adsorbate and substrate, respectively, and f_A and f_B are the corresponding relative sensitivity factors. For an *n*-component system, the denominator becomes

$$\sum_{\{j \mid j = A,B,C...n\}}^{n} I_j / f_j \tag{50}$$

assuming coverage does not affect peak shape, the integrated peak area correlates with peak-to-peak height; this greatly simplifies the quantitation process.

In the present study, a set of Perkin Elmer AES systems (Perkin Elmer-Eden Prairie, MN), which included PE 10-155 Cylindrical-Auger Electron Optics, PE 11-500A Auger Control System, PE 20-075 Electron Multiplier Supply, PE 11-010 Electron Gun Control, and EG&G model 5101 Lock-In-Amplifier (Princeton Applied Research), was used for the surface elemental analysis of the single-crystal electrode. To produce derivative spectra, an AC signal of 12 kHz with amplitude of 5 V and an offset of 5V is superimposed on the DC voltage that is applied to the outer cylinder of the CMA. This signal is later decoupled from the high electron multiplier voltage by lock-in-amplification [114, 115]. The kinetic energy resolution of the CMA is 0.6%; the resulting band pass window is scanned at 4 eV/s. Typical electron gun voltage was 1.5 kV, with a beam current adjusted to 1 μA above background. As in the other techniques used here, this is sufficiently low as to prevent beam induced surface ablation. In this study, quantitative information was obtained by normalizing the peak-to-peak heights relative to the 320 eV (MNN) peak for Pd/Pt(111) formed by direct deposition of the indicated coverage [99].

Electrochemistry

Cyclic Voltammetry

For this study, CV was used as a surface characterization technique with minor application of quantitative analysis. The area under a potentiodynamic peak is essentially the electrical power (iV) of the work done between the scan limits (E_1 and E_2, not the same as above). In practice, the total power is a composition of the power expended by background and faradaic processes. Correction for the background and numerical integration can produce a quantitative measure of the coulombic charge associated with the peak. The value is strictly only an approximation because it is obtained under potentiodynamic conditions; however, a correction is easily determined by the voltammogram obtained in the absence of surface electrochemical processes.

Coulometry

In addition to voltammetry, this investigation includes coulometric techniques. Coulometry is a potential-step experiment and provides a simple and direct determination of Γ. In this technique, the WE is initially held at potential E_0 and switched to E_f; in this capacity it can be viewed as a linear scan voltammtry (LSV) experiment where $v = \infty$. E_0 is selected, such that no faradaic process takes place while E_f represents a potential sufficiently positive to force completion of the process in a short amount of time. The potential window defined by these two potentials is obtained by inspection of a voltammogram.

The charge accumulated in response of the potential step is preferable over those obtained from voltammetry, as a changing background need not be

considered. The charge recorded contains contributions from adsorption, double layer charging, and background processes. The charge due to adsorption in this work is faradaic (Q_F) and thus directly related to coverage by Faraday's law.

$$Q_F = \mathrm{nFA}\Gamma \qquad (51)$$
$$Q_T = Q_F + Q_b$$

Where n is the number moles of electrons required or given up per mole of redox process, A is the electroactive surface area, and F is Faraday's constant. The double layer charging component can be viewed as an RC circuit whose charging is complete in about 3τ, approximately 0.1 ms for reasonably dilute aqueous solutions; thus, its contribution to total charge is negligible [12]. Charges attributable to background processes (Q_b) can be controlled experimentally or corrected for in a similar fashion as for voltammetry.

I_{ads}-Catalyzed Pd Dissolution

Θ_{Pd} was calculated by measuring the charge of I_{ads}-catalyzed anodic dissolution of Pd, in blank supporting electrolyte, using Faraday's law. In all cases, the scan was commenced in the anodic direction from OCP, the LSV was recorded and the Pd dissolution charge was determined by numerical integration of the Pd dissolution peak. When I-catalyzed dissolution of Pd was complete, a second aliquot of iodine was adsorbed on the electrode surface from fresh I^- solution and a second I_{ads}-catalyzed stripping was conducted. From this second scan, it was apparent that a single scan is enough to remove all deposited

Pd, consistent with previous reports [99, 116]. In each case, the second scan was used as a background and subtracted from the first voltammogram. Iodine was adsorbed from 1 mM NaI in 100 mM sulfuric acid at OCP for 3 minutes. The Pd coverage, Θ_{Pd}, is denoted as n ML, with $\Theta_{Pd} = n$; and $\Theta_{Pd} = \Gamma_{Pd} / \Gamma_{Pt}$, where $\Gamma =$ packing density of indicated adsorbate.

UHV-EC Instrumentation

The UHV-EC system employed in this investigation was built from a commercial all stainless steel UHV chamber (Perkin-Elmer- Eden Prairie, MN). A diagram of the chamber is given in Figure 47. For the characterization of Pd-SLR^3 thin films the chamber is equipped with an AES-LEED-EC setup. The base pressure of the vacuum chamber is 5×10^{-10} Torr after extensive bakeout, with a day-to-day operating presuure of 1×10^{-9} Torr. AES data is collected by the CMA and LEED patterns the RFA. The sample is mounted to a sample probe at the top of the chamber. The probe is made out of a highly polished stainless steel tube. On the feed-through, there are four connections: two thermocouple leads, and two oxygen-free highly conductive (OFHC) copper leads for resistive heating of the sample.

Attached to the top of the surface analysis chamber is a "high-pressure" EC ante-chamber designed for electrochemical experiments. For such experiments, the sample was transported to the antechamber, under clean transfer conditions, which was back-filled with UHP N_2 or O_2. The single-crystal electrode was transferred by means of an X-Y-Z manipulator (Varian, Lexington,

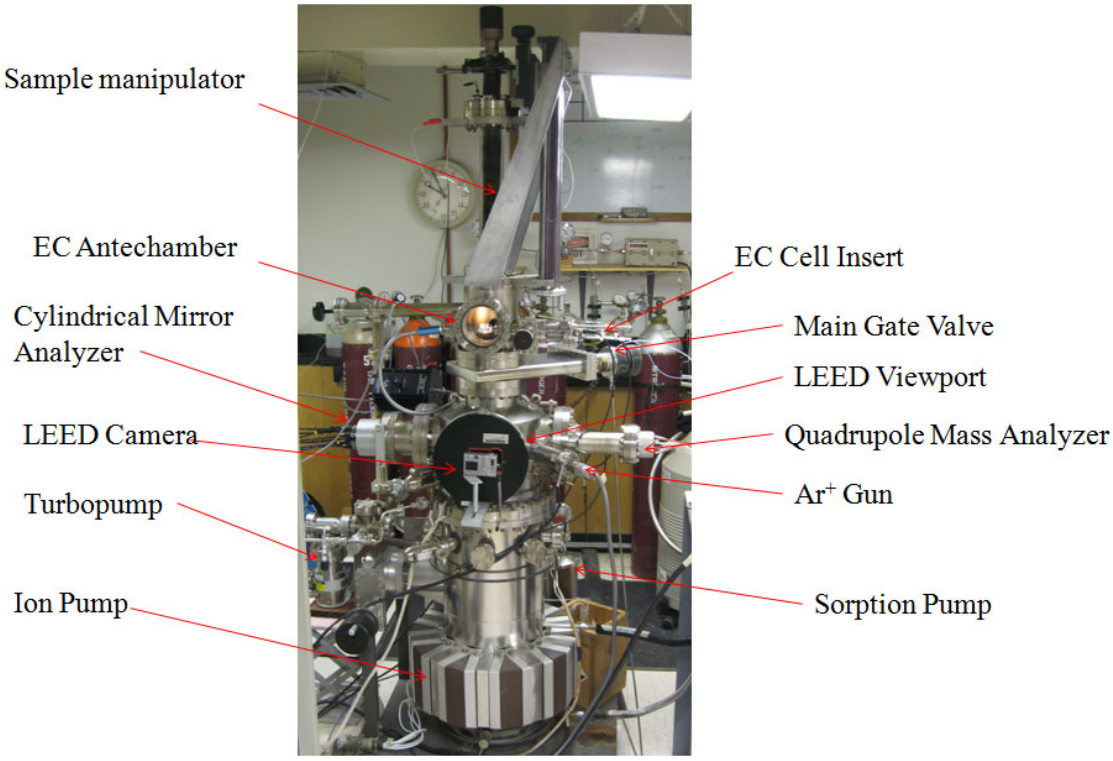

Figure 47. Picture of the AES-LEED-EC instrument used in this study.

MA) mounted on a linear positioning table (LinTech, Los Angeles, CA). To exact the clean sample transfer no exposure to atmosphere was allowed and this was accomplished by a gate-valve (MDC Vacuum Products, Hayward, CA) between the analysis chamber and the ante-chamber. The main advantage in this setup is its simplicity and ease of maintenance as it provides isolation from UHV conditions inside the analysis chamber, during EC experiments.

In addition to the instrumentation, the analysis chamber featured two variable leak valves (Varian, Lexington, MA) for the introduction of ultra-high purity gases. A custom-built ion gun was used for Ar^+-sputtering to clean the electrode surfaces. The analysis chamber was of, cylindrical symmetry with a volume of about 100L. Initial pumping of the chamber from ambient pressure to 10^{-3} Torr, as well as roughing the turbo-pump, was achieved by liquid nitrogen-cooled sorption pumps. A 60 L/s turbomolecular pump (Balzers TPU 060, Hudson, NH) was used to lower the pressure down to 10^{-6} torr. The final pumping stage consisted of a 220 L/s ion pump (Perkin-Elmer TNBX Series 1000- Eden Prairie, MN) and a cryogenically cooled titanium sublimation pump in a poppet valve-isolable ion pump well.. The UHV-EC system was periodically baked at 150 – 200 °C for up to 99 hours to maintain a daily base pressure of 10^{-9} torr. Mass spectra were collected periodically with the on-board UTI 100c QMS (UTI Instruments- Sunnyvale, CA), to check the residual gases present. All UHV seals were made by double-Conflat flanges, with well-maintained knife-edges, crushed into single-use OFHC Cu gaskets.

A single-crystal Pt(111) disc electrode (99.999% purity, 7.5 mm (diameter) and 1.0 mm (thickness), Aremco Products, Ossining, NY) was used for UHV-EC experiments. The disc electrode was oriented to within ±0.5° of the (111) plane and metallurgically polished to a mirror finish. Two segments of Pt wire of 0.5 mm thickness (99.99% purity, Aldrich) were spot-welded to the top edge of the disc to provide electrical contact and mechanical support. A Type S thermocouple (Pt-10%Rh||Pt, Omega Engineering- Stanford, CT) was spot-welded to top dead center of the backside of the sample to provide temperature monitoring and feedback control of a crystal temperature controller (Omega Engineering). The calculated geometric electrode area of the electrode was 1.1192 cm^2.

The EC chamber has a gate-valve (MDC Vacuum Products) isolable electrochemical cell port through which an electrochemical cell assembly can be inserted. Electrochemistry experiments in the UHV-EC system were performed using a custom-built two-compartment glass cell, separated by a fine-frit. EC experiments were conducted using a CV-27 Voltammograph (Bioanalytical Systems- West Lafayette, IN). To facilitate data logging, an analogue to digital data acquisition device (DI-158 UP, DATAQ Instruments- Akron, OH) interfaced with a PC via USB was employed. In this conventional four-electrode potentiostat, the sensing electrode (SE) was shorted to the working electrode (WE). Potentials were applied between the reference (RE) and counter (CE) and current flow between WE and CE were recorded at the WE. The WE was either the pristine or modified Pt(111) disc, CE was a Pt wire of high surface area , and

the RE a custom-built Ag/AgCl (1 mM NaCl). All voltammetric curves presented in this study follow the IUPAC convention; positive potentials are to the right on the X-axis of the cartesian plot and anodic currents reflecting oxidation processes are positive on the Y-axis. Scan rates employed are very slow, 0.1 $mV \cdot s^{-1}$ to 5 $mV \cdot s^{-1}$. Figure 14 shows a photograph of the cell configuration. Potentials referenced are vs. the reversible hydrogen electrode (RHE).

Reagents and Gases

All solutions were prepared using 18.2 Ω Millipore water (Millipore Systems, Houston, TX). The water delivery system consists of a prefilter, two ion exchangers, a trap to remove trace organics, 185 and 254 nm UV lamps (anti-microbial), a 0.22 μm particulate filter, and on-board water quality analysis. All glassware was cleaned using hot chromic acid (3% $K_2Cr_2O_7$ dissolved in 10 M H_2SO_4). The following high-purity reagents were used to prepare all solutions: fuming H_2SO_4 (Aldrich, Milwaukee, WI), $K_2Cr_2O_7$ (EM Science, Gibbstown, NJ), $CuSO_4$ (Aldrich), $PdSO_4$ (Aldrich), NaCl (Johnson Mathey), and NaI (Curtin Matheson Scientific, Houston, TX). High purity gases nitrogen (99.999% purity, BOTCO, Bryan, TX), argon (BOTCO), and oxygen (BOTCO) were used in all experiments. Prior to EC experimentation, solutions were sparged with high purity nitrogen for at least 20 minutes.

Experimental Protocol

A typical set of experiments was executed according to the following procedure: initially the crystal was cleaned by Ar^+ sputtering for 20 - 30 min ($P_{Ar} = 2.2 \times 10^{-4}$ torr, beam current = 10 μA). Following Ar^+ sputtering, all the filaments of the optics and ion gauges were degassed in UHV. Then the crystal was heated in O_2 ($P_O = 3.0 \times 10^{-4}$ torr) at 650 °C for 5 minutes. Once the crystal cooled to 300 °C, the system was pumped down to about 10^{-6} torr. The thermal oxidation was carried out a few more times ($P_O = 3.0 \times 10^{-4}$ torr, 650 °C, for 5 min 2 cycles; $PO_2 = 3.0 \times 10^{-4}$ torr, 750 °C, for 3 min, 3 cycles). During Ar^+ sputtering and thermal oxidation in oxygen, the ion pump was isolated. In the last step, the crystal was flash annealed to 800 °C under ultra-high vacuum (UHV) while operating the liquid nitrogen cooled titanium sublimation pump. The AES and LEED filaments were also degassed during this last step. The cleanliness and surface order was confirmed by AES and LEED. Ar^+ sputtering, thermal annealing in oxygen, and thermal annealing in UHV cycles were continued until the desired cleanliness and order were achieved.

The digital (i.e., layer-by-layer) deposition of Pd ultrathin films on Pt(111) electrode was carried out via surface-limited redox replacement using a Cu_{UPD} adlayer as a sacrificial template. The UPD of Cu on a number of noble metal substrates such as Au, Pt, Ru, and Pd has been studied extensively as a model system. It is fortuitous that Cu shows distinctive UPD features for both Pt and Pd surfaces. Hence, Cu was chosen as a sacrificial template to deposit atomic

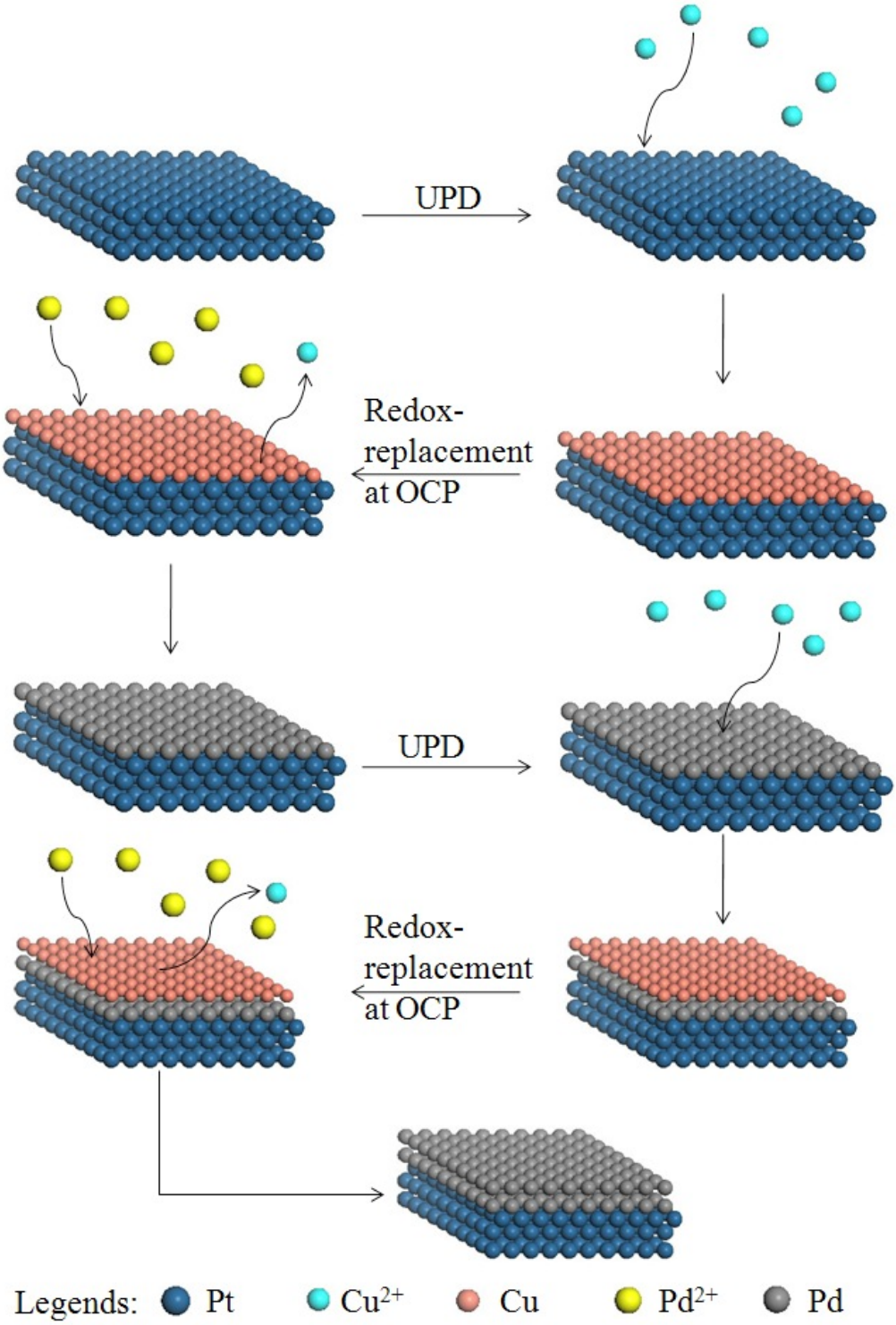

Figure 48. Schematic of the surface-limited redox replacement reaction. Two cycles of underpotential deposition and galvanic exchange are shown.

layers of Pd films on Pt(111) via galvanic displacement, as well as a surface probe. Figure 48 provides a schematic of the digital SLR3 process (following Brankovic et al. [30]). The steps are:

1. Deposition of Cu on Pt(111) via UPD according to the reaction

$$Cu^{2+}_{(aq)} + 2e^- \longrightarrow Cu_{(s)} \qquad (52)$$

2. Emersion and rinsing of the Cu/Pt(111) with pure electrolyte (typically 5 times) at UPD potential (ca. -0.054 V). The Cu-modified electrode is then immersed in 0.5 mM $PdSO_4$ in 100 mM sulfuric acid at OCP for 3 min. Potential control is removed just before the immersion of the Cu-coated electrode into the Pd^{2+} containing solution to avoid direct electrodeposition of Pd. At this step, Pd^{2+} cations oxidize the Cu ad-atoms and are themselves get reduced and deposited on the Pt(111) surface. This process is irreversible.

$$Pd^{2+}_{(aq)} + Cu_{(s)} \longrightarrow Pd_{(s)} + Cu^{2+}_{(aq)} \qquad (53)$$

3. The Pd/Pt(111) electrode is rinsed with pure electrolyte solution at OCP 5 times (this is the end of 1st SLR^3 cycle).
4. Deposition of Cu on Pd/Pt(111) electrode via UPD.
5. Emersion and rinsing of Cu/Pd/Pt(111) with blank (5 times) at a selected UPD potential (ca. -0.100V).

6. Replacement of Cu from Cu/Pd/Pt(111) by Pd^{2+} cations in 0.5 $PdSO_4$ in 100 mM sulfuric acid at OCP.
7. Rinsing of Pd modified Pt(111) with blank at OCP. This is the end of 2nd cycle of SLR^3.

Following the above steps, 2 ML Pd is now deposited on the Pt(111) electrode via two cycles of SLR^3. These steps can be repeated, seemingly *ad infinitum*, to prepare Pd films of desired thickness. The interfacial structure and electrochemical properties of thus prepared films were then compared with those of the electrodeposited films, more specifically, Pd ultrathin films prepared by potential-step or controlled-potential deposition. The methodology of the preparation of the electrodeposited films has been described elsewhere [95, 99]. Briefly, Pd was deposited from 0.5 – 1 mM $PdSO_4$ in 100 mM sulfuric acid by stepping the potential from the open circuit potential to a predetermined value for 2 minutes.

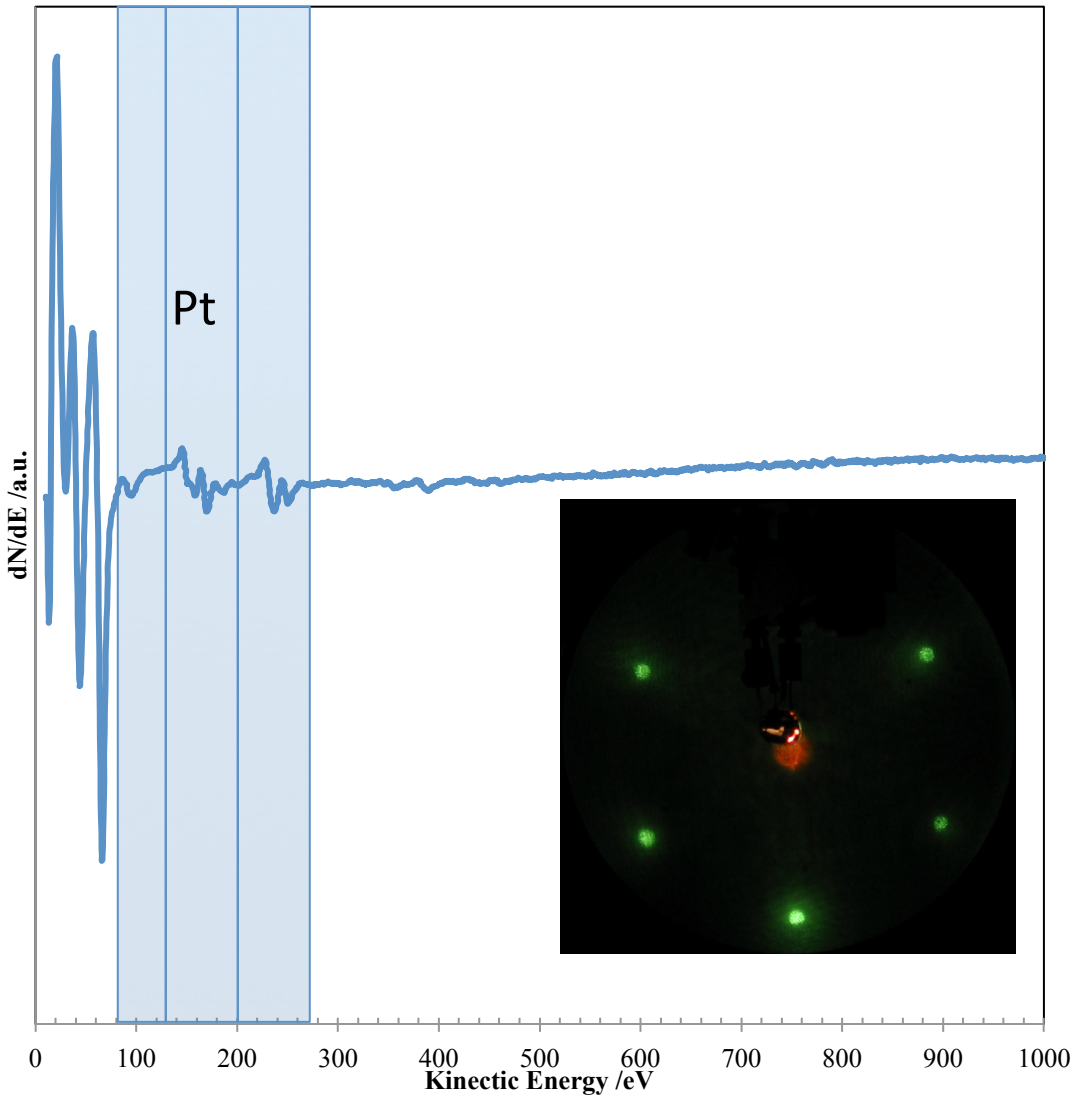

Figure 49. The AES spectrum of a clean Pt(111) electrode. Beam energy = 1.5 keV, Ip = 1 μA. (Inset) LEED pattern of a clean Pt(111) electrode. Beam energy = 62 eV, I_P = 2 μA.

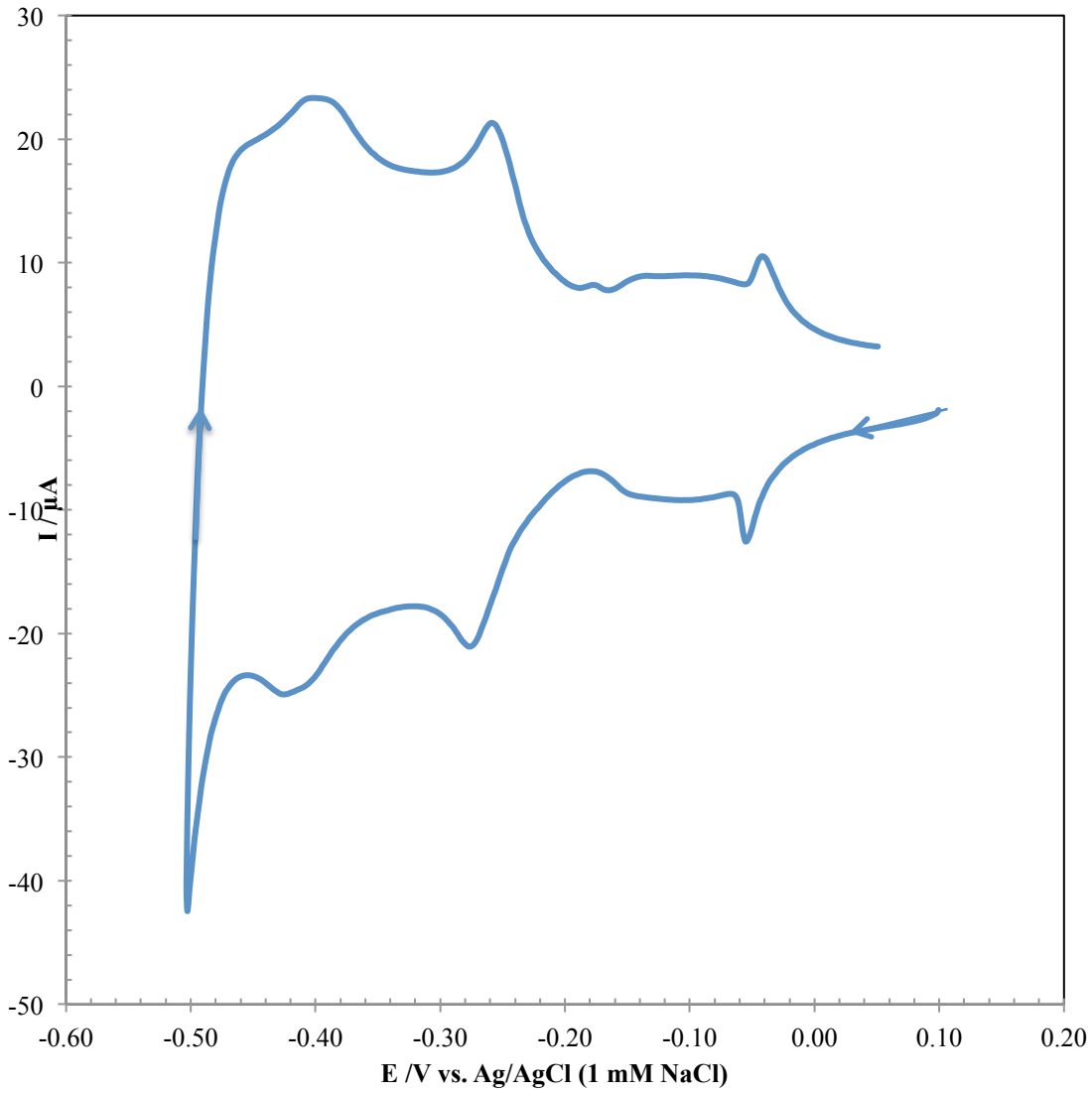

Figure 50. CV of a clean and well-ordered Pt(111) electrode. 100 mM H_2SO_4, r = 20 mV/s.

RESULTS AND DISCUSSION FOR PART II

In this study submonolayer to eight monolayers Pd films were electrodeposited on Pt(111) electrodes via galvanic displacement of Cu UPD. The interfacial structure and electrochemical behavior was investigated by AES, LEED, and EC. After cleaning, the surface structure and composition was confirmed by the regeneration of the AES and (1×1) LEED pattern shown in Figure 49 (and inset), for a clean and well-ordered Pt(111) electrode.

After transfer and prior to EC experiments, the first step was to record the CV of Pt(111) in a blank solution (100 mM H_2SO_4). The scan always commenced from OCP to the cathodic potential limit unless otherwise indicated. Figure 50 shows the CV of a clean and well-ordered Pt(111) electrode in sulfuric acid solution. The "butterfly" peaks at -0.052 V are due to desorption/adsorption of bisulfate and have been shown to be indicative of a Pt(111) surface with large, ordered domains [89, 92, 117]. The broad peaks between -0.45 and -0.22 V are considered to be due to hydrogen adsorption/desorption non-concurrent with anion adsorption/desorption [77]. The observed voltammetric features are fully consistent with those previously observed for clean and ordered Pt(111) [88, 89, 117, 118]. Another indication of the clean and well-ordered nature of the electrode comes from comparison of the steady-state voltammogram (Figure 51, obtained after 20 scans between -.0542 V and 1.00 V at 10 mV/s) with that published by Hubbard et. al. for a parallelepiped Pt(111) [119].

A CV of Pt(111) in 1 mM $CuSO_4$+100 mM H_2SO_4 is shown in Figure 52. As expected [89, 120], a doublet of Cu_{UPD} adsorption/desorption peaks between

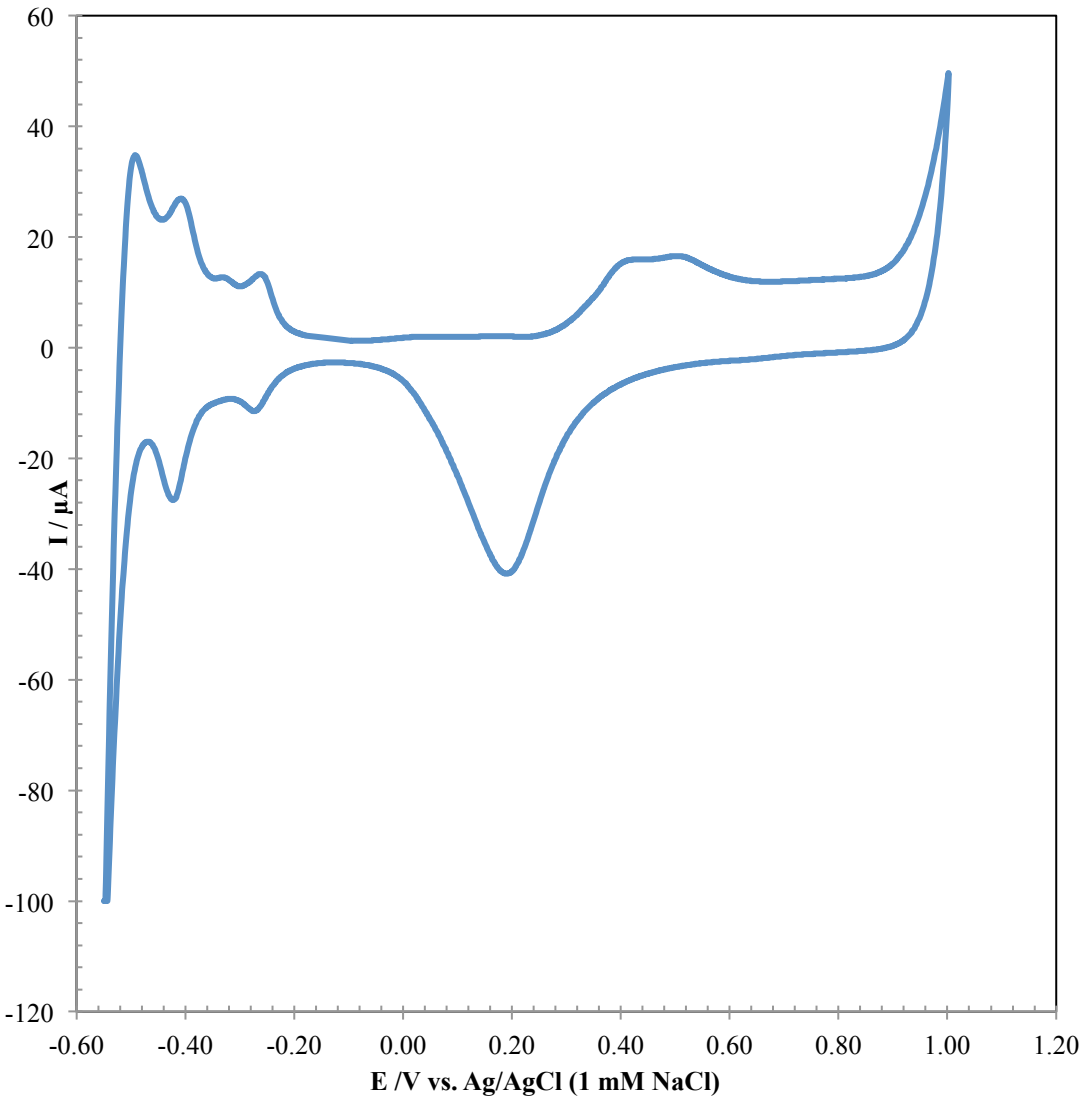

Figure 51. Steady-state cyclic voltammogram of Pt(111) (after 20 cycles). 100 mM H_2SO_4, r = 10 mV/s.

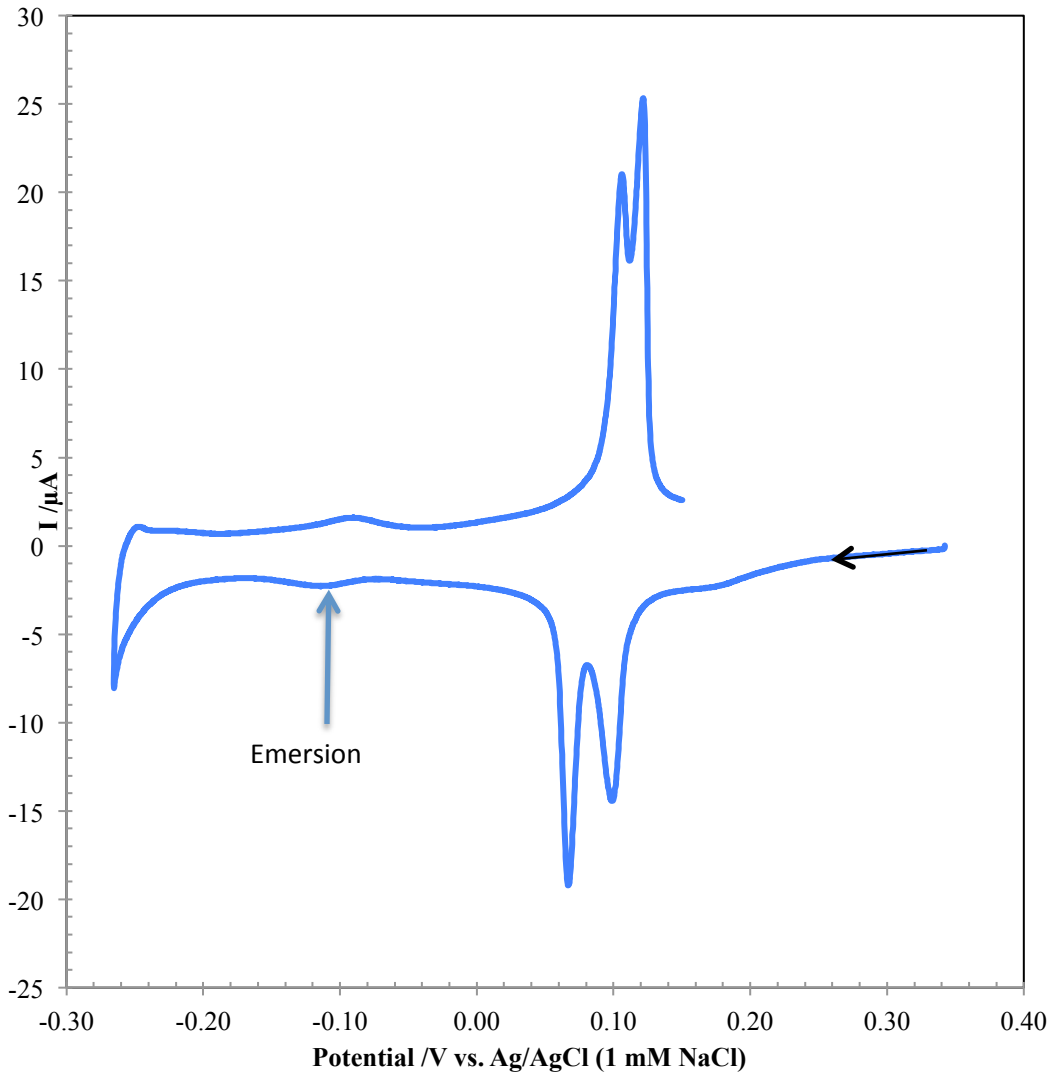

Figure 52. CV of Pt(111) in $CuSO_4$ solution. Initial scan cathodic from OCP. 1 mM $CuSO_4$ + 100 mM H_2SO_4, r = 2 mV/s.

0.10 and -0.05 V was observed. The voltammetric profile has been shown to be dependent upon the electrolyte, its concentration, and true crystallographic orientation of the electrode. In this supporting electrolyte, the initial adsorption of Cu produces a mixed, nearly coplanar, honeycomb structure of Cu/sulfate with Θ_{Cu}= ⅔ ML; at higher overpotentials the full UPD layer is completed [121]. Thus, to facilitate the completion of a full monolayer, the electrode must be emersed cathodic of the second peak but anodic of bulk deposition. Furthermore, enough time must be allowed for full deposition as the process has been shown to be slow [122].

General Properties of SLR^3-Prepared Pd/Pt(111)

Figure 53 shows the AES spectrum for a single UPD layer of Cu on an emersed Pt(111) surface (emersion potential -0.038 V). Peaks at 105, 920, and 940 eV indicate the presence of Cu on the Pt surface. These peaks are non-existent for clean Pt surfaces (Figure 49). It should be noted that prior to the collection of the diffraction patterns, the electrodes were rinsed with 100 mM H_2SO_4 acid and the surface is expected to have an adsorbed layer of electrolyte [48].

The LEED pattern (Figure 54) for the Cu_{UPD}/Pt(111) electrode indicates a Pt(111)-(√3×√3)R30°Cu adlayer structure. This interpretation is consistent with prior LEED [123] and STM reports [117, 124]. At the first UPD peak, bisulfate ions are deprotonated to sulfate ions and Cu is simultaneously adsorbed onto the substrate. At the second UPD peak, Cu adsorption proceeds via replacement of sulfate and a Cu monolayer is completed at the end of the second UPD peak.

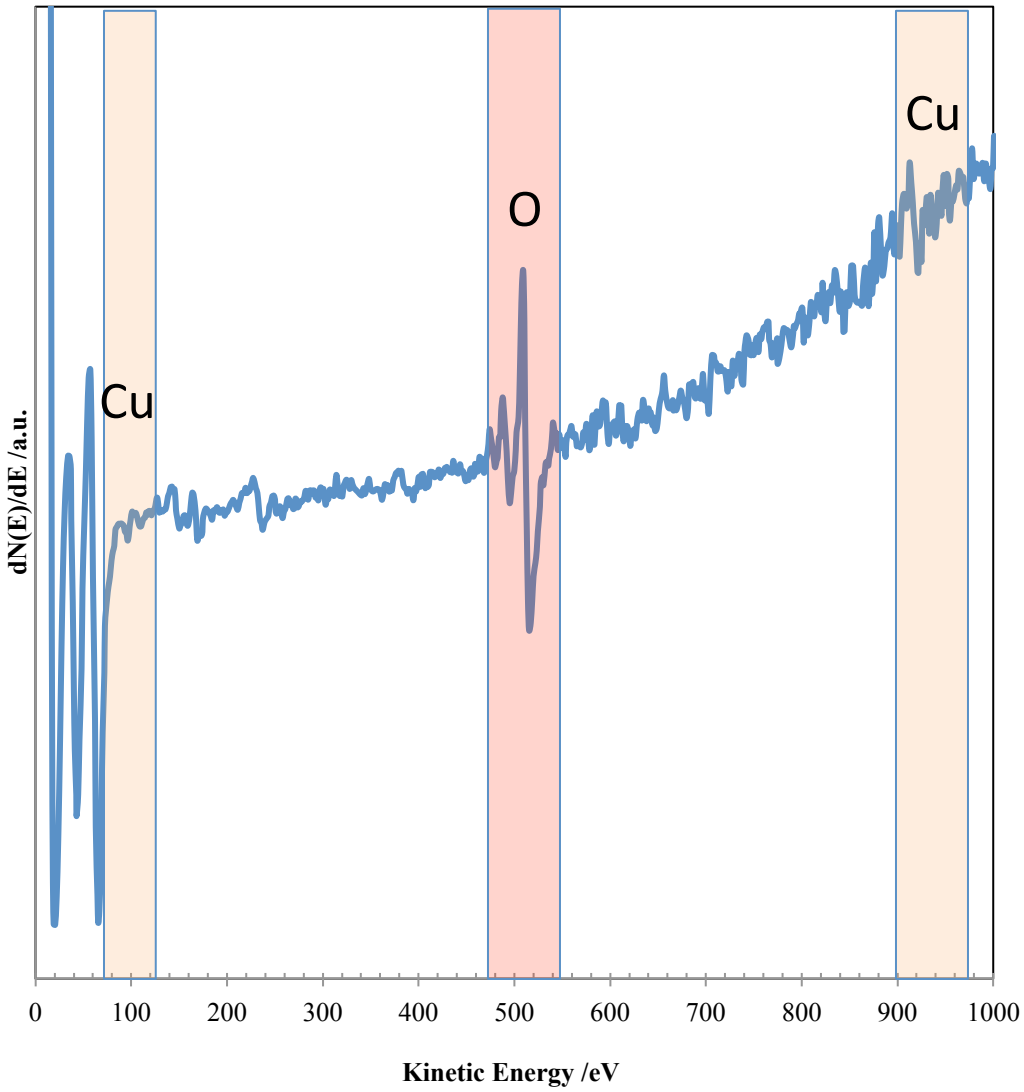

Figure 53. AES spectrum of Cu-coated Pt(111).

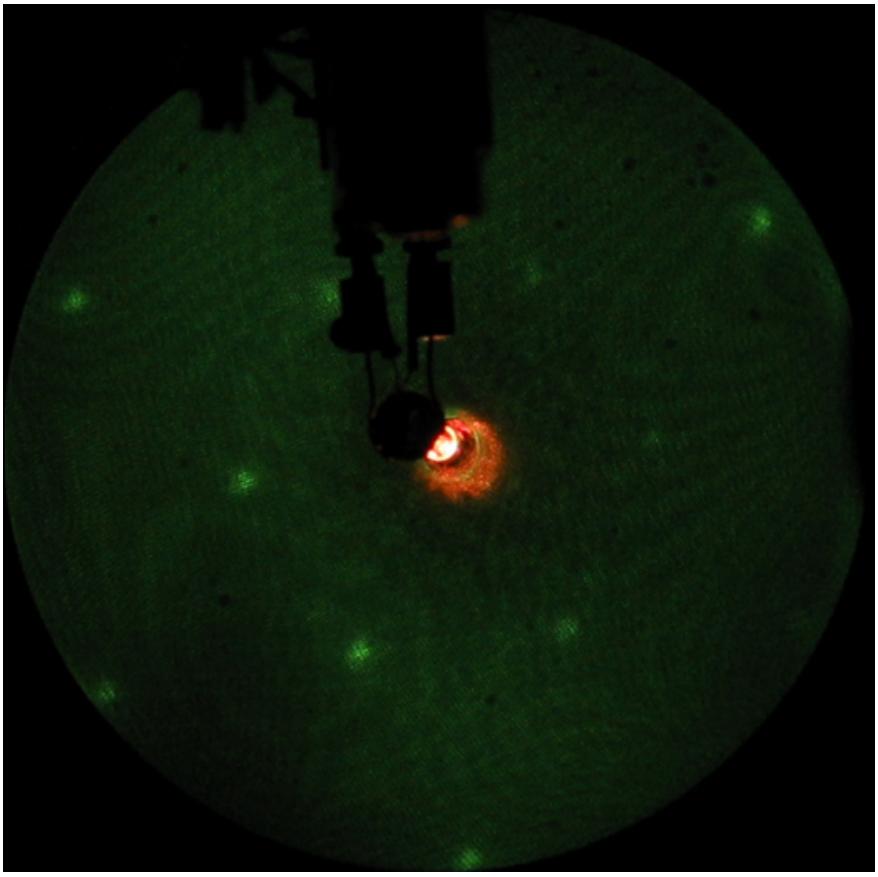

Figure 54. LEED pattern of Cu_{UPD} on Pt(111). Beam energy = 50 eV, Ip = 1 μA.

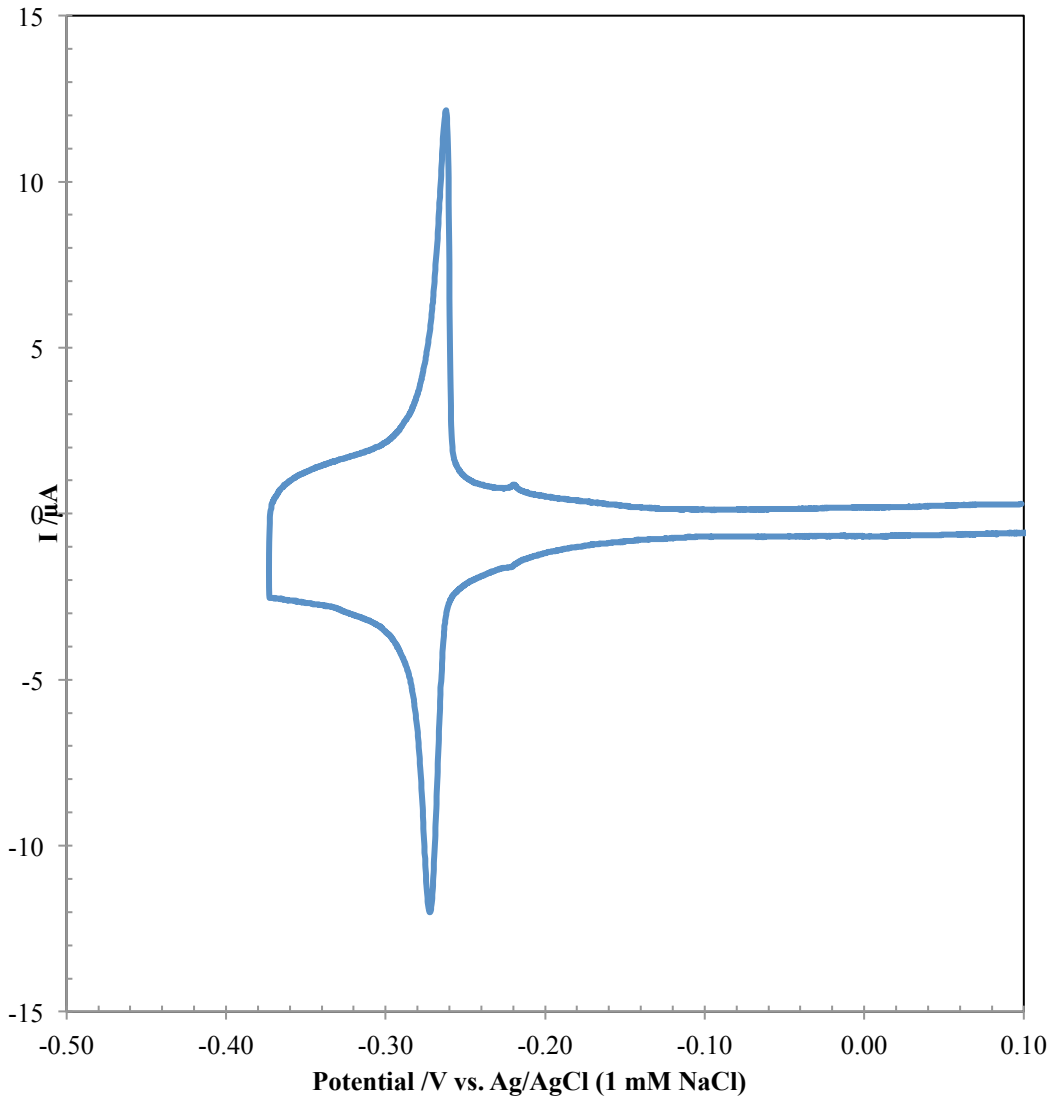

Figure 55. CV of $Pd_{1\ ML\text{-}SLR3}$/Pt(111) film in blank. 100 mM H_2SO_4, r = 2 mV/s.

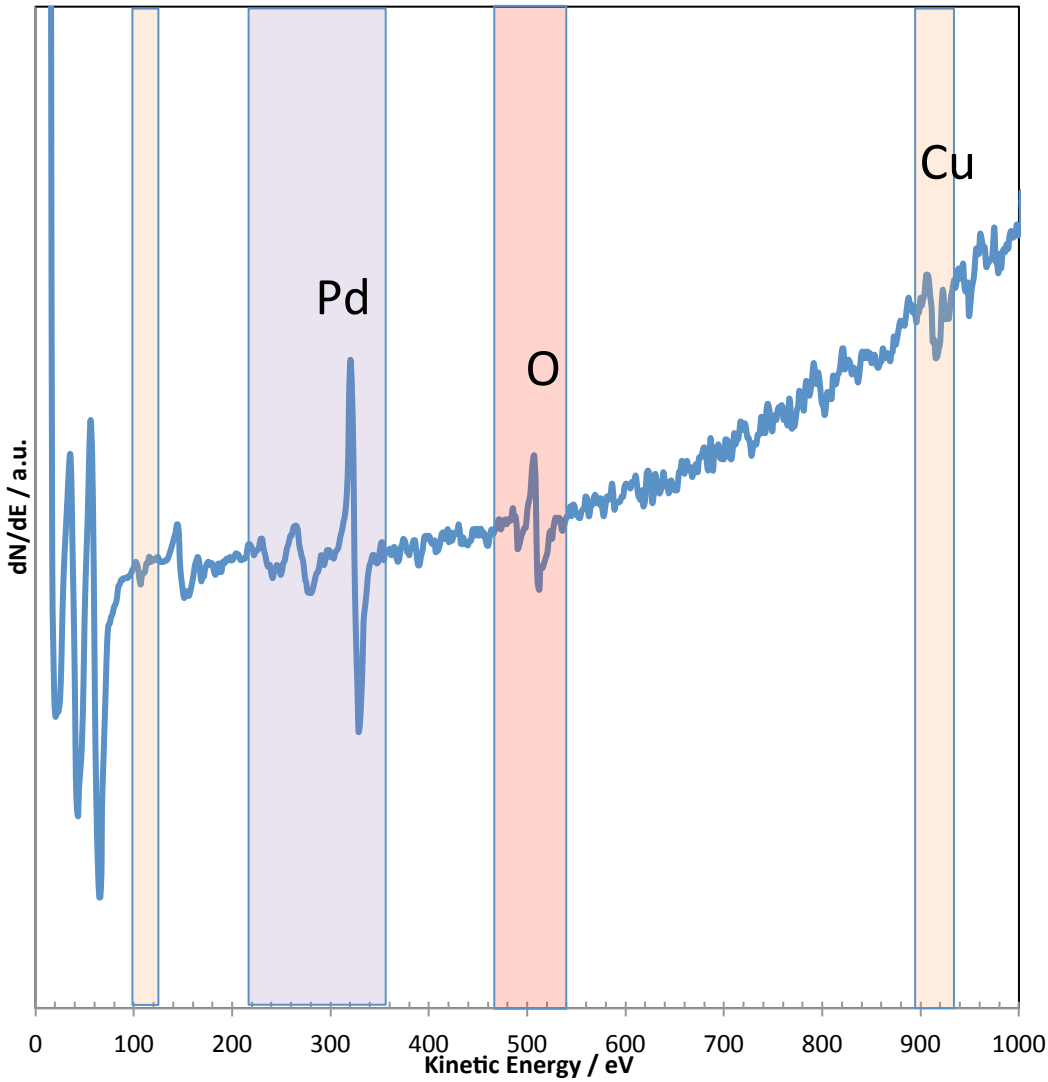

Figure 56. AES of Pd/Pt(111) after completion of the 1st SLR3 cycle.

Much further beyond this, a (√3×√7) structure is expected, given by adsorption of sulfate/bisulfate on a (1×1) Cu-adlayer [125].

Unfortunately, the presence of sulfate or bisulfate on Cu_{UPD} cannot be fully ascertained by AES due to the overlap of the prominent S peak with that of the Pt substrate. The AES spectrum of Cu_{UPD}/Pt(111), however, shows a peak at around 503 eV, which is associated with oxygen. This oxygen might be due to the presence of sulfate or bisulfate adsorbed on Cu, however this is also possibly due to inadvertent oxygen chemisorption.

Following the completion of the $Pd_{1\ ML\text{-}SLR3}$/Pt(111) film, a CV of Pd-modified Pt(111) was collected in blank electrolyte solution (Figure 55). A sharp couple is observed at -0.270 V. This is associated with H_{UPD} with anion desorption/adsorption on the Pd/Pt(111) monolayer [77, 94]. No other features are observed indicating the absence of any residual Cu. This result was further corroborated with AES and LEED results. The AES spectrum of the Pd/Pt(111) monolayer lacked the peaks associated with Cu, instead displaying a group of peaks associated with Pd (Figure 56). The LEED pattern gives a (1×1) structure consistent with a pseudomorphic adlayer of Pd on Pt(111) (Figure 57). These results strongly suggest a complete exchange of Cu with Pd in the SLR^3-prepared Pd film.

Subsequent displacement of Cu_{UPD} with Pd concludes the formation of the first Pd layer and here the results are presented for a Cu_{UPD}-$Pd_{1\ ML\text{-}SLR3}$/Pt(111). As given by the reaction schematic, galvanic displacement by Pd follows Cu_{UPD} deposition and the formation of multilayer Pd-SLR^3 films

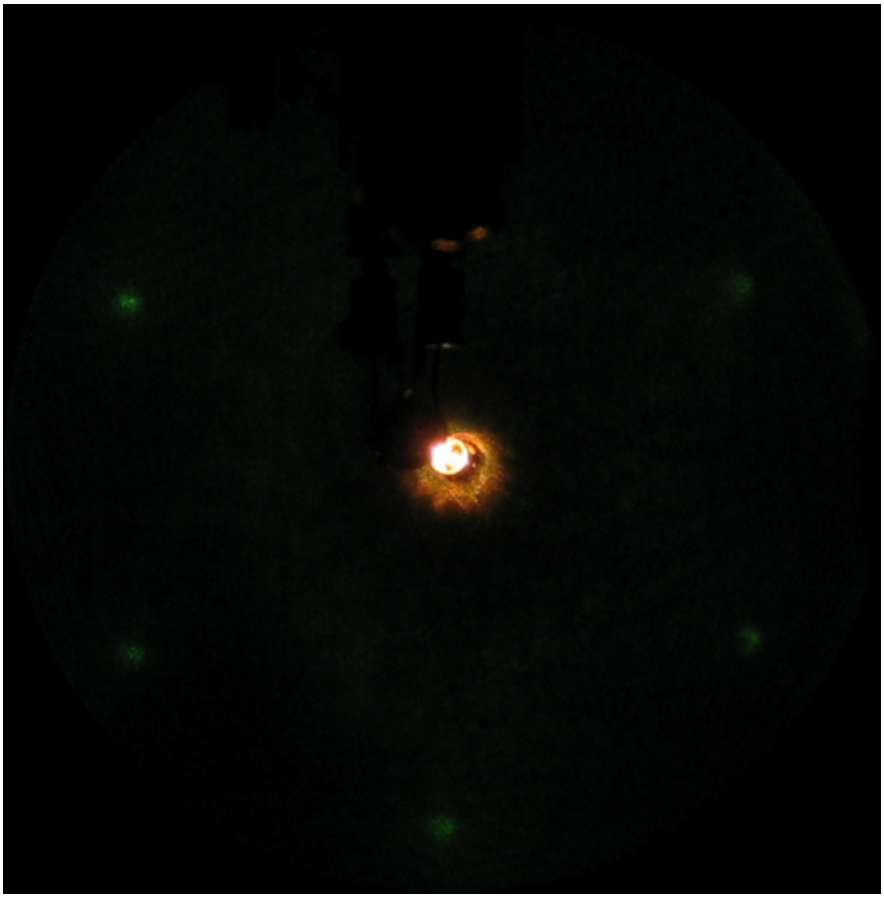

Figure 57. LEED pattern of SLR^3-prepared Pd/Pt(111). Beam energy = 63 eV, Ip = 1μA.

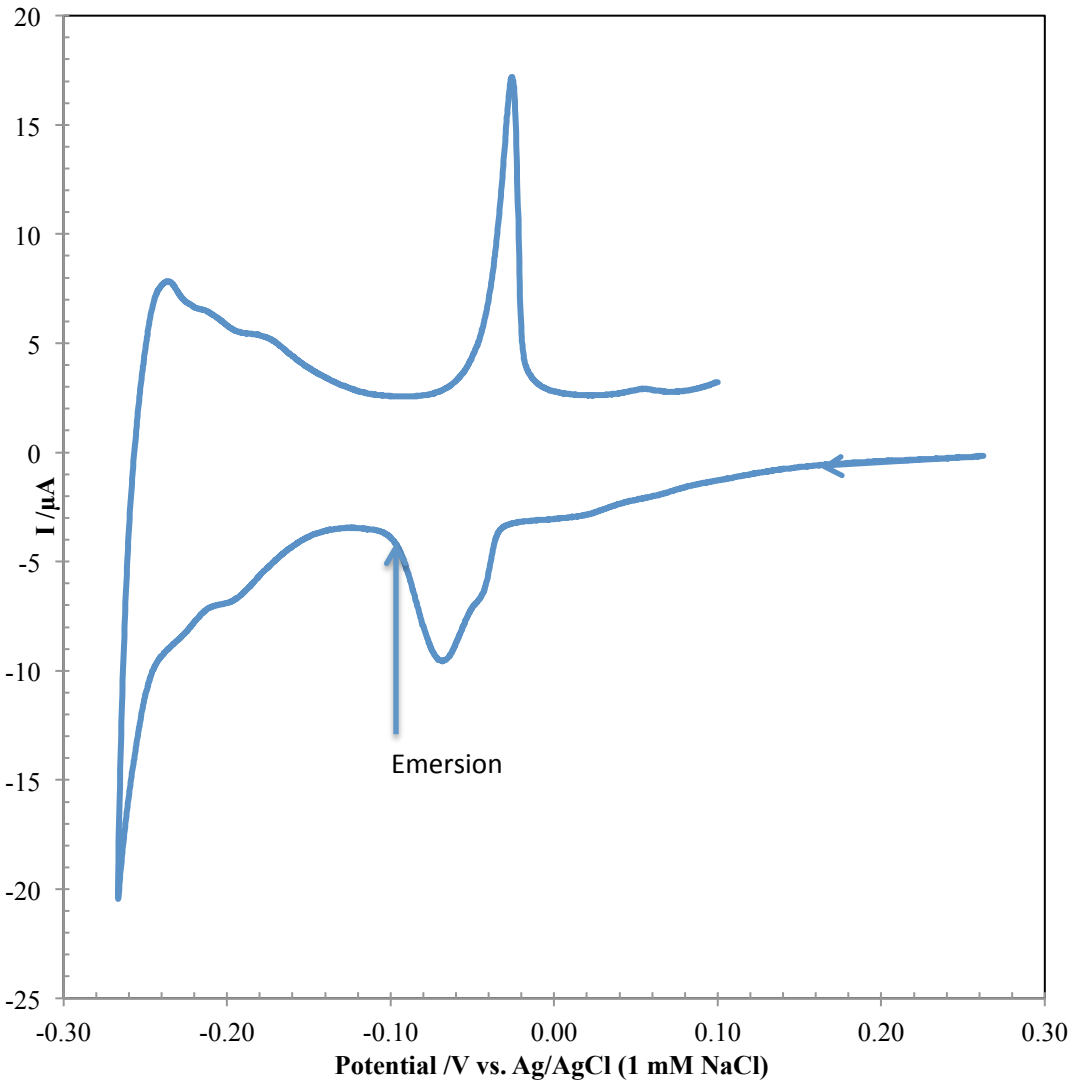

Figure 58. CV of Pd/Pt(111) in $CuSO_4$ in 100 mM H_2SO_4, r = 2 mV/s.

proceeds through a $Cu_{UPD}/Pd_{n\ ML\text{-}SLR}{}^{3}/Pt(111)$ strata; so the following is provided to generalize the behavior of $Pd_{n\ ML\text{-}SLR3}/Pt(111)$ films. Here, the general character of Cu-UPD on Pd-SLR^3 films is presented for 1 ML Pd. On Pd, a single Cu_{UPD} adsorption/desorption peak is expected [120, 121, 126]. The CV did not exhibit a peak due to Cu_{UPD} on Pt(111) (between 0.10 and -0.05 V), indicating that the Pt(111) electrode surface is already fully covered (Figure 58). The peak ca. -0.07 V is, therefore, determined to be due to Cu UPD on SLR^3 Pd film. This is expected and is consistent with observations recounted elsewhere [89, 120]. The H-UPD behavior of this film is reported below.

The AES spectrum and LEED pattern for an emersed Cu_{UPD}-$Pd_{1\ ML\text{-}SLR3}/Pt(111)$ electrode are shown in Figure 59 and Figure 60. The reappearance of peaks at 105, 920, and 940 eV in the AES spectrum support the electrochemical result that a Cu_{UPD} layer on SLR^3 prepared Pd film on Pt(111) has been prepared. The Cu UPD layer on ML Pd film gave a (1×1) LEED pattern, which is in agreement with literature findings [126].

The Pd coverage of the deposited SLR^3-produced Pd films can be calculated by (*i*) measuring the deposition charge of Cu or by (*ii*) measuring the charge of I_{ads}-catalyzed anodic dissolution of Pd using Faraday's law (equation (51). The Pd coverage, Θ_{Pd}, can be defined as,

$$n\ ML \text{ when } \Theta_{Pd} = n \tag{54}$$

where $\Theta_{Pd} = \Gamma_{Pd} / \Gamma_{Pt}$ and Γ_{Pd} = packing density of Pd, Γ_{Pt} = packing density of Pt.

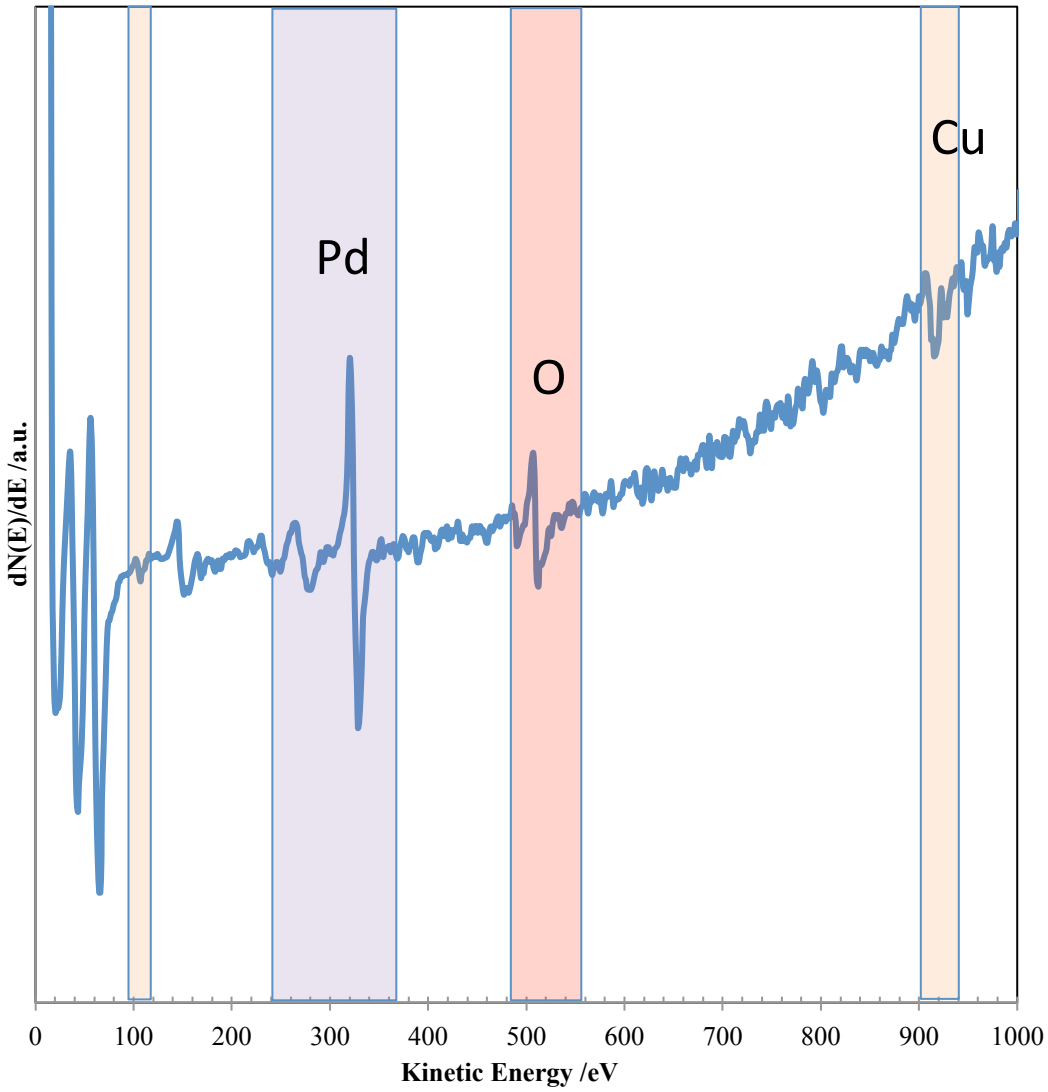

Figure 59. AES spectrum of Cu/Pd/Pt(111) electrode.

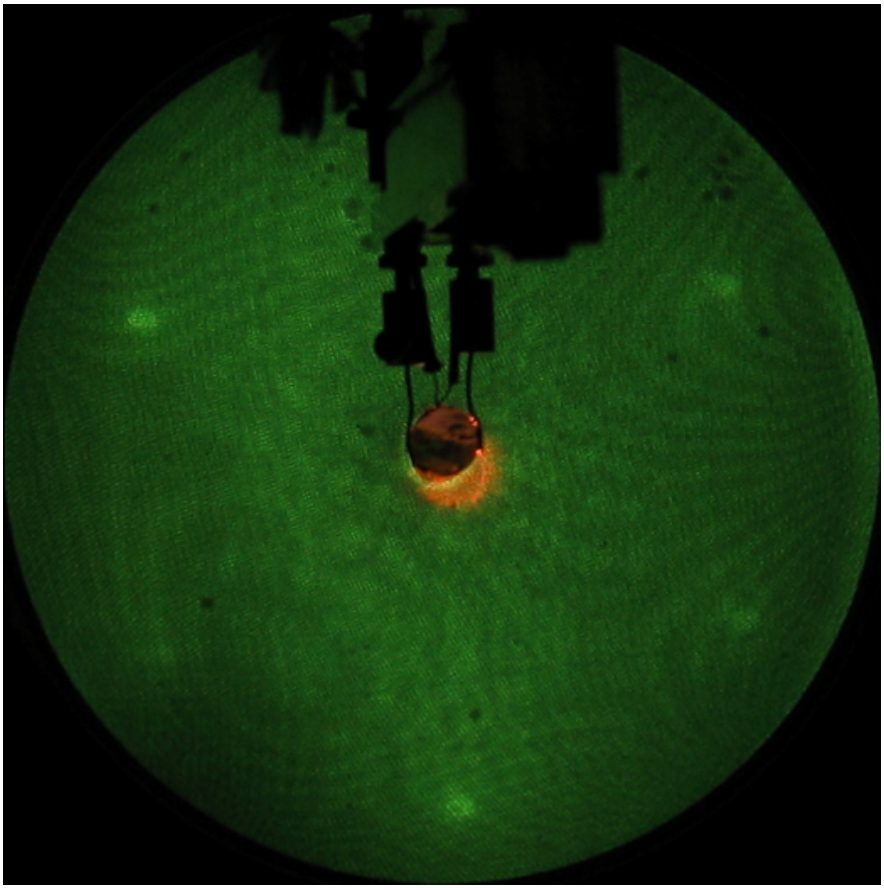

Figure 60. LEED pattern of emersed $Cu_{UPD}/Pd_{1\ ML\text{-}SLR}{}^{3}/Pt(111)$ electrode. Beam energy = 62 eV, I_P = 2 μA.

The reactions involved are Cu deposition by UPD (equation (52)) and I_{ads}-catalyzed dissolution of Pd.

$$I_{(ads)}/Pd_{ML\text{-}SLR3}/Pt(111) \rightarrow Pd^{2+}{}_{(aq)} + I_{(ads)}/Pt(111) + 2e^- \qquad (55)$$

Figure 61 shows the LSV for I_{ads}-catalyzed dissolution of SLR^3-prepared Pd films on Pt(111) in I^--free supporting electrolyte. Based on previous studies, the peak at 0.58 is assigned to Pd dissolution and that at 0.84 V to the 5 e^- oxidation of $I_{ads} \rightarrow IO_3^-{}_{(aq)}$ [127]. The anodic feature at 0.58 V has been shown to correspond to a quantitative and selective removal of the top-most Pd atoms one layer at a time, according to equaiton (55) [128] and has been successfully used to determine the coverage of Pd films deposited on Pt [129]. The calculated charge for 1 ML Cu is given by equation (56).

$$Q_{1\ ML\ Cu} = nFA\Gamma_{Pt(111)} = 537.6\ \mu C \qquad (56)$$

This charge is in good agreement with the empirically determined value of 470 ± 10 μC cm^{-2} and the calculated 486 μC cm^{-2} (relative error 2% and 1%, respectively) reported by Itaya et. al. for 1ML Cu_{UPD}-Pd(111) [126]. Assuming a 1:1 exchange of Cu with Pd, 537.6 μC gives 1 ML Pd coverage as defined henceforth; or an I_{ads}-catalyzed Pd dissolution charge of 537.6 $\mu C \cdot ML^{-1}$.

Figure 62 shows the AES spectrum for I-coated Pd/Pt(111) before dissolution is forced. Two new peaks at 511 and 520 eV indicate the presence of

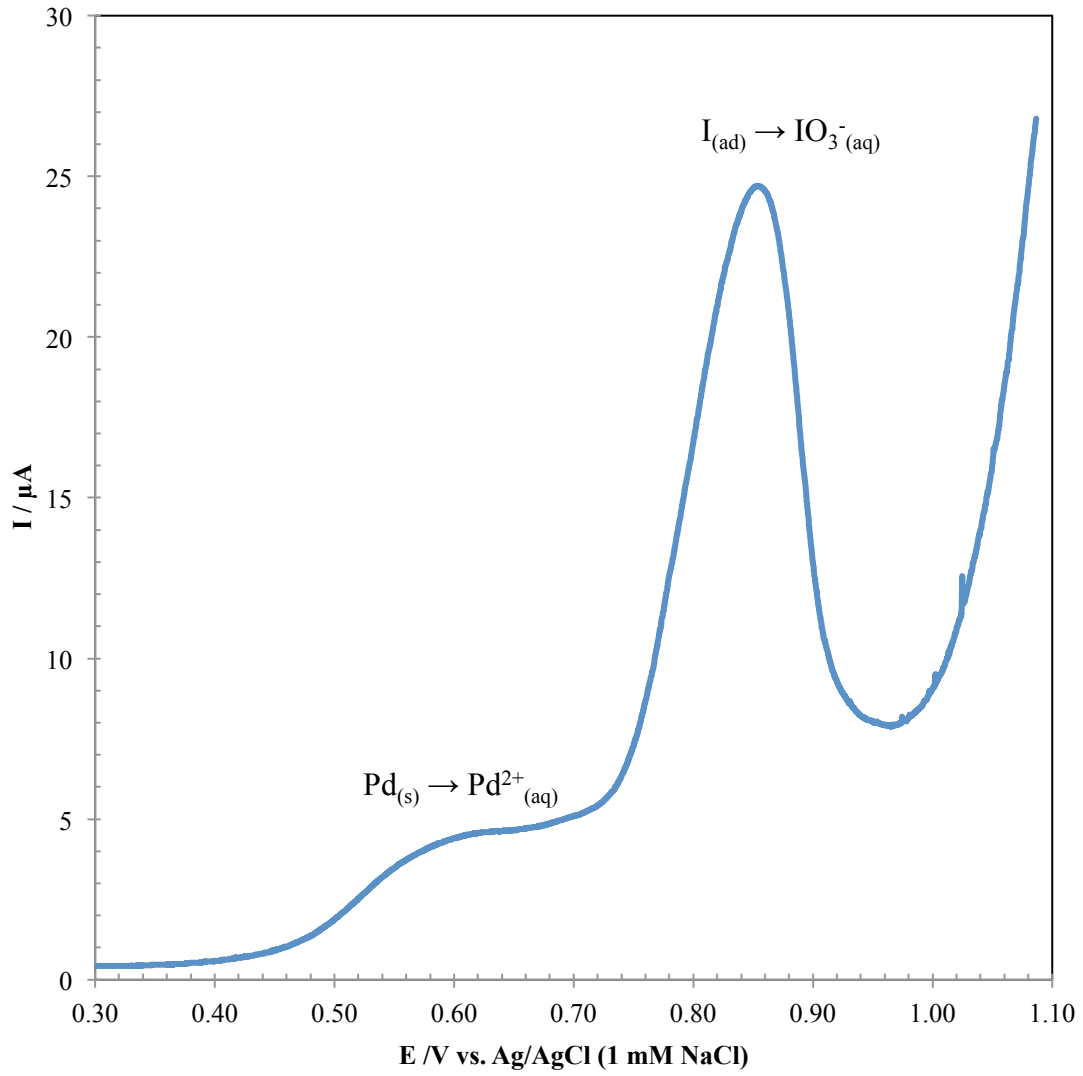

Figure 61. I_{ads}-catalyzed anodic stripping of Pd/Pt(111) after 1st SLR^3 cycle. 100 mM H_2SO_4, r = 2 mV/s.

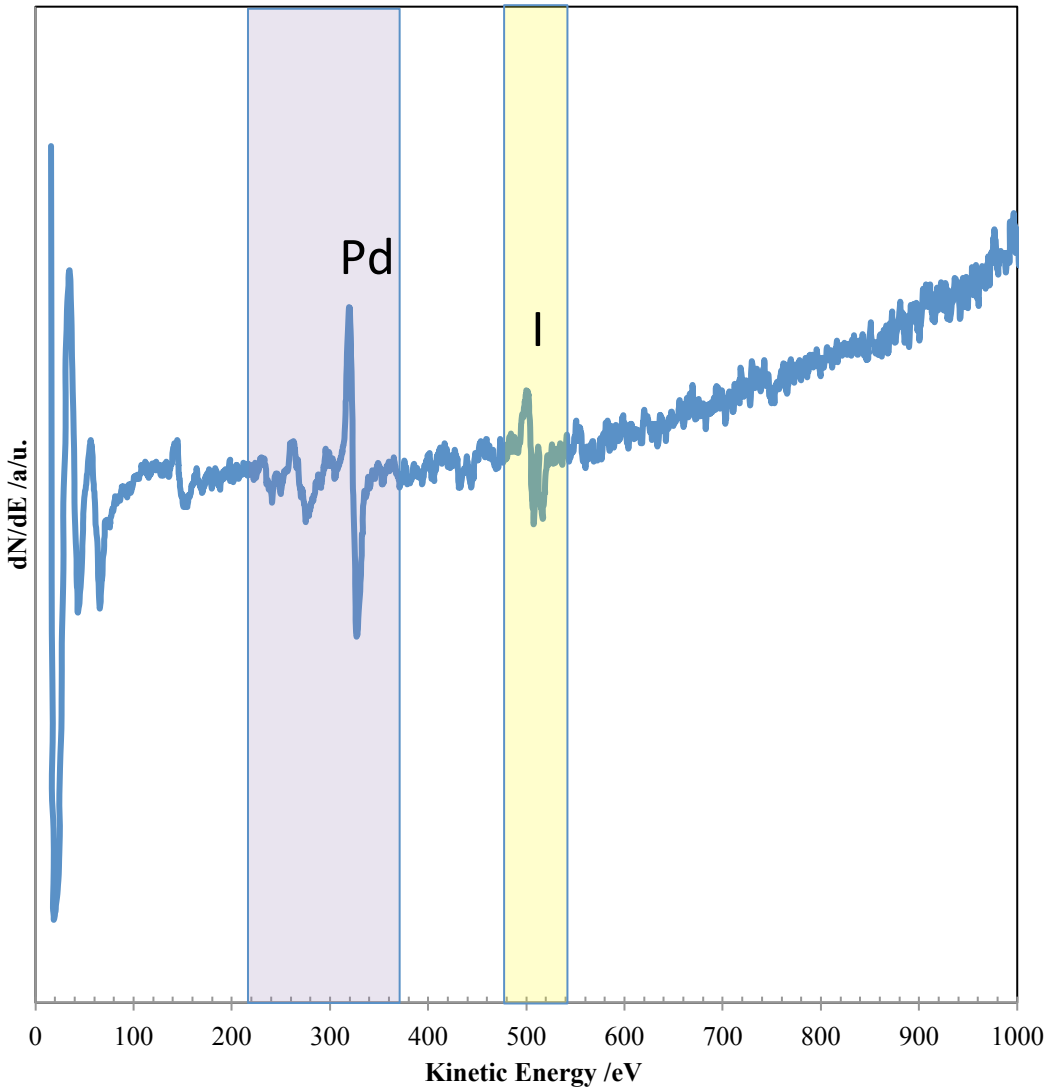

Figure 62. AES of I/Pd/Pt(111) electrode.

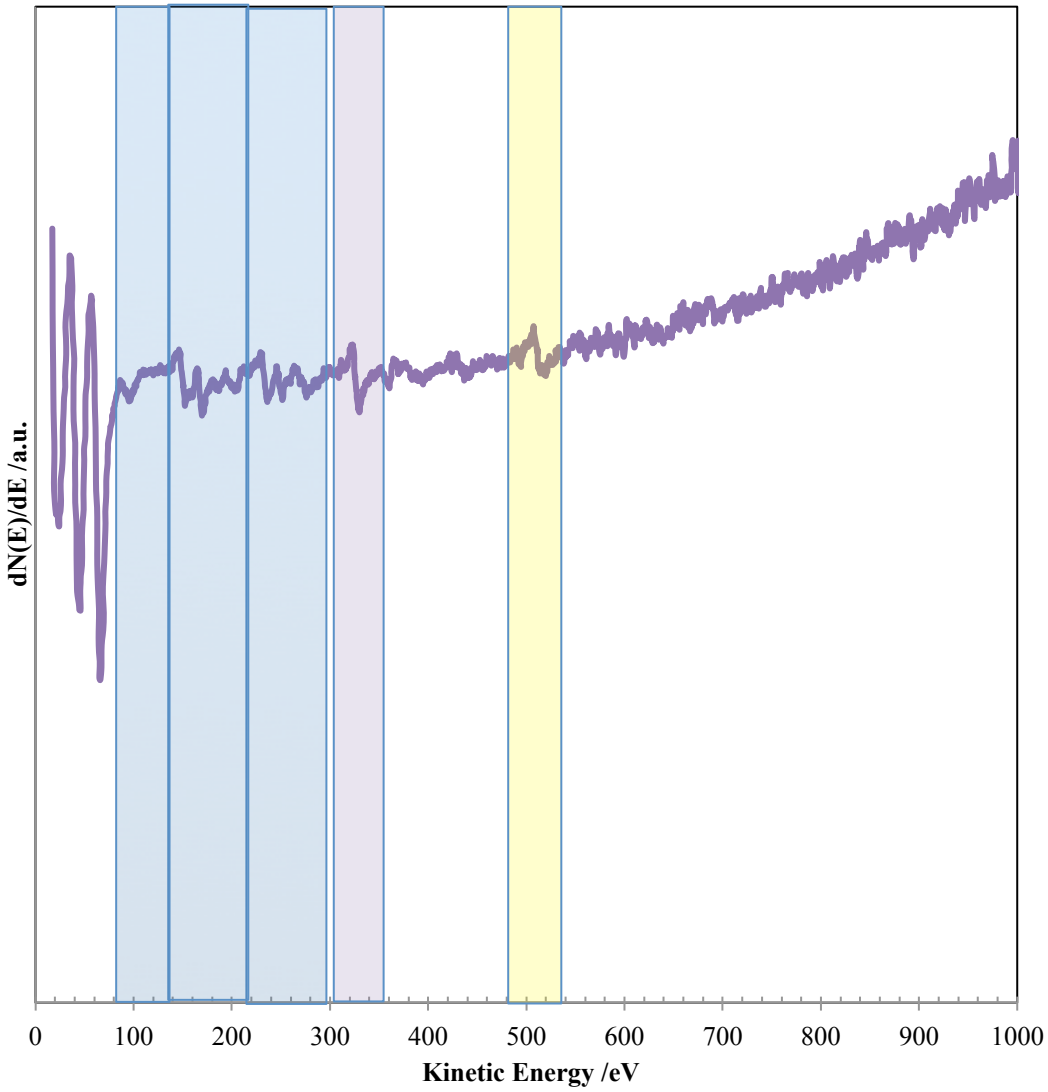

Figure 63. AES spectrum of post I_{ads}-catalyzed anodic dissolution of ca. 8 ML SLR^3-prepared Pd film on Pt(111).

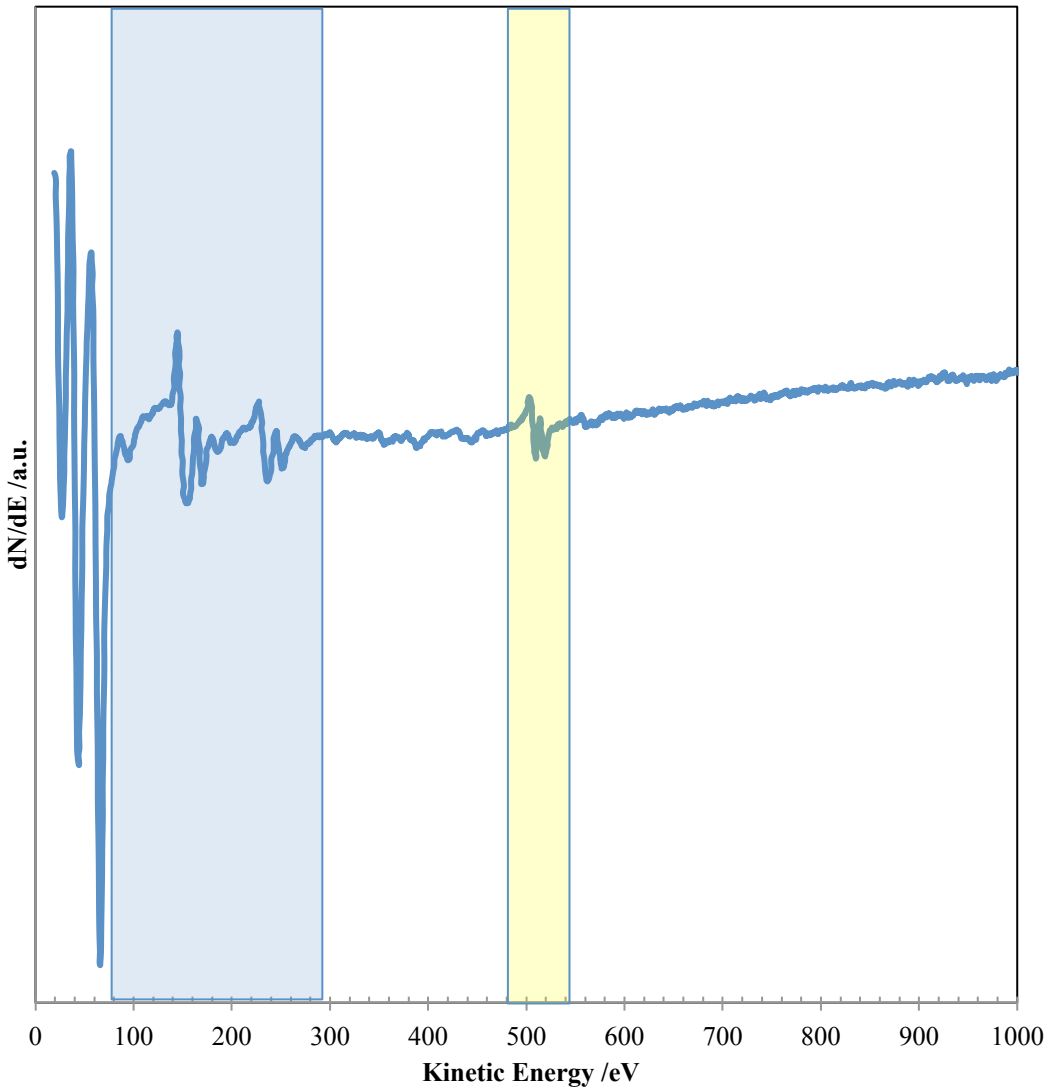

Figure 64. AES spectrum of I/Pt(111) electrode before the second LSV.

the iodine adlayer. The iodine AES peaks are small compared to Pd peaks due to smaller AES relative sensitivity factors for iodine as compared to those of Pd. The relative sensitivity factors for Pt, Cu, Pd, and I are 0.025, 0.225, 0.800, and 0.325, respectively [112]. A representative AES spectrum recorded after I_{ads}-catalyzed anodic stripping of Pd is displayed in Figure 63. It is observed that the AES peaks associated with Pt reemerged concurrent with a considerable diminution of the Pd signal. Compared to the large Pd peaks in Figure 62, the amount of Pd is negligible given the large quotient of Pd/Pt AES relative sensitivity factors ($S_{Pd}/S_{Pt} = 32$). Because one scan is expected to remove the entire Pd adlayer, a second I_{ads}-catalyzed anodic stripping of Pd cycle is performed. As expected, the AES (Figure 64), LEED (Figure 65), and LSV for the I-coated electrode is identical to that of Pt. The LEED pattern indicates the Pt(111)-(1×1)-(√7×√7)R19.1°-I adlattice structure [130].

Properties of Sub-ML to Eight-ML SLR^3-Prepared Pd/Pt(111)

In the present study, submonolayer to eight ML Pd films were deposited on Pt(111) surfaces via SLR^3, *vide supra*. A linear correlation was observed between the cumulative Cu coverage and number of SLR^3 cycles performed (Figure 66); each cycle produces ca. 0.8 ML Cu (i.e., Pd) film. Hence, 0.8 ML Pd is expected to be obtained per cycle of galvanic displacement of Cu.

Figure 67 shows a linear correlation of cumulative Cu deposition charge (background corrected) and I_{ads}-catalyzed Pd dissolution charge. One possible explanation for the deviation from unity can be that some Cu was lost during

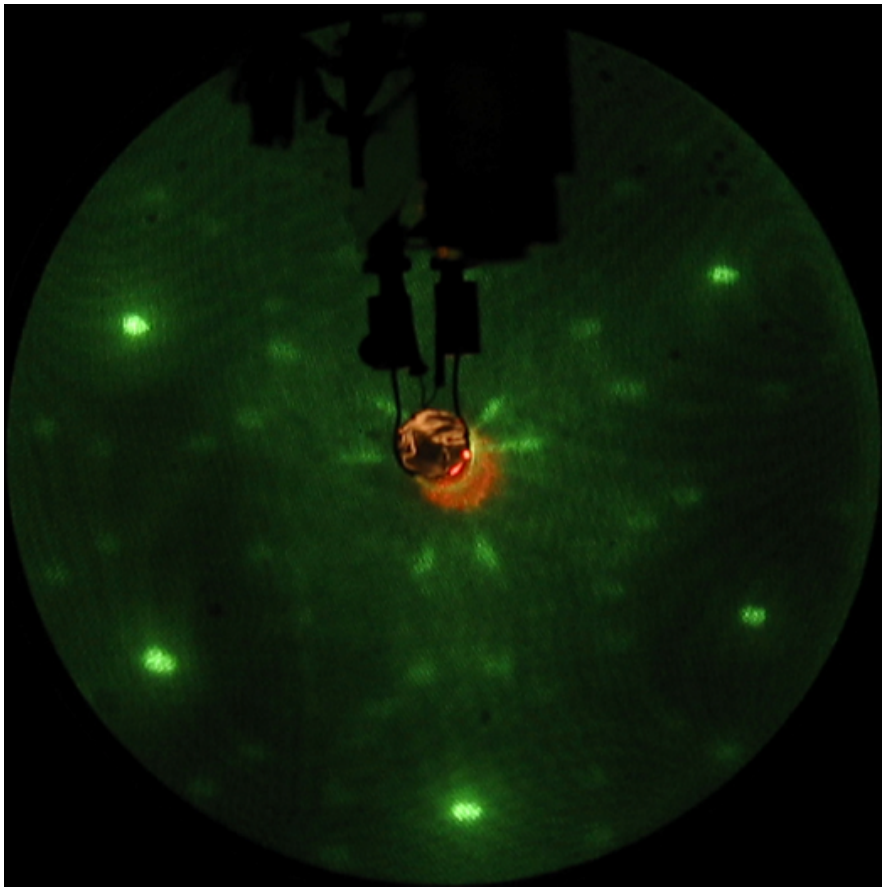

Figure 65. LEED pattern of I/Pt(111) (following readsorption of iodine) . Beam energy = 60 eV, I_P = 2 μA.

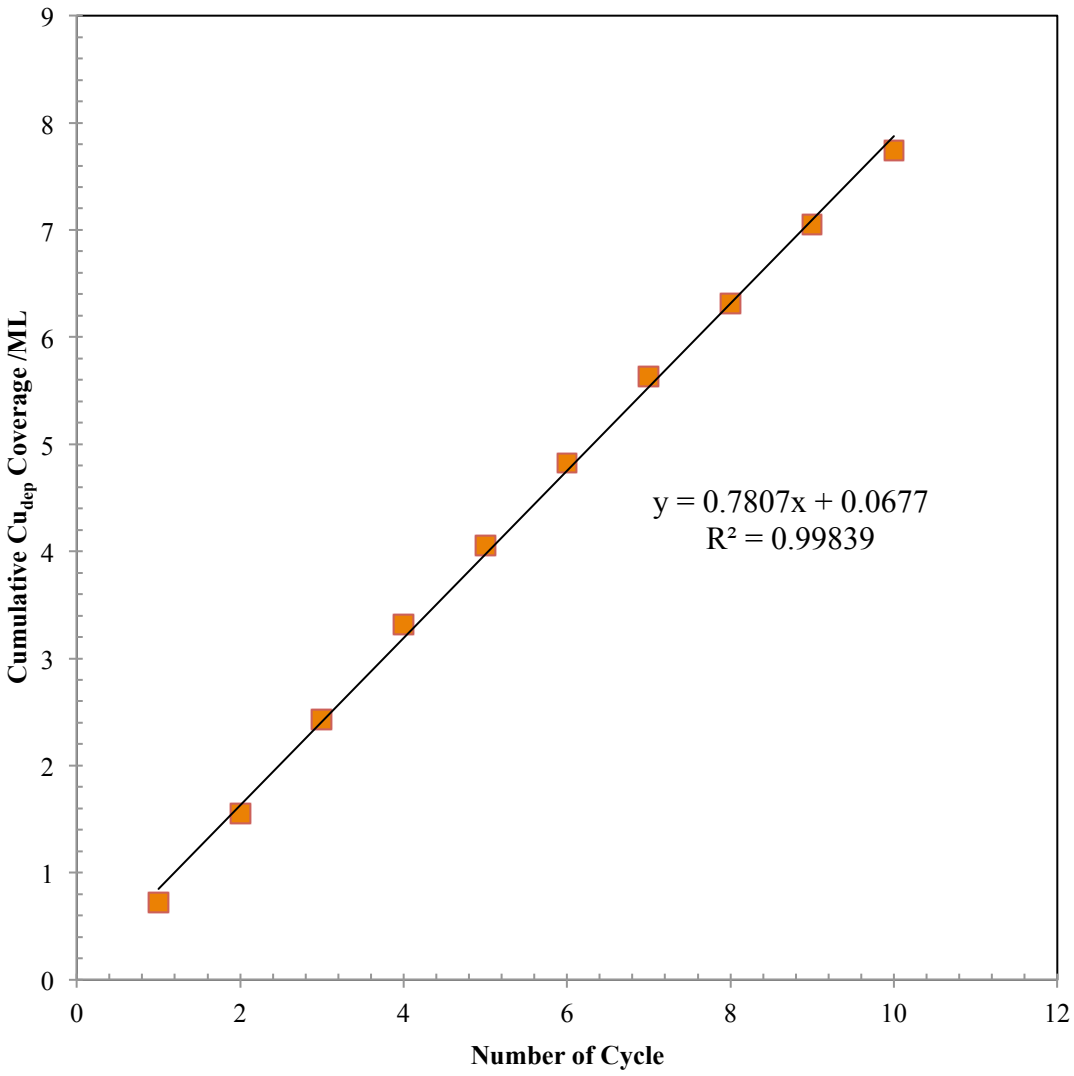

Figure 66. Correlation of cumulative Cu deposition charge and I_{ads}-catalyzed Pd stripping charge.

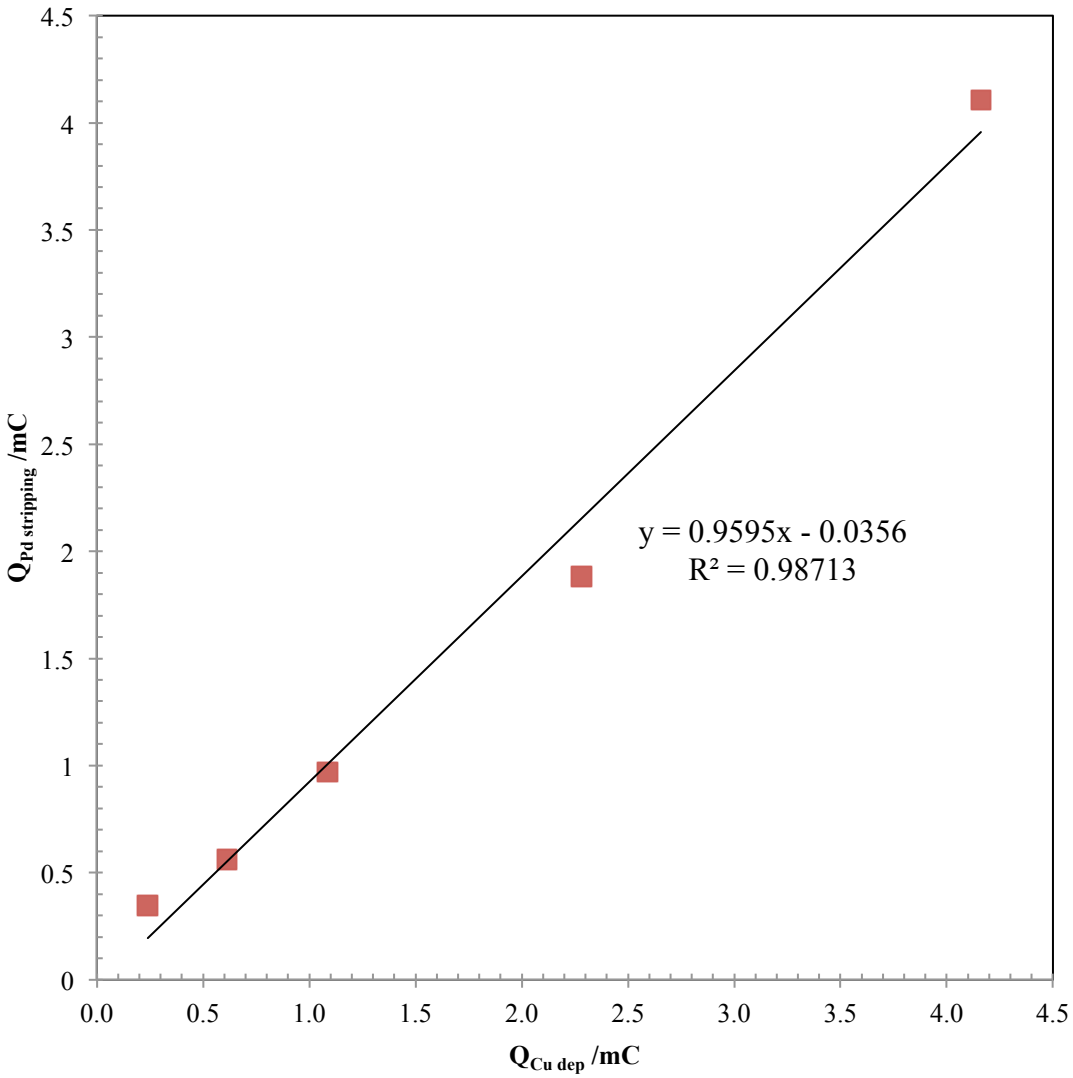

Figure 67. Correlation of Cu deposition charge and I_{ads}-catalyzed Pd dissolution charge.

the rinsing steps following emersion and immersion. Also, It is well known that the UPD of Cu on noble metal substrates (such as Au [131, 132], Pt [133, 134], and Pd [126]) is quite slow and kinetically hindered. For example, on Au(111) surfaces it takes up to 10 minutes to complete the Cu UPD [132]. In the present case case, the current transient, however, for the potential step UPD of Cu on Pt(111) or Pd/Pt(111) was quite flat after 20 – 30 s. Hence, the Cu deposition was carried out for only 3 minutes. As discussed in the experimental section, direct coulometric measurements of charge flowing at the deposition interface tend to ignore the contribution from the coadsorbed (sulfate) ions, and consequently, results in too low values for the deposited Cu coverage particularly on Au(111) electrodes [132, 135]. Furthermore, it has been suggested that oxygen reduction and hydrogen evolution reactions may compete with galvanic displacement of UPD adlayers with noble metal ions [136]. Nevertheless, a definitive explanation for the aforementioned discrepancy in the cumulated Cu deposition charge would require further investigation.

In the following sections, the electrochemical properties and interfacial structures of the Pd films prepared via SLR^3 will be evaluated by their resulting CVs, AES spectra, LEED patterns, and LSVs for I_{ads}-catalyzed dissolution of Pd films. The results will be presented for a given Pd coverage at a time. For the sake of simplicity and reproducibility, the Cu UPD was conducted coulometrically, from OCP to predetermined values where the UPD takes place (typically -0.054 V for clean Pt surface and -0.100 V for Pd-covered Pt), for 3 minutes and the charge was measured. The appropriate UPD potential was

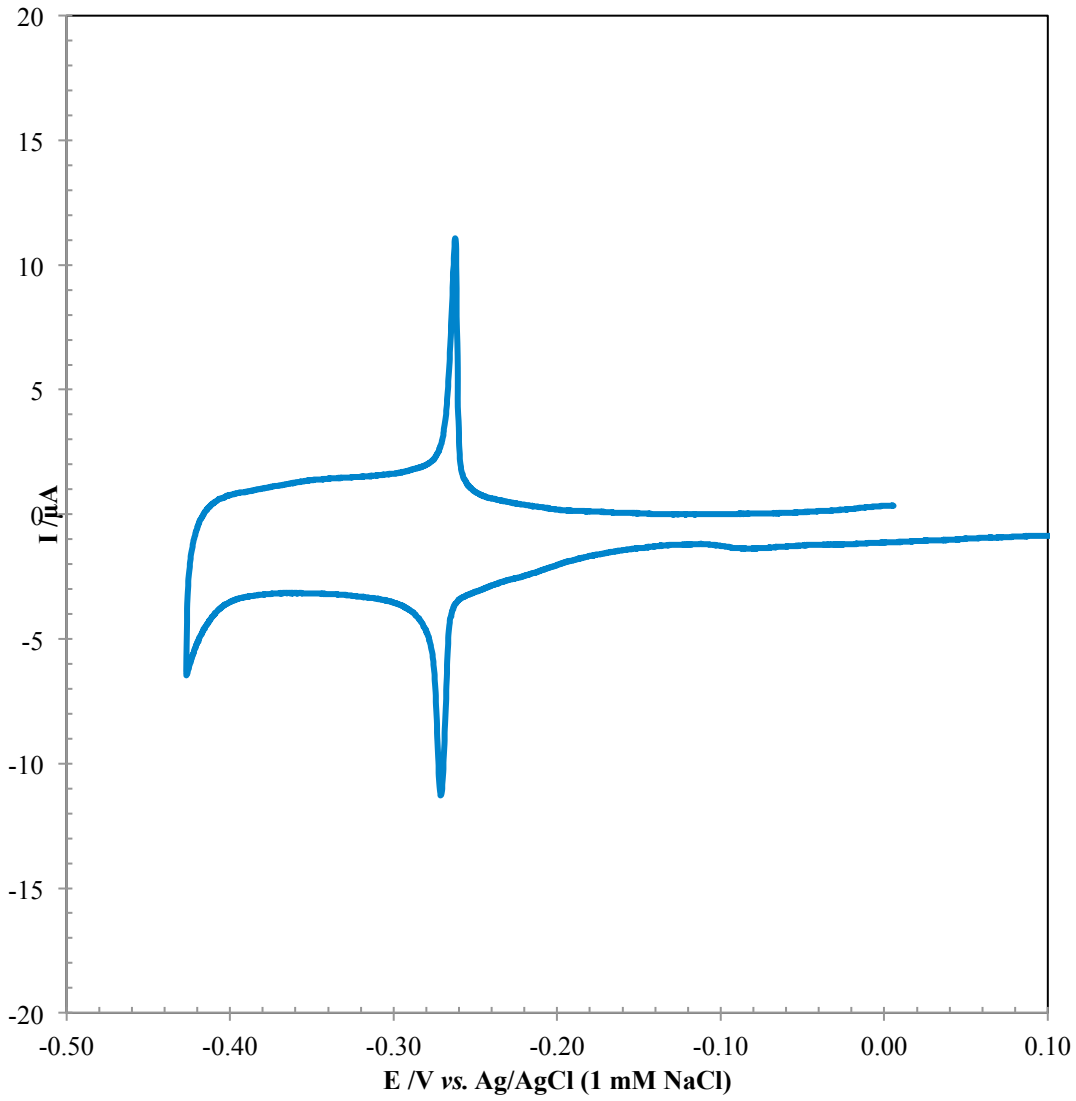

Figure 68. Cyclic voltammogram (hydrogen region only) of Θ_{Pd}= 0.5 ML; 100 mM H_2SO_4, *v*= 2 mV/s, vs Ag/AgCl (1 mM NaCl).

chosen based on the CV of Pt or Pd/Pt(111) in 1 mM $CuSO_4$ in 100 mM H_2SO_4 solution (Figures Figure 52 and Figure 58, respectively). Before each Cu UPD cycle, a blank coulogram was recorded in Cu^{2+} free 100 mM H_2SO_4 solution. All other procedures remain the same as previously described.

ΘPd = 0.5 ML

The cyclic voltammogram for Θ_{Pd}= 0.5 ML SLR^3 film is shown in Figure 68. The H-UPD region shows one sharp peak at -0.270 V, which is due to H adsorption/desorption on Pd terrace sites with total $Q_{H\text{-}UPD}$= 47 μC. The film gives a large Pd peak at 330 eV in the AES spectrum (Figure 69) with the characteristic Pt peaks (at 64, 94, and 237 eV) still visible. The LEED pattern indicates a (1×1) surface structure (Figure 70). The I_{ads}-catalyzed Pd dissolution peak at ca. 0.55 V (Figure 71) gives a small charge, barely visible above baseline. The LSV for a second aliquot of I_{ads} is given in Figure 72; the lack of voltammetric features cathodic of 0.8 V indicates a regenerated bare Pt(111).

ΘPd = 1 ML

For monolayer SLR^3 Pd films on Pt(111), the CV (Figure 73) closely resembles that of the Θ_{Pd}= 0.5 ML SLR^3 film. However, it is clear that an increased H adsorption/desorption peak current results from this coverage. $Q_{H\text{-}UPD}$= 105 μC, approximately double that of Θ_{Pd}= 0.5 ML films, with no contribution from other features. In Figure 74, the AES peaks due to Pt (at 94 and 237 eV) are not as prominent as those for 0.5 ML films. Conversely, the Pd peak at 330 eV increased. The absence of the characteristic Cu peak (at 105 eV) indicates complete exchange of Cu with Pd during the SLR^3 process. The LEED

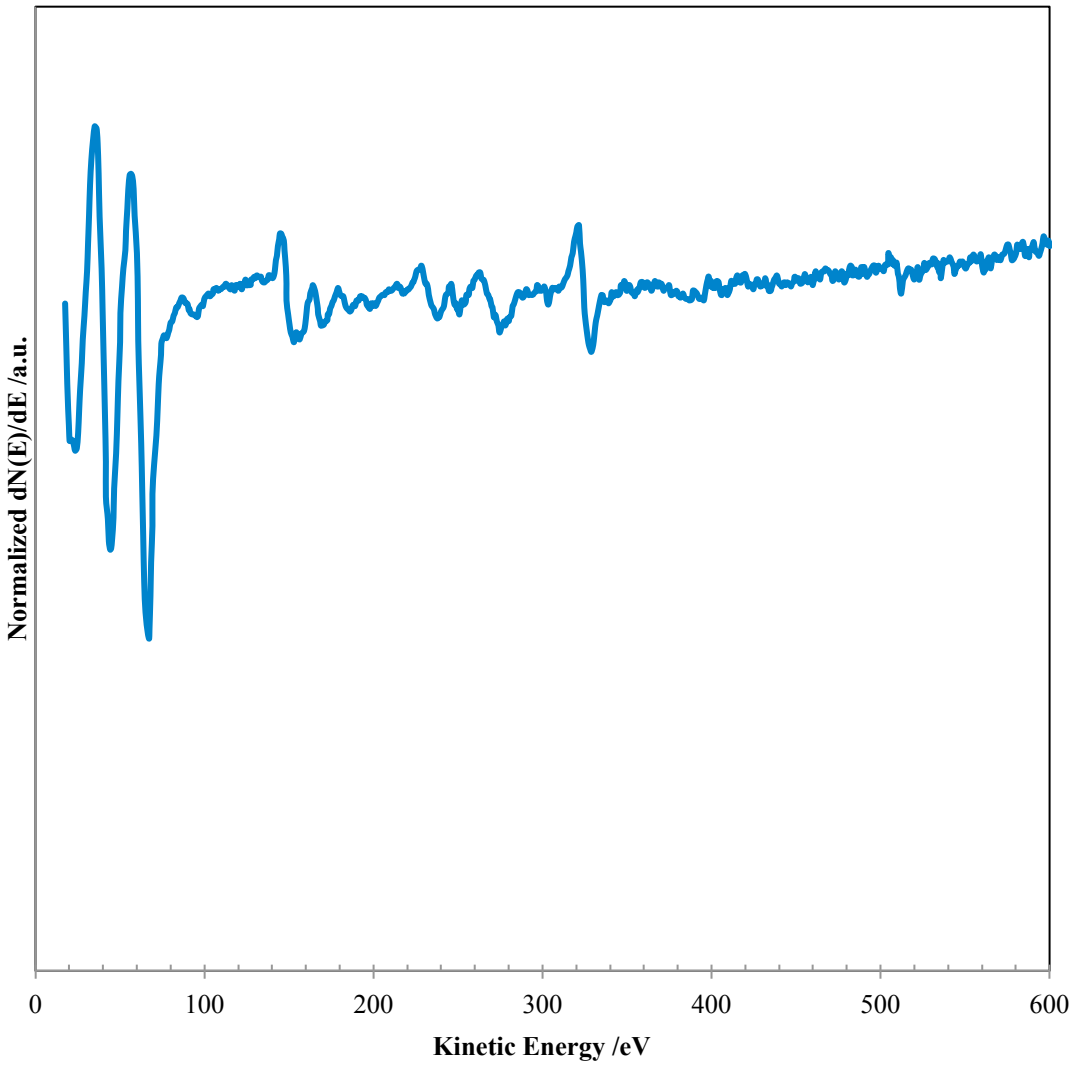

Figure 69. Auger electron spectrum of Θ_{Pd}= 0.5 ML.

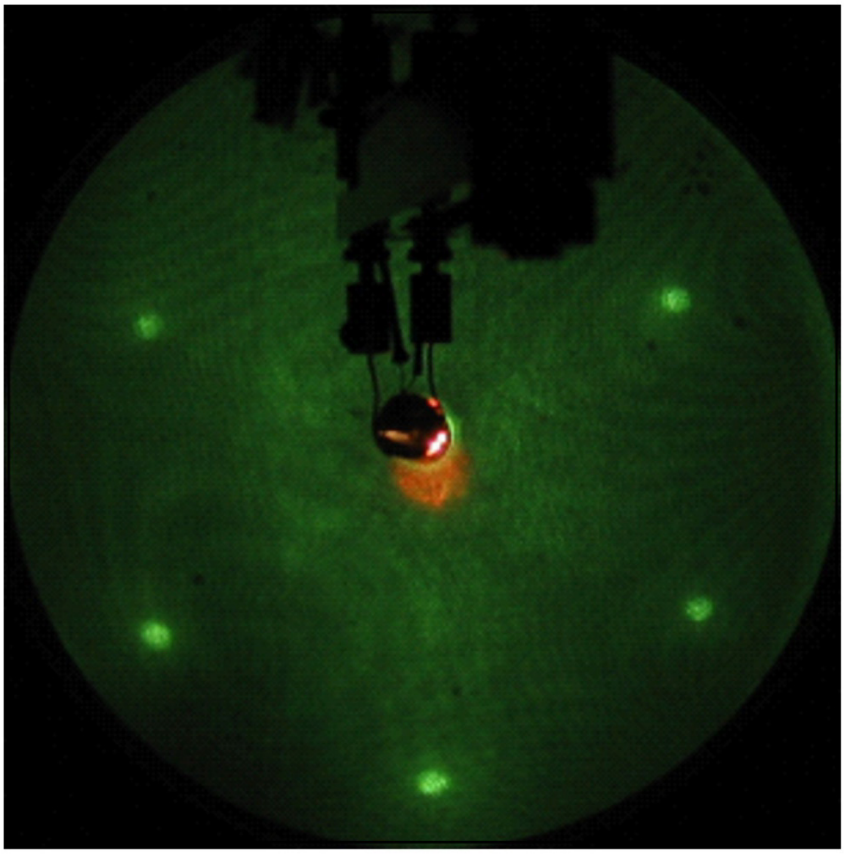

Figure 70. LEED pattern for Θ_{Pd}= 0.5 ML on Pt(111). Beam energy 62 eV, Ip =2 μA.

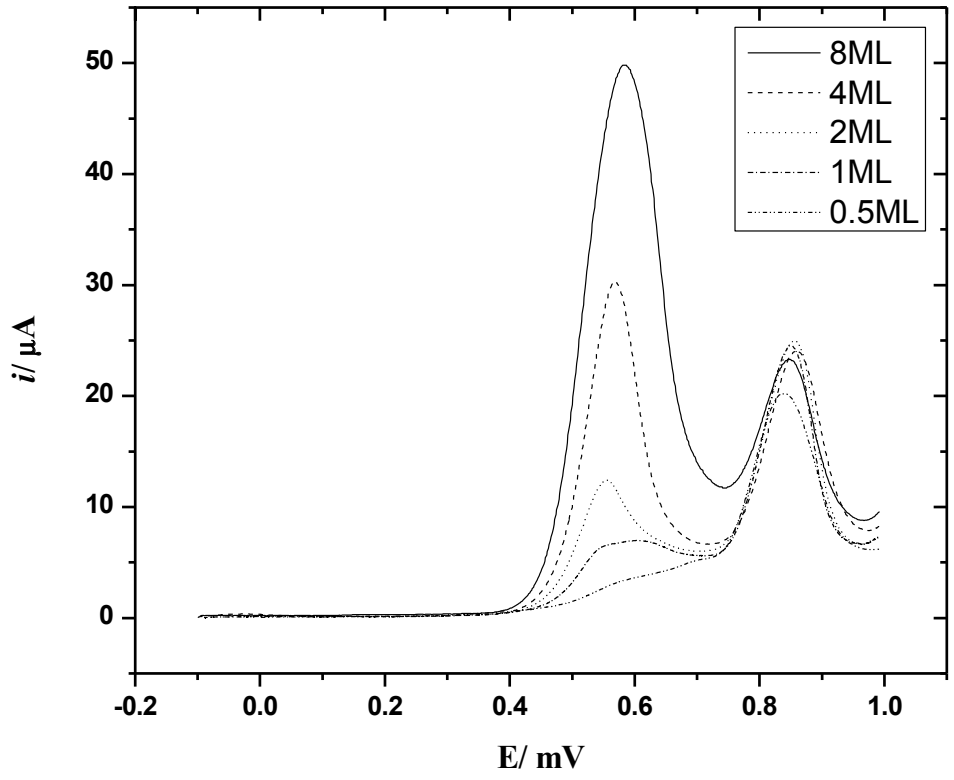

Figure 71. Linear sweep voltammogram of I_{ads}-catalyzed dissolution of SLR^3-prepared Pd films on Pt(111) in iodide-free electrolyte. 100 mM H_2SO_4, v= 2 mV/s, vs Ag/AgCl (1 mM NaCl).

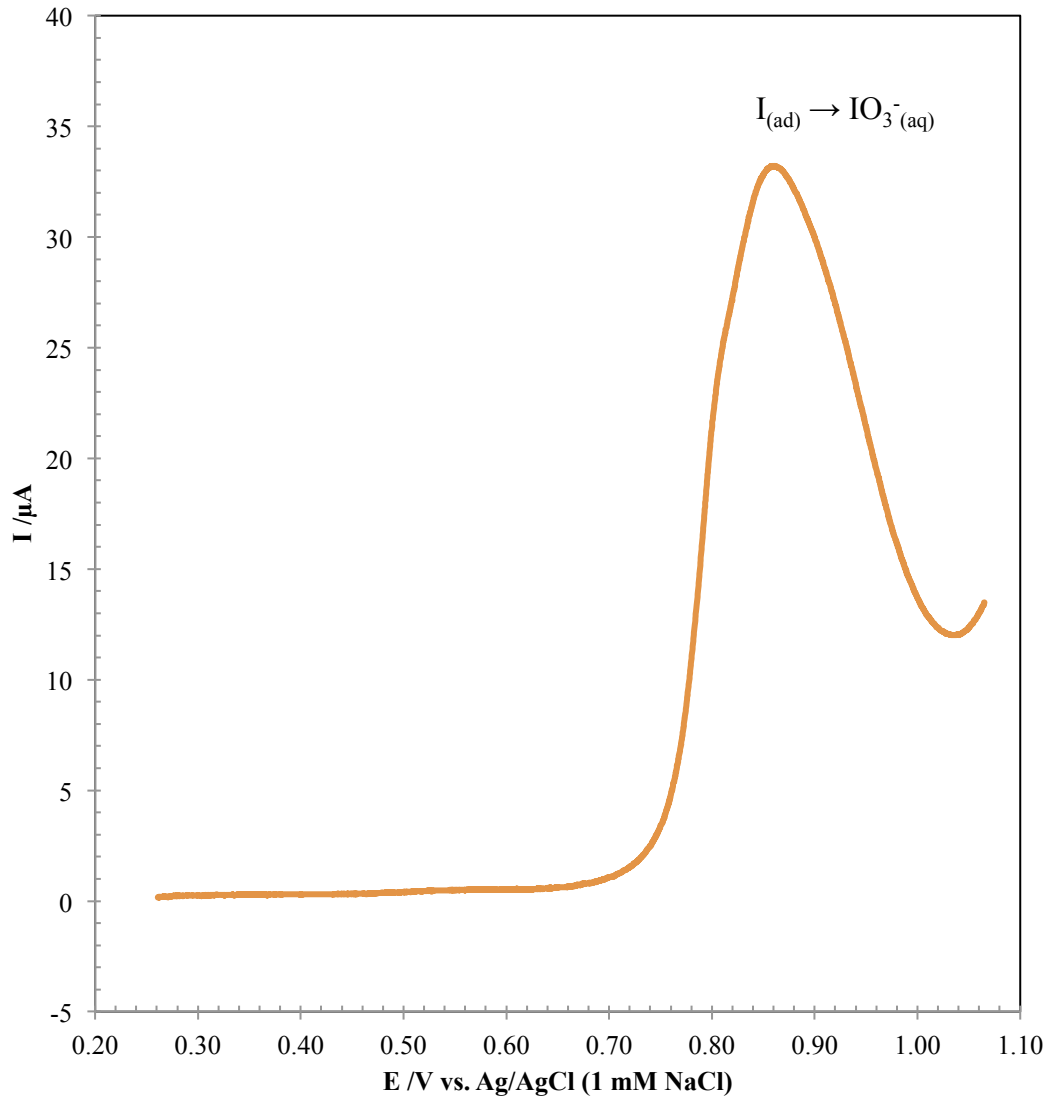

Figure 72. 2nd scan of I_{ads}-stripping of SLR[3]-prepared 8 ML Pd on Pt(111) (following readsorption of iodine) in 100 mM H_2SO_4 (r = 2 mV/s).

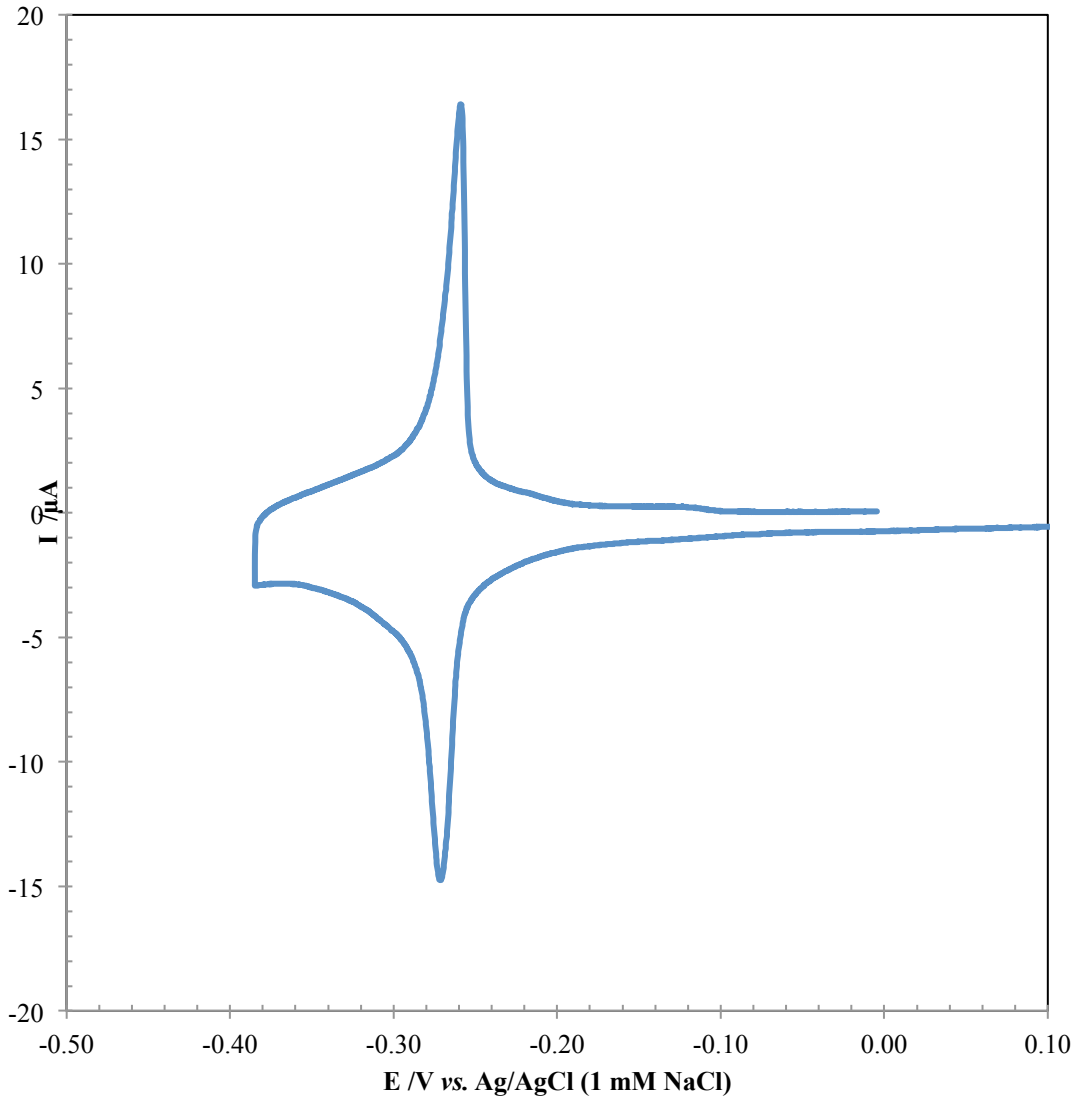

Figure 73. Cyclic voltammogram (hydrogen region only) of Θ_{Pd}= 1 ML; 100 mM H_2SO_4, *v*= 2 mV/s, vs Ag/AgCl (1 mM NaCl).

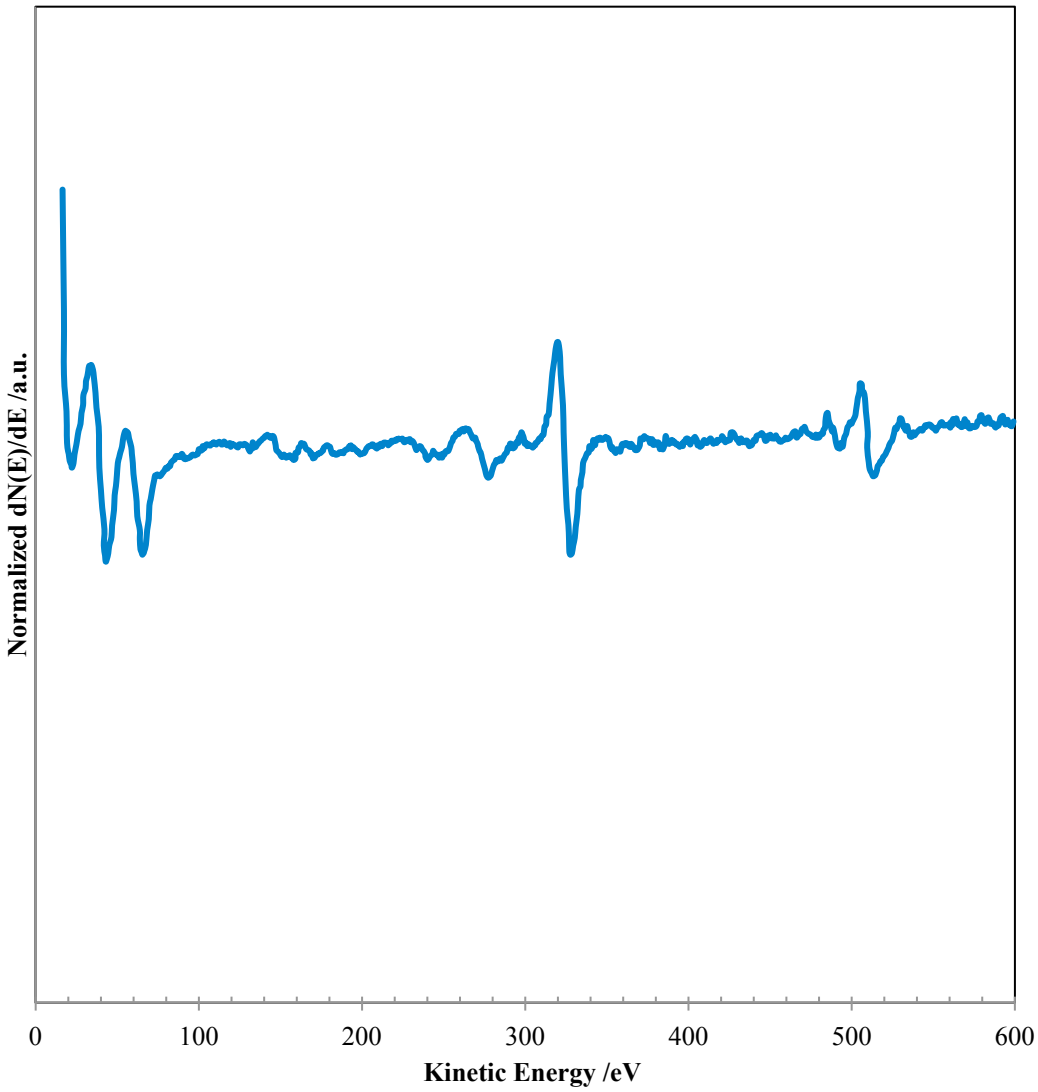

Figure 74. Auger electron spectrum of Θ_{Pd}= 1 ML.

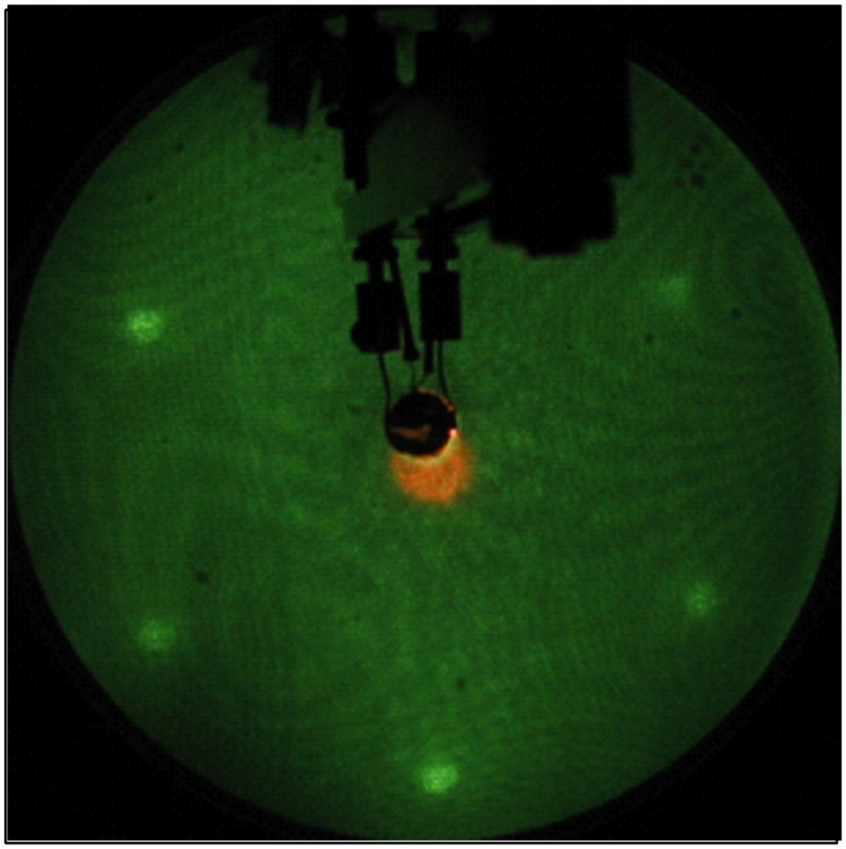

Figure 75. LEED pattern for Θ_{Pd}= 1 ML on Pt(111). Beam energy 62 eV, Ip =2 μA.

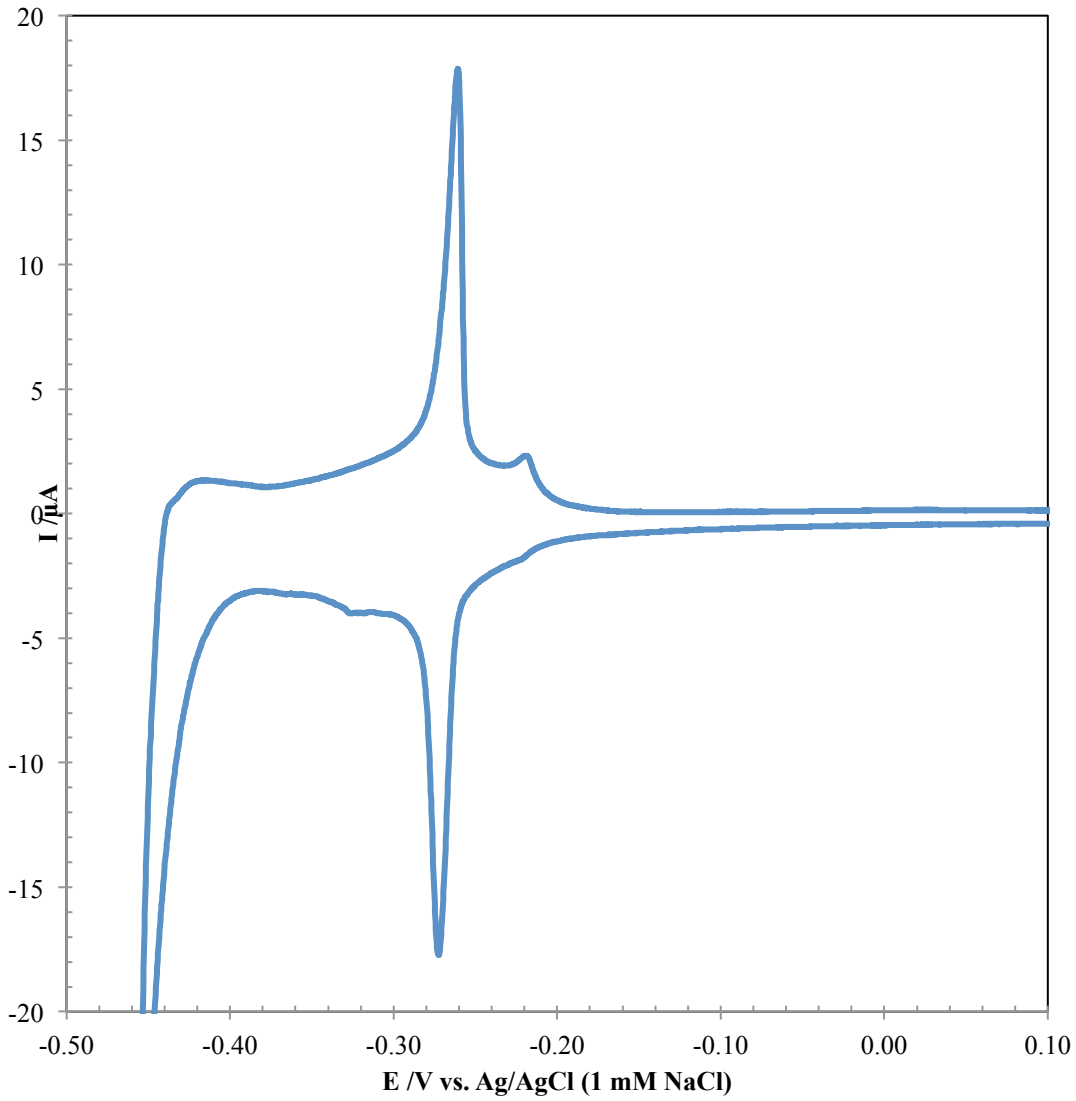

Figure 76. Cyclic voltammogram (hydrogen region only) of Θ_{Pd}= 2 ML; 100 mM H_2SO_4, *v*= 2 mV/s, vs Ag/AgCl (1 mM NaCl).

pattern gives the familiar (1×1) image (Figure 75) with bright and sharp spots. The I_{ads}-catalyzed dissolution gives a broad flat peak.

$$\Theta Pd = 2\ ML$$

For Θ_{Pd}= 2 ML, the H_{UPD} peaks are larger than those for lower coverages (Figure 76), indicating a yet-still rising degree of H_{UPD} activity. The films begin to show a small peak at a more positive potential (ca. -0.21 V). Here, $Q_{H\text{-}UPD}$= 116 μC with a minor contribution from the -0.21 V peak. The AES spectrum (Figure 77) and LEED pattern (Figure 78) show many similarities to those at lower coverages. Again, there was no indication of Cu in the AES spectrum.

The second red-ox couple at lower overpotential has previously been assigned to H_{UPD} adsorption/desorption at step sites [99]. It has also been described as arising from H adsorption/desorption from subsequent Pd adlayer-terrace sites [86, 94, 96]. However, in the context of 3D film growth, the formation of terrace upon terrace does not seem feasible without the introduction of step sites. If both the peaks originate from H_{UPD} on terrace sites the reason for their appearances at different potentials is not fully clear. It could be surmised that a difference in work function may exist between the disparate terraces at these low coverages. However, the second peak remains even at higher Pd coverages, where there is expected to be equivalence among surface Pd atoms on equivalent domains. More work is required to address this ambiguity. Nevertheless, in the present study the second peak (at more positive potential) is attributed to H_{UPD} at step sites.

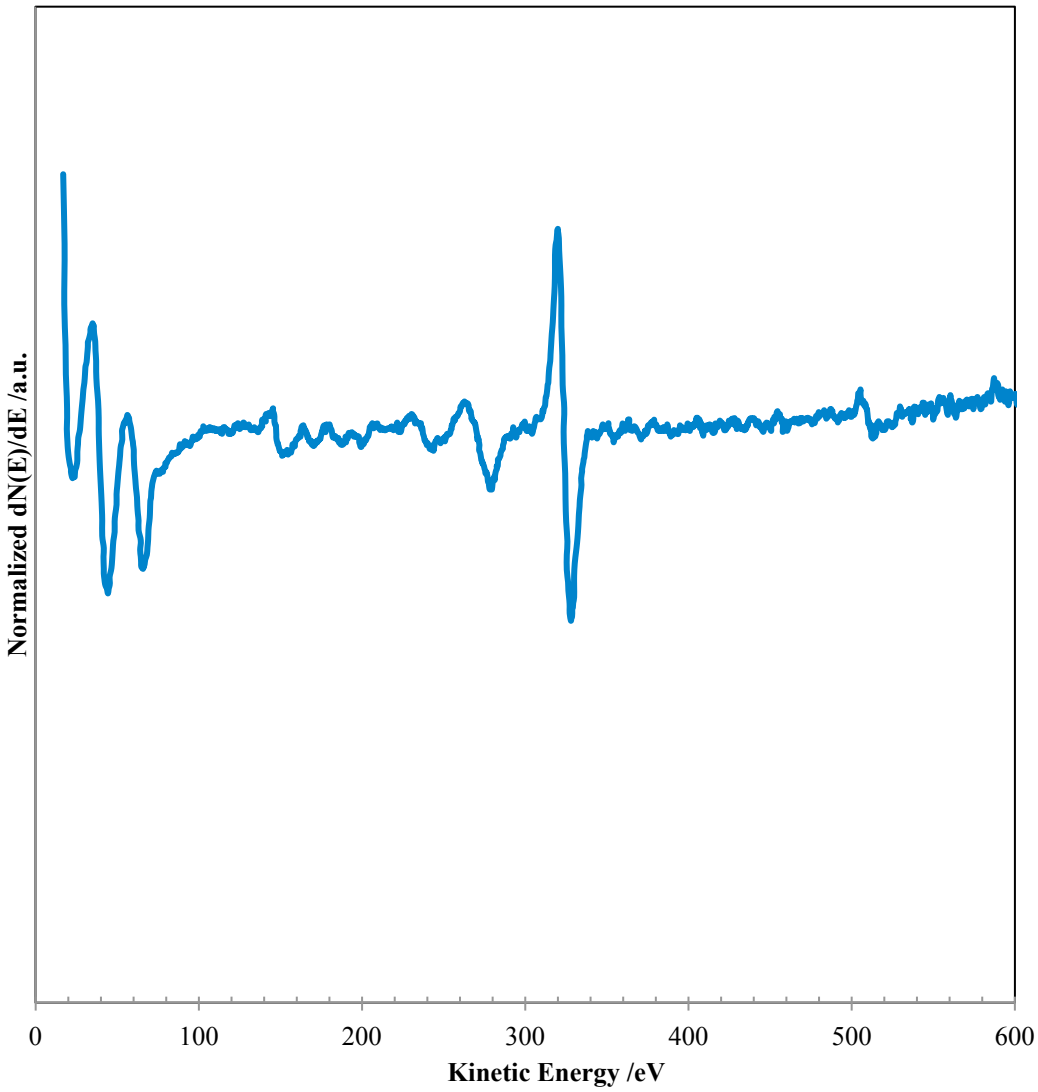

Figure 77. Auger electron spectrum of Θ_{Pd}= 2 ML.

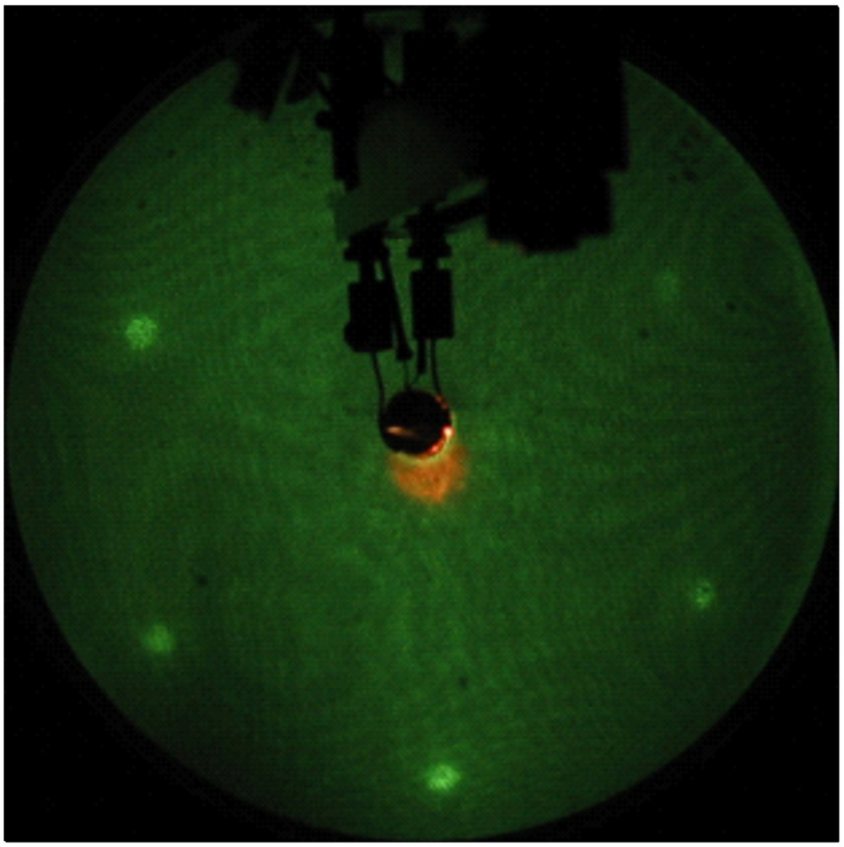

Figure 78. LEED pattern for Θ_{Pd}= 2 ML on Pt(111). Beam energy 62 eV, Ip =2 μA.

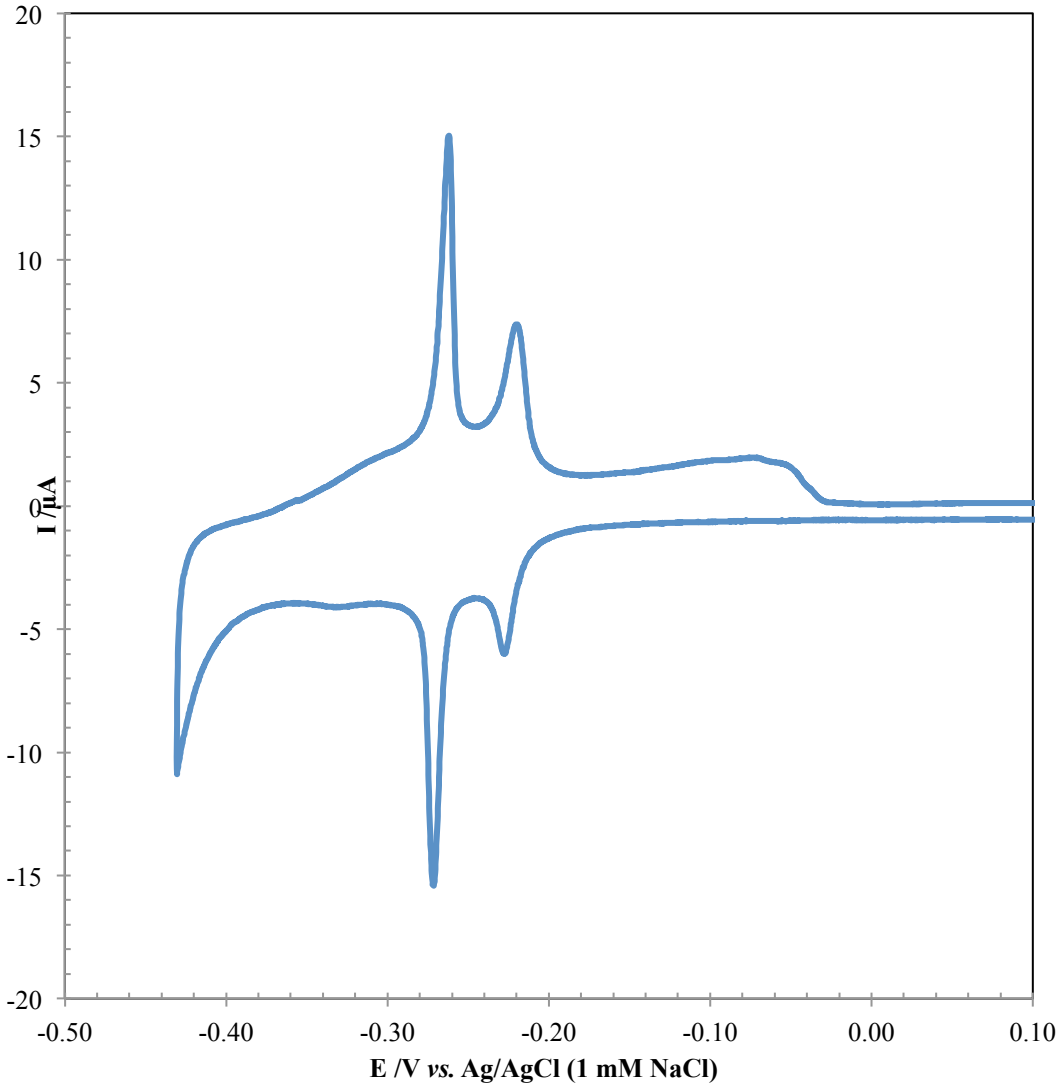

Figure 79. Cyclic voltammogram (hydrogen region only) of Θ_{Pd}= 4 ML; 100 mM H_2SO_4, v= 2 mV/s, vs Ag/AgCl (1 mM NaCl).

$$\Theta Pd = 4ML$$

For Θ_{Pd}= 4 ML, the CV (Figure 79) resembles the lower coverages, however the profile is beginning to show some major differences. For one, the step peak is for the first time a major component of the overall H_{UPD} charge. Also worth noting is the overall $Q_{H\text{-}UPD}$= 100 μC, a slight decrease from Θ_{Pd}= 2 ML films. Alternatively, the size of the terrace peak is still much larger than that of the step. Again, this is an indication that the films produced by SLR^3 up to Θ_{Pd}= 4 ML have a low step density, i.e., high smoothness. More clearly resolved in this CV is the appearance of a third H-related peak at ca. -0.34 V. This peak has been ascribed to a process involving H-absorption and the formation of α-Pd-H [137]; Kolb et. al. observed the emergence of this peak at Θ_{Pd}= 3 ML for Pd/Au(111) films [138]. The AES spectra (Figure 80) again show an increased signal for Pd and these features mask the Pt signal and again show no indication of residual Cu. The LEED pattern indicates a (1×1) structure for the film (Figure 81). Despite the diminished i_p of the H_{UPD} peaks, the I_{ads}-catalyzed dissolution voltammetric wave in Figure 71 gives a charge equivalent to 4 ML.

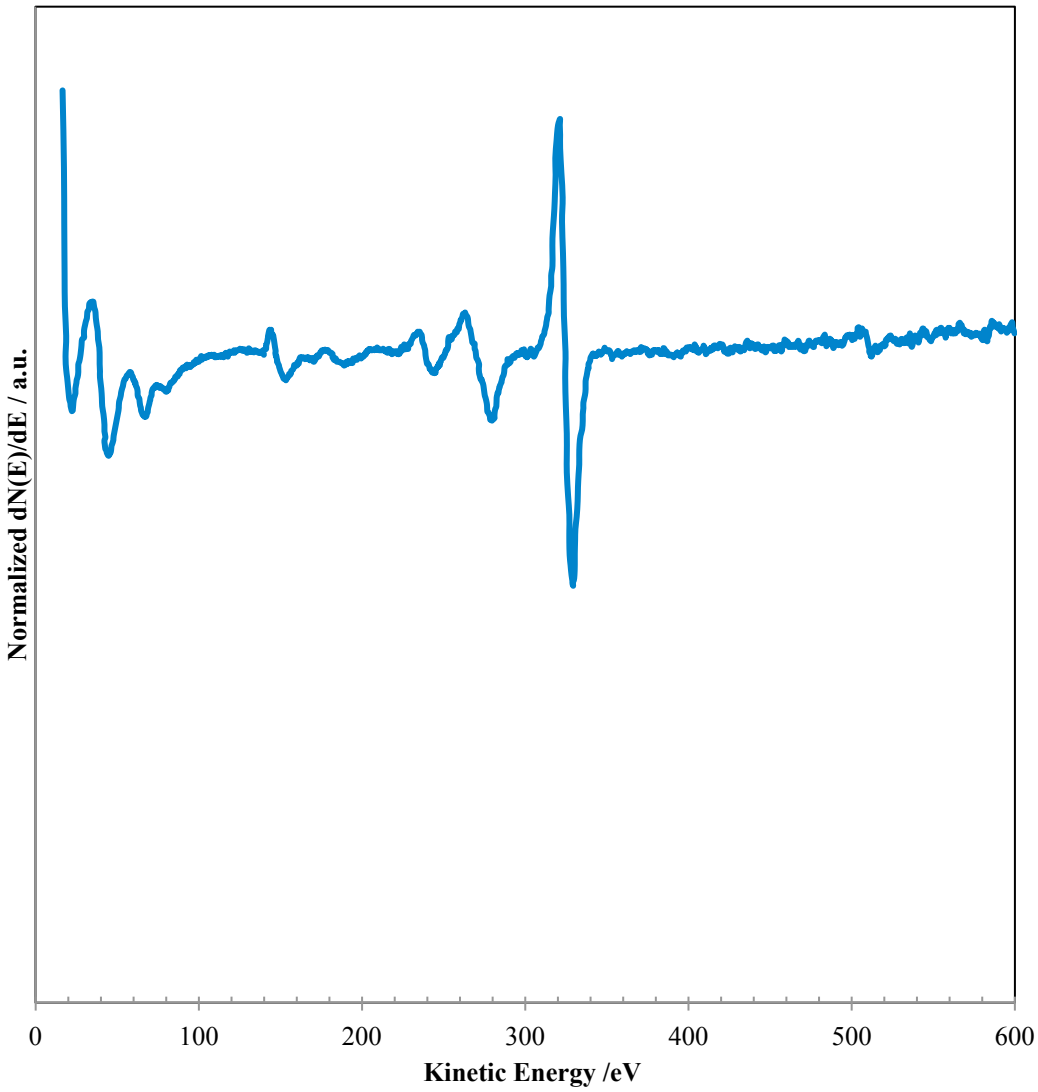

Figure 80. Auger electron spectrum of Θ_{Pd}= 4 ML.

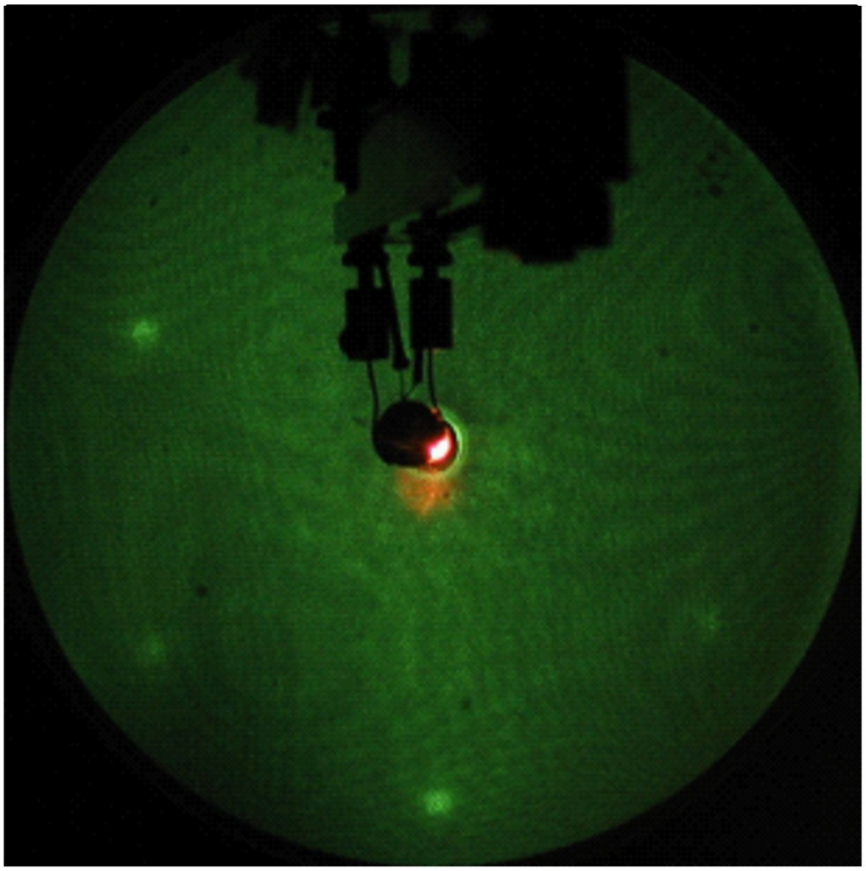

Figure 81. LEED pattern for Θ_{Pd}= 4 ML on Pt(111). Beam energy 62 eV, Ip =2 μA.

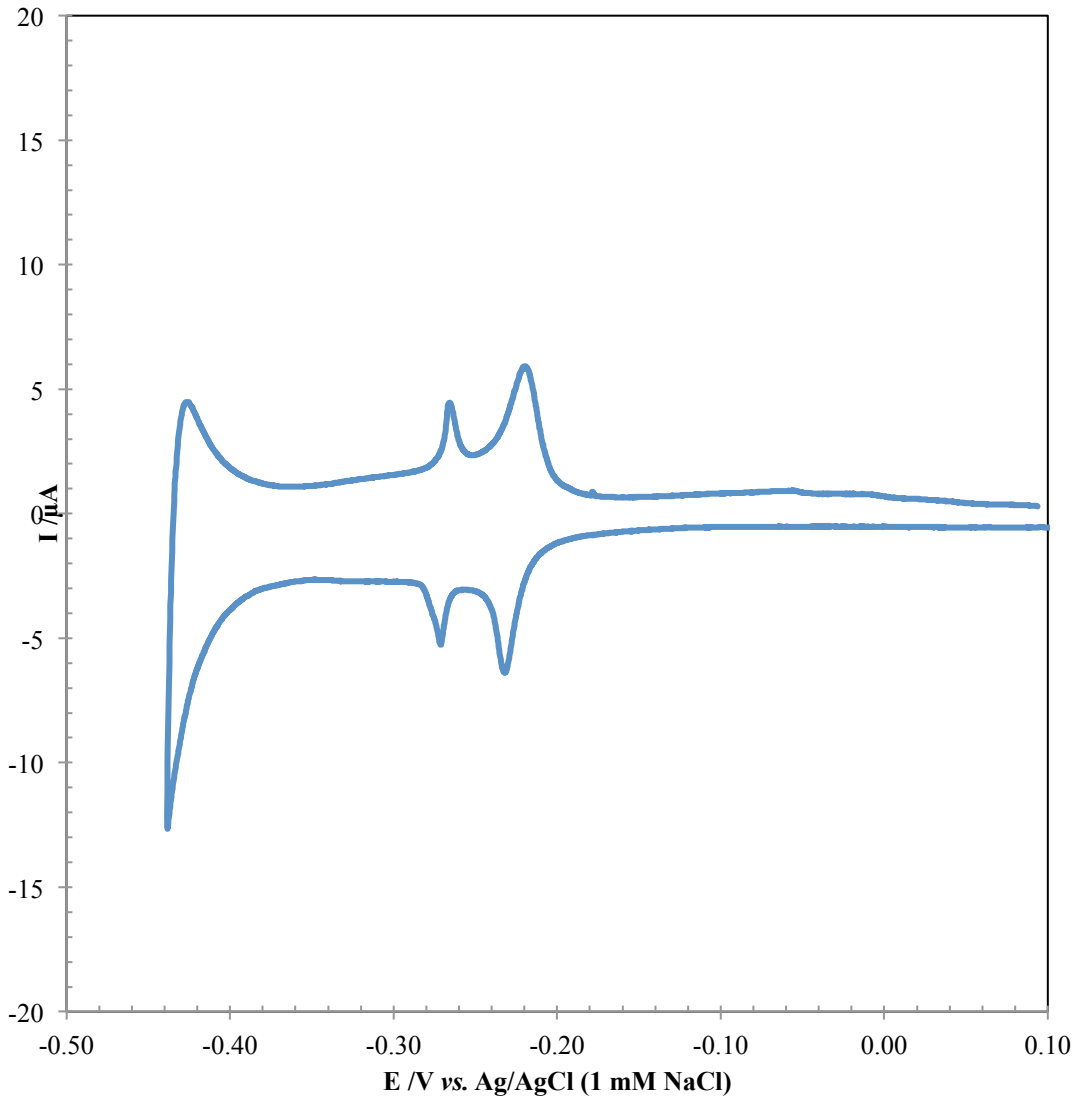

Figure 82. Cyclic voltammogram (hydrogen region only) of Θ_{Pd}= 8 ML; 100 mM H_2SO_4, v= 2 mV/s, vs Ag/AgCl (1 mM NaCl).

ΘPd = 8 ML

For 8 ML-thick films, the H_{UPD} profile, in Figure 82, of hydrogen adsorption/desorption arising from step sites indicates that the films are relatively rough for this method at this coverage and the total $Q_{H\text{-}UPD}$= 56 μC, a substantially lower value. Larger yet, is the α-Pd-H peak. Notably, even at this high coverage, the AES spectrum for SLR^3 films did not show any signal associated with Cu (Figure 83). The film shows a (1×1) LEED pattern (Figure 84) with noticeably dim spots. The I_{ads}-catalyzed dissolution of the film shows anticipated behavior (Figure 71), with a charge corresponding to Θ_{Pd}= 8 ML. Note that E_p for the 5 e^- oxidation of adsorbed iodine is independent of the Pd coverage; this is expected for the surface-limited reaction of $I_{ads} \rightarrow IO_3^-{}_{(aq)}$ on Pt(111).

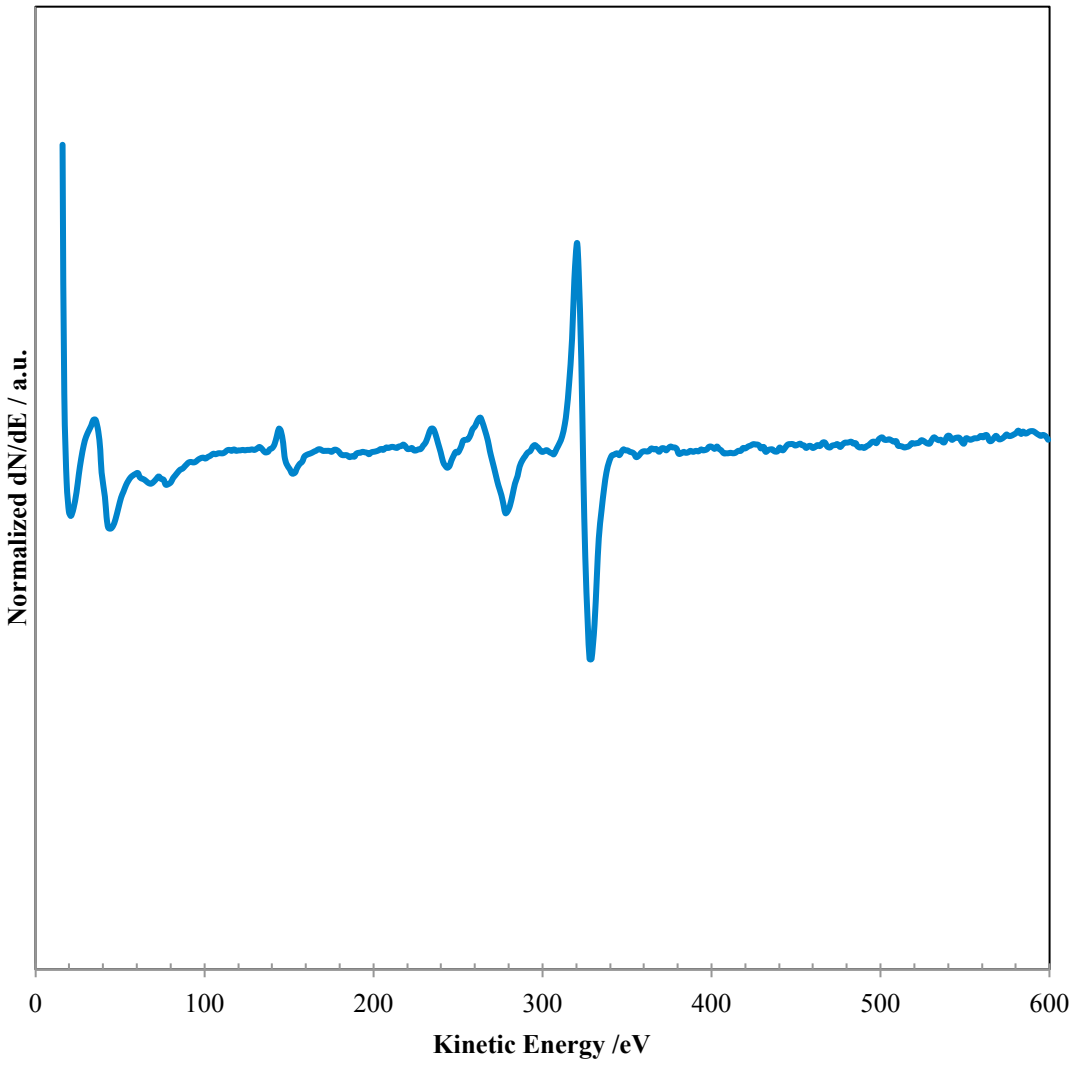

Figure 83. Auger electron spectrum of Θ_{Pd}= 8 ML.

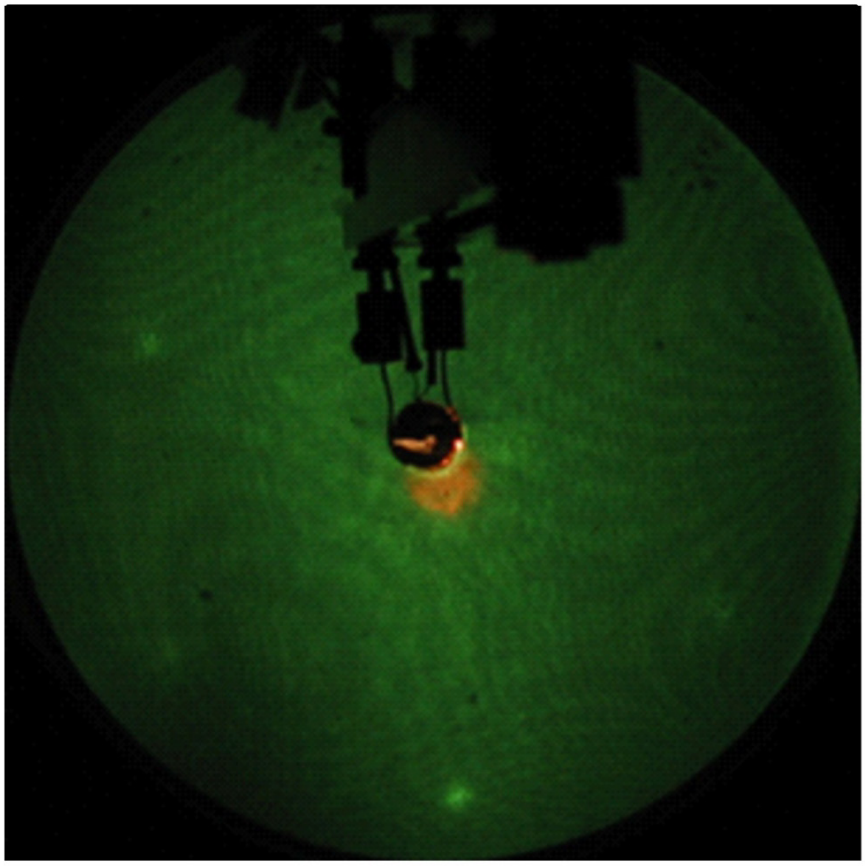

Figure 84. LEED pattern for Θ_{Pd}= 4 ML on Pt(111). Beam energy 62 eV, Ip =2 μA.

Figure 85(a) shows the variation of H_{UPD} desorption charge with Pd coverage for all SLR^3 films as determined by numerical integration of the desorption peak, using the method illustrated by Hoyer et al. [94]. Initially, the films show an increase of H_{UPD} desorption charge from terrace sites with increasing Pd coverage. Then, the relative contribution of H_{UPD} charge from steps sites on multilayer Pd films starts to increase between coverages of 2 and 4 ML. The total H_{UPD} desorption charge also starts to decline after 2 ML. Figure 85(b) displays the % step-H_{UPD} desorption charge for SLR^3 films. For coverages up to 2 ML, the films show H_{UPD} desorption exclusively from terrace sites. This indicates smooth and uniform SLR^3 films in this range.

From electron spectroscopic observations, the SLR^3 method produces familiar Pd film properties and results in the formation of well-ordered ultrathin films free of any copper inclusion. Electrochemical methods, however, reveal some details and minor differences from submonolayer to 8 ML. First, they retain ultrathin properties even at 8 ML coverage and show unique voltammetric signatures in the hydrogen UPD region. Further, the total H_{UPD} desorption charge was miniscule for the highest coverage but retained the ability to adsorb H at potentials prior to absorption. Such behavior is non-existent for surfaces of bulk Pd. Increased step density at higher coverages (between 4 to 8 ML) is observed and is taken as an indication of surface roughness, or more completely, a decrease in the size of well-ordered terrace domains. Finally, as Pd coverage increases, formation of α-Pd-H via H-

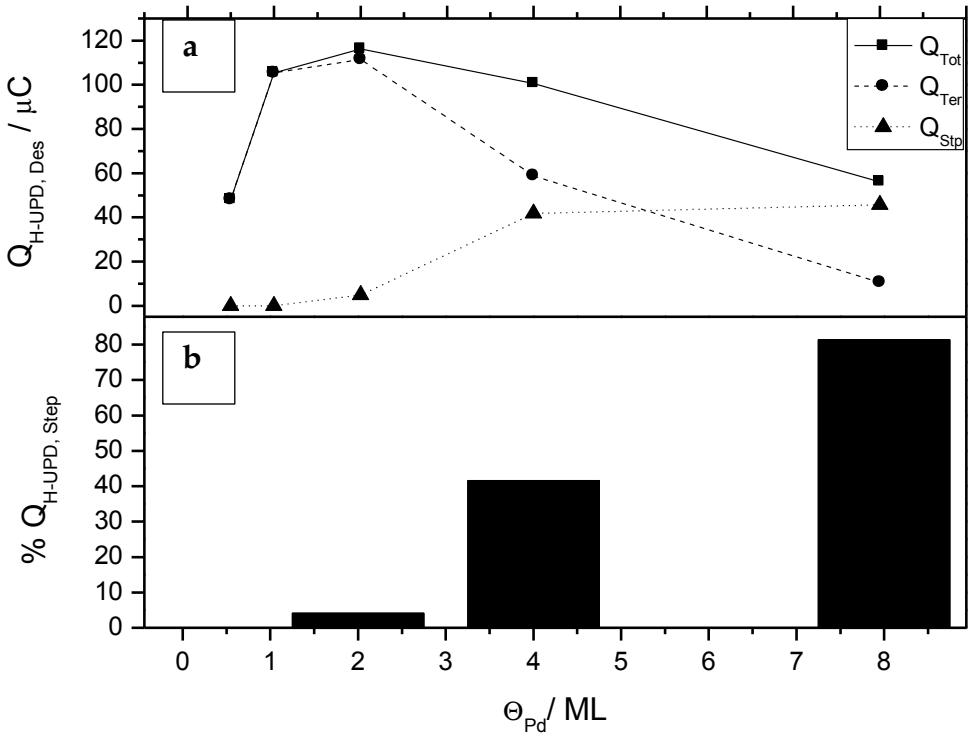

Figure 85. (top) Effect of Pd coverage on H_{UPD} desorption charge for SLR^3 films and (bottom) % H_{UPD} desorption charge from step sites.

absorption can be seen to contribute more and more charge to the overall hydrogen region. This is expected behavior, whereas H-absorption and corresponding Pd-H formation is so fast in bulk Pd electrodes, that the H_{UPD} adsorption/desorption event ultimately becomes unobservable by voltammetry.

The "roughness" observed in SLR^3 films may explained by the nucleation of Cu during the Cu^{+2} discharge process [139]. A surface-mediated charge transfer of electrons from Cu_{UPD} to Pd^{+2} through already reduced Pd_{ads} could also explain the increased roughness. In either instance, the process is likely to result in a relatively flat surface with small 3D clusters, which grow with increasing coverage. This growth mode (Stranski-Krastanov) has been thoroughly reported for Pd-adlayers formed via direct deposition [138, 140]. In a future publication, SLR^3 films will be compared to those formed via direct deposition; initial results show that the films prepared in the present study show a lower step-density. It has been demonstrated elsewhere that as supported Pt nanoparticles grow, an increase in particle size results in an increase in the number of terrace sites without an appreciable increase the number of step sites [141]. Thus, it may be unlikely that pseudomorphic Pd films would significantly roughen (i.e., increased step density) at the highest coverages (between 4 to 8 ML). The observed decrease of H_{UPD} peaks from terrace sites, rather, may be indicative of a thin-film to bulk transition [85, 90]. At low Pd coverages, high strain energy at the Pt/Pd interface resists the expansion necessary to accommodate absorption of hydrogen below the top layer of Pd atoms [77]. As the overlayer grows, the lower cohesive energy of the Pd-Pd lattice allows for this expansion and

hydrogen absorption begins to take place, as it is well known to do in bulk palladium.

CONCLUSION FOR PART II

Pd thin-films prepared via SLR^3 on a Pt(111) substrate have been characterized using auger electron spectroscopy (AES), low-energy electron diffraction (LEED), and electrochemistry (EC). The following conclusions can be drawn:

1. SLR^3 appears to be capable of preparing atomically smooth ultrathin films on Pt(111) without additional thermal or electrochemical annealing for $0.5 \leq \Theta_{Pd} \leq 8$ ML coverages.
2. There is a nearly 1:1 correlation between the cumulative charge of underpotentially deposited Cu (i.e., Pd deposition charge) and that of I_{ads}-catalyzed Pd stripping of SLR^3-prepared films on Pt(111) surfaces. However, each SLR^3 cycle produces *ca.* 0.8 ML of Cu (i.e., Pd) on Pt(111).
3. SLR^3-prepared Pd films show H_{UPD} peaks on terrace- and step-sites, which are indicators of the thin film behavior. Even at 8 ML true bulk properties are not observed.
4. For SLR^3-prepared Pd films, H_{UPD} at step sites begins to appear when $\theta_{Pd} \geq 2$; this may be an indication that films prepared via SLR^3 begin roughening at these coverages.
5. SLR^3 Pd film formation beyond 1 ML coverage follows the Stranski-Krastanov growth mode.

REFERENCES

[1] P.H. Rieger, Electrochemistry, Second ed., Chapman & Hall, New York, 1994.

[2] M. Faraday, Experimental Researches in Electricity. Fifth Series, Philos. Trans. R. Soc. London 123 (1833) 675-710.

[3] M. Faraday, Experimental Researches in Electricity. Seventh Series, Philos. Trans. R. Soc. London 124 (1834) 77-121.

[4] W.R. Grove, On a Gas Voltaic Battery, Proc. R. Soc. (1843) 268-78, 346-54, 422-32.

[5] W. Ostwald, Electrochemistry, History and Theory, Amering Publishing Co., Washington, D. C. , 1980.

[6] W.A. Tilden, Famous Chemists, Ayer Publishing, New York, 1968.

[7] B.J. Crowe, Fuel Cells: A Survey SP-5115, in: NASA (Ed), GPO, 1973.

[8] B. Viswanathan, M.A. Scibioh, Fuel Cells, Principles and Applications, Graphica Printers, Hyderabad, 2007.

[9] C.W.B. Bezerra, L. Zhang, H. Liu, K. Lee, A.L.B. Marques, et al., A review of heat-treatment effects on activity and stability of PEM fuel cell catalysts for oxygen reduction reaction, J. Power Sources 173 (2007) 891-908.

[10] A.J. Appleby, F.R. Foulkes, Fuel cell handbook, 1st ed., Van Nostrand Reinhold, New York, 1989.

[11] Multi-Year Research, Development and Demonstration Plan: Planned Program Activities for 2005-2015, in: DOE-EERE (Ed) DOE Bulletin, 2007.

[12] A.J. Bard, L.R. Faulkner, Electrochemical Methods: Fundamentals and Applications, John Wiley & Sons, Inc., New York, 2001.

[13] K. Kinoshita, Electrochemical Oxygen Technology, 1st ed., John Wiley & Sons, Inc., New York, 1992.

[14] A.J. Appleby, M. Savy, Kinetics of oxygen reduction reactions involving catalytic decomposition of hydrogen peroxide: Application to porous and rotating ring-disk electrodes, J. Electroanal. Chem. 92 (1978) 15-38.

[15] E. Yeager, Dioxygen electrocatalysis: mechanisms in relation to catalyst structure, J. Mol. Catal. 38 (1986) 5-25.

[16] M.L.B. Rao, A. Damjanovic, J.O.M. Bockris, Oxygen adsorptions related to the unpaired d-electrons in transition metals Journal of Physical Chemistry 67 (1963) 2508-9.

[17] Y.X. Wang, P.B. Balbuena, Design of oxygen reduction bimetallic catalysts: Ab-initio-derived thermodynamic guidelines, J. Phys. Chem. B 109 (2005) 18902-6.

[18] T.P. Hoar, E.W. Brooman, The electroreduction of oxygen on Pt-Ru and Pt-Rh Alloys, Electrochim. Acta 11 (1966) 545-7.

[19] S. Mukerjee, S. Srinivasan, M.P. Soriaga, J. McBreen, Role of Structural and Electronic Properties of Pt and Pt Alloys on Electrocatalysis of Oxygen Reduction. An In Situ XANES and EXAFS Investigation, J. Electrochem. Soc. 142 (1995) 1409-22.

[20] B. Hammer, J.K. Nørskov, Electronic factors determining the reactivity of metal surfaces, Surf. Sci. 343 (1995) 211-20.

[21] T. Toda, H. Igarashi, H. Uchida, M. Watanabe, Enhancement of the Electroreduction of Oxygen on Pt Alloys with Fe, Ni, and Co, J. Electrochem. Soc. 146 (1999) 3750-6.

[22] J.L. Fernandez, D.A. Walsh, A.J. Bard, Thermodynamic Guidelines for the Design of Bimetallic Catalysts for Oxygen Electroreduction and Rapid Screening by Scanning Electrochemical Microscopy. M-Co (M: Pd, Ag, Au), J. Am. Chem. Soc. 127 (2005) 357-65.

[23] C.A. Lucas, N.M. Markovic, P.N. Ross, Adsorption of halide anions at the Pt(111)-solution interfacestudied by in situ surface x-ray scattering, Phys. Rev. B: Condens. Matter 55 (1997) 7964-71.

[24] B.C. Beard, P.N. Ross, The Structure and Activity of Pt-Co Alloys as Oxygen Reduction Electrocatalysts, J. Electrochem. Soc. 137 (1990) 3368.

[25] J.T. Glass, G.L. Cahen, G.E. Stoner, The Effect of Metallurgical Variables on the Electrocatalytic Properties of PtCr Alloys, J. Electrochem. Soc. 134 (1987) 58-65.

[26] V. Stamenkovic, T.J. Schmidt, P.N. ross, N.M. Markovic, Surface segregation effects in electrocatalysis: kinetics of oxygen reduction reaction on polycrystalline Pt3Ni alloy surfaces, J. Electroanal. Chem. 554 (2003) 191-9.

[27] V. Stamenkovic, T.J. Schmidt, N.M. Markovic, J. P. N. Ross, Surface composition effects in electrocatalysis: Kinetics of oxygen reduction on well-defined Pt3Ni and Pt3Co alloy surfaces, J. Phys. Chem. B 106 (2002) 11970-9.

[28] J.L. Fernandez, J.M. White, Y. Sun, W. Tang, G. Henkelman, et al., Characterization and Theory of Electrocatalysts Based on Scanning Electrochemical Microscopy Screening Methods, Langmuir 22 (2006) 10426-31.

[29] V. Stamenkovic, T.J. Schmidt, P.N. Ross, N.M. Markovic, Surface composition effects in electrocatalysis: Kinetics of oxygen reduction on well-defined Pt3Ni and Pt3Co alloy surfaces, J. Phys. Chem. B 106 (2002) 11970-9.

[30] S.R. Brankovic, J.X. Wang, R.R. Adzic, Metal monolayer deposition by replacement of metal adlayers on electrode surfaces, Surf. Sci. 474 (2001) L173-L9.

[31] K. Sasaki, J.X. Wang, H. Naohara, N. Marinkovic, K. More, et al., Recent advances in platinum monolayer electrocatalysts for oxygen reduction reaction: Scale-up synthesis, structure and activity of Pt shells on Pd cores, Electrochim. Acta 55 (2010) 2645-52.

[32] J. Zhang, Y. Mo, M.B. Vukmirovic, R. Klie, K. Sasaki, et al., Platinum Monolayer Electrocatalysts for O2 Reduction: Pt Monolayer on Pd(111) and on Carbon-Supported Pd Nanoparticles, J. Phys. Chem. B 108 (2004) 10955-64.

[33] Y. Du, K. Lv, B. Su, N. Zhang, C. Wang, Electro-reduction of oxygen and electro-oxidation of methanol at Pd monolayer-modified macroporous Pt electrode, J. Appl. Electrochem. 39 (2009) 2409-14.

[34] J.B. Abreu, R.J. Barriga, W. Temesghen, J.A. Schimpf, M.P. Soriaga, Electrochemical digital etching in non-corrosive electrolyte: I(ads)-catalyzed dissolution and reordering of ion-bombarded Pd(111), J. Electroanal. Chem. 381 (1995) 239-41.

[35] J.A. Schimpf, A. Carrasquillo, Jr., M.P. Soriaga, Electrochemical digital etching in inert electrolyte: reordering of ion-bombarded Pd(100) by chemisorbed-iodine-catalyzed dissolution, Electrochim. Acta 40 (1995) 1203-5.

[36] M.P. Soriaga, J.A. Schimpf, A. Carrasquillo, Jr., J.B. Abreu, W. Temesghen, et al., Electrochemistry of the I-on-Pd single-crystal interface: studies by UHV-EC and in situ STM, Surf. Sci. 335 (1995) 273-80.

[37] S. Hwang, I. Oh, J. Kwak, Electrodeposition of Epitaxial Cu(111) Thin Films on Au(111) Using Defect-Mediated Growth, J. Am. Chem. Soc. 123 (2001) 7176-7.

[38] J.X. Wang, H. Inada, L. Wu, Y. Zhu, Y. Choi, et al., Oxygen Reduction on Well-Defined Core−Shell Nanocatalysts: Particle Size, Facet, and Pt Shell Thickness Effects, J. Am. Chem. Soc. 131 (2009) 17298-302.

[39] T. Ghosh, M.B. Vukmirovic, F.J. DiSalvo, R.R. Adzic, Intermetallics as Novel Supports for Pt Monolayer O2 Reduction Electrocatalysts: Potential for Significantly Improving Properties, J. Am. Chem. Soc. 132 (2009) 906-7.

[40] W.-P. Zhou, K. Sasaki, D. Su, Y. Zhu, J.X. Wang, et al., Gram-Scale-Synthesized Pd2Co-Supported Pt Monolayer Electrocatalysts for Oxygen Reduction Reaction, J. Phys. Chem. C 114 (2010) 8950-7.

[41] K. Gong, D. Su, R.R. Adzic, Platinum-Monolayer Shell on AuNi0.5Fe Nanoparticle Core Electrocatalyst with High Activity and Stability for the Oxygen Reduction Reaction, J. Am. Chem. Soc. 132 (2010) 14364-6.

[42] F.H.B. Lima, J. Zhang, M.H. Shao, K. Sasaki, M.B. Vukmirovic, et al., Pt monolayer electrocatalysts for O2 reduction: PdCo/C substrate-induced activity in alkaline media, J. Solid State Electrochem. 12 (2008) 399-407.

[43] W.E. Spicer, Photoemissive, photoconductive, and optical absorption studies of alkali-antimony compounds, Phys. Rev. 112 (1958) 114-22.

[44] I. Lindau, W.E. Spicer, The probing depth in photoemission and auger-electron spectroscopy, J. Electron. Spectrosc. Relat. Phenom. 3 (1974) 409-13.

[45] S. J.C, Orientation dependence of overlayer attenuation of electrons for the cylindrical mirror analyzer and a retarding field analyzer, J. Electron. Spectrosc. Relat. Phenom. 3 (1974) 417-25.

[46] M.P. Seah, W.A. Dench, Quantitative electron spectroscopy of surfaces: A standard data base for electron inelastic mean free paths in solids, Surf. Interface Anal. 1 (1979) 2-11.

[47] G.A. Somorjai, Chemistry in Two Dimensions: Surfaces, Cornell University Press, Ithaca, 1981.

[48] M.P. Soriaga, Ultra-high vacuum techniques in the study of single-crystal electrode surfaces, Prog. Surf. Sci. 39 (1992) 325-443.

[49] G. Ertl, J. Kuppers, Low Energy Electrons and Surface Chemistry, 1985.

[50] G. Attard, C. Barnes, Surfaces, Oxford University Press Inc., New York, 1998.

[51] B.K. Agarwal, X-ray spectroscopy : an introduction, Springer-Verlag, Berlin, 1991.

[52] C.R. Brundle, A.D. Baker, Electron spectroscopy : theory, techniques and applications Vol.2, Academic Press., London, 1978.

[53] H. Niehus, W. Heiland, E. Taglauer, Low-energy ion scattering at surfaces, Surf. Sci. Rep. 17 (1993) 213-303.

[54] P.A. Redhead, Thermal desorption of gases, Vacuum 12 (1962) 203-11.

[55] C.J. Jenks, R. Bastasz, Probing the surface structure of quasicrystals via angle-resolved low-energy ion scattering, Prog. Surf. Sci. 75 (2004) 147-60.

[56] R.A. Campbell, D.W. Goodman, A new design for a multitechnique ultrahigh vacuum surface analysis chamber with high pressure capabilities, Rev. Sci. Instrum. 63 (1992) 172-4.

[57] D. Kumar, M.S. Chen, D.W. Goodman, Characterization of ultra-thin TiO2 films grown on Mo(112), Thin Solid Films 515 (2007) 1475–9.

[58] J.A. Venables, G.D.T. Spiller, M. Hanbucken, Nucleation and growth of thin films, Rep. Prog. Phys. 47 (1984) 399-459.

[59] M.S. Daw, S.M. Foiles, Order-Disorder Transition of Au and Pt (110) Surfaces: The Significance of Relaxations and Vibrations, Phys. Rev. Lett. 59 (1987) 2756-9.

[60] E.C. Sowa, M.A. Van Hove, D.L. Adams, The missing-row model for the reconstructed Pt(110)−(1 × 2) surface: A leed intensity analysis showing multilayer distortions, Surf. Sci. 199 (1988) 174-82.

[61] J.L. Fernandez, D.A. Walsh, A.J. Bard, Thermodynamic Guidelines for the Design of Bimetallic Catalysts for Oxygen Electroreduction and Rapid Screening by Scanning Electrochemical Microscopy. M-Co (M: Pd, Ag, Au), Journal of the American Chemical Society. 127 (2005) 357.

[62] S. Zhang, X. Yuan, H. Wang, W. Mérida, H. Zhu, et al., A review of accelerated stress tests of MEA durability in PEM fuel cells, Int. J. Hydrogen Energy 34 (2009) 388-404.

[63] V.R. Stamenkovic, B.S. Mun, K.J.J. Mayrhofer, P.N. Ross, N.M. Markovic, Effect of Surface Composition on Electronic Structure, Stability, and Electrocatalytic Properties of Pt-Transition Metal Alloys: Pt-Skin versus Pt-Skeleton Surfaces, J. Am. Chem. Soc. 128 (2006) 8813-9.

[64] R.A. Campbell, J.A. Rodriguez, D.W. Goodman, Chemical and electronic properties of ultrathin metal films: the palladium/rhenium (0001) and palladium/ruthenium (0001) systems, Phys. Rev. B: Condens. Matter 46 (1992) 7077-87.

[65] B.R. Cooper, Electronic Structure of Ultrathin Transition and Noble Metal Films with Simple Metal Interfaces, J. Vac. Sci. Technol. 10 (1973) 713-6.

[66] M. Andersen, O. Lytken, J. Engbæk, G. Nielsen, N. Schumacher, et al., Search for new catalysts from a fundamental basis, Catal. Today 100 (2005) 191-7.

[67] G.A. Somorjai, The puzzles of surface science and recent attempts to explain them, Surf. Sci. 242 (1991) 481-8.

[68] F. Maroun, F. Ozanam, O.M. Magnussen, R.J. Behm, The Role of Atomic Ensembles in the Reactivity of Bimetallic Electrocatalysts, Science 293 (2001) 1811-4.

[69] A.M. El-Aziz, R. Hoyer, L.A. Kibler, D.M. Kolb, Potential of zero free charge of Pd overlayers on Pt(111), Electrochim. Acta 51 (2006) 2518-22.

[70] B. Alvarez, V. Climent, A. Rodes, J.M. Feliu, Potential of zero total charge of palladium modified Pt(111) electrodes in perchloric acid solutions, Phys. Chem. Chem. Phys. 3 (2001) 3269-76.

[71] A.M. El-Aziz, L.A. Kibler, D.M. Kolb, The potentials of zero charge of Pd(1 1 1) and thin Pd overlayers on Au(1 1 1), Electrochem. Commun. 4 (2002) 535-9.

[72] L.A. Kibler, A.M. El-Aziz, D.M. Kolb, Electrochemical behavior of pseudomorphic overlayers: Pd on Au(111), J. Mol. Catal. A: Chem. 199 (2003) 57-63.

[73] R. Hoyer, L.A. Kibler, D.M. Kolb, Electrochemical Pd deposition onto Rh(1 1 1): from cluster to monolayer growth, Surf. Sci. 562 (2004) 275-83.

[74] M.H. Shao, T. Huang, P. Liu, J. Zhang, K. Sasaki, et al., Palladium Monolayer and Palladium Alloy Electrocatalysts for Oxygen Reduction, Langmuir 22 (2006) 10409-15.

[75] L.A. Kibler, M. Kleinert, R. Randler, D.M. Kolb, Initial stages of Pd deposition on Au(hkl) Part I: Pd on Au(111), Surf. Sci. 443 (1999) 19-30.

[76] M.P. Soriaga, Y.-G. Kim, J.E. Soto, Interfacial Chemistry of Palladium Electrodes, in: A. Wieckowski (Ed) Interfacial Electrochemistry: Theory, Experiment, and Applications, Marcel Dekker, New York, 1999, pp. 249-67.

[77] V. Climent, N.M. Markovic, P.N. Ross, Kinetics of Oxygen Reduction on an Epitaxial Film of Palladium on Pt(111)†,‡, J. Phys. Chem. B 104 (2000) 3116-20.

[78] M. Han, P. Mrozek, A. Wieckowski, X-Ray-Photoelectron-Spectroscopy and Auger-Electron-Spectroscopy Study of Ultrathin Palladium Films on a Pt(111) Substrate, Phys. Rev. B: Condens. Matter 48 (1993) 8329-35.

[79] T.J. Schmidt, N.M. Markovic, V. Stamenkovic, P.N. Ross, G.A. Attard, et al., Surface characterization and electrochemical behavior of well-defined Pt-

Pd{111} single-crystal surfaces: A comparative study using Pt{111} and palladium-modified Pt{111} electrodes, Langmuir 18 (2002) 6969-75.

[80] B. Alvarez, A. Rodes, J.M. Perez, J.M. Feliu, Two-dimensional effects on the in situ infrared spectra of CO adsorbed at palladium-covered Pt(111) electrode surfaces, J. Phys. Chem. B 107 (2003) 2018-28.

[81] K. Umezawa, E. Narihiro, Y. Ohta, Y. Ohira, M. Yoshimura, Pd/Pt(111) surface structure and metal epitaxy by time-of-flight impact-collision ion scattering spectroscopy and scanning tunneling microscopy: Does lattice mismatch really determine the growth mode?, Nucl. Instrum. Methods Phys. Res., Sect. B 266 (2008) 1903-7.

[82] I. Pasti, S. Mentus, First principles study of adsorption of metals on Pt(111) surface, J. Alloys Compd. 497 (2010) 38-45.

[83] B.S. Mun, C. Lee, V. Stamenkovic, N.M. Markovic, J.P.N. Ross, A photoemission study of Pd ultrathin films on Pt (111), J. Chem. Phys. 122 (2005) 184712-4.

[84] D.A.J. Rand, R. Wood, Electrosorption characteristics of thin layers of noble metals electrodeposited on different noble metal substrates, J. Electroanal. Chem. Interfacial Chem. 44 (1973) 83-9.

[85] G.A. Attard, A. Bannister, The electrochemical behavior of irreversibly adsorbed palladium on platinum (111) in acid media, J. Electroanal. Chem. Interfacial Chem. 300 (1991) 467-85.

[86] M.J. Llorca, J.M. Feliu, A. Aldaz, J. Clavilier, Electrochemical structure-sensitive behaviour of irreversibly adsorbed palladium on Pt(100), Pt(111) and Pt(110) in an acidic medium, J. Electroanal. Chem. 351 (1993) 299-319.

[87] R. Gómez, A. Rodes, J.M. Pérez, J.M. Feliu, A. Aldaz, Electrochemical and in situ FTIR studies of the CO adsorption at palladium and rhodium multilayers deposited on platinum single crystal surfaces. I. Pt(110) substrate, Surf. Sci. 327 (1995) 202-15.

[88] J. Clavilier, M.J. Llorca, J.M. Feliu, A. Aldaz, Preliminary study of the electrochemical adsorption behaviour of a palladium modified Pt(111) electrode in the whole range of coverage, J. Electroanal. Chem. 310 (1991) 429-35.

[89] A. Al-Akl, G.A. Attard, Anion effects in the UPD of copper on Pd/Pt(111) bimetallic electrodes, J. Phys. Chem. B 101 (1997) 4597-606.

[90] G.A. Attard, R. Price, A. Alakl, Palladium Adsorption on Pt(111) - a Combined Electrochemical and Ultra-High-Vacuum Study, Electrochim. Acta 39 (1994) 1525-30.

[91] J.M. Feliu, B. Alvarez, V. Climent, A. Rodes, Electrochemical properties of Pd/Pt(111) adlayers, Thin Films Preparation, Characterization, Applications, [Proceedings of a Symposium of the American Chemical Society], San Diego, CA, United States, Apr. 1-5, 2001, 2002, pp. 37-52.

[92] M.J. Ball, C.A. Lucas, N.M. Markovic, V. Stamenkovic, P.N. Ross, From sub-monolayer to multilayer - an in situ X-ray diffraction study of the growth of Pd films on Pt(111), Surf. Sci. 518 (2002) 201-9.

[93] N.M. Markovic, C.A. Lucas, V. Climent, V. Stamenkovic, P.N. Ross, Surface electrochemistry on an epitaxial palladium film on Pt(111): surface microstructure and hydrogen electrode kinetics, Surf. Sci. 465 (2000) 103-14.

[94] R. Hoyer, L.A. Kibler, D.M. Kolb, The initial stages of palladium deposition onto Pt(1 1 1), Electrochim. Acta 49 (2003) 63-72.

[95] Y.S. Park, J. Baricuatro, M. Hossain, M.P. Soriaga, Highly-Ordered Ultrathin Pd Films on Pt(111): Electrodeposition and Structural Characterization, ECS Trans. 3 (2007) 65-103.

[96] H. Duncan, A. Lasia, Hydrogen adsorption/absorption on Pd/Pt(1 1 1) multilayers, J. Electroanal. Chem. 621 (2008) 62-8.

[97] Y.-S. Park, J.H. Baricuatro, M.A. Hossain, M.P. Soriaga, Interfacial Structure and Chemistry of Potentiodynamically Electrodeposited Ultrathin Pd Films on Pt(111), ECS Trans. 19 (2009) 25-42.

[98] J.H. Baricuatro, M.A. Hossain, Y.-S. Park, M.P. Soriaga, UHV-EC characterization of ultrathin films electrodeposited on well-defined noble metals. I: Pd on Pt(111), Electrocatalysis 1 (2010) 28-33.

[99] Y.S. Park, Well-defined ultrathin palladium films on platinum(111): Electrochemical preparation and interfacial chemistry [Dissertation], Texas A&M University, College Station, 2005.

[100] H.D. Young, A.L. Ford, F.W. Sears, M.W. Zemansky, R.A. Freedman, University physics : with modern physics, Pearson Addison-Wesley, San Francisco, 2008.

[101] H. Gerischer, Advances in Electrochemistry and Electrochemical Engineering, Vol. 13, Wiley-Interscience, New York, 1984.

[102] P.J. Estrup, E.G. McRae, Surface studies by electron diffraction, Surf. Sci. 25 (1971) 1-52.

[103] G.A. Somorjai, Introduction to surface chemistry and catalysis, Wiley, New York 1994.

[104] M.A. Van-Hove, Low-energy electron diffraction : experiment, theory, and surface structure determination, Springer, Berlin, 1986.

[105] E. Conrad, Chapter 7 Diffraction methods, in: W.N. Unertl (Ed) Handbook of Surface Science, North-Holland, Amsterdam, 1996, pp. 271-360.

[106] FIZ/NIST, ICSD.

[107] S.U. Jen, Effect of atomic order on some physical properties of Co25Pt75, J. Alloys Compd. 234 (1996) 231-4.

[108] J. Häglund, Theory of bonding in transition-metal carbides and nitrides, Phys. Rev. B: Condens. Matter 48 (1993) 11685-91.

[109] H.E. Swanson, Standard X-ray diffraction powder patterns, University of Michigan Library, Ann Arbor, MI, 1953.

[110] E.A. Wood, Vocabulary of Surface Crystallography, J. Appl. Phys. 35 (1964) 1306-10.

[111] L.B. Leder, J.A. Simpson, Improved electrical differentiation of retarding potential measurements, Rev. Sci. Instrum. 29 (1958) 571-4.

[112] L.E. Davis, N.C. MacDonald, P.W. Palmberg, G.E. Riach, R.E. Weber, Handbook of Auger Electron Spectroscopy, Second ed., Physical Electronics Division, Perkin-Elmer Corp., Eden Prairie, 1978.

[113] D. Briggs, M.P. Seah, Practical Surface Analysis by Auger and X-ray Photoelectron Spectroscopy, John Wiley & Sons, New York, 1983.

[114] T.C. O'Haver, Lock-in amplifiers. I, J. Chem. Educ. 49 (1972) A131-A2, A4.

[115] T.C. O'Haver, Lock-in amplifiers. II, J. Chem. Educ. 49 (1972) A11-A2, A214, A8, A20, A22.

[116] E.A. Lafferty, Surface Electrochemical Studies of Pd Thin Films Electrodeposited at Pt Electrode Surfaces [Dissertation], Texas A&M University, College Station, 1999.

[117] T. Abe, G.M. Swain, K. Sashikata, K. Itaya, Effect of underpotential deposition (UPD) of copper on oxygen reduction at Pt(111) surfaces, J. Electroanal. Chem. 382 (1995) 73-83.

[118] J. Clavilier, The role of anion on the electrochemical behaviour of a {111} platinum surface; an unusual splitting of the voltammogram in the hydrogen region, J. Electroanal. Chem. 107 (1980) 211-6.

[119] A.T. Hubbard, R.M. Ishikawa, J. Katekaru, Study of platinum electrodes by means of electrochemistry and low-energy electron diffraction: Part II. Comparison of the electrochemical activity of Pt(100) and Pt(111) surfaces, J. Electroanal. Chem. 86 (1978) 271-88.

[120] M. Nakamura, Y. Sakurai, M. Ito, Sulfate and CO surface complexes formation with upd copper on Pd(111) and Pt(111) electrode surfaces: abnormal

vibrational frequency shifts of CO and sulfate during upd processes, J. Electroanal. Chem. 563 (2004) 63-9.

[121] A. Al-Akl, G.A. Attard, Anion Effects in the UPD of Copper on Pd/Pt(111) Bimetallic Electrodes, J. Phys. Chem. B 101 (1997) 4597-606.

[122] E. Herrero, L.J. Buller, H.D. Abruña, Underpotential Deposition at Single Crystal Surfaces of Au, Pt, Ag and Other Materials, Chem. Rev. 101 (2001) 1897-930.

[123] H. Ogasawara, J. Inukai, M. Ito, Ex-situ IRAS and LEED studies of underpotentially deposited copper on a Pt(111) electrode in a sulfuric acid solution: layer exchanges of anions with copper, Surf. Sci. 311 (1994) L665-L70.

[124] K. Sashikata, N. Furuya, K. Itaya, In situ scanning tunneling microscopy of underpotential deposition of copper on platinum(111) in sulfuric acid solutions, J. Electroanal. Chem. 316 (1991) 361-8.

[125] Y. Shingaya, H. Matsumoto, H. Ogasawara, M. Ito, In situ and ex situ IRAS, LEED and EC-STM studies of underpotentially deposited copper on a Pt(111) electrode in sulfuric acid solution: coadsorption of sulfate ion with copper, Surf. Sci. 335 (1995) 23-31.

[126] J. Okada, J. Inukai, K. Itaya, Underpotential and bulk deposition of copper on Pd(111) in sulfuric acid solution studied by in situ scanning tunneling microscopy, Phys. Chem. Chem. Phys. 3 (2001) 3297-302.

[127] J.A. Schimpf, J.B. Abreu, M.P. Soriaga, K. Sashikata, K. Itaya, Iodine-catalyzed dissolution of Pd(100) in inert electrolyte: studies by LEED, AFS, STM and electrochemistry, Proc. - Electrochem. Soc. 96-8 (1996) 180-8.

[128] J.A. Schimpf, J.B. Abreu, M.P. Soriaga, Absorbate-catalyzed dissolution in inert electrolyte: layer-by-layer corrosion of palladium(100)-c(2 * 2)-iodine, Langmuir 9 (1993) 3331-3.

[129] E.A. Lafferty, Y.-G. Kim, M.P. Soriaga, Selective and quantitative removal of Pd films from Pt substrates by adsorbed-iodine-catalyzed anodic stripping, Electrochim. Acta 44 (1998) 1031-6.

[130] M. Wasberg, L. Palaikis, S. Wallen, M. Kamrath, A. Wieckowski, Leed / auger verification of the in situ method of preparation of Pt (111) single crystal electrodes, J. Electroanal. Chem. 256 (1988) 51-63.

[131] T. Hachiya, H. Honbo, K. Itaya, Detailed underpotential deposition of copper on gold(III) in aqueous solutions, J. Electroanal. Chem. Interfacial Chem. 315 (1991) 275-91.

[132] Z. Shi, J. Lipkowski, Coadsorption of Cu2+ and SO42- at the Au(111) electrode, J. Electroanal. Chem. 365 (1994) 303-9.

[133] I.M. Tidswell, C.A. Lucas, N.M. Markovicacute, P.N. Ross, Surface-structure determination using anomalous x-ray scattering: Underpotential deposition of copper on Pt(111), Phys. Rev. B: Condens. Matter 51 (1995) 10205–8.

[134] A.I. Danilov, E.B. Molodkina, Y.M. Polukarov, V. Climent, J.M. Feliu, Active centers for Cu UPD-OPD in acid sulfate solution on Pt(111) electrodes, Electrochim. Acta 46 (2001) 3137-45.

[135] Z. Shi, J. Lipkowski, Investigations of SO42- adsorption at the Au(111) electrode in the presence of underpotentially deposited copper adatoms, J. Electroanal. Chem. 364 (1994) 289-94.

[136] R. Vasilic, L.T. Viyannalage, N. Dimitrov, Epitaxial growth of Ag on Au(111) by galvanic displacement of Pb and Tl monolayers, J. Electrochem. Soc. 153 (2006) C648-C55.

[137] C. Gabrielli, P.P. Grand, A. Lasia, H. Perrot, Investigation of Hydrogen Adsorption and Absorption in Palladium Thin Films, J. Electrochem. Soc. 151 (2004) A1937-A42.

[138] M. Baldauf, D.M. Kolb, A hydrogen adsorption and absorption study with ultrathin Pd overlayers on Au(111) and Au(100), Electrochim. Acta 38 (1993) 2145-53.

[139] A.I. Danilov, E.B. Molodkina, Y.M. Polukarov, V. Climent, J.M. Feliu, Active centers for Cu UPD–OPD in acid sulfate solution on Pt(111) electrodes, Electrochim. Acta 46 (2001) 3137-45.

[140] J. Souza-Garcia, A. Berna, E.A. Ticianelli, V. Climent, J.M. Feliu, Electrochemical properties of palladium adlayers on Pt(110) substrates, J. Electroanal. Chem. 660 (2011) 276-84.

[141] M.J. Lundwall, S.M. McClure, D.W. Goodman, Probing Terrace and Step Sites on Pt Nanoparticles Using CO and Ethylene, J. Phys. Chem. C 114 (2010) 7904-12.

APPENDIX A

THE STRUCTURE, COMPOSITION AND REACTIVITY OF CLEAN AND AMBIENT-EXPOSED POLYCRYSTALLINE AND MONOCRYSTALLINE Mg SURFACES*

JUAN B. ABREU[1], JEAN SANABRIA-CHINCHILLA[1], KYLE D. CUMMINS[1],

JOHN L. STICKNEY[2] AND MANUEL P. SORIAGA[1]

[1]Department of Chemistry, Texas A&M University, College Station, TX 77843

[2]Department of Chemistry, University of Georgia, Athens, GA 30602

Journal of Electroanalytical Chemistry

Volume 662, Issue 1, 1 November 2011, Pages 36–42

Special Issue in Honour of A. Wieckowski

ABSTRACT

The present article recounts previous studies on the structure, composition and reactivity of polycrystalline and single-crystal magnesium surfaces, previously exposed to the environment and regenerated to pristine conditions in ultrahigh vacuum. Experimental measurements relied on electron spectroscopy (X-ray photoelectron spectroscopy, Auger electron spectroscopy and low-energy electron diffraction), temperature-programmed mass spectrometry and atomic force microscopy. Reaction-chemistry investigations were primarily with gas-phase reagents although selected treatments in aqueous or ethereal electrolyte were also undertaken. The results obtained have direct relevance in the description of the corrosion characteristics of this industrially important metal. It was found that: (i) The surface of air-exposed Mg is comprised of predominantly magnesium hydroxide with a small amount of magnesium bicarbonate. (ii) Oxidation of a clean Mg(0001) surface by increasing dosages of $O_{2(g)}$ procedes through a (1x1) oxygen layer, followed by a disordered metal-oxide, and finally the generation of a MgO(100)-on-Mg(0001) adlattice. (iii) Exposure of Mg(0001) to $H_2O_{(g)}$, results in a disordered hydroxylated surface. (iv) Carbonation of a clean Mg(0001) surface by increasing dosages of $CO_{2(g)}$ procedes through first, a pseudomorphic adlayer, and finally results in a disordered carbonaceous film. (v) Exposure of an oxide-coated Mg(0001) surface to $H_2O_{(g)}$ yielded a disordered hydroxylated surface. (vi) In regard to Grignard chemistry, treatment of oxided Mg with HCl substantially reduces the amount of surface oxide, resulting in a magnesium chloride film.

KEY WORDS:

Magnesium Corrosion

Reactivity of Clean and Oxidized Magnesium Surfaces

Mg(0001) Single-crystal Surfaces

Surface Chemistry of Magnesium

Grignard Reaction

INTRODUCTION

Magnesium and its alloys have long enjoyed a niche both in science research and in engineering applications. From a basic-science perspective, an important facet of Mg is that it is the active site in Grignard reagents, RMgX (where R is a hydrocarbon and X is a halogen), versatile reactants in organic chemical synthesis [1]. From an applied-engineering point of view, Mg is a low-density structural material that is quite attractive in industries where weight is a major concern. However, magnesium is also a rather reactive metal; hence, it will be important to document its surface characteristics if the critical parameters that would only serve to limit its usability are to be identified.

Our primary research interest in magnesium lies in the heterogeneous (solid-solution) reaction between an alkyl halide and magnesium to generate the Grignard reagent. The reaction presumes the presence of *pure* Mg metal devoid of surface-film contaminants. Such a condition, however, is never satisfied with off-the-shelf Mg due to its aggressive chemistry. In Grignard-reagent formation, therefore, the reaction between Mg and the alkyl halide must take place despite the presence of the inert surface films. The use of promoters for the activation of the surface-impure Mg has been advocated [2-5] on the premise that the promoters are able to etch the film-encrusted surface to generate pure-metal sites. The role of promoters, however, can never be exactly defined unless the chemical nature of the surface films is known in sufficient detail.

It is in this context that a series of studies on the surface structure, surface

composition and surface reactivity of Mg, ambient-exposed, chemically pre-treated and re-purified, was undertaken. The present paper recounts the work performed and the results obtained.

EXPERIMENTAL

Unless indicated otherwise, experiments were performed in an ultrahigh vacuum (10^{-10} torr base pressure) apparatus equipped with low energy electron diffraction (LEED) optics (Perkin-Elmer, Eden Prairie, MN), a cylindrical mirror analyzer (Perkin-Elmer, Eden Prairie, MN) for Auger electron spectroscopy (AES), and a quadruple mass analyzer (UTI Instruments Company, Sunnyvale, CA) for temperature-programmed desorption. X-ray photoelectron spectroscopy (XPS) measurements were carried out with a Perkin-Elmer PHI 5500 ESCA spectrometer (Perkin-Elmer, Eden Prairie, MN) using a Mg $K\alpha_{1,2}$ source at a 42° take-off angle, and 0.65-eV instrumental resolution. The primary interest in XPS was the ability it permitted for the speciation of the surface-film components; for example, whether the films are constituted only of oxides, or if they include hydroxide, carbonate, and/or bicarbonate species. Earlier work [6] had demonstrated that: (i) the O 1s binding energy (E_B) for surface oxide is 2 eV lower than that for surface hydroxide, and (ii) the C 1s E_B for CO_3^{2-} is 1 eV lower than for HCO_3^-.

An oxide-coated Mg surface is a poor electrical conductor; hence, atomic force microscopy (AFM) was utilized instead of scanning tunneling microscopy. Experiments were performed with a Nanoscope III AFM (Digital Instruments, Santa Barbara, CA) equipped with a gold-plated Si_3N_4 cantilever. A custom-made AFM fluid cell was fabricated from glass and Teflon® to mitigate contamination from viton-ring seals built into the commercial cell. The AFM

apparatus was enclosed in an air-tight Plexiglas compartment that was continuously purged with Ar gas.

The 99%-pure polycrystalline Mg foils (Aldrich Chemicals, Milwaukee, WI) were metallographically polished (Buehler, Lake Bluff, IL) prior to use. The polished surfaces were washed and cleaned only with diethyl ether although no extra precautions were taken to ensure that the nonaqueous solvent remained anhydrous. The polishing was done in air for about 30 minutes which means that exposure to atmospheric water vapor could not be avoided. Samples to be acid-etched were simply immersed for 30 seconds in 6% HNO_3 solution followed by a thorough rinse with Milli-Q Plus™ water (Millipore Systems, Houston, TX)). Samples of 98%-pure magnesium turnings (Aldrich Chemicals) were used as received.

All heat treatments were done in a Lindberg 55035 furnace (Lindbergh, Watertown, WI); the samples were placed on a ceramic holder and subjected to a flow of dry nitrogen (Matheson, Laporte, TX) throughout the four-hour heat treatment. The Mg samples were not heated above 450°C to prevent melting and to minimize sublimation of the metal.

For single-crystal work, a 99.999%-pure, crystallographically oriented (± 0.5°) and metallographically polished Mg (0001) single crystal. Sharp diffraction spots were obtained only after Ar^+-ion bombardment (1 kV, 15 mA/cm^2) for at least 24 hours; this drastic pretreatment, unfortunately, lead the crystal to lose its original metallic luster. Thermal annealing at 200°C restored the atomic

smoothness, as evidenced by sharp LEED patterns, but did not regenerate the original mirror finish.

The UHV-prepared clean surfaces were exposed to calibrated doses of O_2 (99.997%, Airco Industrial Gases, Murray Hill, NJ), H2O(g) (Milli-Q Plus™), CO_2 (99.99%, Airco Industrial Gases) at ambient temperatures; exposures ranged from 0.5 Langmuir (L) to 5×10^3 L. The partial pressure of these gases was measured using the quadruple mass analyzer and the measured exposures reported here represent the product of the exposure time and the partial pressure. For exposures from 0.5 to 2 L, the partial pressure was always 5.0×10^{-9} torr; for those higher than 10 L, the partial pressure was increased in steps up to 1×10^{-6} torr while the exposure time was maintained constant at 1000 s.

Reference spectra for MgO (98%; Aldrich Chemicals), $Mg(OH)_2$ (95%; Aldrich Chemicals), Na_2CO_3 (99%; Fisher Scientific, Plano, TX) and $NaHCO_3$ (99%; Fisher Scientific) were obtained by placing a few milligrams of the "as-received" analyte onto the spectrometer sample holder.

RESULTS AND DISCUSSION

Polycrystalline magnesium

The results from our single-crystal studies should be viewed in light of those obtained on polycrystalline Mg. In order to maintain this continuity, our results on polycrystalline Mg have been restated here. The original work can be found in reference 20 and all figures pertinent to these results can be found in said reference. For ease of assimilation all figure numbers in this discussion correspond 1:1 with those in reference 20. The oxygen 1s X-ray photoelectron spectra of solid $Mg(OH)_2$ before and after heat-treatment are shown in reference 20, fig. 1 (R20,F1). It can be seen that, whereas only a single peak is present for the as-received sample, two peaks separated by 2 eV are clearly discernible after the heat treatment. Based upon literature data [6], the higher E_B value is assigned to surface hydroxyl species, while the lower E_B value is attributed to surface oxide. The data in R20, F1 show that a high-temperature treatment of solid $Mg(OH)_2$ results in the dehydration of the interfacial hydroxide to the oxide.

In a separate similar experiment, carried out to generate another set of reference spectra, O 1s XPS spectra were obtained for solid MgO as received, after heat-treatment, and after re-exposure to air. The results are shown in R20, F2. It is interesting to note that the surface of the air-exposed MgO consists predominantly of hydroxides. High-temperature treatment yields the surface oxide although an appreciable quantity of surface hydroxyl remains. Exposure

of the post-heated MgO to air for about 48 hours partially regenerates the surface hydroxides; much longer exposures (ca. 4 days) to ambient environments yield spectra identical to the "as-received" sample.

Based upon the set of results shown in R20, F1-F2, the surface compositions of polycrystalline Mg foils "activated" either by metallographic polishing or via an acid-etch were determined. R20, F3 displays the O 1s XPS spectra for a HNO_3-etched Mg foil. As should be expected, since the reaction is carried out in an aqueous solution, only one peak, that due to surface hydroxyls, appears in the spectrum for the etched surface. When the crystal was then heated to 450°C, significant conversion to the oxide form was indicated by the new spectrum. Subsequent re-exposure to air showed the propensity of the oxided material to re-hydrate and form surface magnesium hydroxide.

The O 1s XPS data that pertain to the metallographically polished Mg crystal are shown in R20, F4. The results are congruous to those obtained for the acid-etched metal in the sense that: (i) only one peak (hydroxyl oxygen) is observed immediately after polishing, (ii) the hydroxides are dehydrated to the oxide form upon prolonged heating at 450°C, and (iii) the hydroxides are regenerated after the heat-produced surface oxide is re-exposed to air at room temperature.

Whereas the appearance of only the hydroxyl peak may not have been unexpected for the acid-etched material, it is rather surprising in the case of the unetched foil simply because O_2 is present in air at much higher quantities than water vapor. This may mean that the diethyl ether, which was handled in air,

was not absolutely anhydrous; or that a thirty-minute air-exposed polishing completely converted the initially-formed oxide to hydroxide. Other experiments, such as one which showed that complete re-hydration of the heat-treated sample did not transpire until after four days, point to the former as the most likely scenario.

The question of carbonates present in the hydroxide layer, due to absorption of atmospheric CO_2, was also addressed. Experiments were carried out in which C 1s XPS spectra were obtained for commercial Mg turnings before and after heating; the spectra were then compared with those for sodium bicarbonate and sodium carbonate. The results are presented in R20, F5. It can be seen that the hydroxylated (as-received) Mg turnings exhibit two peaks: One, at the lower E_B value, is characteristic of "adventitious" hydrocarbon; the other is due to bicarbonate carbon. That HCO_3^-, and not CO_3^{2-}, is present on the surface is indicated by comparison of the spectrum for Mg with those for reference $NaHCO_3$ and Na_2CO_3 solids: the C 1s E_B for CO_3^{2-} is lower than that for HCO_3^- and only the higher E_B peak is observed for the Mg turnings. The data in R20, F5 also show that interfacial CO_2 can be eliminated by prolonged heating at 450°C.

It is important to note that, although the presence of HCO_3^- in the surface film of air-exposed Mg has been established, only less than 25% of it actually exists in the near-surface layers. This conclusion can be arrived at by comparison of the areas under the O 1s (not shown in R20, F5) and C 1s peaks, corrected for the differences in the scattering cross-sections for the O and C atoms.

The results described here indicate that any detailed mechanism for the reaction of an air-exposed Mg metal with an alkyl halide must address the existence of a multilayer surface film composed predominantly of magnesium hydroxide and a small but appreciable quantity of magnesium bicarbonate.

Monocrystalline Mg(0001)

Initial pretreatments

The post-polished oriented Mg(0001) crystal contained residues of the polishing wax. Removal of the latter required immersion in acetone for at least six hours. The sample was then etched in 6% aqueous HNO_3 for several minutes, rinsed with pure water, and mounted into the UHV-EC system. A cursory LEED and AES examination indicated, as expected, a non-crystalline oxide coating on the surface. Heat treatment to 250°C resulted in neither ordering nor removal of the oxide film; no work was done at higher temperatures since, in ultrahigh vacuum, Mg sublimes without immediate changes in the amount of surface oxide.

A sequence of experiments was then performed to determine the reactivity of this ambient-environment-generated oxide film. The results, in terms of AES data, are summarized in Figure 1. In this context, it is first important to mention that the Auger spectrum of a clean Mg(0001) surface is characterized by a large Mg($L_{23}VV$) Auger peak at 45 eV. For pure surface oxide, a signal at 27 eV [$Mg^{2+}(L_{23})O(L_1)Mg(V)$] is diagnostic; for a fully oxided surface, the two prominent peaks, $Mg(L_1)O(L_1)O'(L_1)$ (35 eV) and $O(KL_{23}L_{23})$ (505 eV) are identical to those for bulk MgO [7,8].

Figure 1A: Under an Ar atmosphere, the Mg crystal was dipped in a 6% aqueous HNO3 solution for 3 minutes and then rinsed with pure water. No LEED pattern was obtained. In the AES spectrum, only peaks characteristic of bulk-like MgO [7,8] were found. It is most likely that the initial surface oxide was etched by the acid but that a new oxide was formed during the water rinse. Solid $Mg(NO_3)_2$, produced from a $MgO_{(s)}$-$HNO_{3(aq)}$ acid-base reaction, is retained on the surface if the water rinse is omitted.

Figure 1B: The oxided Mg crystal was ion-bombarded with a custom-built ion "cage" (similar to a Bayerd-Alpert gauge except that the single-crystal sample is at the center) at 10 μA cm^{-2} for 6 hours and then annealed at 250°C. No LEED pattern was observed and, except for the appearance of a small Ar peak at ca. 200 eV, the resulting Auger spectrum was identical to that shown in Figure 1A. Evidently, ion-bombardment under these conditions is insufficient to remove the oxide crust; in fact, a small but detectable extent of Ar^+-ion implantation occurred.

Figure 1C: Under an Ar atmosphere, the crystal was dipped in a 6% aqueous HBr solution for 30 seconds. Under such short exposure time, it was deemed that retention of $MgBr_2$ [from the $MgO_{(s)}$-$HBr_{(aq)}$ acid-base reaction] at the surface would be minimal, an expectation that was verified by comparison with a crystal dipped in $MgBr_2$-saturated ether; hence, without any water-rinse, the crystal was immediately transferred into the surface analysis chamber. As before, no LEED pattern was generated. However, a diminution of the MgO-related peaks was found, accompanied by the appearance of an appreciable Br

signal. An acid-base reaction is clearly implied by the data.

Figure 1D: Immersion of the $HBr_{(aq)}$-reacted surface in pure water removed the (imbedded) bromide salt and restored the full oxide coating. The oxided crystal was then dosed with HCl gas at 10^{-5} torr for 3 minutes. Although no LEED pattern was obtained, a significant change in the AES spectrum was observed: the characteristic MgO peaks were diminished and a prominent Cl signal emerged. These results serve to establish an acid-base reaction between the oxide film and the HCl gas.

Figure 1E: While in the electrochemistry chamber under an Ar atmosphere, a fully oxided Mg single-crystal was dipped in an anhydrous ethereal 1.0 *M* HCl solution for 3 minutes. The solution turned cloudy and was flushed out with a fresh aliquot; immersion was extended for another 3 minutes. No LEED pattern could be discerned but the amount of surface oxide was greatly diminished; in addition, an unusually large Cl signal was generated. In this experiment, it appears that the ethereal HCl reacted with the surface oxide to expose metallic Mg. Re-oxidation of the latter was largely prevented by the anhydrous medium. Cl was then chemisorbed on the oxide-free Mg surface.

Figure 1F: As a final treatment, the fully oxided crystal was sputter-cleaned using a commercial (line-of-sight) ion gun for 24 hours at 20 μA cm-2. The face of the crystal in front of the ion gun regained its original metallic luster, in sharp contrast to the opacity of the back side which could not be subjected to the direct ion bombardment. The Auger spectrum now showed only a large Mg peak; the O signal was no longer observed. After annealing at 200°C, a distinct

(1×1) LEED pattern was finally observed (*vide infra*).

Atomic Force Microscopy

A Mg(0001) surface pre-exposed to air was placed in the AFM fluid cell and immersed for 10 minutes in an aqueous 6% HNO_3 solution; the aim was to dissolve the native oxide crust. The etched crystal was then flushed with pure water and an AFM image, in the presence of water, was obtained. This image, shown in Figure 2A, is characterized by atomic-scale rows; Fourier transformation of the image (Figure 2B) indicated a periodicity of 0.34 nm.

It is certain that, based upon the UHV results, an oxide-free Mg cannot result from exposure of metallic Mg to water. Hence, the periodicity derived from the AFM image cannot be due to the interatomic distance in metallic Mg, 0.32 nm [9]. It is likewise not reasonable to identify the structure with bulk-like MgO, not only because water dosing in UHV does not generate the O_2-induced Mg(0001)-Mg(100) pattern, but also because the Mg-O distance in MgO is 2.1 nm [9]. It would be more plausible to postulate a surface species based upon $Mg(OH)_2$. In the bulk, solid $Mg(OH)_2$ is hexagonal with a lattice parameter, in the basal plane, of 0.32 nm; the latter value is not too different from the AFM-measured periodicity.

The absence of distinct LEED spots in the water-dosed surface and the presence of a periodic structure in the AFM image suggests that localized ordering in hydrous-oxide-coated Mg may exist in domains less than 10 nm x 10 nm in area, the minimum required to obtain discernible LEED patterns [10].

Exposure to $O_{2(g)}$

The AES spectrum of the UHV-prepared clean Mg (0001) single crystal surface is characterized by a prominent Mg($L_{23}VV$) peak at 45 eV [8, 11-13]. The uptake of oxygen on the clean surface was monitored via the changes in the intensities of the following Auger lines: (i) metallic Mg($L_{23}VV$), (ii) metal-oxide $Mg^{2+}(L_{23})O(L_1)Mg(V)$, and (iii) oxide $Mg(L_{23})O(L_{23})O(L_{23})$ and (iv) oxygen $O(KL_{23}L_{23})$.

Figure 3 shows the changes in the derivative Auger spectra of Mg (0001) as a function of the O_2 dosage. It can be noted that exposure of the clean surface to increased doses of O_2 results in the attenuation of the 45-eV Auger transition and the simultaneous growth of the 34-eV oxide and 510-eV oxygen transitions. In addition, a new peak at 27 eV emerges. The latter has been proposed to arise from the cross-over transition involving levels from the oxygen and from the metal at the oxide-metal "interface" [12]; it becomes discernable at 0.5 L O_2 and reaches a maximum intensity at ca. 3 L O_2 exposure. Maximum intensity is attained when the Mg(0001) surface is covered with an ultrathin MgO film but before the formation of bulk MgO. In other words, formation of the bulk oxide layer commences at $O_{2(g)}$ exposures above 3 L.

Figure 4 shows the peak-to-peak heights of the Mg($L_{23}VV$) transition, normalized to that of the clean magnesium signal, as a function of $O_{2(g)}$ exposure. Three stages in the oxidation of magnesium may be discerned from the data in Figure 4; these stages are designated as R_1, R_2, and R_3. In the initial stages, (0 - 3 L O_2), the O_2 molecules are dissociatively chemisorbed on the magnesium surface; this is then followed by oxide nucleation and island-formation. The

second stage occurs between 3 to 10 L of $O_{2(g)}$ exposure and leads to the formation of the surface metal oxide. In the third stage, at O_2 doses greater than 10 L, thickening of the oxide film results. These processes are as observed from previously reported work on magnesium [14-16].

In order to gain better insight on the rate of oxygen uptake by the magnesium sample, the intensity of the $O(KL_{23}L_{23})$ peak was monitored as a function of O_2 dosage; the results are shown in Figure 5 in terms of the AES peak-to-peak height ratio, $\frac{O(KL_{23}L_{23})}{Mg(L_{23}VV)}$. In this oxygen-uptake curve, the logarithmic dependence of the oxide intensity on O_2 dosage is evident above 10 L. It can also be seen that the surface is independent of the partial pressure of $O_{2(g)}$ as the plots are invariant when P_{O_2} is increased from 5×10^{-9} to 1×10^{-8} torr. The independence of the rate of oxidation on the partial pressure of O_2 suggests that the oxidation process is limited by the diffusion of the metal cations through the oxide film; that is, from the metal/oxide interface to the oxide/gas interface. Similar results were reported earlier for the oxidation of polycrystalline magnesium by water vapor [17].

The LEED patterns obtained at selected stages of the surface oxidation are shown in Figure 6. The sharp LEED pattern of the clean surface (Figure 6A) is as expected of the six-fold symmetry of the Mg (0001) surface. At low oxygen exposure (< 0.5 L O_2), an increase in the background intensity and broadening of the integral-index spots are observed, (Figure 6B). The diffuseness of the LEED pattern is evidently due to the formation of a chemisorbed (1x1) oxygen overlayer. Upon further oxygen exposure (> 3 L), a different LEED pattern

emerged (Figure 6C) characterized not only by broader integral-index spots, but also by a new set of (diffuse) diffraction spots rotated 30° with respect to the substrate unit cell. This rotated hexagonal structure was observed earlier [13] but was explained as due to a superposition of Mg(0001)-(1×1) and Mg(0001)-(1×1)-R30°-Mg0(111). At an O_2 dosage of 10 L, a LEED pattern is generated that is decidedly more distinct (Figure 6D). The data in Figure 6D was interpreted earlier as due to a square lattice of MgO(100) growing epitaxially in three equivalent domains in the Mg(0001) surface [15]. We concur with this interpretation.

The dependence on the temperature of the LEED pattern in Figure 6D was determined up to 250°C. At 125°C, the intensity and sharpness of the spots remained unaltered. In the range of 150 - 200°C, the spots became more distinct but, the LEED pattern deteriorated above 200°C due to sublimation of the Mg substrate. No desorption of oxygen was detected during the thermal treatment.

Exposure to $H_2O_{(g)}$

The clean Mg (0001) surface was exposed to increasing calibrated doses of water vapor up to 100 L. Surface reactions were monitored, as described above, in terms of the oxygen uptake. The AES spectra obtained after the $H_2O_{(g)}$ exposure were identical to the one obtained after exposure to $O_{2(g)}$; that is, an oxygenated surface was formed when the surface was exposed to water vapor. However, the rate of the oxidation reaction was much slower with water vapor than with $O_{2(g)}$.

Figure 7 shows a plot of the AES peak-to-peak intensity ratio, $\frac{O(KL_{23}L_{23})}{Mg(L_{23}VV)}$, as a function of $H_2O_{(g)}$ exposure. In this oxygen-uptake plot, the three stages of surface oxidation exhibited by an $O_{2(g)}$-dosed Mg surface were not observed. The differences between the data in Figures 10 (O_2 exposure) and 12 (H_2O exposure) are most probably due to the fact that the surface layers in both cases have different structures and compositions.

The oxidation of magnesium surfaces by water vapor has been investigated in other laboratories [18-20], but the issue of surface composition has not been resolved. It has been suggested [18] that the film contain appreciable amounts of hydroxylated species; another suggestion was that the film is constituted by only MgO [19]. Neither of the studies investigated the adlattice structure of the $H_2O_{(g)}$-exposed surface.

In the present investigation, we characterized the $H_2O_{(g)}$-exposed surface via LEED. We noted that upon $H_2O_{(g)}$ exposure, the LEED pattern for the clean surface became diffuse. Contrary to what was observed for the $O_{2(g)}$-exposed Mg, the same degree of diffuseness was shown throughout the entire range (1 - 100 L) of water vapor exposure. The difference in the structures of the film obtained after O_2 and $H_2O_{(g)}$ exposure suggests that the compositions of the two oxided films are not the same.

Based upon X-ray photoelectron spectroscopic measurements, we recently reported that, at least for polycrystalline Mg, the presence of water vapor led to the formation of hydroxylated surface species [20].

Exposure to CO_2

CO_2 adsorption on Mg(0001) was monitored in terms of Mg($L_{23}VV$), O($KL_{23}L_{23}$) and C($KL_{23}L_{23}$) AES transitions. Figure 8A, as well as the changes in the LEED patterns, marked the oxygen-uptake of the surface as the exposure to CO_2 was increased up to 5000 L. The oxidation rate was quite slow compared with those for exposures to O_2 and H_2O(g). Figure 7B shows the AES peak-to-peak intensity ratios, C/Mg and O/Mg, normalized to the O/Mg intensity at 2500 L (*cf.*, Figure 8A). Since the C-to-O ratio is constant at all dosages, the data in Figure 8B demonstrates that exposure of Mg(0001) to CO_2 yields a carbonaceous oxide film. Carbonates and/or oxalates are possibilities.

Also indicated in Figure 8A are the regions where the LEED patterns are diffuse or simply non-existent (i.e., totally disordered structure). LEED patterns obtained during the initial exposure (500 L CO_2) were characterized by sharp spots of the same symmetry as those for the clean surface. At higher dosages, no extra spots resulted but the integral-index spots became considerably broadened. At still higher exposures (2500 L), the LEED pattern completely disappeared; this is probably due to formation of an amorphous magnesium carbonate and/or oxalate.

CONCLUSION

The present article describes results from studies on the structure, composition and reactivity of polycrystalline and single-crystal magnesium surfaces, previously exposed to the environment and regenerated to pristine conditions in ultrahigh vacuum. Experimental measurements relied on electron spectroscopy, mass spectrometry and atomic force microscopy. Reaction-chemistry investigations were primarily with gas-phase reagents although selected treatments in aqueous or ethereal electrolyte were also undertaken. The more significant observations: (i) Air-exposed Mg invariably formed a surface film composed predominantly of magnesium hydroxide but with a detectable quantity of magnesium bicarbonate. (ii) The exposure of a clean Mg(0001) surface to gradually increased dosages of $O_{2(g)}$ initially yielded a (1×1) oxygen layer that suffered surface disorder at the incipient stages of metal-oxide formation; eventually, an epitaxial MgO(100)-on-Mg(0001) adlattice was generated. (iii) Exposure of Mg(0001) to $H_2O_{(g)}$, regardless of the dosage applied, resulted in a non-ordered hydroxylated surface. (iv) Upon exposure of a clean Mg(0001) surface to $CO_{2(g)}$, an ordered carbonaceous oxide film was initially found; at much higher dosages, the pseudomorphic adlayer was transformed into a totally disordered film. (v) Exposure of an oxide-coated Mg(0001) surface to $H_2O_{(g)}$ yielded a disordered hydroxylated surface. (vi) With pertinence to Grignard chemistry, treatment of the oxided metal with either gaseous or (anhydrous) ethereal HCl enforced an acid-base reaction that led to a substantial reduction in the amount of surface oxide and the concomitant accumulation of a

metal-chloride film.

ACKNOWLEDGMENTS

Acknowledgment is made to The Welch Foundation (A-1064) for support of the work. Dr. J.-J. Jeng, Dr. J. E. Soto and Dr. T. L. Wade assisted in the early experiments and helped initiate the project.

REFERENCES

A-1. M. S. Kharasch and O. Reinmuth. "Grignard Reactions of Substances." Prentice-Hall, New York (1954).

A-2. (a) R. D. Riek, Science, 246, 1260 (1989). (b) K. V. Baker, J. M. Brown, N. Hughes, A. Skarnulis and J. Sexton, J. Org. Chem., 56, 698 (1991). (c) J. Lorimer and T. J. Mason, Chem. Soc. Rev., 16, 239 (1987).

A-3. D. E. Pearson, D. Cowan and J. D. Beckler, J. Org. Chem., 24, 504 (1959).

A-4. M. Gomberg and J. E. Bachmann, J. Am. Chem. Soc. 49, 236 (1927).

A-5. J. F. Garst, K. E. Lawrence, R. Batlaw and J. R. Boone, Inorg. Chim. Acta, 222, 365 (1994).

A-6. (a) X. D. Peng and M. A. Barteau, Surf. Sci., 233, 283 (1990). (b) U. Gelius, P. F. Heden, J. Hedman, B. J. Lindberg, R. Manne, R. Nordberg, C. Nordling and K. Siegbahn. Phys. Scripta. 2, 70 (1970).

A-7. C. D. Wagner, W. M. Riggs, L. E. Davis, J. F. Moulder and G. E. Muilenberg. "Handbook of X-ray Photoelectron Spectroscopy." Perkin-Elmer: Eden Prairie, MN (1981).

A-8. (a) A.P. Jansen, R.C. Schoonmaker, A. Chambers and M. Prutton, Surf. Sci. 45, 45 (1974). (b) A.P. Jansen, R.C. Schoonmaker, J.A.D. Matten and A. Chambers, Solid State Commun., 14, 63 (1974).

A-9. R. W. Wyckoff. "Crystal Structures". Wiley-Interscience, New York (1972).

A-10. G. A. Somorjai. "Introduction to Surface Chemistry and Catalysis". Wiley-Interscience, New York (1994).

A-11. A. P. Jansen, R. C. Schoonmaker and A. Chambers. Surf. Sci. 47, 41 (1975).

A-12. H. Namba, J. Darville and J. M. Gilles. Surf. Sci. 108, 446 (1981).

A-13. B. E. Hayden, E. Scheweizer, R. Kötz and A. M. Bradshaw. Surf. Sci. 111, 26 (1981).

A-14. S. A. Flodström and C. W. B. Martinsson. Surf. Sci. 118, 513 (1982).

A-15. X. D. Peng and M. A. Barteau. Surf. Sci. 233, 283 (1990).

A-16. S. J. Splinter, N. S. McIntyre and G. Palumbo. Surf. Sci. 292, 130 (1993).

A-17. S.J . Splinter, N. S. McIntyre and G. Palumbo, Surf. Sci. 302, 93 (1994).

A-18. C. Au, S. Singh-Boparai and M. Roberts. J. Chem. Soc. Faraday Trans. 79, 1779 (1983).

A-19. L. Mooney, S. Rassias and M. W. Roberts. Surf. Sci. 105, L249 (1981).

A-20. J. B. Abreu, J. E. Soto and M. P. Soriaga. J. Coll. Interf. Sci. 206, 247 (1998).

FIGURES

Figure Captions

Figure A-1. Auger electron spectra for Mg(0001) after various pretreatments. Experimental procedures and conditions were as described in the text.

Figure A-2. *In situ* AFM image of Mg(0001) surface immersed in pure water after it was etched in 6% HNO_3. Top (A): Original image. Bottom (B): After Fourier transformation of (A). Experimental procedures and conditions were as described in the text.

Figure A-3. Auger electron spectra (AES) of Mg(0001) before and after dosage with $O_{2(g)}$.

Figure A-4. Peak-to-peak heights of the Mg($L_{23}VV$) transition, normalized to that of the clean magnesium signal, as a function of $O_{2(g)}$ exposure.

Figure A-5. Oxygen-uptake isotherm of Mg(0001) at two different $O_{2(g)}$ pressures.

Figure A-6. Low-energy electron diffraction (LEED) patterns of Mg(0001) before and after dosage with gaseous oxygen;.beam energy used as follows. (A): 51.9 eV, (B): 52.0 eV, (C): 52.1 eV,

Figure A-7. Oxygen-uptake of Mg(0001) as a function of $H_2O_{(g)}$ dosage.

Figure A-8. A: Oxygen-uptake of Mg(0001) as a function of CO_2 dosage. B: Mg-normalized O and C AES peaks as functions of CO_2 dosage.

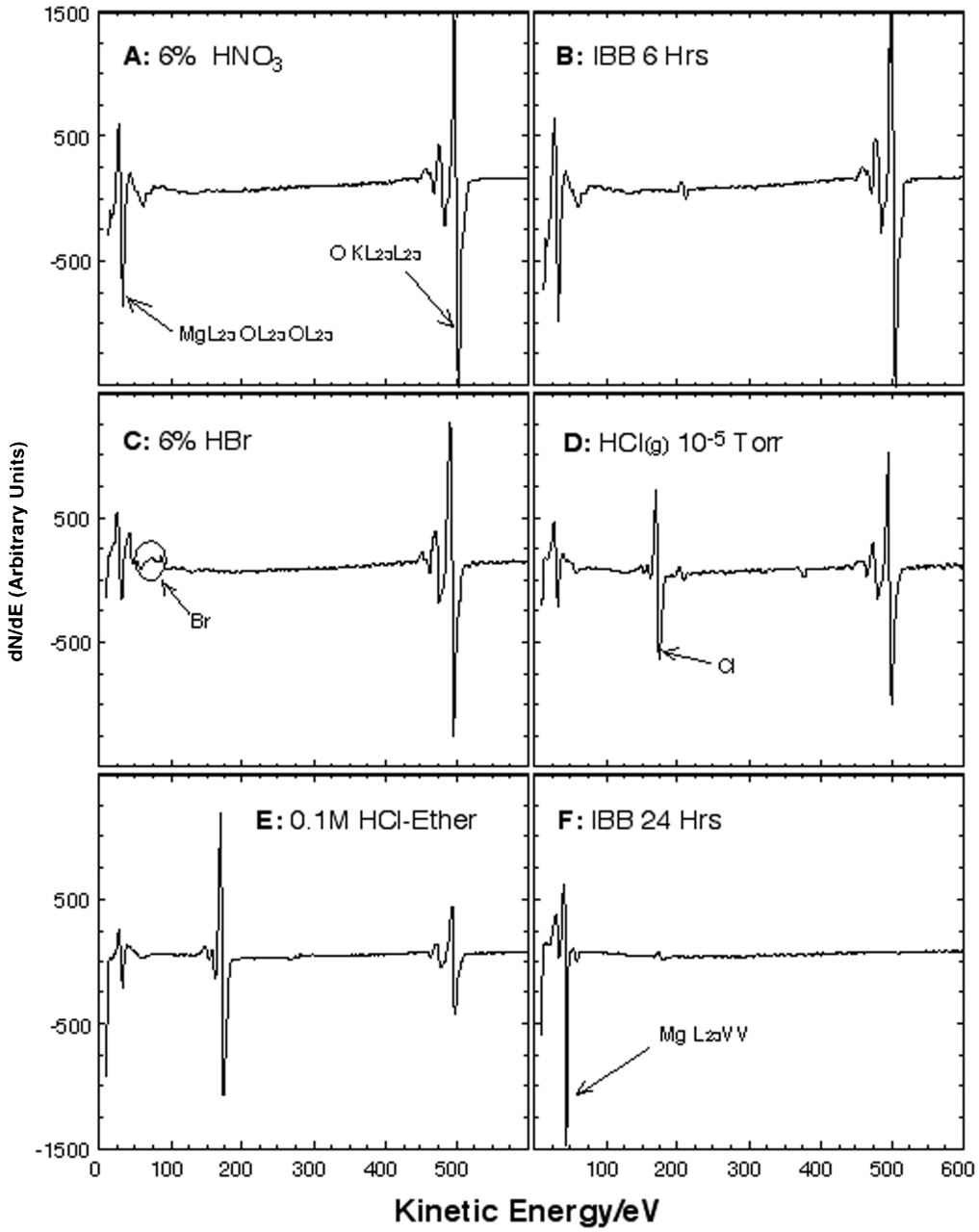
A: 6% HNO3
B: IBB 6 Hrs
C: 6% HBr
D: HCl(g) 10-5 Torr
E: 0.1M HCl-Ether
F: IBB 24 Hrs
O KL2,3L2,3
Mg L2,3 O L2,3 O L2,3
Br
Cl
Mg L2,3 V V
dN/dE (Arbitrary Units)
Kinetic Energy/eV
1500
500
-500
-1500
0
100
200
300
400
500
600

Figure A-1.

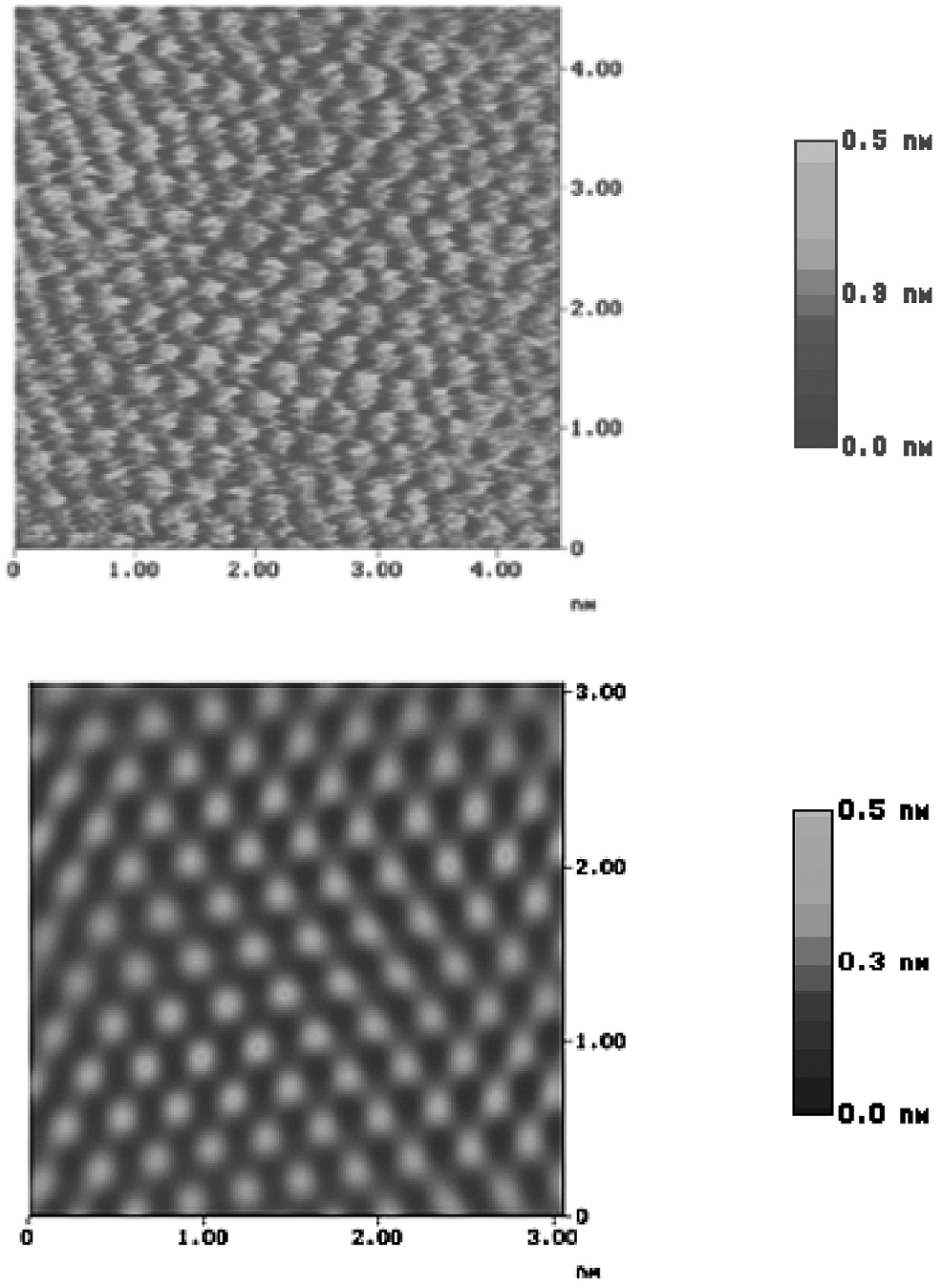
4.00
3.00
2.00
1.00
0
0
1.00
2.00
3.00
4.00
nm
0.5 nm
0.8 nm
0.0 nm
3.00
2.00
1.00
0
0
1.00
2.00
3.00
nm
0.5 nm
0.3 nm
0.0 nm

Figure A-2.

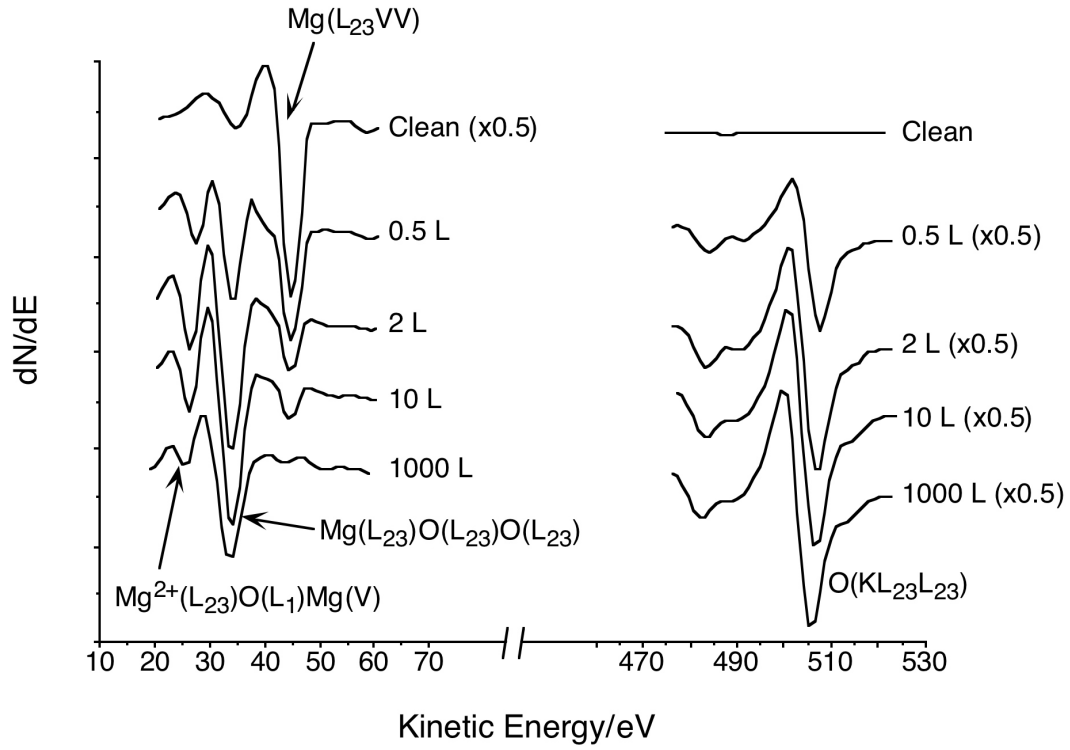
Mg(L23VV)
Clean (x0.5)
0.5 L
2 L
10 L
1000 L
Mg(L23)O(L23)O(L23)
Mg2+(L23)O(L1)Mg(V)
Clean
0.5 L (x0.5)
2 L (x0.5)
10 L (x0.5)
1000 L (x0.5)
O(KL23L23)
dN/dE
10 20 30 40 50 60 70
470 490 510 530
Kinetic Energy/eV

Figure A-3.

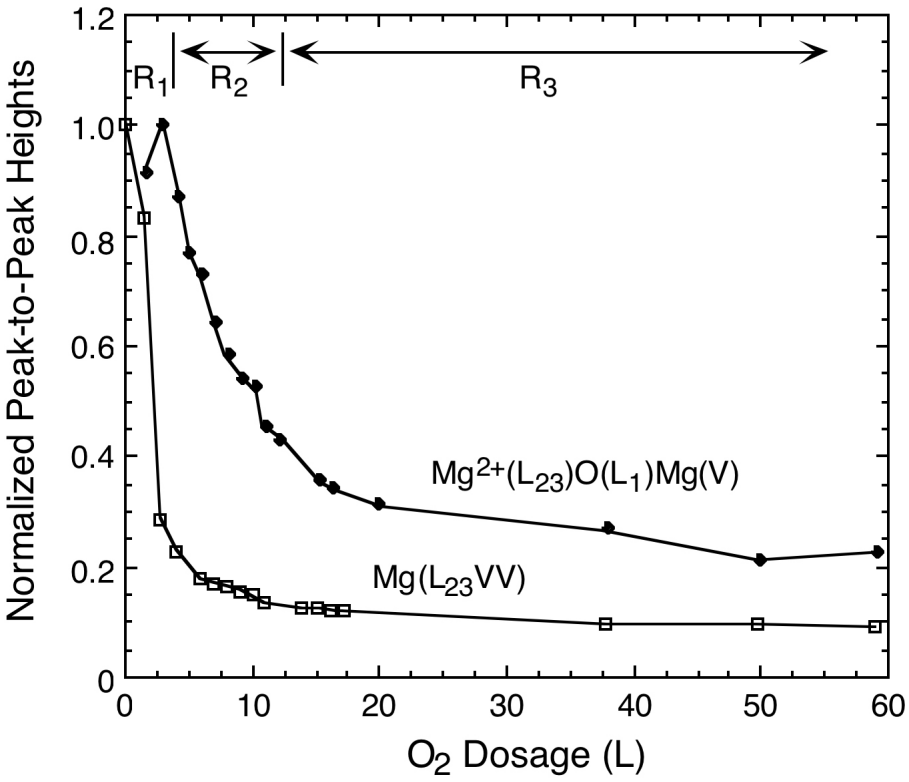
1.2
1.0
0.8
0.6
0.4
0.2
0
Normalized Peak-to-Peak Heights
R1
R2
R3
Mg2+(L23)O(L1)Mg(V)
Mg(L23VV)
0
10
20
30
40
50
60
O2 Dosage (L)

Figure A-4.

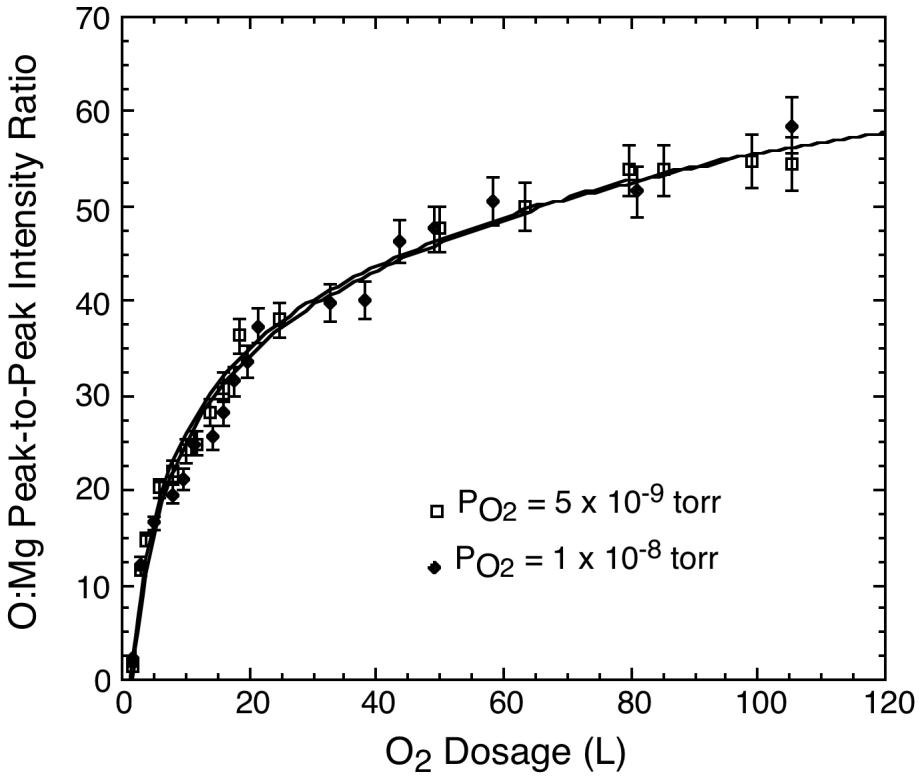
O:Mg Peak-to-Peak Intensity Ratio
O2 Dosage (L)
P_O2 = 5 x 10^-9 torr
P_O2 = 1 x 10^-8 torr
0
10
20
30
40
50
60
70
0
20
40
60
80
100
120

Figure A-5.

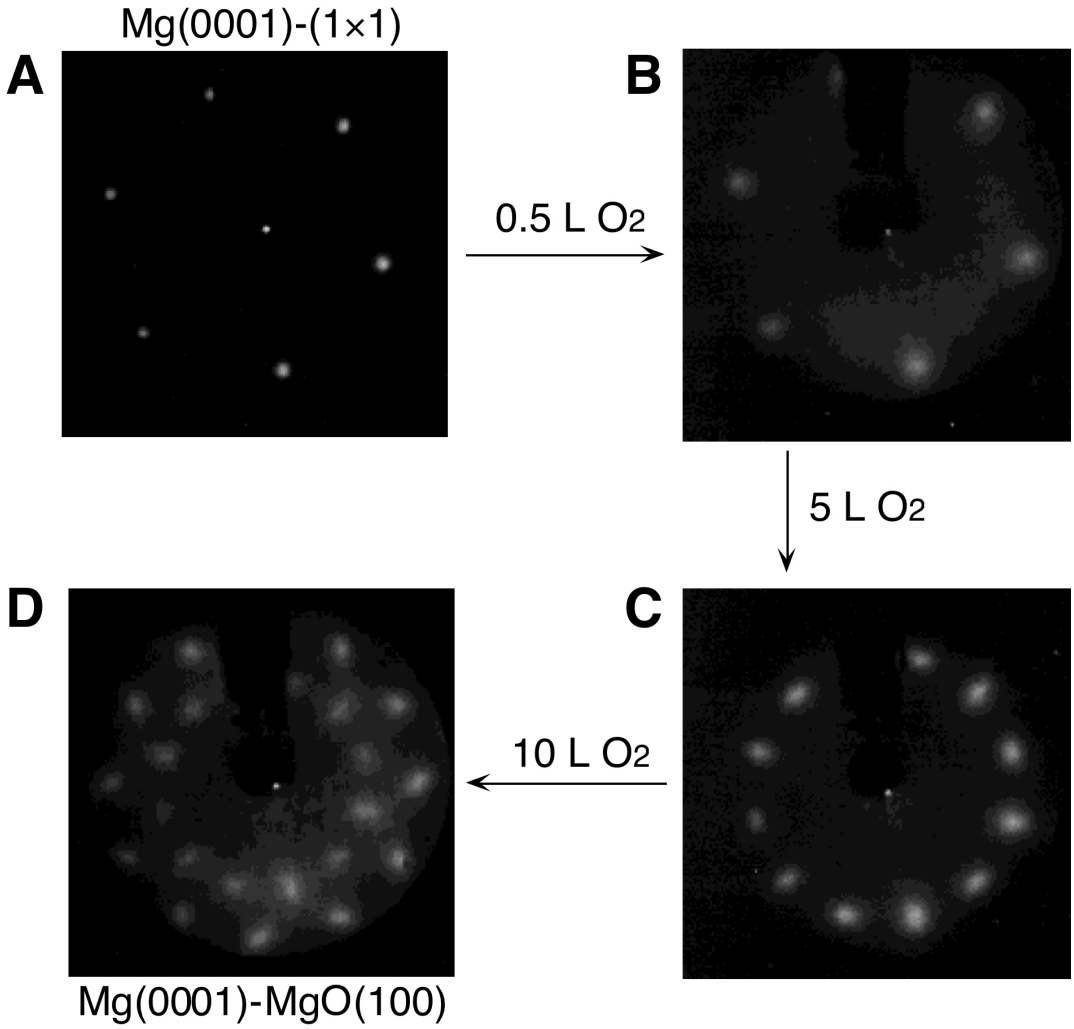

Figure A-6.

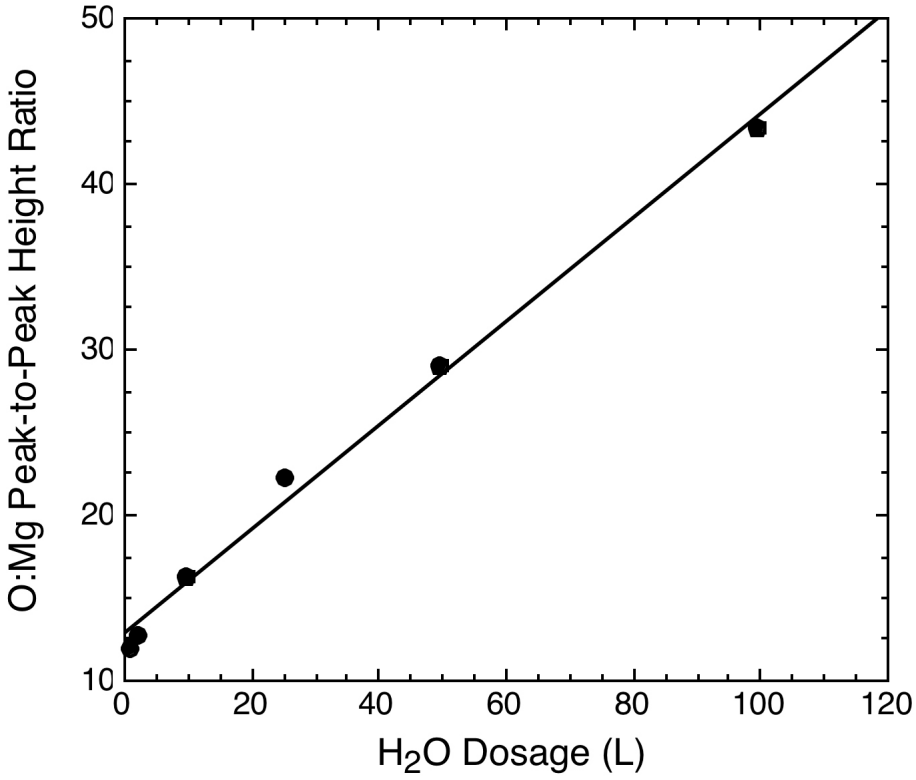
O:Mg Peak-to-Peak Height Ratio
50
40
30
20
10
0
20
40
60
80
100
120
H2O Dosage (L)

Figure A-7.

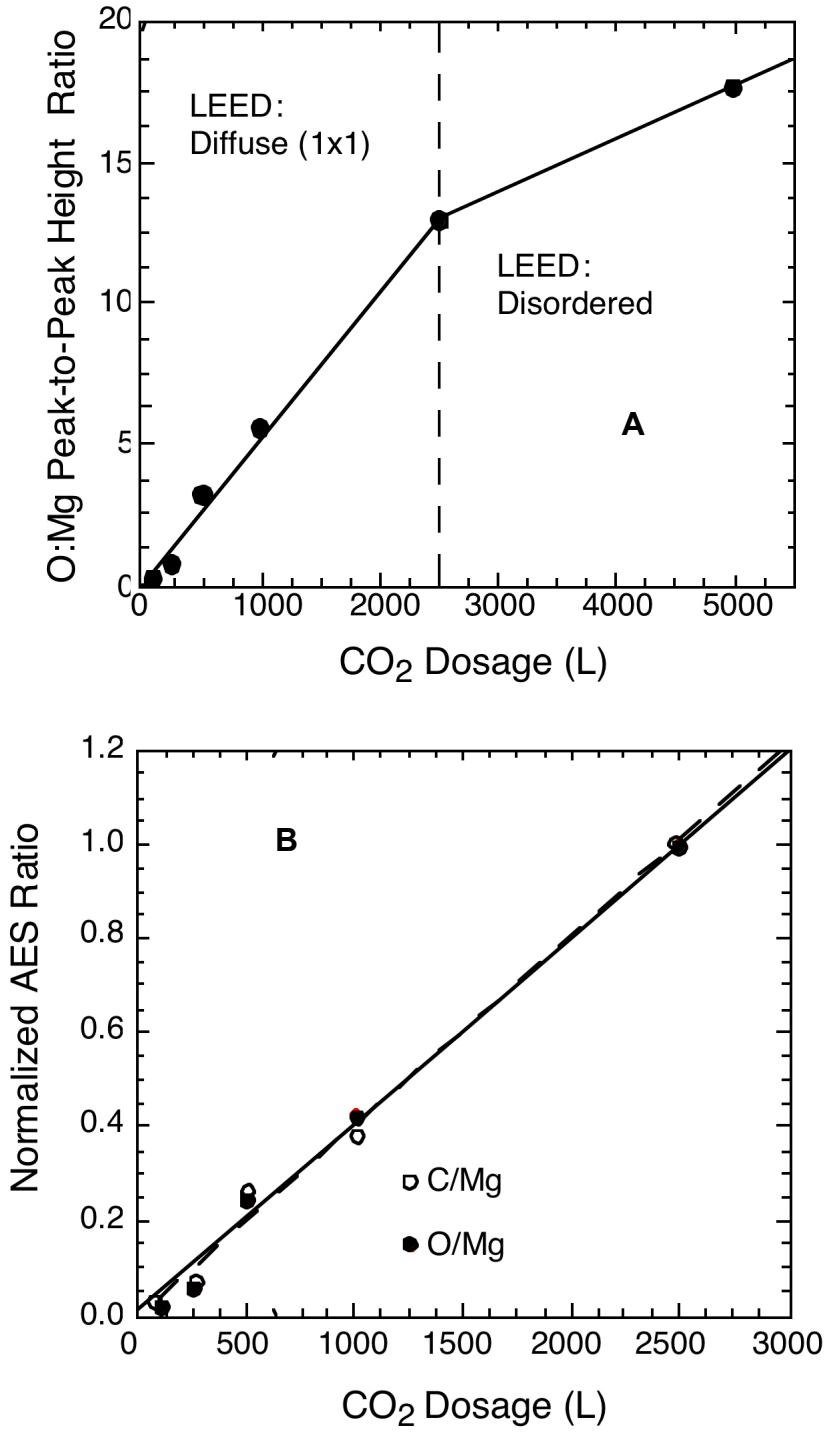
O:Mg Peak-to-Peak Height Ratio
LEED:
Diffuse (1x1)
LEED:
Disordered
A
CO_2 Dosage (L)
Normalized AES Ratio
B
C/Mg
O/Mg
CO_2 Dosage (L)

Figure A-8.

APPENDIX B

INTERNALIZATION OF CARBON BLACK AND MAGHEMITE IRON OXIDE NANOPARTICLE MIXTURES LEADS TO OXIDANT PRODUCTION*

J. MICHAEL BERG[†], SHU HO[‖], WONJOONG HWANG[‡], REMA ZEBDA[†], KYLE CUMMINS[¥], MANUEL P. SORIAGA[¥], ROBERT TAYLOR[§], BING GUO[‡], AND CHRISTIE M. SAYES[†‖]

[†]Department of Veterinary Physiology and Pharmacology, Texas A&M University, College Station TX 77843

[‖] Department of Biomedical Engineering, Texas A&M University

[‡]Department of Mechanical Engineering, Texas A&M University

[¥] Department of Chemistry, Texas A&M University

[§] Department of Veterinary Integrative Biosciences, Texas A&M University

Chemical Research in Toxicology

Volume 23, Issue 12, 1 November 2010, Pages 1874-1882

Abstract

Potential human exposure to mixed nanomaterials in consumer, occupational, and medicinal settings is increasing as nanomaterials enter the workplace and the marketplace. In this study, the toxicity of mixed engineered carbon black (ECB) and maghemite iron oxide (Fe_2O_3) nanoparticles was investigated in a cellular system in order to understand the mechanism of toxicity and potential methods of toxicity mitigation. Lung epithelial cells (A549) were exposed to mixed Fe_2O_3 and ECB nanoparticles, mixed Fe_2O_3 and ECB nanoparticles with addition of L-ascorbic acid, and mixed Fe_2O_3 and surface-oxidized engineered carbon black (ox-ECB) nanoparticles. The nanoparticles were characterized using transmission electron microscopy, nitrogen adsorption surface area measurement (BET), x-ray diffraction, and surface charge measurement. The carbon black nanoparticles were also characterized with a reductive capacity assay, and by x-ray photoelectron spectroscopy (XPS). Cellular uptake of nanoparticles was analyzed via transmission electron microscopy and fluorescence microscopy; cellular uptake of iron was quantified using inductively coupled plasma mass spectrometry (ICP-MS). Both the MTT assay and the Ethidium Homodimer and Calcein AM live/dead assay were used to measure cellular proliferation and cytotoxicity, respectively. The DCFH assay was used to measure intracellular generation of reactive oxygen species. Results showed that the iron oxide and carbon black nanoparticles were co-localized in acidic intracellular vesicles (pH<5.2) after cells were exposed to mixed nanoparticles; quantitative cellular uptake of Fe_2O_3 nanoparticle was

unaffected by mixing with ECB. Significant oxidant production occurred in cells exposed to mixed Fe_2O_3 and ECB, but not in cells exposed to mixed Fe_2O_3 and ox-ECB, nor in cells exposed to Fe_2O_3 and ECB with ascorbic acid addition. Furthermore, exposure to mixed Fe_2O_3 and ECB exhibited a dose-dependent decrease in cellular proliferation (MTT assay) and a decrease in cellular viability (Ethidium Homodimer and Calcein AM live/dead assay) that were not seen in the Fe_2O_3 and ox-ECB scenario. The results support the hypothesis that exposure to mixed Fe_2O_3 and ECB produces oxidants that is mediated by the surface reductive capability of ECB when both particle types are co-localized in acidic cellular compartments. This oxidant production mechanism may lead to oxidative stress, but it can be mitigated by an anti-oxidant such as ascorbic acid, or by surface treatment of the ECB to decrease its surface reductive capacity.

Introduction

Metal oxide nanomaterial systems are promising candidates for many industrial, consumer, and medical applications due to their unique physicochemical properties (i.e. high surface areas and extraordinary electronic properties) (*1-4*). Given the widespread applications and their commercialization, there is an increasing potential for humans to be exposed to a multitude of nanomaterials. While much work in nanotoxicology has focused upon the etiology of specific nanoparticle effects, little attention has been given to the effects of mixtures, or combinations, of various nanoparticles on biological systems.

However, real-world exposure is very likely to be a mixture of multiple substances, such as airborne particles in the atmosphere. Previously, epidemiological data had suggested that airborne particulate matter (a mixture of many different substances) were more toxic than the sum of its parts. This was attributed to some sort of "synergistic" effect (*5*). In the nanotoxicology setting, human exposure to mixed nanomaterials is likely because multiple types of nanomaterials are often used simultaneously. For example, both metal oxide nanoparticles (e.g. Fe_2O_3) and graphitic carbon nanoparticles (e.g. carbon black) are likely to be used in various industrial applications (*6-8*). Therefore, it is imperative to understand the toxicological effect due to exposure to mixed nanomaterials. Recent publications have highlighted the importance of studying multiple nanoparticle exposure scenarios (*9, 10*). Additionally, while the nanoparticles used in this study (carbon black and iron oxide) are specific

nanoparticle-types, they may be considered as representative ambient amorphous carbon or transition metal oxides found in the urban atmosphere (*11*).

Previously, we have evaluated the oxidative stress of cells after simultaneous exposure to iron oxide (Fe_2O_3) and engineered carbon black (ECB) nanoparticles by a means of both protein and lipid oxidation. Results indicated that exposure to both materials simultaneously induced a synergistic oxidative stress effect to a human lung epithelial cell line, even though exposure to either nanomaterial alone induced no significant oxidative stress. Our findings indicated that the ECB and Fe_2O_3 caused a synergistic effect greater than the sum of each particle tested individually.

We explained the synergism between engineered carbon black and iron oxide nanoparticles through an oxidative stress paradigm. This effect was largely attributed to the surface reductive capacity of the carbon black nanoparticles, which enabled redox cycling of the iron ions and hence caused significant oxidative stress in cells (*12*). Graphitic (non-diamond) nanomaterials such as carbon black have chemically active sites (functional groups) on their surfaces that give rise to surface redox capabilities. In aqueous solutions, carbon black nanoparticles can reduce Fe^{3+} ions to Fe^{2+} (*13*). This involves the oxidation of the surface functional groups, for example (*14*, *15*):

$$\sim C\text{-}OH + Fe^{3+} \rightarrow \sim C{=}O + Fe^{2+} \quad (1)$$

Fe^{2+} is membrane permeable and has the ability to undergo further intracellular Fenton reactions in the cytosol (*16-18*). Thus, Fe^{2+} can facilitate the generation of reactive oxygen species, for example, through the Fenton reaction (*13*):

$$Fe^{2+} + H_2O_2 \rightarrow Fe^{3+} + OH\cdot + OH^- \quad (2)$$

It should be noted that nanoparticles could induce reactive oxygen species (ROS) production through abiotic and/or biotic pathways. For example, nano-sized TiO_2, in the anatase crystal form, is able to generate $\cdot OH$ radicals from water in the presence of UV light (*19*), which may then elicit a biological response such as inflammation or oxidation of cellular substructures (*20, 21*). This type of ROS generation apparently has little dependence on the biological system, because TiO_2 nanoparticles have been shown to generate ROS in abiotic aqueous environments under UV irradiation. On the other hand, the ROS generation that was proposed in the previous study requires the dissolution of the Fe^{3+} from Fe_2O_3 nanoparticles, which would be pH-dependent and hence related to the locality within the biological system. Also, the synergism mechanism proposed above requires the Fe_2O_3 nanoparticles and the carbon black nanoparticles to be collocated in the same cellular compartments so that the dissolved Fe^{3+} ions would have access to the reductive sites on the surface of carbon black particles; this is evidently dependent on the interaction between the particles and the biological system.

With this study, we set out to elucidate the mechanism behind the synergistic toxicological effect of mixed Fe_2O_3 and carbon black. One objective of the study was to determine whether the two types of particles were indeed co-

localized inside acidic cellular compartments. A second objective was to determine if ROS generation was indeed responsible for the observed synergistic toxicity of Fe_2O_3 and ECB. In addition, this study aimed to determine whether there was a synergistic effect between Fe_2O_3 nanoparticles and surface-oxidized ECB (ox-ECB). Since the reductive capacity of engineered carbon black nanoparticles may be diminished by surface oxidation, we hypothesized that exposure to mixed Fe_2O_3 and ox-ECB (with a decreased reductive capacity relative to ECB), would have a mitigated synergistic effect in comparison to the mixed Fe_2O_3 and ECB.

Experimental Procedures

Nanomaterial Preparation. Maghemite iron oxide (Fe_2O_3) nanoparticles were produced using a flame synthesis method that has been described in detail in Guo et. al. (*17*). Carbon black particles were produced in a hydrocarbon/air diffusion flame. Ethylene (C_2H_4) was used as a hydrocarbon fuel gas for the flame-engineered carbon black (ECB) nanoparticle synthesis. The burner features a fuel/oxidant co-flow structure described in Guo et al (*17*). Oxidized engineered carbon black (ox-ECB) was prepared by vigorous stirring in a neutral aqueous suspension under O_2 purge in continuous light for 2 weeks (*22*). Fe_2O_3, ECB, and ox-ECB nanoparticles were suspended in deionized water (*12*).

Chemical and Physical Characterization. Nanoparticle size was measured via transmission electron microscopy (TEM). Nanoparticle zeta potential was measured using a Malvern Nano-ZS (Malvern Inc, Worcestershire, UK) using dynamic light scattering (DLS) combined with phase analysis light scattering

(PALS) (*23*). Samples for surface charge measurements were suspended in ultrapure water (18.2 MΩ) at a pH of 5.9 and bath sonicated for 30 minutes at 40 kHz. Nanoparticle specific surface area (SSA) was measured via the BET method under N_2 absorption (*24*). Size from SSA measurements was calculated. Discrepancies between TEM size and SSA size are discussed elsewhere (*12*). Furthermore, surface oxygen species for the ECB and ox-ECB samples were quantitated via X-ray photoelectron spectroscopy (XPS) following published procedures (*25-31*). Samples were dried onto a micro coverslip and analyzed on a Kratos Axis Ultra Imaging X-ray photoelectron spectrometer.

Reductive Capacity of Engineered Carbon Black and Oxidized Engineered Carbon Black Nanoparticles, Ex Vivo Analyses. The reductive capacities of the engineered carbon black and oxidized engineered carbon black particles were measured using a spectrophotometric method that was modified from a previous method (*12, 17*). Briefly, 30 mg of ECB (or ox-ECB) nanoparticles and 9 mg of $Fe_2(SO_4)_3$ was added to 75 ml of ultrapure water to obtain a suspension of carbon black nanoparticles in ferric sulfate solution. This suspension was incubated in a water bath at 37 ˚C for 16 hours. Then the carbon black particles were filtered out to obtain a clear solution containing Fe^{3+} and Fe^{2+} ions. To this clear solution, 0.25 ml 20% sulfuric acid was added to adjust the pH; then the solution was diluted to 100 ml in a volumetric flask. The concentrations of Fe^{3+} and Fe^{2+} ions in the solution were determined using the spectrophotometric method at an absorbance wavelength of 512 nm, as described previously (*12, 17*).

Cell Culture Conditions. Human lung epithelial cells (A549, ATCC) were cultured using F-12K media supplemented with 10% fetal bovine serum and 1% penicillin, streptomycin, and amphotercin B (Sigma Aldrich, St. Louise, MO). Cells were seeded at 1.5 x 10^4 cells/well in 96 well-plates. This cell seeding concentration was predetermined to yield ~90% confluency at time of analysis. After allowing 24 hrs for attachment, cells were exposed to known concentrations of nanoparticle suspensions ranging from 0.01 mg/mL to 100 μg/mL. Cells were co-exposed to differing ratios of Fe_2O_3:ECB or Fe_2O_3:ox-ECB, including 0.01:4, 0.1:4, and 1.0:4 and 100:4 μg/mL. For exposure scenarios, a stock solution of Fe_2O_3, ECB, or ox-ECB (1000 μg/mL) was prepared in ultrapure water. Stock solutions were serially diluted in F-12K medium containing serum. Care was taken to preserve similar osmolarity between samples.

Intracellular Nanomaterial Localization Analyses. A549 cells were treated with Fe_2O_3, ECB, ox-ECB, Fe_2O_3 and ECB, or Fe_2O_3 and ox-ECB for 25 hours. The inoculated culture media was replaced with 3% (v/v) glutaraldehyde in 1X Hank's balanced salt solution (HBSS). After incubation, the cells and fixative were placed in a PELCO Biowave cold microwave (Ted Pella, Redding, Ca) at 250 W for a 6 minute cycle. Following washing, post-fixation was performed with a 1% osmium tetroxide (wt/v) solution overnight. Samples were then washed with HBSS and dehydrated in increasing methanol steps. An epoxy formula was prepared using Quetol 651, Araldite, and DDSA (A:E ratio 1:1) with benzyldimethyl-amine (BDMA) used as the accelerant. Following polymerization, the blocks were sectioned, mounted on grids, and examined.

Post staining was performed using both a 2% uranyl acetate (wt/v) and Reynolds lead citrate (*32*). Care was taken to prepare the samples with freshly boiled water as to eliminate any lead carbonate precipitation. After thoroughly washing, samples were placed in lead citrate (pH ~12) for 2 min with potassium hydroxide (KOH). The grids were washed, dried, and examined using transmission electron microscopy (TEM). TEM analysis was performed using a Morgani Electron Microscope (FEI corp.) at 100 keV.

Intracellular Metal Analysis. Iron content within the cells was analyzed using inductively coupled plasma-mass spectroscopy (ICP-MS). A549 cells were seeded, exposed to 50 μg/mL of Fe_2O_3, or co-exposed to equal parts of 50 μg/mL ECB and Fe_2O_3 nanoparticle suspensions. Following a 25 hr exposure time, the cell culture media was removed from cells and kept for analysis. Cells were washed with warm PBS repeatedly to remove residual nanoparticles on the surface of the cells. Following washing, exposed cells were detached from the culture dish with 1X Trypsin-EDTA and collected. All suspensions were digested under heat (60^{o}C) and acid (5% HCl and 1% nitric acid, by volume), and analyzed for iron content via ICP-MS using an Elan DRC II, Perkin Elmer SCIEX (Waltham, MA, USA).

Lysosomal Characterization. Visualization of lysosomal presence was analyzed using florescence microscopy techniques. Briefly, A549 cells were incubated with 10 μg/mL Fe_2O_3 nanoparticles and 4 μg/mL ECB (or ox-ECB) nanoparticles for 1 hr, 3 hrs, or 24 hours. Following nanoparticle incubation, Lysotracker™ (75 nM, Invitrogen Corp., Carlsbad, CA, USA) was added to both

control (unexposed) and nanoparticle exposed cells and incubated for 1.5 hrs. Cells were fixed with paraformaldehyde and subsequently counterstained with DAPI (4',6-diamidino-2-phenylindole) (300 nm, Invitrogen Corp., Carlsbad, CA, USA) . Following staining, cells were preserved with Slo-fade® (Invitrogen Corp, Carlsbad, CA, USA) and imaged on an Olympus inverted fluorescent microscope.

Cellular Proliferation. The 1-(4,5-dimethylthiazol-2-yl)-3,5-diphenylformazan (MTT) assay (Sigma Aldrich, St. Louise, MO) is a spectrophotometric way to assess cellular proliferation via quantification of the enzyme mitochondrial dehydrogenase. Actively respiring mitochondria reduce the tetrazolium salt to a water insoluble purple formazan dye, which is solubilized in MTT solubilization solution (10% Triton X-100 in 0.1 N HCl in anhydrous isopropanol). After solubilization in acidic isopropanol, the product was quantified by measuring absorbance at 570 nm. Briefly, cultured cells were exposed to nanoparticles as described above. After 25 hrs, MTT (5 mg/mL) was added to each well and incubated for 4 hr. Subsequent experiments were performed using the ECB and ox-ECB nanomaterials in cell-free conditions to verify the absence of *ex vivo* reduction of the salt by the particles themselves.

Cellular Viability. Cellular viability was assessed using the LIVE/DEAD Viability/Cytotoxicity assay (Molecular Probes). This assay utilizes the fluorescent dyes ethidium homodimer and calcein AM. Ethidium homodimer increases in fluorescence intensity upon binding to DNA. Calcein AM is hydrolysed by intracellular hydrolases found in living cells and subsequently

increases in fluorescence intensity. Therefore, in this assay, viable cells fluoresce green while non-viable cells fluoresce red. Briefly, cells were exposed to nanoparticles as described above. Following a 25 hour exposure, cells were washed and incubated with 2 μM EthD-1 and 1.5 μM Calcein AM for 40 minutes. For control wells in which dead cells were needed, cells were incubated with 70% methanol in PBS for 30 minutes. Nanoparticle-only controls were incorporated to assure no interference with the assay. Following dye incubation, stained cells were viewed under an inverted fluorescence microscope. Multiple field images (~2500 cells) were collected and cell viability was assessed as follows:

$$\text{Percent Dead Cells } (\%) = \frac{\text{Number of dead cells}}{\text{Total cell count}} * 100 \qquad (3)$$

Intracellular ROS Detection. DCFH-DA (2'7'-dicholorfluorescin diacetate) was used to measure the levels of intracellular reactive oxygen species (Sigma Aldrich, St. Louise, MO). Briefly, a 20 μM DCFH-DA solution in Hank's balanced salt solution (HBSS) was made without serum or other additives. A549 cells were cultured and exposed to nanoparticle suspensions as described above and incubated for 2.5 hrs or 25 hrs. After washing, cells were then incubated with the DCFH-DA working solution for 30min. Fluorescence was measured at 485/520 nm (excitation/emission) using a fluorescence plate reader (Synergy MX, BioTek).

Antioxidant Addition. A 1 mM L-ascorbic acid solution was prepared. A549 cells were incubated in appropriate media and inoculated with Fe_2O_3:ECB, as described above. For the 2.5 hr nanoparticle co-exposure, ascorbic acid was

added at t=0 hr. For the 25 hr co-exposure, ascorbic acid was added after 19 hrs. L-ascorbic acid was added to yield a concentration of 0.083 mM in total cell culture media volume. Intracellular reactive species were probed via DCFH-DA, as described above, after either 2.5 hr or 25 hr post-exposure.

Results

Physicochemical Characterization. Nanomaterial characterization was assessed with a variety of methods and reported in Table 1. The size of the Fe_2O_3 particles, assessed by transmission electron microscopy, was 41 ± 17 nm, while that of ECB and ox-ECB (surface oxidized ECB) was 47 ± 7 nm. Surface charge was assessed through measurement of the zeta potential. All three types of nanoparticles displayed highly negative zeta potentials when dispersed in ultrapure water. Iron oxide nanoparticles had a zeta potential of -44.2 ± 5.9 mV. The zeta potential of ECB and ox-ECB was -51 ± 6.02 mV and 52 ± 6.02 mV, respectively. The reductive capacity of ECB towards Fe^{3+} was measured to be 9.0×10^{-3} g(iron)/g(carbon). Following surface oxidation, the ability for ox-ECB to reduce Fe^{3+} was decreased significantly to 2.4×10^{-4} g(iron)/g(carbon). This actuates to a 97.3% loss of ECB reductive capacity following surface oxidation. The XPS measurements showed that surface oxidation of the ECB resulted in a 15% increase in the ratio of oxidized to unoxidized C, from 0.113 in ECB to 0.130 in ox-ECB. Quantitation of the deconvoluted [142-148] C1s XPS peaks for ox-ECB further indicated a remarkable increase in the fraction of interfacial quinonoid moieties: the ratio $Q_{(s)}/H_2Q_{(s)}$ in ox-ECB was found to be *ca.* 5000

times greater than in ECB. It may be mentioned that, based upon a molecular model of the carbon nanoparticles, estimated from TEM experiments to be cubic with a 50-nm edge, in conjunction with the escape-depth properties of X-ray photoelectrons, at least 90% of the XPS carbon peaks may be presumed to emanate from edge-sites; surface redox activity is possible only on such sites and not on the terrace (graphene) sheets. Whereas specific surface area (SSA) was found to be 49 m^2/g for the iron oxide nanoparticles and 63 m^2/g for the ECB nanoparticle sample, none was measured for the ox-ECB sample as it remained in aqueous suspension.

Intracellular Nanomaterial Localization Analyses. Figure 2 shows TEM images of ultrathin sections of, A549 human lung epithelial cells after being incubated with mixed Fe_2O_3 and ECB for 25 hours. The TEM results indicate that both Fe_2O_3 and ECB were internalized into micron-sized vesicles within A549 epithelial cells. These intracellular organelles most resemble an early or late endosome and/or lysosome (REFs). Ultrathin, 2-D sections, revealed the presence of both ECB (or ox-ECB) and Fe_2O_3 nanoparticles co-localized within the same intracellular vesicle. In exposures to both ECB and Fe_2O_3 (Figure 2A & 2B) and ox-ECB and Fe_2O_3 (Figure 2C & 2D), intracellular uptake and co-localization the two types of particles occurred. The presence of large agglomerates of both Fe_2O_3 and ECB or ox-ECB nanoparticles was observed. The ECB and the Fe_2O_3 particles were readily distinguishable in the TEM images due to their morphological differences; Fe_2O_3 particles exhibited multifaceted sides whereas ECB particles exhibited a more amorphous, rounded shape. TEM

images of particles under cell free conditions can be seen in Guo et. al. (2009) [149].

Additional Intracellular Metal Analysis. The presence of intracellular Fe_2O_3 was confirmed through inductively coupled plasma-mass spectroscopy (ICP-MS) (Figure 3). These measurements show the total intracellular iron. Results indicate similar Fe_2O_3 uptake in both the single and co-exposure scenarios. The iron content in the cell culture media removed from cell culture after Fe_2O_3 exposure is 0.017 $\mu g/mL$. The iron content in cells exposed to 50 $\mu g/mL$ Fe_2O_3 is 0.175 $\mu g/mL$. The total iron content in the cell and culture media system exposed to 50 $\mu g/mL$ Fe_2O_3 is 0.193 $\mu g/mL$. The iron content in the cell culture media removed from cell culture after ECB and Fe_2O_3 exposure is 0.014 50 $\mu g/mL$. The iron content in cells exposed to 50 $\mu g/mL$ ECB and 50 $\mu g/mL$ Fe_2O_3 is 0.177 $\mu g/mL$. The total iron content in the cell and culture media system exposed to 50 $\mu g/mL$ ECB and 50 $\mu g/mL$ Fe_2O_3 is 0.192 $\mu g/mL$. Furthermore, the sum of Fe_2O_3 in the spent cell culture medium (CCM) and total intracellular iron (cells) agrees with the exposure concentration (total).

Lysosomal Characterization. The increased presence of lysosomal compartments was confirmed through florescence microscopy with the use of Lysotracker red dye. Lysotracker dye consists of a fluorophore linked to a weak base that accumulates in cellular compartments with a low internal pH. Additionally, cell nuclei were counterstained with DAPI. Figure 4 indicates a low basal of lysosomal presence in many control cells at the 1 hr, 3 hr, and 24 hr time points. While a low basal level may be seen in the control cells, actively

proliferating cells exhibited higher fluorescence intensity. Additionally, by visual inspection, the A549 control cells appeared to be increasing in number and confluency as the time points progressed. In cells exposed to 10 μg/mL Fe_2O_3 and 4 μg/mL ECB, an increase in fluorescence was observed at all time points. At 1 hour following exposure, a low basal level of lysosomal presence was observed similar to the control however, some individual cells exhibited increased punctuate fluorescence. At 3 hours, this trend was exacerbated, coupled with a moderate degree of fluorescence. Following 24 hour exposure, the A549 cells continued to proliferate, albeit with slightly different confluencies, with fluorescence intensity comparable to the 3 hour post-exposure time point. Similar trends were observed in the co-exposure consisting of 10 μg/mL Fe_2O_3 and 4 μg/ml ox-ECB.

Oxidant Production. The DCFH assay provides an estimation of instantaneous intracellular ROS (Figure 5). While, relatively non-specific, the DCFH-DA is a cell based assay for measuring relative concentrations of hydroxyl, peroxyl, and oxidants and has been suggested as a good measure of the oxidative status in cells in culture [150, 151]. Control cells exhibited little intracellular ROS. This is hypothesized to be a byproduct of normal cellular respiration. While the lower concentration of Fe_2O_3, at the 2.5 hr time point, did not generate significant or increasing amounts of oxidative species as determined by fluorescence spectroscopy (increase of 6.9% for 0.01 μg/mL and 5.4% for 0.1 μg/mL), Fe_2O_3 at a higher dose (100 μg/mL) showed a heightened response (28.1%) when compared to the control. At the 25 hour time point the

cells exposed to 100 $\mu g/mL$ Fe_2O_3 still exhibited a heightened response, however the difference between the high (increase of 35%) and low doses (increase of 31.3% for .01 $\mu g/mL$ and 24.0% for 0.1$\mu g/mL$) is not as significant as was observed in the 2.5 hr time point. In addition, A549 cells were exposed to mixtures of both Fe_2O_3 and ECB simultaneously. This scenario produced a significant amount of ROS when compared to the control. Mixture scenarios at the 25 hr time point produced an increase of 103.6% for the 0.01:4 ratio, 51.9% for the 0.1:4 ratio, and 34.8% for 100:4 ratio. A similar pattern existed at the 2.5 hr time point. This response was proportionally related to the increasing ratios of ECB to Fe_2O_3. Confirmation that the generation of intracellular ROS was not, in fact, an artifact produced by the nanoparticles, was studied via the addition of L-ascorbic acid. L-ascorbic acid is a well characterized antioxidant that is able to function as an oxygen scavenger, thus limiting intracellular ROS. DCFH oxidation was diminished with the use of L-ascorbic acid.

Similarly, a secondary means of ameliorating the ROS generation via oxidation of the ECB to form ox-ECB was examined. Here, it was discovered that the oxidation of the surface of ECB resulted in florescence that was not significantly different from the control. Additionally, it was noted that for all co-exposure exposure values, at the 25 hr time point, ox-ECB produced less ROS than did the co-exposures incubated with L-ascorbic acid although these differences were not statistically significant.

Cellular Proliferation Assay. The MTT assay was used to compare the proliferative ability, in both control and groups containing ECB and ox-ECB co-

exposure with Fe_2O_3 (Figure 6). Results indicate that there is a decrease in formazan formation at higher exposure limits in the Fe_2O_3 and ECB scenario, thus indicating a dose-response relationship. Throughout the dose-response curve, the Fe_2O_3 and ECB-exposed cells demonstrated a decrease in cell proliferation at 0.01 μg/mL by 16.8% relative to control, at 0.1 μg/mL by 16.9%, and at 1 μg/mL by 16.8%; however at the higher doses of 10.0 μg/mL and 100 μg/mL, the cells exhibited a significant decrease in cell proliferation by 24% and 29.6%, respectively. However, the cells exposed to both Fe_2O_3 and ox-ECB did not exhibit this dose-dependent response. The highest exposure scenario (100 μg/mL) did not exhibit a significant difference when compared to both that of the other exposures as well as the control. Background absorbance values, due to nanoparticles, were subtracted out of final absorbance value. As a number of reports suggest reduction of the tetrazolium salt to formazan by exogenous sources, *ex vivo* (cell free) incubations of ECB and ox-ECB nanoparticles incubated with MTT showed little to no interference (data not shown) [152-155].

Cellular Viability. A live/dead cytotoxicity assay was employed to determine the absolute percentage of dead cells following co-exposures to the aforementioned nanoparticles (Figure 6). Results indicate a slight dose-dependent decrease in cellular viability following co-exposure to 0.01 μg/mL Fe_2O_3 combined with 4 μg/mL ECB to 10 μg/mL Fe_2O_3 and 4 μg/mL ECB. This decrease ranged from 0.69% dead to 7.62% dead. At an exposure of 100 μg/mL Fe_2O_3 and 4 μg/mL ECB, a decrease in the amount of death was noted (3.48% dead). This decrease in cellular viability was not noted in the co-exposed

samples dosed with Fe_2O_3 and ox-ECB. In the ox-ECB co-exposure results indicate a slight dose-dependent decrease in cellular viability following co-exposure to 0.01 $\mu g/mL$ Fe_2O_3 combined with 4 $\mu g/mL$ ECB (.39% dead) to 10 $\mu g/mL$ Fe_2O_3 and 4 $\mu g/mL$ ECB (1.75% dead). These results indicate that while a slight decrease in cellular viability exists in a co-exposure scenario (max. 7.62% dead, 10 $\mu g/mL$ Fe_2O_3 and 4 $\mu g/mL$ ECB) at a 24 hour time point, this decrease may be eliminated by surface oxidation of the ECB nanoparticle.

Discussion

Over the course of this examination, we aimed to continue to investigate the cellular response to exposure to a synergistic mixture of Fe_2O_3 and ECB nanoparticles in an *in vitro* cell culture model. While the A549 lung epithelial cell line is not a phagocytic cell line, it is routinely used to assess uptake of inhaled particulate in situations where the capacity of the alveolar macrophage to mitigate particle clearance has been exceeded. The human lung epithelial cell line A549 has been previously shown to be of utility for alveolar epithelial cell interaction with micro-sized particles and dusts [149, 156]. Previously, Guo et. al. (2009) suggested that mixtures of Fe_2O_3 and ECB nanoparticles induced cellular toxicity through an oxidative stress mechanism because the ECB nanoparticles were able to reduce Fe^{3+} to Fe^{2+} through surface functional groups. This paper expands upon this toxicity paradigm by not only confirming previous results, but elucidating a mechanism through which these nanoparticles elicit their effect.

Intracellular Localization and Lysosomal Analysis. All three nanoparticle-types were seen to be internalized into the cell in co-exposure scenarios. This study confirms the ability of both Fe_2O_3 and ECB and/or ox-ECB nanoparticles to enter the intracellular environment in a time-dependent fashion. Interestingly, the nanoparticles were localized in vesicles (i.e. endosomes and/or lysosomes) as either a single species (i.e. either Fe_2O_3 *or* ECB) or as a mixture of species (Fe_2O_3 *and* ECB). This leads to the possibility that each type of nanoparticle enters the cell through independent events, either through a type of receptor-mediated endocytosis or non-specific fluid phase uptake. Recent work has demonstrated the ability for nanoparticles to bind biological molecules including proteins in the physiological environment [157]. This protein adherence may lead to differences in the mechanism responsible for each specific endocytic event. Furthermore, many studies have demonstrated that nanoparticles enter a cellular system through a variety of mechanisms including clathrin-mediated endocytosis, macropinocytosis, phagocytosis, as well as simple passive diffusion [158-162]. Intracellular trafficking normally directs endocytosed macromolecules into endosomal or lysosomal compartments. It is in these locations that the decrease in pH is responsible for not only the hydrolysis of ligands from their receptors, but additionally the degradation of macromolecules. Examinations by TEM and fluorescence microscopy confirm a similar fate (lysosomal incorporation) for both the carbonaceous and metal oxide nanoparticles studied here.

Zhang et al. (2009) demonstrated similar results with quantum dot nanoparticles. They examined an increase in lysosomal accumulation at 24 hours as verified by fluorescence co-localization of quantum dot and CD63/Lamp-1 in an HEK cell line [163]. Nanoparticle accumulation in lysosomal compartments after 24 hours provides the correct conditions (acidic pH) to begin the intracellular release of Fe^{3+} ions from the surface of the Fe_2O_3 nanoparticle.

The Role of Reactive Oxygen Species. The oxidative stress paradigm has thus far had a major impact in the nanotoxicology literature. The data here indicates that this particular particle-cell interaction is no different. While Fe_2O_3 at the highest dose exhibits a significant amount of oxidant production, Fe_2O_3 alone at lower concentrations (0.1 and 0.01 μg/mL) does not induce oxidative stress or produce oxidant species at the time points reported in this study. At the 2.5 hour time point, oxidation of DCFH is seen at similar levels throughout all the co-exposed ratios, however at the 25 hr time point this is not the case. The lowest ratio (0.01 Fe_2O_3:4.0 ECB) of nanoparticles exhibited the highest oxidative stress of all the co-exposure scenarios. This effect may be due to the decrease in cellular proliferation and slight decrease in cellular viability occurring at the higher nanoparticle ratios as evidenced by the MTT assay.

Co-exposures to Fe_2O_3 and ECB demonstrated significant oxidant production in previous cell culture studies, while exposures to Fe_2O_3 or ox-ECB alone did not induce significant oxidative stress [149]. In these studies, we have shown that after cell culture inoculation to Fe_2O_3 and ECB and/or ox-ECB, both

materials are endocytosed within the same vesicular structure. Furthermore, intracellular reactive oxygen species were found. However, the oxidant production of Fe_2O_3 and ECB was mitigated when the surface of the carbon black was oxidized before co-exposure or prevented after addition of L-ascorbic acid to the culture medium as an antioxidant.

Cellular Proliferation and Viability. Cellular proliferation was measured via the MTT assay. The MTT assay is very widely accepted in the literature as a measure of cell proliferation, mitochondrial activity, and/or cytotoxicity [164]. However, in this manuscript, we conclude that while the MTT assay shows a decrease in cellular proliferation, a similar degree of cell death was not observed using the live/dead assay. Therefore, it remains possible that exposure to ECB and Fe_2O_3 causes inhibition of cellular proliferation without appreciable cell death occurring. Similar results have been shown by Stone et. al. (1998) [165]. In the manuscript by Stone et. al., the MTT assay was used to study the relative inhibitory effects of particles. Furthermore, it is indicated that the A549 cell line shows inhibition of proliferative effects following exposure to fine-sized carbon black, which may be recovered at later time points. Similarly, a decrease in proliferation rate, combined with no reduction in cellular viability was shown in A549 cells grown under hyperoxic conditions [166]. As only slight cell death was noted at the 24 hour time point, it may be possible that the cells utilized for this experiment yield a different cytotoxic response at a later time point.

Previously, we asked if this oxidative stress was particle generated or if the oxidative stress had basis within a cellular mediated event. We concluded

that this mechanism demonstrates qualities of both. Here, we have shown that both Fe_2O_3 and ECB or ox-ECB are endocytosed and subsequently contained in acidified lysosomes. From *ex vivo* analysis, we have previously shown that under acidic conditions (i.e. lysosome), Fe^{3+} is released from the surface of the Fe_2O_3 nanoparticle. Second, interactions between nanoparticles in close proximity allow ECB to reduce the Fe^{3+}, thus producing soluble Fe^{2+} ions. These Fe^{2+} ions are then thought to proceed through well documented intracellular redox cycling reactions, such as the Fenton Reaction, in which ROS are inherently generated. Furthermore, we have shown that this reaction can be mitigated by prior oxidation of the ECB to ox-ECB before entering the biological environment.

Toxicity data sets collected from cellular systems exposed to a nanomaterial or a mixture of nanomaterials can aid in the material design process and risk assessment. Nanoparticle-specific modes/mechanisms of toxicity are, in some cases, complex. This is especially true when combining the enormous range of nanoparticle-types, morphologies, and redox capacities with the uncertainty of both occupational exposures and subsequent consumer use of nanoparticle-enabled products. Particle toxicology in this emerging area must provide a basis for predicting how the biological behavior after a nanomaterial exposure relates to the nanomaterial physicochemical properties, including chemical composition and reduction capacity.

Our aim is that this work will establish a new scenario for future efforts to characterize the environmental and health impacts of nanoparticle mixtures.

This proactive approach is necessary to the nanomaterial design process and the regulatory environment.

Acknowledgements

The authors would like to thank the Microscopy Imaging Center (Dr. Andreas Holzenburg and Ann Ellis) and the Image Analysis Laboratory (Dr. Ross Payne and Dr. Robert Burghardt) at Texas A&M University for providing the electron microscopy facilities. JMB and CMS thank Dr. Weston Porter and Kelly Scribner for their help in acquisition of florescence microscopy images. The authors would like to thank Texas A&M University and Texas Engineering Experiment Station for their financial support.

FIGURES

Figure Captions

Table C-1. Characterization of Fe_2O_3, ECB, and ox-ECB nanoparticles.

Figure C-1. Intracellular nanomaterial localization analyses. Internalization of both Fe_2O_3 and ECB agglomerates into A549 cells visualized through the use of electron microscopy. While in a majority of instances cellular vesicles contained either Fe_2O_3 or ECB, many cases where apparent where both nanoparticle types were internalized into the same cellular vesicles. This was equally apparent with the ECB and Fe_2O_3 mixtures (a&b) as it was with the ox-ECB and Fe_2O_3 (c&d) mixtures leading to the fact that oxidizing the surface of ECB does not inhibit uptake of ox-ECB nanoparticles.

Figure C-2. Intracellular metal analysis of lung epithelial cells dosed with either Fe_2O_3 nanoparticles or ECB and Fe_2O_3 nanoparticles alone via inductively coupled plasma-mass spectroscopy. The iron content in the cell culture media removed from cell culture after Fe_2O_3 exposure is 0.017 mexposure is 0.017 the cell culture media removed from$_2O_3$ is 0.175 mis 0.175 is 0.017 the cell culture media removed from cell culture after Fe inhibit uptak$_2O_3$ is 0.193 mis 0. The iron content in the cell culture media removed from cell culture after ECB and Fe_2O_3 exposure is 0.014 mexposure is 0.014 the cell culture media removed from cell culture afte$_2O_3$ is 0.177 mis 0.177

is 0.014 the cell culture media removed from cell culture after ECB and Fe uptak e of ox-ECB nan$_2$O$_3$ is 0.192 mis 0.

Figure C-3. Lysosomal characterization. Lung epithelial cells were exposed to both Fe_2O_3 and ECB/ox-ECB nanoparticles for a variety of time points ranging from 1 hr to 24 hours and subsequently incubated with Lysotracker red dye. Low basal levels of lysosomes were found in control cells at all time points with an increase seen in actively dividing cells. Similar amounts of acidified lysosomes (pH<5.2) (red) are increasingly visualized in both ECB and ox-ECB co-exposed samples. Lysosome fluorescence is found to increase throughout both exposed cell populations as the time increases from 1 hr to 24 hrs. This increase in acidified lysosomes yields conditions which may promote dissolution of the surface of the Fe_2O_3 nanoparticle. Scale bar = 100 mna

Figure C-4. ROS detection and the addition of L-ascorbic acid. Human lung epithelial cells were exposed to Fe_2O_3 only, Fe_2O_3 and ECB, Fe_2O_3 and L-ascorbic acid, or Fe_2O_3 and ox-ECB for both 2.5 hours (top) and 25 hours (bottom). Results indicate that co-exposure to Fe_2O_3 and ECB generate intracellular oxidative stress that can be lessened by the addition of L-ascorbic acid or through surface oxidation of the ECB (ox-ECB). Values given are means ± SD (*$p < 0.05$ relative to control cell population).

Figure C-5. Cellular Proliferation and Viability. Human lung epithelial cells were exposed to both Fe_2O_3 nanoparticles and ECB nanoparticles or Fe_2O_3 nanoparticles and oxidized ECB nanoparticles at varying degrees of particle concentrations. (A) Cellular proliferation, as measured by mitochondrial dehydrogenase activity, of cells exposed to Fe_2O_3 (concentration noted on x-axis) spiked with 4.0 m(concentration noted on x-axis) spiked with 4.0 varying degrees of particle concentrations$_2O_3$ (concentration noted on x-axis) spiked with 4.0 m(concentration noted on x-axis) spiked with 4.0 varying degrees of particle concentrations. (A) Cellular prolif$_2O_3$ and 4
mnd 4 entration noted on x-axis) spiked with 4.0 vwhile dead cell nuclei fluoresc e red. (D) Live/Dead cytotoxicity assay of cells exposed to 10 mnd 4 en$_2O_3$ and 4 mnd 4 entration noted on x-axis) spiked with 4.0 vwhile dead cell nuclei fluoresc e red. (D) Live/Dead cytotoxicity assay of cells exposed to 1noted in the co-exp osure with ECB, which is not noted, to a similar extent, with ox-ECB.

Table B-1. Characterization of Fe_2O_3, ECB, and ox-ECB nanoparticles.

Property	**Fe_2O_3**	**ECB**	**ox-ECB**
Size, nm	41 ± 17	47 ± 7	47 ± 7
Zeta Potential, mV*	-44.2 ± 5.9	-51.2 ± 6.02	-52.4 ± 6.02
Crystalline Structure	Maghemite	Amorphous	Amorphous
Specific Surface Area, m^2/g	49	63	Not measured
SSA Calculated Size†, nm	23.5	52.8	N/A
Reductive Capacity, $g(Fe^{3+})/g(carbon)$	Not Measured	9.0×10^{-3}	2.4×10^{-4}
%C:%O (O/C Ratio)	Not measured	89.88:10.12 (0.1126)	88.53:11.47 (0.1295)

* Zeta Potential measured in DDH_2O; pH = 5.9

† Size calculated using the formula: Size = 6000/(BET SSA) x (Density)

Figure B-1. Intracellular nanomaterial localization analyses via electron microscopy.

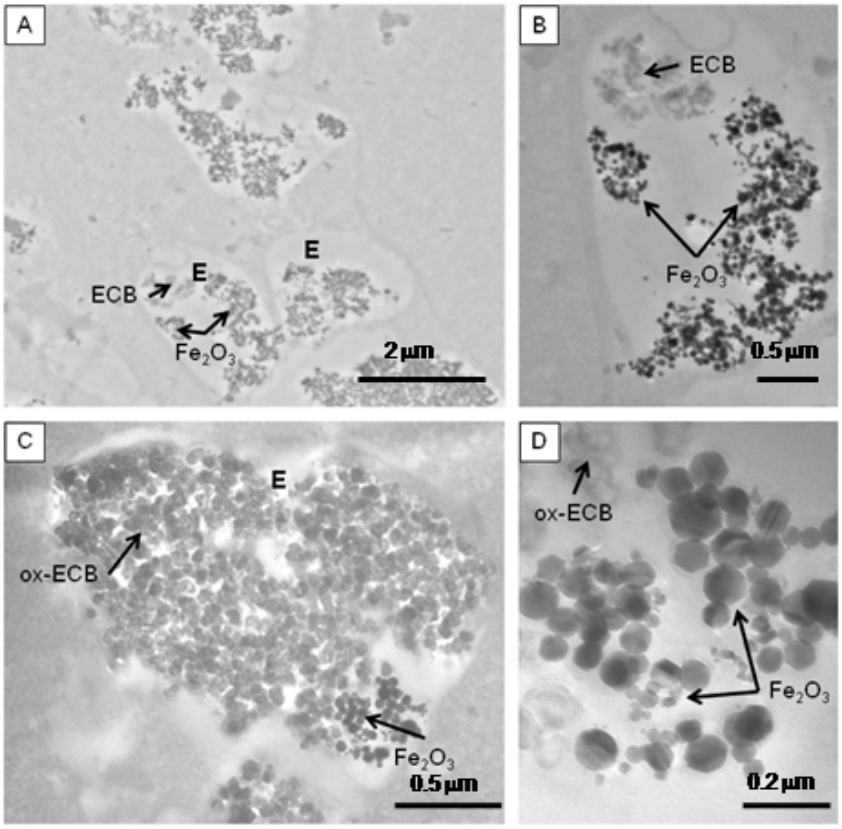

Figure B-2. Intracellular metal analysis via inductively coupled plasma-mass spectroscopy.

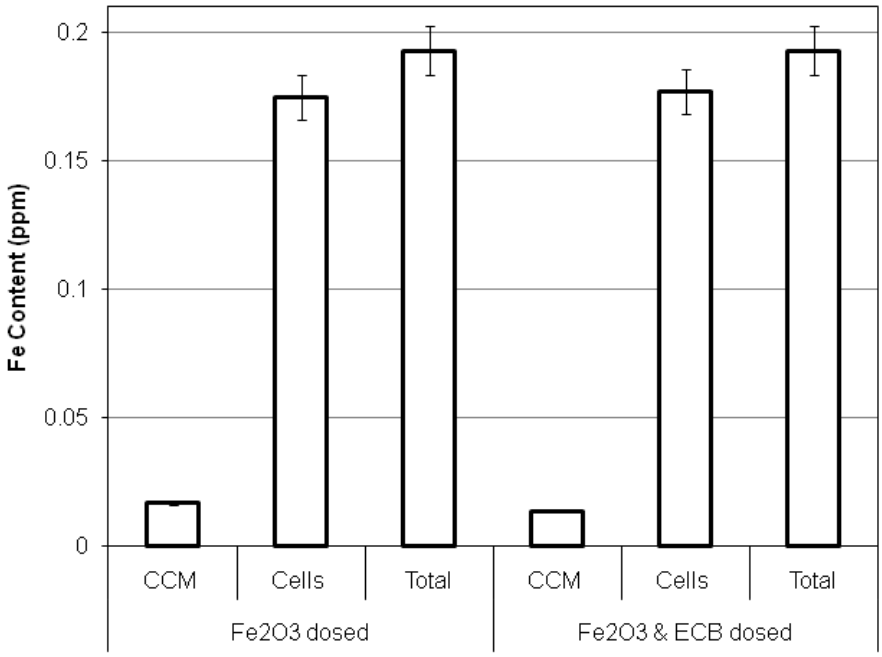

Figure B-4. Lysosomal characterization.

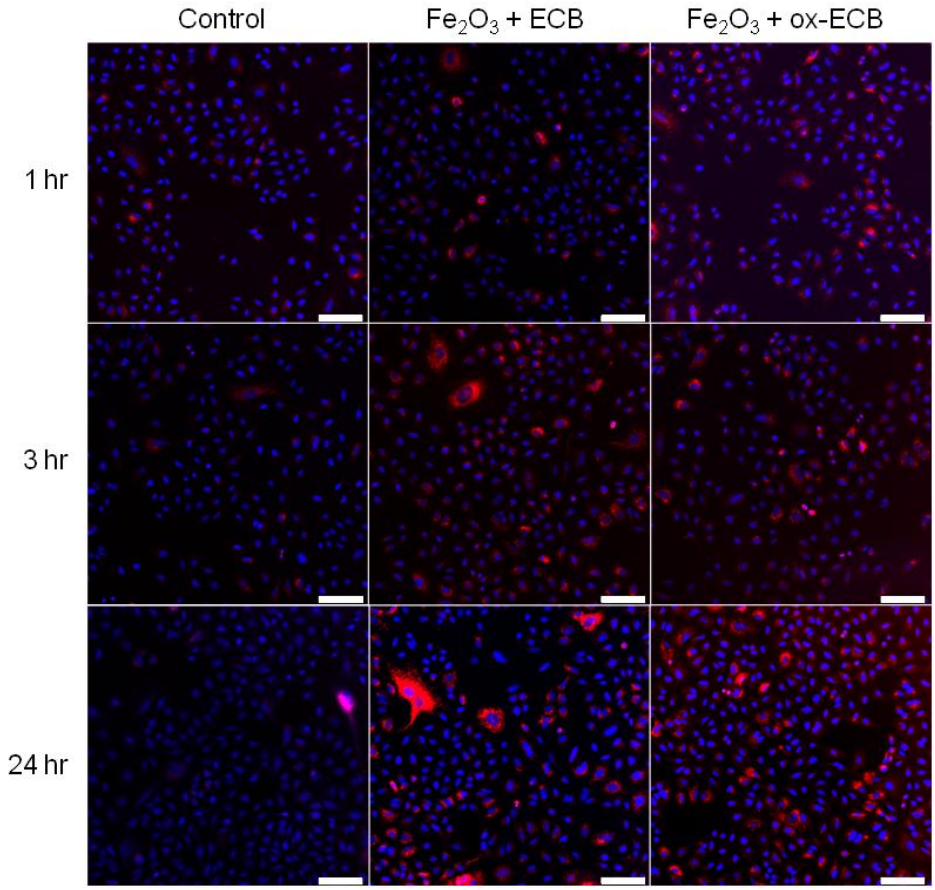

Figure B-5. Oxidant production.

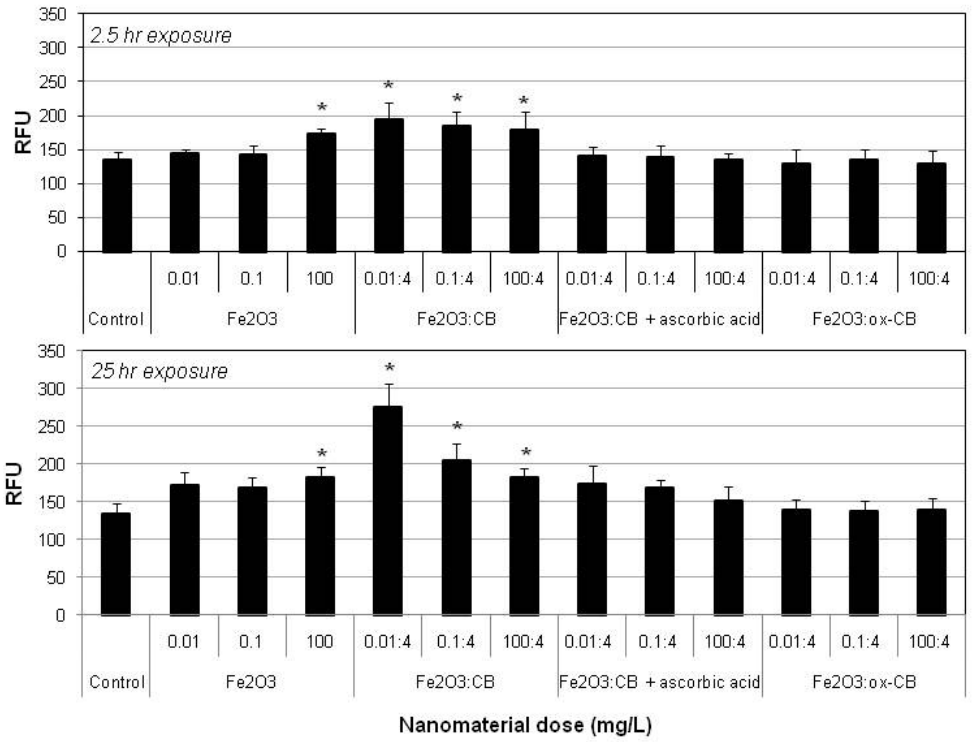

Figure B-5. Metabolic activity and cell death of lung epithelial cells after exposure to iron oxide and engineered carbon black versus iron oxide and oxidized engineered carbon black.

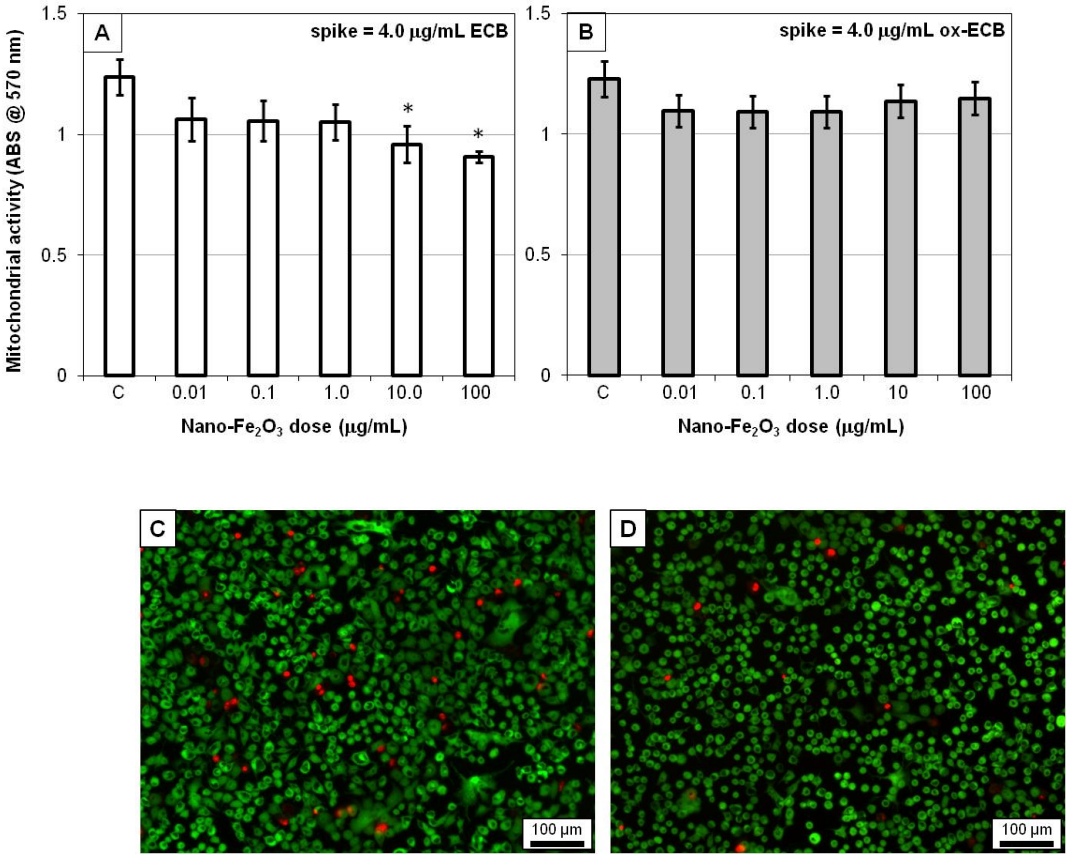

Fe_2O_3 dose (mdose	% Dead co-exposed to ECB (4 mCB (4	% Dead co-exposed to ox-ECB (4 mx-ECB
0.01	0.69	0.39
0.1	1.48	0.59
1.0	1.59	0.58
10	7.62	1.48
100	3.48	1.75

References

(B-1) Li, M., Hong, Z., Fang, Y., and Huang, F. (2008) Synergistic effect of two surface complexes in enhancing visable-light photocatalytic activity of titanium dioxide. *Materials Research Bulletin*, *43*, 2179-2186.

(B-2) Provenzale, J. M., and Silva, G. A. (2009) Uses of nanoparticles for central nervous system imaging and therapy. *AJNR Am J Neuroradiol*, *30*, 1293-1301.

(B-3) Choquenet, B., Couteau, C., Paparis, E., and Coiffard, L. (2008) Quercetin and Rutin as Potential Sunscreen Agents: Determination of Efficacy by an in Vitro Model. *Journal of Natural Products*, *71*, 1117-1118.

(B-4) Hexsel, C. L., Bangert, S. D., Herbert, A. A., and Lim, H. W. (2008) Current Sunscreen issues: 2007 Food and Drug Administration Sunscreen labelling recommendations and combination sunscreen/insect repellent products. *J. Am. Acad. Dermatol*, *59*, 316-323.

(B-5) Valberg, P. A., Long, C. M., and Sax, S. N. (2006) Integrating studies on carcinogenic risk of carbon black: Epidemiology, animal exposures, and mechanism of action. *Journal of Occupational and Environmental Medicine*, *48*, 1291-1307.

(B-6) Alcantara, R., Lavela, P., Ortiz, G. F., Tirado, J. L., Stoyanova, R., Zhecheva, E., and Mateos, J. (2004) Modification of petroleum coke for lithium-ion batteries by heat-treatment with iron oxide. *Journal of the Electrochemical Society*, *151*, A2113-A2119.

(B-7) Bulushev, D. A., Kiwi-Minsker, L., Yuranov, I., Suvorova, E. I., Buffat, P. A., and Renken, A. (2002) Structured Au/FeOX/C catalysts for low-temperature CO oxidation. *Journal of Catalysis*, *210*, 149-159.

(B-8) Martirosyan, K. S., Chang, L., Rantschler, J., Khizroev, S., Luss, D., and Litvinov, D. (2007) Carbon combustion synthesis and magnetic properties of cobalt ferrite nanoparticles. *Ieee Transactions on Magnetics*, *43*, 3118-3120.

(B-9) Schulte, P. A., Schubauer-Berigan, M. K., Mayweather, C., Geraci, C. L., Zumwalde, R., and McKernan, J. L. (2009) Issues in the development of epidemiologic studies of workers exposed to engineered nanoparticles. *J Occup Environ Med*, *51*, 323-335.

(B-10) Sharma, M. (2010) Understanding the mechanism of toxicity of carbon nanoparticles in humans in the new millennium: A systemic review. *Indian Journal of Occupational & Environmental Medicine*, *14*, 3-5.

(B-11) Cass, G. R., Hughes, L. A., Bhave, P., Kleeman, M. J., Allen, J. O., and Salmon, L. G. (2000) The chemical composition of atmospheric ultrafine particles. *Philos T Roy Soc A*, *358*, 2581-2592.

(B-12) Guo, B., Zebda, R., Drake, S. J., and Sayes, C. M. (2009) Synergistic effect of co-exposure to carbon black and Fe2O3 nanoparticles on oxidative stress in cultured lung epithelial cells. *Part. Fib. Tox.*, *6*, 4.

(B-13) Guo, B., Zebda, R., Drake, S. J., and Sayes, C. M. (2009) Synergistic effect of co-exposure to carbon black and Fe2O3 nanoparticles on oxidative stress in cultured lung epithelial cells. *Particle and Fibre Toxicology*, *6*, 4.

(B-14) Fu, R. W., Zeng, H. M., and Lu, Y. (1993) The Reduction Property of Activated Carbon-Fibers. *Carbon*, *31*, 1089-1094.

(B-15) Kung, K. H., and McBride, M. B. (1988) Electron transfer processes between hydroquinone and iron oxides. *Clays and Clay Minerals*, *36*, 303-309.

(B-16) Hediger, M. A. (1997) Membrane permeability. The diversity of transmembrane transport processes. *Curr Opin Cell Biol*, *9*, 543-546.

(B-17) Guo, B., and Kennedy, I. M. (2007) Gas-phase flame synthesis and characterization of iron oxide nanoparticles for use in a health effects study. *Aerosol Sci Tech*, *41*, 944-951.

(B-18) Rauen, U., Petrat, F., Sustmann, R., and de Groot, H. (2004) Iron-induced mitochondrial permeability transition in cultured hepatocytes. *J Hepatol*, *40*, 607-615.

(B-19) Serpone, N., Salinaro, A., and Emeline, A. V. (2001) Deleterious effects of sunscreen Titanium Dioxide Nanoparticles on DNA. Efforts to limit DNA Damage by Particle Surface Modification. *Proceedings of SPIE* , *4258*, 86-98.

(B-20) Warheit, D. B., Webb, T. R., Reed, K. L., Frerichs, S., and Sayes, C. M. (2007) Pulmonary toxicity study in rats with three forms of ultrafine-TiO2 particles: Differential responses related to surface properties. *Toxicology*, *230*, 90-104.

(B-21) Sayes, C. M., Wahi, R., Kurian, P. A., Liu, Y., West, J. L., Ausman, K. D., Warheit, D. B., and Colvin, V. L. (2006) Correlating nanoscale titania

structure with toxicity: a cytotoxicity and inflammatory response study with human dermal fibroblasts and human lung epithelial cells. *Toxicol Sci*, *92*, 174-185.

(B-22) Cheng, X. M., Kan, A. T., and Tompson, M. B. (2004) Naphthalene adsorption and desorption from aqueous c60 fullerene. *J. Chem. Eng. Data*, *49*, 675-683.

(B-23) Berne, B. J., and R., P. (1976) *Dynamic Light Scattering*. John Wiley & Sons, Inc., New York.

(B-24) Brunauer, S., Emmett, P. H., and Teller, E. (1938) Adsorption of gases in multimolecular layers. *J Am Chem Soc*, *60*, 309-319.

(B-25) Fairley, N., Carrick, A., and Fairly, N. (2005) *The Casa cookbook : Pt. 1: Recipes for XPS Data Processing*. Acolyte Science, Knutsford.

(B-26) Briggs, D., and Seah, M. P. (1990) *Practical surface analysis. Vol. 1, Auger and X-ray photoelectron spectroscopy*. Wiley, Chichester.

(B-27) Xie, Y., and Sherwood, P. M. A. (1991) X-ray photoelectron-spectroscopic studies of carbon fiber surfaces. Part 13. Valence-band studies of oxidized fibers interpreted by X.alpha. calculations. *Chemistry of Materials*, *3*, 164-168.

(B-28) Canas-Ventura, M. E., Klappenberger, F., Clair, S., Pons, S., Kern, K., Brune, H., Strunskus, T., Woll, C., Fasel, R., and Barth, J. V. (2006) Coexistence of one- and two-dimensional supramolecular assemblies of terephthalic acid on Pd(111) due to self-limiting deprotonation. *The Journal of Chemical Physics*, *125*, 184710-184718.

(B-29) Popat, R. P., Sutherland, I., and Sheng, E.-S. (1995) Vapour-phase chemical derivatisation for the determination of surface functional groups by X-ray photoelectron spectroscopy. *Journal of Materials Chemistry*, *5*, 713-717.

(B-30) Estrade-Szwarckopf, H. (2004) XPS photoemission in carbonaceous materials: A "defect" peak beside the graphitic asymmetric peak. *Carbon*, *42*, 1713-1721.

(B-31) Szabó, T., Berkesi, O., Forgó, P., Josepovits, K., Sanakis, Y., Petridis, D., and Déckány, I. (2006) Evolution of Surface Functional Groups in a Series of Progressively Oxidized Graphite Oxides. *Chemistry of Materials*, *18*, 2740-2749.

(B-32) Reynolds, E. S. (1963) The Use of Lead Citrate at High pH as an Electron-Opaque Stain in Electron Microscopy. *The Journal of Cell Biology*, *17*, 208-212.

(B-33) Wang, H., and Joseph, J. A. (1999) Quantifying cellular oxidative stress by dichlorofluorescein assay using microplate reader. *Free Radic Biol Med*, *27*, 612-616.

(B-34) Foucaud, L., Wilson, M. R., Brown, D. M., and Stone, V. (2007) Measurement of reactive species production by nanoparticles prepared in biologically relevant media. *Toxicol Lett*, *174*, 1-9.

(B-35) York, J. L., Maddox, L. C., Zimniak, P., McHugh, T. E., and Grant, D. F. (1998) Reduction of MTT by glutathione S-Transferase. *Biotechniques*, *25*, 622-+.

(B-36) Wang, P. W., Henning, S. M., and Heber, D. (2010) Limitations of MTT and MTS-Based Assays for Measurement of Antiproliferative Activity of Green Tea Polyphenols. *Plos One*, *5*, -.

(B-37) Maioli, E., Torricelli, C., Carlucci, F., Tommassini, V., and Pacine, A. (2009) Critical Appraisal of the MTT Assay in the Presence of Rottlerin and Uncouplers. *Biological Procedures Online*, *11*.

(B-38) Babior, B. M. (1984) Oxidants from Phagocytes - Agents of Defense and Destruction. *Blood*, *64*, 959-966.

(B-39) Stringer, B., Imrich, A., and Kobzik, L. (1996) Lung epithelial cell (A549) interaction with unopsonized environmental particulates: quantitation of particle-specific binding and IL-8 production. *Exp Lung Res*, *22*, 495-508.

(B-40) Lundqvist, M., Stigler, J., Elia, G., Lynch, I., Cedervall, T., and Dawson, K. (2008) Nanoparticle size and surface properties determine the protein corona with possible implications for biological impacts. *PNAS*, *105*, 14265-14270.

(B-41) Dausend, J., Musyanovych, A., Dass, M., Walther, P., Schrezenmeier, H., Landfester, K., and Mailander, V. (2008) Uptake mechanism of oppositely charged fluorescent nanoparticles in HeLa cells. *Macromol Biosci*, *8*, 1135-1143.

(B-42) Chithrani, B. D., Ghazani, A. A., and Chan, W. C. (2006) Determining the size and shape dependence of gold nanoparticle uptake into mammalian cells. *Nano Lett*, *6*, 662-668.

(B-43) Davada, J., and Labhasetwar, V. (2002) Characterization of nanoparticle uptake by endothelial cells. *International journal fo Pharmaceutics , 233*, 51-59.

(B-44) Qaddoumi, M. G., Gukasyan, H. J., Davda, J., Labhasetwar, V., Kim, K. J., and Lee, V. H. (2003) Clathrin and caveolin-1 expression in primary pigmented rabbit conjunctival epithelial cells: role in PLGA nanoparticle endocytosis. *Mol Vis*, *9*, 559-568.

(B-45) Harush-Frenkel, O., Rozentur, E., Benita, S., and Altschuler, Y. (2008) Surface charge of nanoparticles determines their endocytic and transcytotic pathway in polarized MDCK cells. *Biomacromolecules*, *9*, 435-443.

(B-46) Zhang, L. W., and Monteiro-Riviere, N. A. (2009) Mechanisms of quantum dot nanoparticle cellular uptake. *Toxicol Sci*, *110*, 138-155.

(B-47) Mosmann, T. (1983) Rapid colorimetric assay for cellular growth and survival: application to proliferation and cytotoxicity assays. *J Immunol Methods*, *65*, 55-63.

(B-48) Stone, V., Shaw, J., Brown, D. M., Macnee, W., Faux, S. P., and Donaldson, K. (1998) The role of oxidative stress in the prolonged inhibitory effect of ultrafine carbon black on epithelial cell function. *Toxicol In Vitro*, *12*, 649-659.

(B-49) McGrath-Morrow, S. A., and Stahl, J. (2002) Inhibition of glutamine synthetase in a549 cells during hyperoxia. *Am J Respir Cell Mol Biol*, *27*, 99-106.

VITA

KYLE DOUGLAS CUMMINS
Dept. of Chemistry, c/o Dr. Manuel P. Soriaga, Texas A&M University
College Station, TX 77842-3012
(979) 845-6914; kyle.cummins@gmail.com

EDUCATION

Ph.D., Analytical Chemistry, Texas A&M University,
College Station, TX, 2012
B.S. Chemistry, *Magna cum laude,* Rockhurst University,
Kansas City, MO, 2005

SELECTED PUBLICATIONS

"Molecular Chemisorption at Electrocatalyst Surfaces. A Bibliography." P. Kar, K. Cummins, J. H. Baricuatro, M. A. Hossain, D. Li, and M. P. Soriaga, ECS Transactions, 3, 187-211(2007).

"Characterization of Alloy Electrocatalysts by Combined Low-Energy Ion Scattering Spectroscopy and Electrochemistry." S. Axnanda, K. D. Cummins, D. W. Goodman, and M. P. Soriaga, In Modern Aspects of Electrochemistry, ed. P. B. Balbuena and V. R. Subramanian, 50, 1-23(2010)

"Internalization of Carbon Black and Maghemite Iron Oxide Nanoparticle Mixtures Leads to Oxidant Production." J. M. Berg, S. Ho, W. Hwang, R. Zebda, K. Cummins, M. P. Soriaga, R. Taylor, B. Guo, and C. M. Sayes, Chemical Research in Toxicology, 23, 1874-1882(2010).

"Structural, Compositional and Electrochemical Characterization of Pt-Co Oxygen-Reduction Catalysts." S. Axnanda, K. D. Cummins, T. He, D. W. Goodman, and M. P. Soriaga, ChemPhysChem, 11(2010).

"The Structure, Composition and Reactivity of Clean and Ambient-Exposed Polycrystalline and Monocrystalline Mg Surfaces." J. B. Abreu, J. Sanabria-Chinchilla, K. D. Cummins, J. L. Stickney, and M. P. Soriaga, Journal of Electroanalytical Chemistry, 662, 36-42(2011).

"Digital Deposition of Ultrathin Pd Films on Well-Defined Pt(111) Electrodes Via Surface-Limited Redox Replacement Reaction: An Electron Spectroscopy-Electrochemistry Study." M. A. Hossain, K. D. Cummins, and M. P. Soriaga, To-be-published, (2012).

"Highly-Ordered Ultrathin Pd Films on Pt(111): Preparation by Galvanic Displacement and Structural Characterization." K. D. Cummins, M. A. Hossain, M. P. Soriaga, and J. L. Stickney, To-be-published, (2012).

"Selective and Quantitative Removal of Pd Films from Au Substrates by Adsorbed-Iodine-Catalyzed Anodic Stripping." E. A. Lafferty, M. A. Hossain, K. D. Cummins, and M. P. Soriaga, To-be-published, (2012).